Time Domain Filtered Cross Spectral Density detection and direction finding of spread spectrum signals, and implementation using acousto-optic correlation.

by

Andrew Warren Houghton

A thesis submitted to the University of Plymouth
for the degree of

Doctor of Philosophy

School of Electronic Communication and Electrical Engineering

Work carried out in

Electrical and Electronic Engineering Department
Royal Naval Engineering College

in collaboration with

DRA Funtington

January 1996

Time Domain Filtered Cross Spectral Density detection and direction finding of spread spectrum signals, and implementation using acousto-optic correlation.

by Andrew Warren Houghton

Abstract

This thesis presents a technique for the detection of spread spectrum signals, of arbitrary form, even when the signal power spectral density (PSD) is well below the surveillance receiver noise spectral density, using a pair of antennas with broadband (1 GHz or more) receivers. Cross correlating the outputs of two receivers, spatially separated by a distance of the order of one metre or more, produces a cross correlation function (ccf) in which the noise components are spread uniformly over the whole width while the signal component, the narrow autocorrelation function (acf) of the spread spectrum signal, is concentrated near to the centre. The acf is displaced from the centre of the ccf by a small time shift equal to the time difference of arrival of the signal at the two antennas. A simple time domain filter can select a narrow centre portion of the ccf, rejecting the remainder which contains only noise. Taking the Fourier transform of this windowed ccf produces the "time domain filtered cross spectral density" (TDFCSD), in which the signal to noise ratio is independent of receiver bandwidth. Spread spectrum signals can then be both detected and characterised in an extremely sensitive broadband system by threshold detection applied to the magnitude of this TDFCSD. High resolution direction finding can then be achieved by estimating the time difference of arrival at the two antennas from the phase slope of the appropriate part of the TDFCSD. An analysis of the performance of this dual receiver system is presented. A computer simulation illustrates the signal processing involved and shows excellent agreement with the analysis. An analysis of the detection performance of this system acting in an electronic support measure (ESM) role and comparison with other

systems shows that, in addition to being able to obtain more information, this system can offer significantly greater sensitivity than a crystal video receiver.

Acousto-optic correlation may be used to perform the cross correlation and time domain filtering of wideband signals in real time, with final processing of the much reduced data set to obtain and analyse the TDFCSD being carried out digitally. A novel non-heterodyning space integrating architecture capable of forming the true correlation function using the zeroth diffraction orders from acousto-optic cells was invented, the operation of which is not explained by the commonly used methods of analysis. By looking again at the acousto-optic interaction, it is shown that there is considerable information in the zeroth diffraction order and a unified theory of one dimensional space integrating correlators is developed, in which many known architectures can be treated as special cases of a general all order correlator. Because of practical difficulties in using a space integrating correlator to obtain the TDFCSD for continuous inputs, later work concentrated on time integrating correlation. Theoretical analysis and practical results are presented for a time integrating acousto-optic correlator, demonstrating that it gives itself naturally to the signal processing operations required and could be used in a real surveillance system making use of the TDFCSD for detection and direction finding.

List of Contents

page

Abstract iii

List of Tables and Figures x

Acknowledgements xvii

Authors declaration xviii

1. Introduction 1

1.1. Introduction to spread spectrum signals 1

1.1.1. Spread spectrum communication systems 1

1.1.2. Spread spectrum radar systems 5

1.2. Introduction to the cross correlation receiver and the "TDFCSD" 10

1.3. Degree of spatial coherence between the antennas 14

1.4. Outline of the thesis 17

2. The cross correlation process 21

2.1. Introduction 21

2.2. Different correlation processes 23

2.3. Finite sample time domain correlation noise performance 26

2.3.1. Noise-noise cross correlations 26

2.3.2. Signal-noise cross correlations 31

2.3.3. Total output SNR 34

2.3.4. Output SNR for CW signals 36

2.4. True continuous and finite sample frequency domain correlation 36

2.4.1. Output SNR 36

2.4.2 Output SNR for CW signals 38

2.5. The radar correlation process 38

2.6. Simulation 40

2.7. Summary 43

3. The Time Domain Filtered Cross Spectral Density **44**

3.1. SNR in the Cross Spectral Density 44

3.2. Effect of time domain filtering on the cross spectral density 45

3.2.1. SNR using a FSFD or TC correlator, LFM signals 46

3.2.2. SNR using a FSTD correlator, LFM signals 47

3.3. Biphase coded signals 48

3.4. Comparison of SNR in the ccf and the TDFCSD 50

3.5. Simulation 54

4. ESM System performance **58**

4.1. Introduction 58

4.2. Threshold SNRs for signal detection 59

4.3. Power managed LPI radars 61

4.4. Range advantage of ESM systems 64

4.5. Minimum detection range 66

4.6. The crystal video receiver 68

4.7. The cross correlation receiver 73

4.7.1. The ccf receiver and pulsed radar - advantage over crystal video receiver 73

4.7.2. The ccf receiver and CW radar 77

4.8. The TDFCSD receiver 80

4.8.1. The TDFCSD receiver and pulsed radar 80

4.8.2. The TDFCSD receiver and CW radar 83

4.9. Conclusions 85

5. Direction finding **88**

5.1. Introduction 88

5.2. Effect of noise on the phase of the TDFCSD 89

5.3. Condition for phase unwrap without error 93

5.4. Error in estimation of phase slope 94

5.5. Accuracy of direction finding 97

5.6. Simulation 102

5.7. Separation of multiple signals 104

6. Implementation using acousto-optic correlators 106

6.1. Introduction 106

6.2. Space integrating correlation 106

6.3. Time integrating correlation 108

6.4. Joint transform correlation 109

7. The acousto-optic interaction 111

7.1. Introduction 111

7.2. Bragg diffraction 112

7.3. Raman-Nath diffraction 114

7.4. Derivation of diffraction orders 116

7.5. Focusing of the diffraction pattern 118

7.6. Fine structure of the principal diffraction orders 120

7.7. Experimental evidence 123

7.8. Conclusions 124

8. Space-integrating acousto-optic correlators 129

8.1. Introduction 129

8.2. The general all order space integrating correlator 131

8.2.1. Analysis based on Raman-Nath diffraction theory 131

8.2.2. Bragg diffraction 138

8.3. Zeroth order non-heterodyning correlator 140

8.3.1. Operation in the Raman-Nath mode 141

8.3.2. Operation in the Bragg mode 141

8.4. Experimental results for zeroth order non heterodyning correlator 142

8.5. Zeroth order non-heterodyning correlator using a photographic mask 148

8.5.1. Operation in the Raman-Nath mode 148

8.5.2. Operation in the Bragg mode 150

8.6. First order non-heterodyning correlator 150

8.6.1. Operation using DSBLC modulation 150

8.6.2. Operation in the Bragg mode 151

8.6.3. Operation using DSBSC modulation 151

8.6.4. Operation in the Bragg mode 154
8.7. Heterodyning correlator using 0 and +1 diffraction orders 154
8.7.1. Operation in the Raman-Nath mode, DSBSC modulation 155
8.7.2. Operation in the Bragg mode 157
8.8. Heterodyning correlator using both first diffraction orders 157
8.8.1. Operation using DSBLC modulation 158
8.8.2. Operation using DSBSC modulation 159
8.9. Summary 159

9. The theory of time integrating correlators 161
9.1. Introduction 161
9.2. Correlator due to Montgomery 161
9.3. Correlator due to Sprague and Koliopoulos 162
10.3.1. Use of an acousto-optic cell for the first signal input 163
10.3.2. Analysis of operation 164
9.4. The electronic reference correlator 167
9.5. Discussion 171

10. Experimental results from a time-integrating acousto-optic correlator 173
10.1. Introduction 173
10.2. Removal of background from ccf 177
10.3. Frequency response 180
10.3.1. Calibration of time and frequency scales 180
10.3.2. Measurement of frequency response 180
10.4. Quantisation noise at the framegrabber 181
10.5. Results: variation of SNR_o with SNR_i 185
10.5.1. Generation of inputs with specified SNR 185
10.5.2. Measurements taken 186
10.5.3. Results: variation of SNR_o with SNR_i 189
10.6. Accuracy of time delay measurement 189
10.7. Conclusions 191

11. Conclusions and recommendations for further work **193**

11.1. Conclusions 193

11.2. Recommendations for further work 196

11.2.1. Multiple signal sources 196

11.2.2. Complete prototype system 196

11.2.3. Digital implementation 197

11.2.4. Other applications 198

Appendices:

A. Simulation for single FMCW signal 199

B. Simulation for biphase coded signal 208

C. Simulation for 2 FMCW signals with an interfering pulse 217

D. Estimation of SNR in Mathcad simulation 229

E. Measurement of errors in phase terms in simulated TDFCSD 234

F. Probability density functions 239

G. Mathcad file use to process data from time-integrating correlator 246

H. Results for time-integrating correlator 251

I. Details of equipment used 265

J. Published work 268

List of Symbols and abbreviations **317**

References and bibliography **320**

List of Tables and Figures

Page

Figure 1-1. PSD of a PRK signal before and after spreading. 2

Figure 1-2. acf of continuously repeated maximum length sequence 3

Figure 1-3. acf of a 13 bit Barker code. 6

Figure 1-4. acf of an isolated single cycle of a maximum length sequence. 6

Figure 1-5. A chirp pulse, as used in pulse compression radar, and its acf. 7

Figure 1-6. Frequency of transmitted and returning signals for an FMCW radar. 8

Figure 1-7. Simplified block diagram of dual receiver cross correlating system proposed for the detection of LPI radar signals. 10

Figure 1-8. Illustrating the van Cittert-Zernicke theorem 14

Figure 1-9. Complex aperture illumination function for one antenna 17

Figure 1-10. Magnitude of complex degree of coherence as a function of antenna separation 17

Figure 2-1. Mean amplitude spectrum of noise input. 27

Figure 2-2. Amplitude spectrum of the noise-noise cross correlation. 28

Figure 2-3. Amplitude envelope of the noise-noise cross correlation. 29

Figure 2-4. Amplitude spectrum of a chirp signal (approximate) 30

Figure 2-5. R.M.S. envelope of the signal-noise cross correlation. 32

Figure 2-6. Variation of the processing gain of the correlator with input signal power for a time domain cross correlating ESM receiver 35

Figure 2-7. The variations in peak signal to mean noise power ratio with input signal power, at the outputs of both time domain and frequency domain cross correlating ESM receivers and a matched filter radar receiver. 40

Figure 2-8. Typical pair of channel inputs. 41

Figure 2-9. acf of one channel input 42

Figure 2-10. ccf of both channel inputs 42

Figure 3-1. Envelope of combined noise terms in the output of a time domain correlator for a CW signal, showing section selected by time domain windowing. 47

Figure 3-2. Variation, with input signal power, of the output SNR in the TDFCSD and the ccf derived from a FSFD or TC correlator 51

Figure 3-3. Variation, with signal bandwidth B_s, of output SNR in TDFCSD and ccf for a fixed receiver noise bandwidth of B_n = 1 GHz. 52

Figure 3-4. Variation, with receiver noise bandwidth B_n,, of output SNR in TDFCSD and ccf for a fixed signal bandwidth B_s = 100 MHz. 52

Figure 3-5. Variation, with receiver integration time, of output SNR for TDFCSD and ccf when input signal is an FMCW signal. 54

Figure 3-6. Unfiltered power spectral density of one channel input. 55

Figure 3-7. Unfiltered cross spectral density of both channel inputs 55

Figure 3-8. "Zooming in" on the centre of the ccf by a factor of 2048 56

Figure 3-9. Magnitude of the TDFCSD, showing application of a threshold 56

Table 4.1. Parameters used in Mathcad model 60

Figure 4-1. Variation of transmitter power with range, for a selection of radar integration times, for a power managed CW LPI radar. 63

Figure 4-2. Variation of signal power at ESM receiver input with range from radar to ESM platform for a power managed CW LPI radar. 63

Figure 4-3. Variation of the sensitivity of a basic ESM receiver with no processing gain with receiver RF noise bandwidth. 65

Figure 4-4. Variation of the ESM range advantage with radar maximum range for a basic ESM receiver with no processing gain, for two different ESM RF noise bandwidths 66

Figure 4-5. Variation of minimum detection range with ESM RF noise bandwidth for an ESM system with no processing gain against a power managed pulsed LPI radar. 68

Figure 4-6. Variation of sensitivity with RF noise bandwidth for a crystal video receiver with different video bandwidths 69

Figure 4-7. Variation of ESM range advantage with radar maximum range for a crystal video receiver of fixed video bandwidth and radar pulses of length 100 μs, for different ESM RF bandwidths 70

Figure 4-8. Variation of minimum detection range with ESM RF noise bandwidth for a crystal video receiver with a fixed video bandwidth of 1 MHz against a power managed pulsed LPI radar with different pulse lengths..... 71

Figure 4-9. Variation of ESM range advantage with radar maximum range for a crystal video receiver with video bandwidth matched to the radar pulse length and radar pulses of 100 μs..... 72

Figure 4-10. Variation of minimum detection range with ESM noise bandwidth for crystal video receiver with video bandwidth matched to radar pulse length against power managed pulsed LPI radar with different pulse lengths..... 72

Figure 4-11. Variation of sensitivity, to pulsed radar signals, with RF noise bandwidth for a cross correlation receiver applying threshold detection to the ccf, using different integration times..... 73

Figure 4-12. Variation with integration time of the sensitivity advantage of cross correlating receiver applying threshold detection to ccf over a crystal video receiver with video bandwidth matched to the pulse length, for different combinations of radar pulse length and p.r.i., duty cycle is 1/10..... 74

Figure 4-13. Variation with integration time of the sensitivity advantage of cross correlating receiver applying threshold detection to ccf over a crystal video receiver with video bandwidth matched to the pulse length, for different combinations of radar pulse length and p.r.i., duty cycle is 1/2..... 75

Figure 4-14. Variation, with radar maximum range, of the ESM range advantage of a cross correlating receiver applying threshold detection to the ccf, over a pulsed radar, for different RF noise bandwidths..... 76

Figure 4-15. Variation, with receiver RF noise bandwidth, of the minimum detection range for a ccf receiver against a power managed pulsed radar, for different ESM integration times..... 76

Figure 4-16 Variation, with receiver RF noise bandwidth, of the sensitivity of a cross correlating ESM receiver applying threshold detection to the ccf to CW LPI radar signals, for different ESM integration times..... 78

Figure 4-17. Variation, with radar maximum range, of ESM range advantage of a cross correlating ESM receiver applying threshold detection to the ccf over a CW LPI radar, for different ESM integration times..... 79

Figure 4-18. Variation, with ESM receiver RF noise bandwidth, of minimum detection range for a cross correlating ESM system applying threshold detection to the ccf against a power managed CW LPI radar, for different ESM integration times..... 79

Figure 4-19. Variation (or in fact lack of variation!), with receiver RF noise bandwidth, of the sensitivity of a cross correlating ESM receiver applying threshold detection to the TDFCSD to pulsed LPI radar signals 81

Figure 4-20. Variation, with **signal** bandwidth, of the sensitivity of a cross correlating ESM receiver applying threshold detection to the TDFCSD to pulsed LPI radar signals, for different ESM integration times 81

Figure 4-21. Variation, with radar maximum range, of ESM range advantage of a cross correlating ESM receiver over a pulsed LPI radar, for different ESM integration times. 82

Figure 4-22. Variation, with **signal** bandwidth, of minimum detection range for cross correlating ESM system applying threshold detection to the TDFCSD against a power managed pulsed LPI radar 82

Figure 4-23. Variation, with signal bandwidth, of the sensitivity of cross correlating ESM receiver applying threshold detection to the TDFCSD to CW LPI radar signals, for different ESM integration times 83

Figure 4-24. Variation, with radar maximum range, of ESM range advantage of a cross correlating ESM receiver applying threshold detection to the TDFCSD over a CW LPI radar, for different ESM integration times. 84

Figure 4-25. Variation, with **signal** bandwidth, of minimum detection range for cross correlating ESM system applying threshold detection to TDFCSD against power managed CW LPI radar, for different ESM integration times. 84

Figure 5-1. Vector representation of kth component of TDFCSD plus noise represented in quadrature form. 90

Figure 5-2. Phase errors measured in Mathcad simulation against theoretical prediction. . 92

Figure 5-3. AOA estimation error as a function of ESM receiver input signal power for a fixed signal bandwidth of 100 MHz 98

Figure 5-4. AOA estimation error as a function of ESM receiver input signal power for a fixed ESM integration time of 10 ms 99

Figure 5-5. AOA estimation error as a function of range of radar from ESM platform, against power managed CW LPI radar with radar integration time of 1 ms, fixed signal bandwidth 100 MHz, for different ESM integration times. 100

Figure 5-6. AOA estimation error as function of range of radar from ESM platform, against power managed CW LPI radar with radar integration time of 1 ms, fixed ESM integration time of 10 ms 100

Figure 5-7. AOA estimation error as function of range of radar from ESM platform, against power managed CW LPI radar with radar integration time of 10 ms and fixed signal bandwidth 100 MHz 101

Figure 5-8. AOA estimation error as function of range of radar from ESM platform, against power managed CW LPI radar, radar integration time of 10 ms, fixed ESM integration time of 10 ms 102

Figure 5-9. Phase terms for whole receiver bandwidth, showing straight line fitted to terms within signal bandwidth 103

Figure 5-10. Phase terms for just the signal bandwidth, showing fitting of straight line. 103

Figure 5-11. Magnitude of TDFCSD for two simultaneous FMCW signals 104

Figure 5-12. Phase of TDFCSD for two simultaneous FMCW signals 104

Figure 6-1. Time-integrating correlator. 108

Figure 6-2. Schematic diagram of a joint transform correlator 109

Figure 7-1. Acousto-optic cell showing directions of optic and acoustic waves 111

Figure 7-2. Bragg diffraction: (a) upshift mode and (b) downshift mode. 113

Figure 7-3. Acousto-optic cell showing directions of propagation of diffraction orders. . 117

Figure 7-4. Formation of Fourier transform by lens. 119

Figure 7-5. Focusing of a diffraction order in the FT plane. 119

Figure 7-6. Fine structure of principal diffraction orders for sinusoidal modulation of carrier injected into acousto-optic cell. 122

Figure 7-7. Experimental arrangement for measuring the form of the zeroth diffraction order. 125

Figure 7-8. Actual output from photodiode array (top) and theoretical prediction (bottom) - large m. 126

Figure 7-9. Actual output from photodiode array (top) and theoretical prediction (bottom) - moderate m. DSBLC modulation. 127

Figure 7-10. Actual output from photodiode array (top) and theoretical prediction (bottom) - moderate m. DSBSC modulation. 128

Figure 8-1. General all order space-integrating acousto-optic correlator. 131

Figure 8-2. Form of zeroth diffraction order at photodetector plane 135

Figure 8-3. Component of photodetector output due to a^2 terms..... 137

Figure 8-4. Zeroth order, non-heterodyning, space integrating correlator..... 141

Figure 8-5. Experimental arrangement of zeroth order non-heterodyning space integrating correlator. 143

Figure 8-6. Experimental correlator output and theoretical form of the acf for a chirp pulse from 4.25 to 5.75 MHz in 15 μs . (BT = 22.5)..... 144

Figure 8-7. Experimental correlator output and theoretical form of the acf for a chirp pulse from 3 to 6 MHz in 15 μs . (BT = 45) 145

Figure 8-8. Experimental correlator output and theoretical form of the acf for a chirp pulse from 3 to 7.5 MHz in 15 μs . (BT = 67.5) 146

Figure 8-9. Experimental correlator output and theoretical form of the acf for a chirp pulse from 2 to 8 MHz in 15 μs (BT = 90)..... 147

Figure 8-10. Zeroth order correlator using photographic mask for one input. 148

Figure 8-11. First order, non-heterodyning, space integrating correlator. 150

Figure 8-12. Heterodyning correlator/convolver using 0 and +1 diffraction orders from first acousto-optic cell. 154

Figure 9-1. Time-integrating correlator due to Montgomery. 162

Figure 9-2. Time-integrating correlator due to Sprague and Koliopoulos. 162

Figure 9-3. Use of Bragg cell for first signal input. 163

Figure 10-1. Experimental time-integrating correlator using narrow beam laser with external beam expansion. 174

Figure 10-2. Experimental time-integrating correlator using laser with internal beam expansion. 175

Figure 10-3. Photographs of the time-integrating correlator using laser with internal beam expansion..... 176

Figure 10-4. A ccf (top) and pre-recorded background(middle) as taken in by Mathcad file and the ccf after subtraction of the background (bottom)..... 178

Figure 10-5. Frequency response of experimental time-integrating correlator..... 181

Figure 10-6. Variation of SNR in output TDFCSD with number of quantisation levels spanned by the correlation peak, for a range of input SNRs 184

Figure 10-7. Raw outputs from framegrabber as imported into Mathcad file. 187

Figure 10-8. CCD array outputs after subtraction of background. 187

Figure 10-9. ccfs after further windowing. 187

Figure 10-10. Magnitudes of TDFCSDs obtained by FFT from the windowed ccfs shown in figure 10-9 188

Figure 10-11. Difference between phase terms of the TDFCSDs, with straight line fitted. 188

Figure 10-12. Measured and predicted output SNRs in the TDFCSD for a range of input SNRs 189

Figure 10-13. Estimates of delay line length plotted against the correlator input SNR used when the estimates were obtained. 191

Acknowledgements

The Defence Research Agency at Funtington provided the initial motivation for this work and generous funding. Regular consultation, particularly with Dr Juliet Dunn-Rogers, provided valuable encouragement and direction.

The work was carried out at the Royal Naval Engineering College and the author was allowed to use College facilities and devote a significant portion of his time to this work.

The author would like to thank all those in the EE department at RNEC who provided support and encouragement, particularly Commander Nick Haines who allowed him the time to carry out the work, Paul Brooks who provided useful practical help and advice and Dudley Bryant, of West Kentucky University, who wrote the data conversion programme used in the experimental work. The most gratitude of all is owed to the author's supervisor, Kit Reeve, for his continual and invaluable help, advice and encouragement throughout the period of this work.

Thanks are also due to the author's wife, Stephanie, and children, Helen and Arran, who had to put up with "daddy playing with his 'puter" when he should have been playing with them.

Authors declaration

At no time during the registration for the degree of Doctor of Philosophy has the author been registered for any other University award.

This study was financed under a research agreement with the Defence Research Agency at Funtington, and carried out by the author while employed by the Royal Navy at the Royal Naval Engineering College.

Regular visits were paid to DRA Funtington and DRA Portsdown West for consultation purposes.

Relevant scientific conferences were attended regularly and the following papers published:

Houghton, A.W. and Reeve, C.D.: 'A zeroth order non-heterodyning space integrating acousto-optic correlator', Inst. Phys. Conf. Ser. No 139: Part III, pp 325-328, presented at Opt. Comput. Int. Conf., Edinburgh, 22-25 Aug 1994.

Reeve, C.D. and Houghton, A.W.: 'Performance of an acousto-optic joint transform correlator', Inst. Phys. Conf. Ser. No 139: Part III, pp 321-324, presented at Opt. Comput. Int. Conf., Edinburgh, 22-25 Aug 1994.

Houghton, A.W. and Reeve, C.D.: 'Direction finding on spread spectrum signals using a cross correlation receiver', Microwaves 94 Conf. Proc. pp 304-308. (Int. Conf. sponsored by IEE/IEEE/MTT, Wembley, October 1994)

Reeve, C.D. and Houghton, A.W.: 'Performance modelling of an acousto-optic joint transform correlator', Microwaves 94 Conf. Proc. pp 430-433. (Int. Conf. sponsored by IEE/IEEE/MTT, Wembley, October 1994)

Houghton, A.W. and Reeve, C.D.: 'Detection and direction finding on spread spectrum signals using the time domain filtered cross spectral density, IEE Colloquium on High Resolution Spectral Estimation and Direction Finding, April 1995.

Houghton, A.W. and Reeve, C.D.: "Spread spectrum signal detection using a cross correlation receiver", Sixth International conference on 'Radio Receivers and Associated Systems', University of Bath, 26-28 September 1995.

Houghton, A.W. and Reeve, C.D.: "Detection of spread spectrum signals using the time domain filtered cross spectral density", IEE Proceedings: Radar, Sonar and Navigation. (Accepted and awaiting publication.)

Signed .....

Date ..... January 1996 .....

1. Introduction

1.1 Introduction to spread spectrum signals

Many modern communication and radar systems transmit spread spectrum signals. The principle advantages of using spread spectrum techniques are that they can make transmissions more difficult to jam and the transmitter more difficult for a surveillance receiver to detect: i.e. they have low probability of intercept properties (LPI). [1,2,3,4]. This thesis considers techniques that can be used for detection and direction finding of spread spectrum signals and therefore starts with a brief summary of the spread spectrum techniques in common use.

1.1.1 Spread spectrum communication systems

In a radio communication link, which is concerned with the transmission of information, the system is using a spread spectrum technique if the RF bandwidth used is significantly greater than that conventionally required for the transmission of the information. For example, the use of broadband frequency modulation (FM) in analogue systems, though not strictly defined as a spread spectrum technique, illustrates some of the advantages. An audio signal of bandwidth B can readily be transmitted using single sideband suppressed carrier amplitude modulation (SSBSC AM) with an RF bandwidth of B. Broadband FM systems use an approximate RF bandwidth, given by Carson's rule, of $2B(1+\beta)$ where β is the modulation index typically taking values of 5 or more. RF bandwidths at least an order of magnitude greater than B are often used, principally in order to take advantage of the considerable processing gain that can be achieved in the receiver. Processing gain is defined here as the signal to noise ratio (SNR) at the demodulator output divided by the SNR at the demodulator input. We shall concern ourselves here, however, with more deliberate techniques designed to achieve LPI and anti-jamming performance in the transmission of digital information. The two most popular spread spectrum techniques used in data transmission are "direct sequence" and "frequency hopping".

Direct sequence. In direct sequence spread spectrum systems, the signal is multiplied by a high data rate pseudo-random code. Consider a system transmitting data using a phase reverse keying (PRK) modulation scheme. The transmitted signal would, in a normal system, take the form

$$e(t) = d(t)\cos(\omega_c t) \tag{1.1}$$

where d(t) is a bipolar non return to zero (NRZ) binary data signal taking values ±1, and the amplitude term has been omitted for clarity. The power spectral density (PSD) of this signal is a $sinc^2$ function centred at f_c ($\omega_c = 2\pi f_c$) with a null to null bandwidth of $2r_b$ where r_b is the bit rate of $d(t)$. To "spread" this signal, it is multiplied by a bipolar NRZ pseudo-random code $c(t)$ at a "chip" rate r_c, so that the transmitted signal becomes

$$e(t) = c(t)\,d(t)\cos(\omega_c t) \tag{1.2}$$

r_c will typically be of the order of 1000 times greater than r_b [1], and the null to null bandwidth is now $2\,r_c$. The total power of the signal remains unchanged, but since the bandwidth has been increased by a factor of r_c/r_b the PSD at any given frequency has been reduced by the same ratio. For large processing gains this can easily take the PSD of the spread spectrum signal at the input of a surveillance receiver well below the receiver's input noise spectral density. This is illustrated, for a very small r_c/r_b ratio of 5, in figure 1-1.

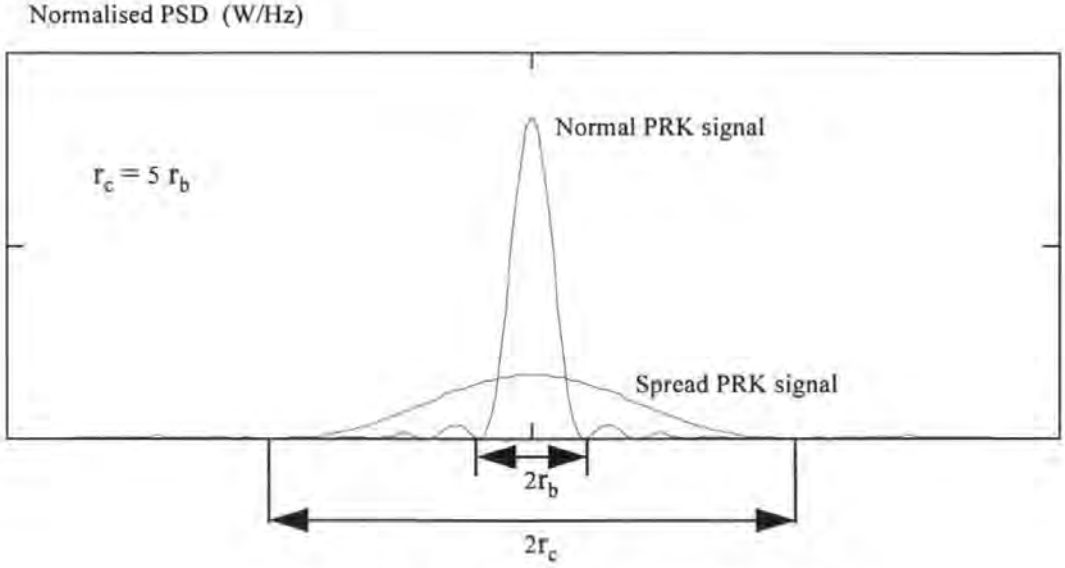

Figure 1-1. PSD of a PRK signal before and after spreading.

[1] r_c/r_b is often referred to as the processing gain, but though usually numerically close, this is not quite the same as the definition of processing gain used in this thesis.

The difference between the unspread and spread spectra in a real system is, of course, much greater than shown in figure 1-1. A cooperating system, with a priori knowledge of the spreading code *c(t)*, can form what is effectively a matched filter or correlation receiver. Once it has locked onto the phase of the code, it simply multiplies the incoming signal by *c(t)*, to give

$$c^2(t)\,d(t)\cos(\omega_c t) \;=\; d(t)\cos(\omega_c t) \qquad (1.3)$$

Since *c(t)* takes values ±1, $c^2(t) = 1$. The signal spectrum has been collapsed back to its initial unspread form and can be demodulated as normal. Any narrowband interfering or jamming signal will also be multiplied by *c(t)*. This will spread the spectrum of the interfering signal so that the subsequent narrowband filtering inherent in the receiver will reject most of it.

Very long codes can be used and are readily generated using shift registers with feedback. If the feedback is taken from the correct tapping points, then the sequence formed is a maximal length sequence such that the code repeat length is $2^n - 1$, where n is the number of stages in the shift register. When continuously repeated, maximal length sequences have very sharp autocorrelation peaks one chip period wide with no secondary peaks or sidelobes, as shown in figure 1-2, making them ideal for this application. The acf peaks in figure 1-2 are all main peaks occurring at intervals equal to the period of the code.

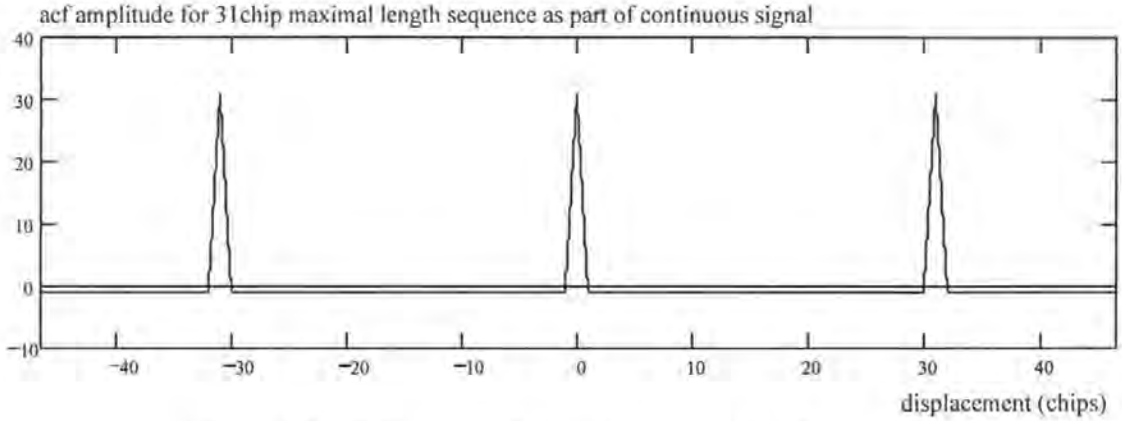

Figure 1-2. acf of continuously repeated maximum length sequence.

There is a limited number of maximal length sequences. Gold codes can be used if there is a requirement to multiplex a number of direct sequence spread spectrum signals in a code division multiple access (CDMA) system, and different codes need to be made available to different users. The peak magnitudes of the cross correlations of any two maximal length

sequences or two Gold codes are very much lower than those of the codes' acfs, allowing many communication links to operate, using different codes, in the same frequency band without being able to decode each other's signals. Gold codes are generated by combining the outputs from 2 maximal length sequence shift register generators. Different codes can be generated simply be changing the relative phases of the 2 maximal length sequences. Gold codes are not quite so easy for a correlation receiver to lock onto since their autocorrelation functions have a number of secondary peaks.

The direct sequence spread spectrum signal gains its LPI performance from the fact that its PSD may be well below the noise spectral density at the input of a surveillance receiver. Without the cooperating receiver's a priori knowledge the surveillance receiver cannot form a matched filter and take advantage of the available processing gain. A scanning superheterodyning receiver, as commonly used in communications surveillance, will not detect such a signal. A sufficiently sensitive radiometer might detect such a signal provided the background noise level is sufficiently constant (i.e. if the noise is a stationary signal) and there are no other signals. Biphase coded signals are vulnerable, however, to detection by a surveillance receiver that squares its input, giving it the ability to detect the carrier at the cost of losing all other information.

Frequency hopping. Frequency hopping systems are more popular than direct sequence systems for military applications. The available RF channel is split up into a large number of channels (of the order of 1000 or more), and the system hops rapidly, following a pseudo-random sequence, among these channels. In fast hopping systems the hop rate is such that the system will change frequency for every data bit, or even hop several times during one data bit. Allocating several "chips" to each message data bit enables the more extreme forms of error control coding that allow frequency hopping systems to overcome jamming. Since, at any instant, all the transmission power is concentrated within one narrow channel the system can break through any form of broadband jamming. A jammer has to concentrate on jamming a limited number of the channels used by its target communication link so as to cause a significant error rate. The communication link then has to use error control coding to correct these errors while accepting the overhead of a reduced information rate. Since the transmission comprises a stream of short narrowband pulses, a single link does not present an enormous detection problem to the surveillance receiver. A scanning superheterodyne

receiver would have a rather low probability of intercept since it only looks at one narrow frequency band at a time, but a channellised crystal video receiver should have little difficulty in detecting activity. However, in an environment containing a large number of frequency hopping systems, all hopping pseudo-randomly, the task of identifying individual links becomes virtually impossible using conventional techniques.

1.1.2 Spread spectrum radar systems

Pulsed radar. The development of spread spectrum techniques in radars has been different from that in communications. Radars have traditionally used pulses rather than CW (continuous wave) signals, and spread spectrum pulses were not originally developed purely for their LPI properties. The range resolution of a radar is a function of the pulse length, while its maximum detection range is a function of the total energy, the mean power times the length, of the transmitted pulse. The requirement for large maximum range and small range resolution puts conflicting pressures on the pulse length. For a radar using simple unmodulated pulses, large range with small resolution can only be achieved by using short very high power pulses, requiring large, expensive and power hungry transmitters. The answer is to use pulse compression. In a pulse compression system, the transmitted pulses are of relatively low power and relatively long so as to give the total pulse energy necessary for the required maximum range. Modulation is applied to the transmitted pulse so that it can be collapsed in time in the receiver to produce the short pulse required for good range resolution. The reduction in transmitter power and the spreading of the signal spectrum caused by the modulation lead to LPI properties, initially more as a fringe benefit than by intention. This process is best illustrated by using the two most common techniques as examples.

Phase coded pulses. One way of modulating the transmitted pulse is to apply biphase or PRK modulation using a code such as a Barker code. Barker codes exist up to 13 bits long and have acfs (autocorrelation functions) one bit period wide. If a 13 bit code is transmitted, the radar's matched filter receiver will effectively cross correlate the returning echo with the original pulse to produce the code's acf plus noise. Since this acf is one bit period wide the pulse has been compressed by a factor of 13. Barker codes acfs have a number of equal sidelobes with a peak to sidelobe magnitude ratio of N where N is the length of the code. The

number of sidelobes is equal to N-1. As an example the acf of a 13 bit Barker code is shown in figure 1-3 [5].

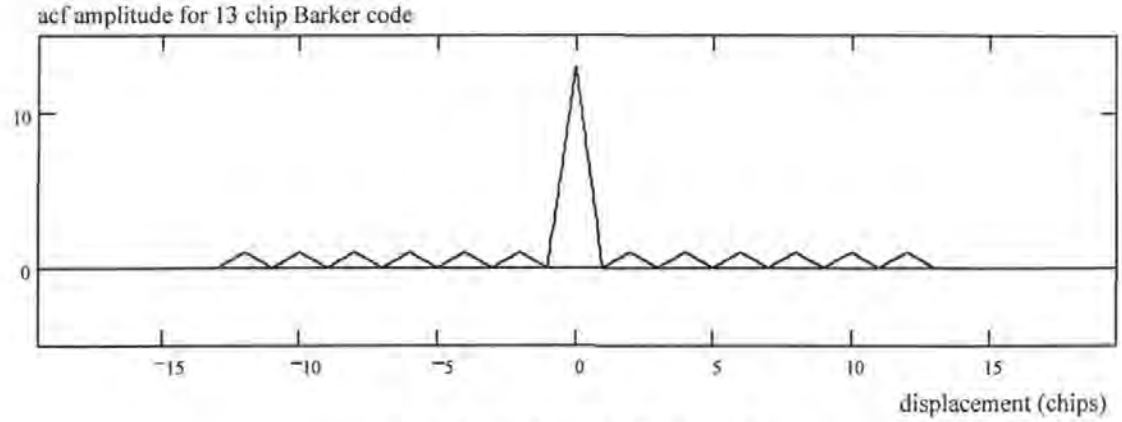

Figure 1-3. acf of a 13 bit Barker code.

Maximal length sequences can also be used, but when they are used in aperiodic form, with one cycle contained in a pulse, their acfs are a little different from when they are used in continuous periodic mode. The acf of a single repeat of a maximal length sequence in isolation contains many secondary peaks that could give rise to false targets or range ambiguities in a radar. The acf of such a single cycle as a pulse is shown in figure 1-4.

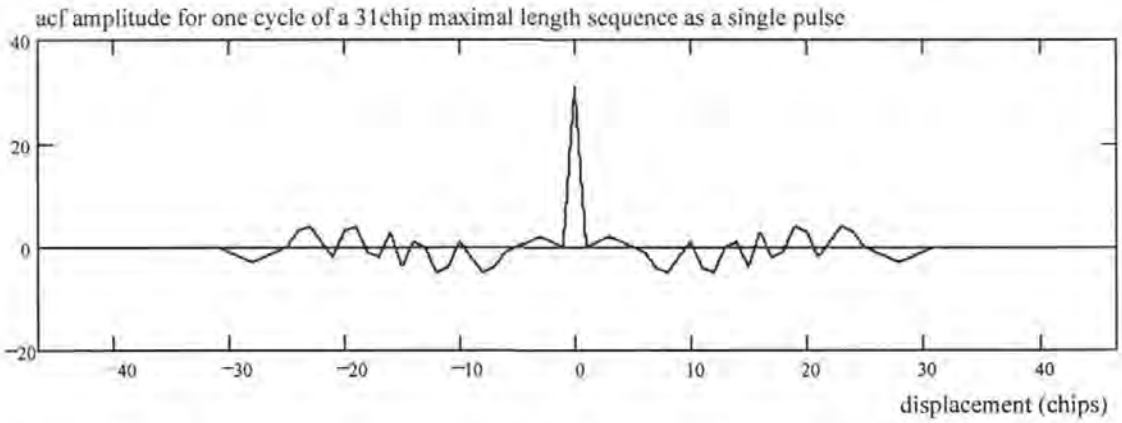

Figure 1-4. acf of an isolated single cycle of a maximum length sequence.

LFM pulses. A more common technique, offering the possibility of much larger compression ratios, is to create linear frequency modulated (LFM) or chirp pulses. The frequency of the transmitted pulses either rises (up chirp) or falls (down chirp) linearly with time throughout the pulse. This type of pulse can be created easily by passing a short pulse through a SAW (surface acoustic wave) chirp filter. The short pulse necessarily contains a

wide range of frequencies. The SAW chirp filter is a frequency dependant delay line that, for an up chirp, applies a longer delay to higher frequency signals, expanding the pulse so that the low frequency energy leaves the transmitter first, followed the high frequency energy. The receiver then contains a matched SAW filter that reverses this expansion process by compressing the returning pulse back to its original short length. Again, this matched filter effectively cross correlates the returning echo with the transmitted pulse forming the pulse's acf plus noise. The length of the transmitted pulse over its length after passing through the matched filter, the width of the acf, is known is the compression ratio, and it is equal to the bandwidth-time or BT product of the transmitted chirp. An unmodulated pulse of length T has an approximate bandwidth of 1/T, giving the pulse a BT product of 1. Figure 1-5 shows an up chirp with a BT product of 20, as transmitted, and its acf, as formed at the matched filter output.

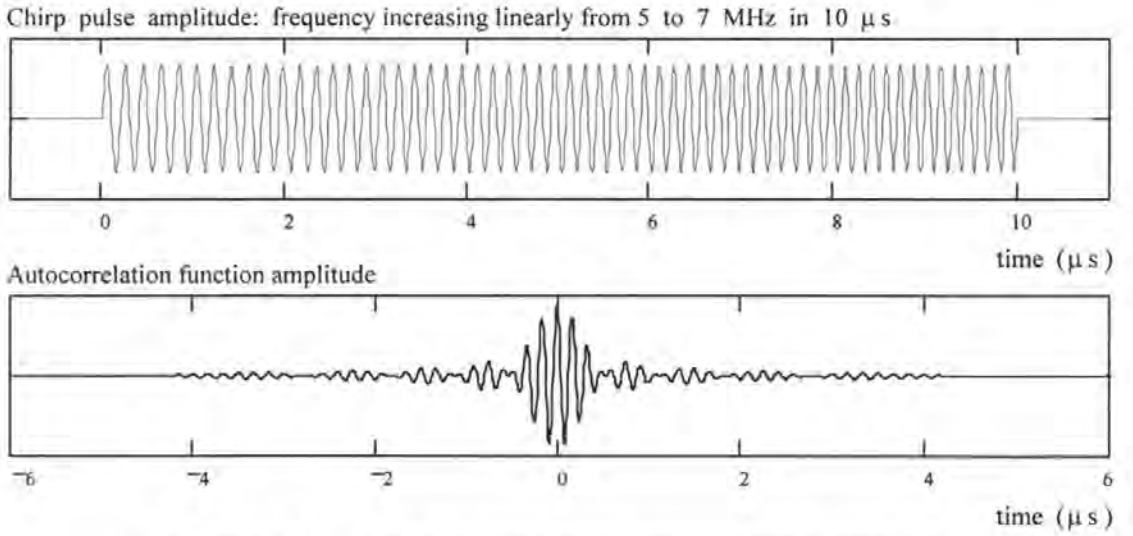

Figure 1-5. A chirp pulse, as used in pulse compression radar, and its acf.

For the pulse shown in figure 1-5, the bandwidth is 2 MHz, the pulse length is 10 μs and the width of the main peak of the envelope of the acf is approximately 0.5 μs. Low frequencies are used in figure 1-5 for illustration purposes. In a real system the centre frequency will be of the order of GHz and the bandwidth of the order of a few tens of MHz. BT products of the order of 100 or even 1000 are feasible, and such large BT products enable radars to achieve very large maximum ranges with excellent range resolution while using low power, compact semiconductor based transmitters. They also make them difficult for a surveillance or ESM receiver, which does not have the matched filter, to detect. Non linear frequency modulation is discussed in the literature but does not seem to be popular in real systems.

CW radar. As radar pulses are made longer their transmitted power levels drop lower and they become more difficult to detect. The logical extension, in deliberately designing an LPI radar, is to continue lengthening the pulses, increasing the duty cycle of the radar, until there are no gaps between pulses and the transmitted signal has become continuous.

FMCW radar. Frequency modulated continuous wave radar is the logical extension of LFM pulse radar. The transmitter uses a voltage controlled oscillator to produce a continuous transmitted signal that ramps up and down in frequency. An existing example of this is the "PILOT" (otherwise known as Scout) tactical navigation radar which operates at around 9 GHz. Pilot [6] employs a sawtooth frequency sweep of 50 MHz with a time period of 1 ms. Since the transmitted frequency is normally increasing linearly the returning echo is at an earlier lower frequency. This is illustrated in figure 1-6. Mixing the returning echo with the signal currently being transmitted then produces a signal at the difference frequency, Δf, which is directly proportional to the time, Δt, taken for the echo to travel to a target and back.

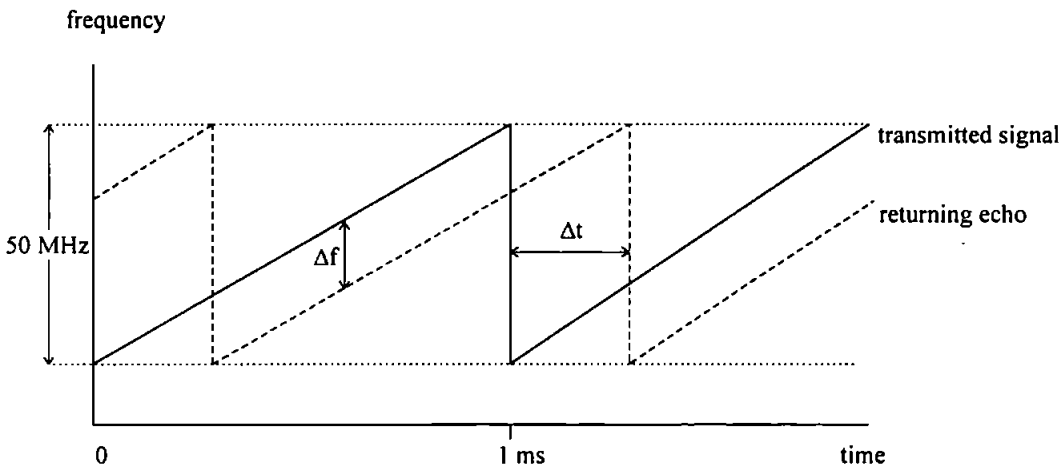

Figure 1-6. Frequency of transmitted and returning signals for an FMCW radar.

Transmission powers in pulsed radars are typically of the order of kilowatts or tens of kilowatts. PILOT has a transmission power of the order of 1W spread over 50 MHz. Future FMCW radars will use digital signal processing techniques to form a matched correlation receiver and extract multiple target information including Doppler information. The bandwidth can be expected to increase significantly and, with their very low transmitter powers, such radars will be very difficult to detect. This thesis will concentrate on methods for detecting and direction finding on this type of radar. It is by no means the only type of

signal source of interest, but it does provide a good example with which to work, and the techniques applied to detecting FMCW signals can be readily extended to other types of signal.

Phase coded CW radar. As mentioned above, in discussing phase coded pulsed radar, if one cycle of a maximal length sequence is used in isolation to code a pulse then secondary peaks or sidelobes occur in the acf. These could give rise to false targets. When the signal is continuous, however, there are no secondary peaks whatever in the acf. With one single sharp peak in the acf a very long maximal length sequence biphase coded signal becomes an excellent radar signal, if the practical difficulties of building a full duplex system and designing a matched filter receiver that can operate without a priori timing information can be overcome. The sequence has to be long enough to avoid "second time around" range ambiguities. For example a radar with a maximum range of 40 km and a code chip rate of 25 MHz would require a minimum code length of 8191. Generation of this is relatively easy but construction of a good matched filter receiver is rather more difficult. Such a signal will look almost exactly like a direct sequence spread spectrum communication signal. Such signals are extensively used in range finding and navigation systems such as GPS.

Other LPI techniques. Designing LPI radars also involves the use of other techniques, such as tight control on number and timing of pulses emitted, frequency hopping between pulses, power management and antenna sidelobe suppression. Continual regular emission of radar pulses may not be necessary for a platform that can fuse data from other sources, such as its ESM systems, to build up a radar picture using a carefully controlled minimum of active emissions to resolve ambiguities. A radar tracking a single target can make itself much more difficult to detect by adjusting its power output, keeping it at the minimum level required for effective tracking. As such a radar approaches its target it will automatically reduce its transmitter power. ESM systems can usually make use of radiation in the radar antenna sidelobes to help in sorting pulses and forming a track. The use of ultra-low sidelobe antennas by the radar denies the ESM system the extra information that this makes available. In this thesis it will generally be assumed that only the antenna mainlobe transmissions are worth trying to detect. The effects of power management will be considered in some detail.

1.2 Introduction to the cross correlation receiver and the "TDFCSD"

A normal surveillance system does not have the required a priori information to form a matched filter receiver and make use of the processing gain available from a signal with a large BT product. However, if it uses two spatially separated antennas with wideband receivers and cross correlates the two outputs (figure 1-7), much of the available processing gain can be accessed, without any a priori knowledge of the signal.

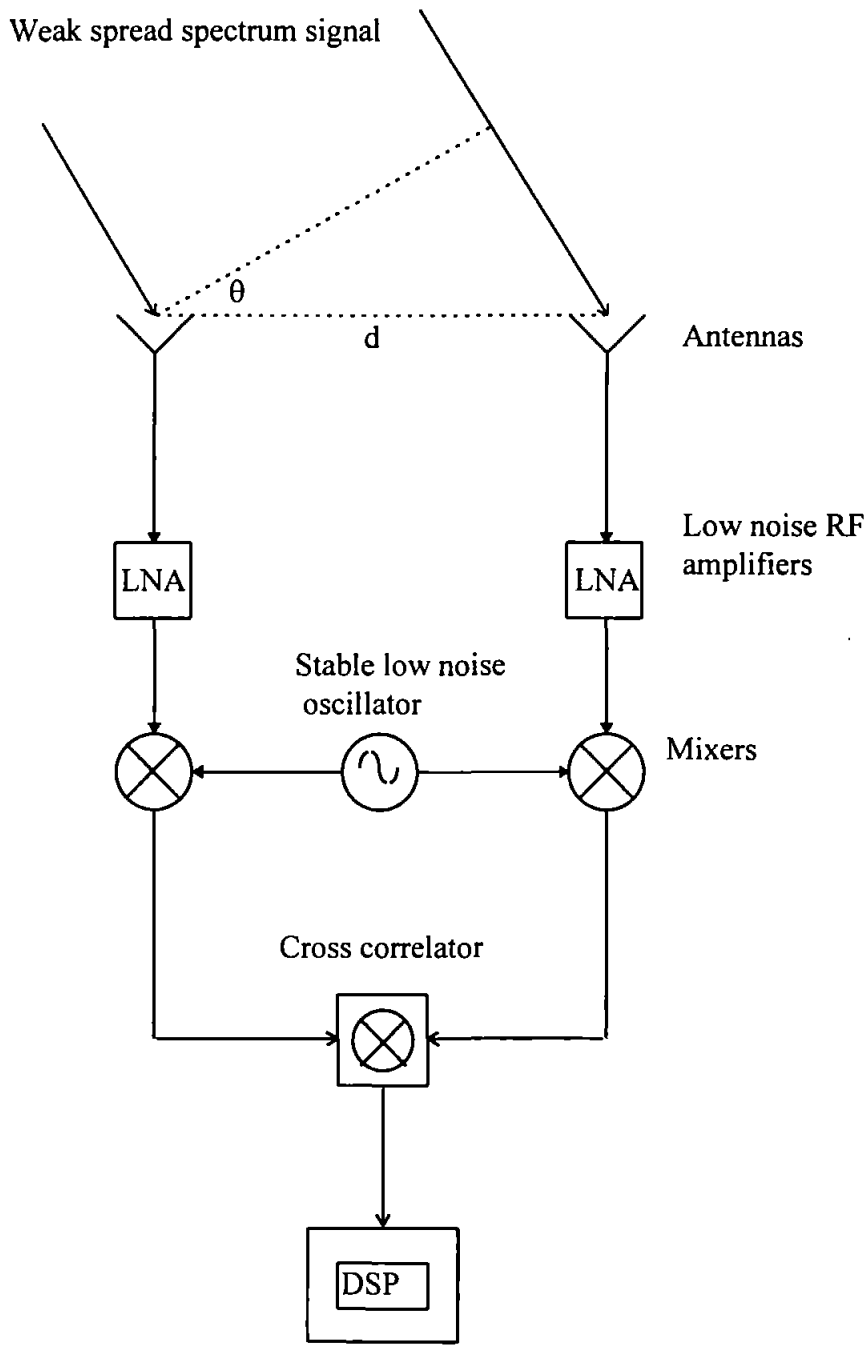

Figure 1-7. Simplified block diagram of dual receiver cross correlating system proposed for the detection of LPI radar signals.

The two signals will contain both antenna noise and internal receiver noise. The internal receiver noise in the two receivers will be independent and will not correlate. (It is assumed that the system is front end noise limited so that noise from the common local oscillator can be neglected.) The antenna noise in the two receivers comes from the same sources, but if these sources can be assumed to be spatially distributed over the full width of the antenna radiation patterns then the signals from these noise sources arrive at the two antennas with a distribution of time delays. The result is that there is effectively no correlation between the antenna noise inputs to the two receivers, provided that the antenna separation is large enough. This assumption is clearly fundamental to this thesis and is examined in more detail in the next section. Any signal source, such as a radar, will be transmitting from one fixed point and the signal will therefore be present in both receiver outputs with a single fixed time delay[1]. Cross correlation will therefore yield the acf of the signal, plus noise. In principle the operation being carried out is similar to that in the co-operating receiver: the surveillance system has formed its own partially matched filter. The difference is that whereas the radar correlates signal plus noise with pure signal, the surveillance system correlates signal plus noise with a time shifted version of the same signal plus an independent noise input. The surveillance system will achieve a processing gain that can approach but not equal that of the co-operating receiver.

It should be noted that the correlation process described here is different from that often described under the heading of correlation receivers. Systems described under this heading often involve multiplying the two receiver inputs and using a low pass filter to integrate the product [7]. Wiley [8] gives a diagram of a receiver forming a true correlation function but offers no analysis for such a system. Torrieri [4] does analyse a true correlation receiver and compares it to a radiometer. Comparisons will be made with his results in chapter 4. The simple multiplier type of "correlation receiver" gives the value of the cross correlation function (ccf) for a time shift which is either zero or fixed over any integration time (though sometimes variable between integrations). The analysis of signal to noise ratio (SNR) generally involves comparison of receiver output levels, for this one time shift, with and without a signal present. While this process may be useful, there is far more to a ccf than

[1] This thesis will concentrate on the simple case of a single signal source. The ability of the system to detect and discriminate between multiple sources is a function of the receiver separation and the degree of spectral overlap between the signals. This is discussed briefly but a rigorous analysis will not be presented: it may represent a worthwhile subject for further study.

just its value for zero time shift. The system described in this thesis obtains the true ccf over a range of time shift. SNR analysis will compare levels within the ccf for different time shifts, to assess the detection performance achievable by examining one ccf without referring to previous or subsequent ccfs. By obtaining the whole of the ccf rather than just one central value we acquire much more information. The phase information in this ccf is particularly valuable.

The proposed system can detect spread spectrum signals of arbitrary waveform and spectrum, with a power spectral density (PSD) below receiver noise levels, by direct threshold detection applied to the ccf. Alternatively, threshold detection can be carried out in the frequency domain, giving greater sensitivity in very broadband (greater than 1 GHz) systems and the possibility of determining the signal's spectrum. Forming the cross spectral density (CSD) by taking the Fourier transform usually produces a frequency domain signal which is too noisy to be of much use. However, the properties of a spread spectrum signal make it possible to improve the signal to noise ratio (SNR) in the CSD by 30 dB or more. The signal part of the ccf is the time shifted acf of the spread spectrum signal. Due to the signal's broadband nature this acf will be very narrow, typically a few tens of nanoseconds wide. If the two antennas are separated by only a few metres then this acf is shifted from the centre of the total ccf by no more than a few nanoseconds. The noise components of the ccf are spread uniformly over the whole width of the ccf, which will be of the order of milliseconds or more. A time domain filter can then be used to select, or window, a narrow central portion of the ccf, capturing virtually all of the signal but rejecting most of the noise. Taking the Fourier transform of this windowed ccf produces the time domain filtered cross spectral density (TDFCSD)[1]. Threshold detection in this TDFCSD will then not only reveal the presence of a spread spectrum signal, but also give its spectrum.

Forming the initial ccf is clearly extremely demanding computationally. To sample the signals from the two receivers and perform the necessary cross correlations in real time may not be feasible, especially if we wish to design a system with large channel bandwidths and long sample lengths. For example: a channel bandwidth of 500 MHz and a sample length of 500 μs would require analogue to digital conversion at a sampling frequency of 1 GHz and

[1] It should be noted that the phrase "time domain filtered" is not being used here to describe the filtering of a time domain signal by means of a convolution process in the time domain. It is being used to describe the filtering of a frequency domain signal by means of windowing in the time domain.

data sets of 500,000 points. Acousto-optic correlators can provide the answer to the problem of forming the initial correlation function, making signal detection and analysis in real time, for large bandwidths and integration times perfectly feasible. (Acousto-optic cells with bandwidths in excess of 2 GHz are available enabling the construction of correlators with a bandwidth of 1 GHz.) The fact that we only want to sample a relatively small portion of the ccf is very convenient since this means that the number of data points we have to extract for further processing is very much reduced. One commonly quoted disadvantage of acousto-optic signal processing systems is that they have a limited dynamic range. Optical systems have been devised which overcome earlier problems but even if this were not the case it need not be a problem here. Since we are looking for signals below the noise level, the system would be set up with RF and IF gains such that the standard deviation of the noise is approximately one third of the amplitude range of the correlator inputs so as to present the correlator with signals at the maximum power without causing excessive clipping of noise plus low power signals. Short high power pulses will be severely clipped. This goes some way towards eliminating the non LPI pulses that would be detected by a conventional system, although they would of course be better excluded by the use of notch filters, switched in for the duration of high power pulses, to block known signals. There are three main types of acousto-optic correlator that could be used: space integrating, time integrating and joint transform.

If we want to derive the TDFCSD from the output of an acousto-optic correlator it is essential that the output is a true correlation function and not the square of the ccf as produced by the joint transform correlator and some forms of space integrating correlator [9]. Some forms of space integrating correlator [10] do produce a true ccf, and these are discussed in detail, but they still suffer from the major drawback that one of the input signals must be time reversed. This makes the system more complicated and also forces us to break the signal up to perform a succession of finite sample time domain cross correlations. The time integrating correlator [11], however, is ideal for our purposes. Time reversal is not required, the output is a true correlation function and very long integration times are possible. The required ccf of the two inputs is formed as a spatially varying function at a photodetector array which can be periodically transferred from the array into a DSP system. It is also shown that the way in which the correlation function is formed in the time integrating correlator is such that it gives itself naturally to the time domain filtering process described above.

1.3 Degree of spatial coherence between the antennas

A good initial optical analogy of the two antenna system can be envisaged by considering a Young's slits experiment. If a point source is used good fringes can be obtained. However, if a distributed source is used the visibility of the fringes is reduced because the light at the two slits is not perfectly spatially coherent: the two optical signals are not fully correlated. The light at the two slits is never totally coherent since we can never realise a perfect point source, and is never completely incoherent. It is generally partially coherent with the complex degree of coherence, μ_{12} having magnitude between 0 (total incoherence) and 1 (total coherence). We can treat the noise outputs from the antennas as uncorrelated if the degree of coherence $|\mu_{12}| \ll 1$. The complex degree of coherence is given by [12]

$$\mu_{12} = \frac{\langle \mathbf{V}_1(t)\,\mathbf{V}_2^*(t)\rangle}{\sqrt{I_1\,I_2}} \tag{1.4}$$

where $\mathbf{V}_1(t)$ and $\mathbf{V}_2(t)$ are the analytic functions of which the signals at the two antenna outputs are the real parts, and I_1 and I_2 are the mean intensities or powers of these signals. This complex degree of coherence between two points in a plane, illuminated by an extended quasi-monochromatic incoherent source, is given by the van Cittert-Zernicke theorem, which is described fully by Born and Wolf [13].

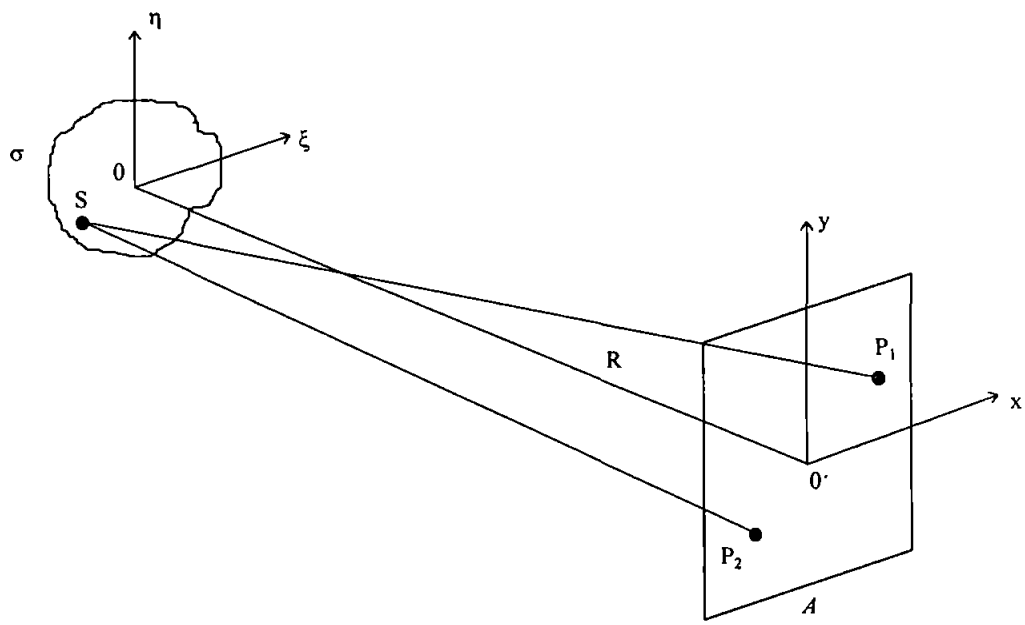

Figure 1-8. Illustrating the van Cittert-Zernicke theorem

In terms of figure 1-8 (taken from Born and Wolf, p 508) we wish to know the complex degree of coherence for points P_1 and P_2 in a plane A illuminated by an extended quasi-monochromatic incoherent source σ. To find this we divide the source up into elements $d\sigma_1$, $d\sigma_2$, . . . centred on points S_1, S_2, . . . and consider the total coherence, or cross correlation, function for the points P_1 and P_2 as the sum of the cross correlations due to each of these elements. We assume that the linear dimensions of the source and the separation between P_1 and P_2 are small relative to the distance R between the two planes. This is the same assumption underlying the Fraunhoffer approximation for diffraction patterns and can alternatively be stated as an assumption that the angles subtended by the source at plane A and by the line P_1P_2 at the source plane are small. Making this assumption, the van Cittert-Zernicke theorem then gives the complex degree of coherence

$$\mu_{12} = \frac{e^{j\psi} \iint_{\sigma} I(\xi,\eta) e^{-j\frac{k}{R}(p\xi+q\eta)}\, d\xi\, d\eta}{\iint_{\sigma} I(\xi,\eta)\, d\xi\, d\eta} \qquad (1.5)$$

where $I(\xi,\eta)$ is the intensity distribution in the source plane,

$$\psi = \frac{k\left[\left(x_1^2+y_1^2\right)-\left(x_2^2+y_2^2\right)\right]}{2R} \quad , \quad p = x_1 - x_2 \quad , \quad q = y_1 - y_2 \quad \text{and} \quad k = \frac{2\pi}{\lambda}$$

and x_1,y_1 and x_2,y_2 are the coordinates of the points P_1 and P_2 in plane A. If P_1 and P_2 are positioned symmetrically either side of the centre of plane A, then the phase term ψ is equal to zero and μ_{12} is simply a normalised two dimensional Fourier transform of the intensity distribution of the source σ. We assume here that the antennas are illuminated by a spatially incoherent source of uniform intensity. The intensity distribution in the source plane **perceived** by the antennas is therefore a function of their far field radiation patterns. (We assume that the antennas are identical and therefore have identical far field radiation patterns.) If the antennas have high gains (e.g. 40 dB) then their angular field of view is small and the Fraunhoffer approximation applies. Thinking of an antenna as a transmitter, this gives the far field complex amplitude $u_\sigma(\xi,\eta)$ due to a complex antenna illumination function $u_A(x,y)$, as

$$u_\sigma(\xi,\eta) = K \iint_{\substack{\text{antenna}\\ \text{aperture}}} u_A(x,y)\, e^{-j\frac{k}{R}(x\xi+y\eta)}\, dx\, dy \qquad (1.6)$$

where K is a constant. Considering an antenna as a receiver, $u_A(x,y)$ is the complex amplitude at the antenna aperture due to a source of spatially invariant complex amplitude in the far field. $u_\sigma(\xi,\eta)$ is the apparent complex amplitude of the far field source if the antenna is treated as a point (isotropic) receiver. Hence, if we treat the antennas as points, the **apparent** source intensity distribution is

$$I(\xi,\eta) = \left|u_\sigma(\xi,\eta)\right|^2 \qquad (1.7)$$

The complex degree of coherence between the signals at the antenna terminals is therefore given by equations 1.5, 1.6 and 1.7 as

$$\mu_{12} = \frac{e^{j\psi} \iint_\sigma \left|u_\sigma(\xi,\eta)\right|^2 e^{-j\frac{k}{R}(p\xi+q\eta)}\, d\xi\, d\eta}{\iint_\sigma \left|u_\sigma(\xi,\eta)\right|^2 \, d\xi\, d\eta}$$

where $$u_\sigma(\xi,\eta) = K \iint_{\substack{\text{antenna}\\ \text{aperture}}} u_A(x,y)\, e^{-j\frac{k}{R}(x\xi+y\eta)}\, dx\, dy \qquad (1.8)$$

Hence, the complex degree of coherence between the signals at the antenna terminals is found as follows. We take the Fourier transform of the complex aperture illumination function, $u_A(x,y)$, for one antenna to obtain the far field complex amplitude function $u_\sigma(\xi,\eta)$. We then square the magnitude of $u_\sigma(\xi,\eta)$ to obtain $I(\xi,\eta)$. We then take the normalised[1] Fourier transform of $I(\xi,\eta)$ to obtain the complex degree of coherence, μ_{12}. We can compare this to one process that will yield the acf of any finite energy signal $x(t)$: first take the Fourier transform and square its magnitude to obtain the energy spectral density, $E_{xx}(f) = |X(f)|^2$, and then, applying the Wiener Kintchine theorem, take the

[1] to ensure that $0 \le |\mu_{12}| \le 1$.

inverse Fourier transform of $E_{xx}(f)$ to obtain the acf, $r_{xx}(\tau)$. Apart from a difference between taking the Fourier transform and taking the inverse Fourier transform in the final stage, irrelevant in an even symmetrical system, these two processes are the same. Hence, we see that the complex degree of coherence between the signals at the two antenna terminals, as a function of antenna separation, is given by the autocorrelation function (acf) of the aperture illumination function of one antenna. E.g. if the aperture illumination function of one antenna is as shown (one dimension only) in figure 1-9, where the diameter of the antenna is *a*, then the magnitude of the complex degree of coherence between the signals at the antenna terminals is as shown in figure 1-10.

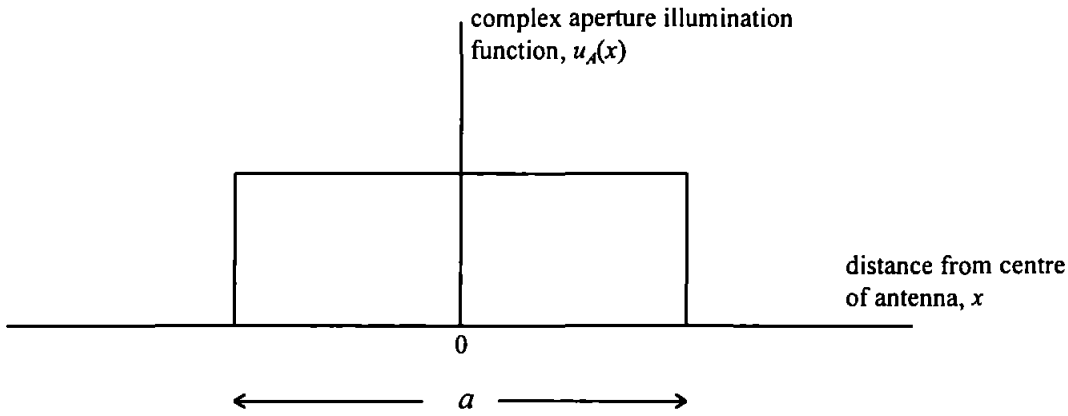

Figure 1-9. Complex aperture illumination function for one antenna.

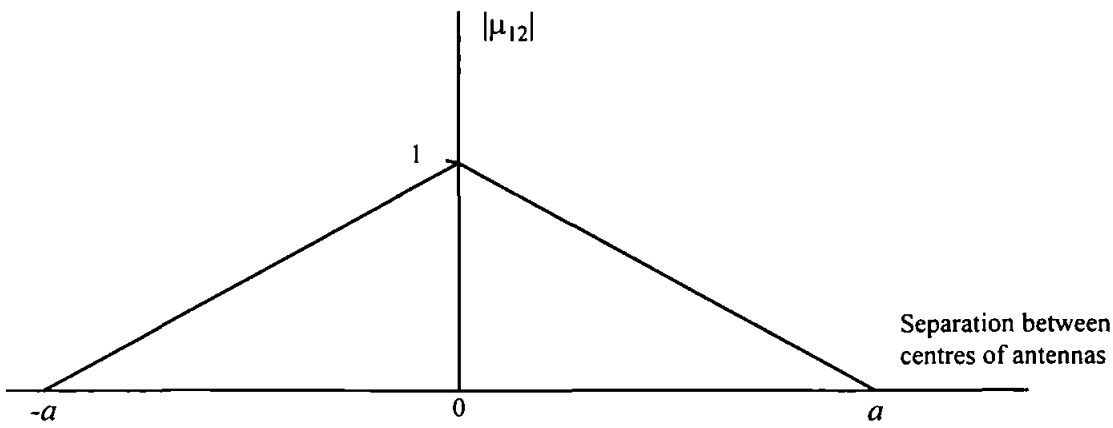

Figure 1-10. Magnitude of complex degree of coherence as a function of antenna separation.

Regardless of the actual form of the complex illumination function for one antenna, within the range $-\frac{a}{2} \leq x \leq +\frac{a}{2}$, the complex degree of coherence will be zero for antenna separations greater than a. If the antennas are separate aperture antennas (e.g. horn of parabolic reflector) the centres of the antennas cannot physically be brought closer than the aperture diameter, a, without overlapping so that one blocks the other. Using one parabolic reflector with two feeds would clearly not be acceptable. The higher the gain of the antennas, the narrower their field of view and the greater their separation must be for the signals at their terminals to be uncorrelated. However, the higher the antenna gain, the larger the antenna diameter, and meeting the physical requirement to move them further apart to avoid overlap as they get bigger will always lead to their separation being great enough to ensure that the signals at their terminals are uncorrelated.

Two assumptions have been made in applying the van Cittert-Zernicke theorem in this way. One fundamental assumption made in both the Fraunhoffer approximation and the van Cittert-Zernicke theorem equates to the assumption that the antennas have high directivity. In reality, in order to gain a wide field of view, we would expect to use antennas with rather low gains (e.g. 6 dB). For such low gains the complex degree of coherence function may differ a little from that predicted by the above simple theory. It is helpful to consider some typical figures. At a frequency of 10 GHz a high gain of 40 dB can be achieved with antenna diameters of the order of 1 m. A separation of 1 m can therefore be achieved under conditions where this assumption is valid. If we now reduce the gain of the antennas while maintaining the separation, the complex degree of coherence function might not shrink spatially as quickly as the antenna dimensions, but it will still shrink and the noise signals at the antenna outputs will remain uncorrelated. Hence it seems safe to state that if the antennas are illuminated by an incoherent source of uniform intensity distributed over their full view and their separation is large relative to their dimensions then their outputs are effectively uncorrelated. A more rigorous analysis would probably support a stronger statement involving smaller separations, but this statement is sufficient for our purposes.

1.4 Outline of the thesis

This thesis comprises two parts. The first part, chapters 2 to 5 inclusive, present an analysis of the cross correlation receiver regardless of the technology used to perform the initial correlation, while the remaining chapters consider implementation using acousto-optic correlators. Chapter 2 deals with the correlation process, chapter 3 with the TDFCSD. Expressions for SNRs in the ccf and TDFCSD are derived in terms of input signal and receiver system parameters for different classes of correlator. There are a number of different correlators that could be considered, but the important division as regards analysis is that between finite sample time domain and frequency domain (FFT based) correlators. The finite sample time domain correlator takes time windowed samples of the two signals, length T_s, and then cross correlates them as if they were isolated pulses to produce a ccf of total length $2T_s$. An FFT based correlator produces a correlation function of length T_s. The significance of these and other differences is discussed in detail. A space integrating acousto-optic correlator forms a finite sample time domain correlation. The time integrating acousto-optic correlator actually forms a true continuous correlation function rather than either of the above, but it is shown that it gives a performance that can be effectively modelled by the FFT based correlator. The processes of cross correlation and the generation of the TDFCSD is illustrated by a computer simulation which also offers results to compare against the predictions of the analysis. Chapter 4 places the cross correlation receiver and use of the TDFCSD into context by considering ESM system performance. A particular scenario is considered: that of a ship's ESM system trying to detect an incoming missile using a power managed LPI radar. The detection performance of the ccf and the TDFCSD is calculated and compared against a crystal video system. The concept of the minimum detection range (the range *below* which a power managed radar becomes undetectable) is introduced and used as the main criterion for comparison. Direction finding using the phase terms of the TDFCSD is considered in chapter 5 and expressions for the accuracy of angle of arrival estimation are calculated. This is again supported and illustrated by the results of computer simulation.

The second part of the thesis, chapters 6 to 10 inclusive, considers acousto-optic correlation, and can itself be split into 2 main parts. After an introduction, chapter 6, chapters 7, and 8 are devoted to space integrating correlation. The path that the research presented in this thesis eventually took lead away from the use of space integrating correlators. However,

the work started with space integrating correlators before the application of cross correlation receivers to the detection of spread spectrum signals had been suggested, and the results obtained are believed to be of merit in their own right. Earlier work carried out by Reeve and Wombwell [10] showed that whereas previously described non heterodyning space integrating architectures [9] did not produce the true correlation function, a simple non heterodyning correlator could produce a true correlation function using the first diffraction order from the acousto-optic cells if the signals to the acousto-optic cells took a certain form - a carrier modulated by the input signals using double sideband large carrier modulation. Further work [14] showed that a true correlation function could also be obtained using the zeroth diffraction order. Although it became obvious, in retrospect, why such a correlator should work it was not explained by any of the theories currently used in the literature to describe space integrating correlators. Indeed, according to the analysis generally offered there should be no information in the zeroth diffraction order. To explain the operation of the zeroth order correlator it was necessary to start the analysis virtually from scratch. Chapter 7 takes a fresh look at the acousto-optic interaction, initially in the limit of pure Raman Nath diffraction, and demonstrates that there *is* information in the zeroth diffraction order. This basic theory is then used in chapter 8 to develop a unified general theory of all one dimensional space integrating acousto-optic correlator. Equations are first developed for a "general all order" correlator. A range of other correlators, both heterodyning and non-heterodyning, including ones previously described in the literature and the zeroth order correlator, are then shown to be special cases of this general all order correlator. Some experimental results from a practical zeroth order non-heterodyning correlator are also presented.

The time integrating acousto-optic correlators described in chapters 9 and 10 are not new. It is the application to which they are being put that is new. Existing theory adequately predicts the performance of these time integrating correlator and this is presented, in modified form, in chapter 9. Three types of time integrating acousto-optic correlator are described and two of them analysed in some detail, leading to a discussion of the most suitable architecture. Chapter 10 presents results from a practical time integrating correlator, demonstrating that it can indeed perform the processing required to enable extraction of both the magnitude and the phase of the TDFCSD. Chapter 11 then presents conclusions and recommendations for further work.

2. The Cross Correlation Process

2.1 Introduction

We consider the cross correlation of the two unknown bandpass signals, that have undergone no processing other than amplification, entering the two receivers and treat the two sets of noise, $n_1(t)$ and $n_2(t)$, as independent. If only one signal source is present, then the correlation formed is:

$$s(t) \otimes s(t - t_d) \quad + \quad s(t) \otimes n_2(t) \quad + \quad n_1(t) \otimes s(t - t_d) \quad + \quad n_1(t) \otimes n_2(t) \qquad (2.1)$$

where $\otimes$ denotes cross correlation and t_d is the time difference of arrival of the signal at the two receivers. It should be noted that we are using a completely general representation of the input signals. We are not even using a complex amplitude representation since we have no prior knowledge of any carrier frequency. The first term is the acf of $s(t)$, $r_{ss}(\tau)$, time shifted by t_d, and forms the signal part of the correlator output. The peak signal power, $\hat{S}_o$, of the correlator output is the square of the peak value, $r_{ss}(0)$, of this acf , which equals the energy of the signal pulse, E_p. Hence

$$\hat{S}_o = E_p^{\,2} \qquad (2.2)$$

Equation 2.2 clearly does not balance dimensionally, and this deserves some explanation. A clear distinction must be made between measurements of voltage, power and energy before and after the correlator. Dimensionally the correlation process has the same effect as the convolution process carried out by any filter. If we apply a finite energy voltage signal $x(t)$ to the input of a filter with an impulse response $h(t)$, then the output, defined as $y(t) = \int x(\tau) h(\tau - t) d\tau$, has the units, V^2s, of energy. However, the output $y(t)$ is really a voltage signal with units V rather than V^2s. Though not normally mentioned, the convolution describing the filter action includes an implicit transfer coefficient with units V^1s^{-1}. Throughout this chapter the output of the correlator will be treated as a voltage signal. Input

signal and noise powers and signal to noise ratios will refer to values derived directly from the voltage signals at the antenna terminals due to electric fields at the antenna apertures. Output signal and noise powers and signal to noise ratios will refer to values derived from the voltage signals at the correlator outputs. For example, in equation 2.2 the left hand side of the equation refers to the power (units V^2) of the voltage signal at the output of the correlator whereas the right hand side refers to the square of the energy (units $(V^2s)^2$) of finite time samples of the voltage signals at the antenna terminals. The equation is balanced dimensionally by the square of the implied transfer coefficient (units $(V^1s^{-1})^2$). In general, throughout this chapter, whenever we see an expression referring to the correlator output on one side and correlator input on the other the units of the side referring to correlator input should be multiplied by the appropriate power of V^1s^{-1} in order to balance the equation dimensionally.

We account for both pulsed and CW signals here. A CW signal is treated as a pulse of length equal to the length of the samples taken into the correlator. It should be noted that the value of E_p and hence $\hat{S}_o$ depends on the mean power and the length of the signal sample and not on its bandwidth. A larger bandwidth does not make the signal more or less detectable by threshold detection applied to the ccf. It affects the width of the central peak of the autocorrelation function, but not its height.

The noise part of the correlator output, assuming the correlator adds no further noise of its own, is made up of the last three terms, two of which can be grouped together. To determine the output noise power we must calculate the power of the signal-noise and the noise-noise cross correlation terms. Which of these noise terms is more important will depend on the input SNR. For large input SNRs the signal-noise cross correlation terms, $r_{n_1 s}(\tau)$ and $r_{s n_2}(\tau)$, will be the more important. For low (< 0 dB) SNRs the noise-noise cross correlation, $r_{n_1 n_2}(\tau)$, will dominate, and this is the case that will generally be of more interest.

There are a number of distinctly different correlation processes that must be considered. The three different processes that will be discussed will be described as true continuous (TC) correlation, finite sample time domain (FSTD) correlation and finite sample frequency domain (FSFD) correlation.

2.2 Different correlation processes

Consider two continuous (finite power) real signals, x(t) and y(t). Their true ccf, taken over infinite time is

$$r_{xy}(\tau) = \lim_{T \to \infty} \frac{1}{T} \int_{-\frac{T}{2}}^{+\frac{T}{2}} x(t) y(t+\tau) dt \tag{2.3}$$

If we consider a finite integration time, T_s, we can form the function

$$r_{cont}(\tau) = \int_{0}^{T_s} x(t) y(t+\tau) dt \tag{2.4}$$

If we add N successive true continuous correlations of this sort we obtain the ccf for the longer integration time NT_s

$$R(\tau) = \int_{0}^{NT_s} x(t) y(t+\tau) dt = \sum_{n=0}^{N-1} \int_{nT_s}^{(n+1)T_s} x(t) y(t+\tau) dt \tag{2.5}$$

This adding of successive ccfs to produce a larger correlation is only possible if we can form the TC ccf of the form shown in equation 2.4. It will be shown, in chapter 9 , that a time integrating acousto-optic correlator does produce this TC ccf, for a limited range of τ, and is therefore capable of extremely long integration times. However, some commonly used correlation processes produce ccfs which cannot be added in this way. Many practical correlators operate by first grabbing finite samples of the signals x(t) and y(t). The FSTD correlator takes these windowed samples of the two signals, of length T_s, and then correlates them as if they were isolated pulses to produce a ccf of total length $2T_s$. The FSFD correlator (usually based on the FFT) performs a cyclic correlation on these samples to produce a ccf of length T_s.

In FSTD correlation, the two samples are correlated as if they are isolated (finite energy) pulses. The ccf produced is of the form

$$r_{fstd}(\tau) = \int_{0}^{T_s-\tau} x(t)\,y(t+\tau)\,dt \tag{2.6}$$

for $\tau > 0$. (For $\tau < 0$ the limits of integration are τ and T_s.) The difference between this and the TC ccf is

$$r_{fstd}(\tau) - r_{conv}(\tau) = -\int_{T_s-\tau}^{T_s} x(t)\,y(t+\tau)\,dt \tag{2.7}$$

Summing N successive FSTD correlations gives

$$\sum_{n=0}^{N-1} \int_{nT_s}^{(n+1)T_s-\tau} x(t)\,y(t+\tau)\,dt = R(\tau) - \sum_{n=0}^{N-1} \int_{(n+1)T_s-\tau}^{(n+1)T_s} x(t)\,y(t+\tau)\,dt \tag{2.8}$$

which is still limited to a width of $2T_s$. If we form one long FSTD ccf using samples of length NT_s, we obtain

$$\int_{0}^{NT_s-\tau} x(t)\,y(t+\tau)\,dt = R(\tau) - \int_{NT_s-\tau}^{NT_s} x(t)\,y(t+\tau)\,dt \tag{2.9}$$

Hence, we see that, except for when $\tau = 0$, the FSTD ccf is different from the TC ccf and that we cannot add successive FSTD ccfs to produce one long ccf. This does not mean that the FSTD correlation is of no value. It is of interest because it is the form of cross correlation performed by a space integrating acousto-optic correlator, and it will provide a good starting place to start the discussion of the noise performance of cross correlation processes.

In FSFD (finite sample frequency domain) cross correlation (usually involving the FFT) the correlation is cyclic. The samples are effectively treated as if they are single periods of continuous periodic signals. Hence the output looks, at first sight, much more like the TC ccf. The FSFD ccf is of the form (for $\tau > 0$)

$$r_{fsfd}(\tau) = \int_{0}^{T_s-\tau} x(t)y(t+\tau)dt + \int_{T_s-\tau}^{T_s} x(t)y(t-T_s+\tau)dt \tag{2.10}$$

The difference between this FSFD ccf and the TC ccf is

$$r_{fsfd}(\tau) - r_{conv}(\tau) = \int_{T_s-\tau}^{T_s} x(t)\left[y(t-T_s+\tau) - y(t+\tau)\right]dt \tag{2.11}$$

Summing N successive FSFD ccfs gives

$$\sum_{n=0}^{N-1}\left\{\int_{nT_s}^{(n+1)T_s-\tau} x(t)y(t+\tau)dt + \int_{(n+1)T_s-\tau}^{(n+1)T_s} x(t)y(t-T_s+\tau)dt\right\} \tag{2.12}$$

$$= R(\tau) + \sum_{n=0}^{N-1}\left\{\int_{(n+1)T_s-\tau}^{(n+1)T_s} x(t)\left[y(t-T_s+\tau) - y(t+\tau)\right]dt\right\}$$

However, if we form one long FSFD ccf using samples of length NT_s, we obtain

$$R(\tau) + \int_{NT_s-\tau}^{NT_s} x(t)\left[y(t-NT_s+\tau) - y(t+\tau)\right]dt \tag{2.13}$$

which has a much smaller difference from $R(\tau)$. Hence, we see that, as for FSTD correlation, FSFD correlation is different from TC correlation and successive correlations cannot be added to produce one long ccf. The results of FSTD and TSFD correlation are also clearly different. FSFD correlation is very important since FFT based correlation is the technique used in DSP systems. It is also important in that, as we shall see, SNR analysis for FSFD and TC correlation processes is virtually the same, provided that the input signals are stationary. If we consider the cross correlation of two independent noise signals the envelope of the FSTD ccf will be triangular, whereas it will be flat for both FSFD and TC correlation.

2.3 Finite sample time domain correlation noise performance

2.3.1 Noise-noise cross correlation.

When the input signal to noise ratio is very low it is the noise-noise correlation term that will dominate. If the noise in the two correlator inputs were the same then we would be simply considering a noise autocorrelation function which will give a large narrow peak at the centre of the function. If noise terms in the two inputs are completely independent, however, there will be no such central peak. If a time domain correlator is used, the cross correlation of 2 independent rectangular windowed samples of noise, of equal length T_s , has a triangular mean power envelope of length $2T_s$. In order to calculate the power of this cross correlation function we can consider the process of cross correlation in the frequency domain. In the time domain we are correlating two sets of passband noise of length T_s to give

$$n_{out}(\tau) = n_1(t) \otimes n_2(t) \tag{2.14}$$

Correlation is performed over a finite sample or integration time and hence we must consider both signal and noise inputs as finite energy signals. The input noise signals are assumed to have constant mean power throughout the sample length and the continuous signals of which they are samples are assumed to be bandpass white Gaussian random signals. In the time domain each noise set is a continuous signal multiplied by a rect function of unit height and width T_s. The continuous signal has a power spectrum but a Fourier transform cannot be defined. The finite signal of length T_s must have a Fourier transform $N(f)$ but although this can be calculated for any given $n(t)$ we cannot define a general form for the phase of $N(f)$, except in statistical terms. The amplitude of the Fourier transform will be the convolution of a rectangular function derived from the power spectrum of the continuous passband white noise signal and a function of the form sinc(fT) due to the rectangular windowing function used in taking the noise sample. If the BT product of the noise sample is large, the width of this sinc function, $1/T$, is small with reference to the bandwidth of the noise and the amplitude of the frequency spectrum approximates to that shown in figure 2-1.

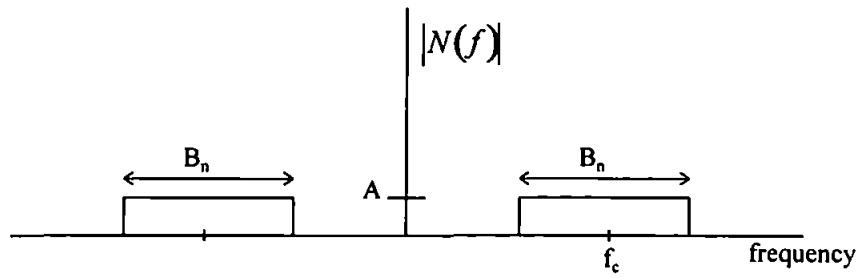

Figure 2-1. Mean amplitude spectrum of noise input.

Then, referring to the amplitude of the Fourier transform shown in figure 2-1, the total Energy of the noise sample is given by

$$E_n = 2B_n A^2 \tag{2.15}$$

But the energy of the noise sample must be given by

$$E_n = \sigma_n^2 T_s = \eta B_n T_s \tag{2.16}$$

where σ_n^2 is the variance (power) and $\frac{\eta}{2}$ the power spectral density of the continuous noise signal at the antenna terminals. Therefore

$$A^2 = \frac{\sigma_n^2 T_s}{2B_n} = \frac{\eta T_s}{2} \tag{2.17}$$

$$A = \sigma_n \sqrt{\frac{T_s}{2B_n}} = \sqrt{\frac{\eta T_s}{2}} \tag{2.18}$$

and so

$$|N(f)| = \sqrt{\frac{\eta T_s}{2}} \left\{ \text{rect}\left(\frac{f - f_c}{B_n} \right) + \text{rect}\left(\frac{f + f_c}{B_n} \right) \right\} \tag{2.19}$$

Where $|N(f)|$ is non zero, the phase of the signal $\theta_n(f)$ will be random with p.d.f. given by

$$p(\theta_n)=\frac{1}{2\pi} \quad \text{for} \quad 0 \le \theta \le 2\pi \tag{2.20}$$

and the spectrum of a noise sample $n(t)$ is given by

$$N(f)=\sqrt{\frac{\eta T_s}{2}}\left\{\text{rect}\left(\frac{f-f_c}{B_n}\right)e^{j\theta_n(f)}+\text{rect}\left(\frac{f+f_c}{B_n}\right)e^{-j\theta_n(f)}\right\} \tag{2.21}$$

If we correlate two samples of noise $n_1(t)$ and $n_2(t)$ then the Fourier transform of the correlation function, the Cross Energy Spectral Density is given by

$$N_1^*(f)N_2(f)=\frac{\eta T_s}{2}\left\{\text{rect}\left(\frac{f-f_c}{B_n}\right)e^{j[\theta_{n2}(f)-\theta_{n1}(f)]}+\text{rect}\left(\frac{f+f_c}{B_n}\right)e^{j[\theta_{n1}(f)-\theta_{n2}(f)]}\right\} \tag{2.22}$$

The average amplitude spectrum of the cross correlation function $r_{n_1n_2}(\tau)$ therefore takes the form shown in figure 2-2.

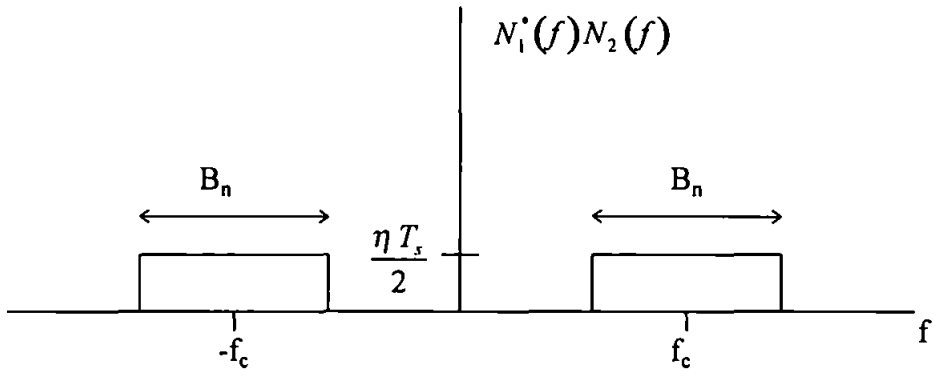

Figure 2-2. Amplitude spectrum of the noise-noise cross correlation.

The total energy of the noise-noise cross correlation function is therefore

$$\left(\frac{\eta T_s}{2}\right)^2 \times 2B_n = \frac{\eta^2 B_n T_s^2}{2} \tag{2.23}$$

To re-emphasise the comments made at the start of this chapter regarding units of expressions referring to signals before and after the correlator: if figure 2-2 shows the amplitude spectrum of the noise-noise correlation at the correlator output (units $V/\sqrt{Hz}$), integrating under the square of this function gives the total energy for a finite time period of the voltage signal at the correlator **output** (*units* V^2s). The expression in equation 2.23 is made up from terms relating to the voltage signals at the correlator **input** and has units V^4s^3. Equating this to a quantity of units V^2s at the output is balanced dimensionally by remembering that there is an implicit transfer coefficient of units V^1s^{-1} (as described in section 2.1), which is squared since we are considering the square of the output voltage.

An obvious point to note here is that in attempting to minimise this noise signal in the output of the correlator the input noise spectral density is more important than the noise bandwidth. If the separation between the two antennas is a few metres the time difference of arrival between the two input signals is small of the order of nanoseconds and the signal peak occurs very close to the centre of the ccf . We are therefore concerned with the noise power at the centre. Since we are considering the cross correlation of two samples of noise with rectangular amplitude envelopes, we assume the correlation in the time domain to have a varying r.m.s. voltage with an amplitude envelope of the form shown in figure 2-3.

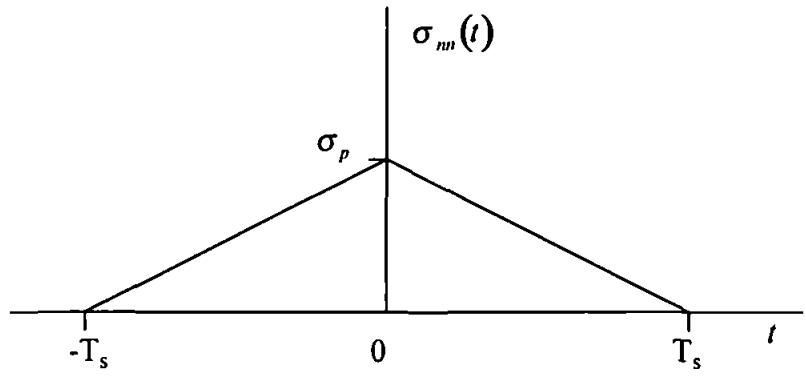

Figure 2-3. Amplitude envelope of the noise-noise cross correlation.

The total energy of the function, in terms of σ_p and T_s, is

$$2\int_0^{T_s}\left(\sigma_p\left(1-\frac{t}{T_s}\right)\right)^2 dt \;=\; 2{\sigma_p}^2\int_0^{T_s}\left(1-\frac{2t}{T_s}+\frac{t^2}{T_s^2}\right)dt$$

$$=\; 2{\sigma_p}^2\left(T_s - T_s + \frac{T_s}{3}\right) \;=\; \frac{2}{3}\sigma_p^2 T_s \qquad (2.24)$$

Equating this to the expression we obtained from integrating under the energy spectral density (equation 2.23) gives us

$$\frac{2}{3}\sigma_p^2 T_s \;=\; \frac{\eta^2 B_n T_s^2}{2}$$

$$\sigma_p^2 \;=\; \frac{3}{4}\eta^2 B_n T_s \qquad (2.25)$$

Now the peak correlator output signal power is given by $\hat{S}_o = E_p^2$ (equation 2.2) where E_p is the energy of the signal pulse at the antenna terminals. Since the time difference of arrival between the two input signals will be small (of the order of 10 ns), the signal peak occurs close to the centre of the whole cross correlation function. Therefore the peak signal to mean noise power ratio in the correlator output, for very low input SNR and ignoring noise added by the correlator is, dividing the correlator output signal power, E_p^2, by the mean noise power, given by equation 2.25,

$$\left(\frac{\hat{S}}{N}\right)_o = \frac{E_p^2}{\frac{3}{4}\eta^2 B_n T_s} \qquad (2.26)$$

We see that for constant receiver and noise parameters the output peak signal to mean noise power ratio increases as the square of the input signal energy, i.e. a plot of output SNR to input SNR will show a 20 dB/decade slope. Since the energy of pulse equals its power times its temporal length, $E_p = S_i T_p$, and $\eta B_n = N_i$, the noise power at the terminals of one antenna, we can rewrite equation 2.26 as

$$\left(\frac{\hat{S}}{N}\right)_o \;=\; \frac{S_i^2\, T_p^2\, B_n}{\frac{3}{4}\, T_s\, \eta^2\, B_n^2} \;=\; \frac{4\, T_p^2\, B_n}{3\, T_s}\left(\frac{S}{N}\right)_i^2 \qquad (2.27)$$

where B_n is the noise bandwidth, T_p the length of the signal pulse, T_s the length of the sample, and S_i the input signal power. The 20 dB/decade slope is not suprising since both output signal and output noise come from effectively squaring (cross correlation) input signal nd input noise respectively.

2.3.2 Signal-noise cross correlations (finite sample time domain correlation).

For larger input SNRs we must consider the signal-noise cross correlations, again by multiplication in the frequency domain. The form of the noise sample in the frequency domain has already been discussed. The Fourier transform of the signal can obviously vary depending on the signal. If it is simply a square pulse of a single frequency the Fourier transform is a sinc function; if the signal is a chirp pulse the spectrum is more complicated. However, if the frequency band occupied by the pulse lies totally inside the noise bandwidth of the receiver the precise form does not matter: it is the area under it that is important. Consider a chirp with an amplitude spectrum of the form shown in figure 2-4.

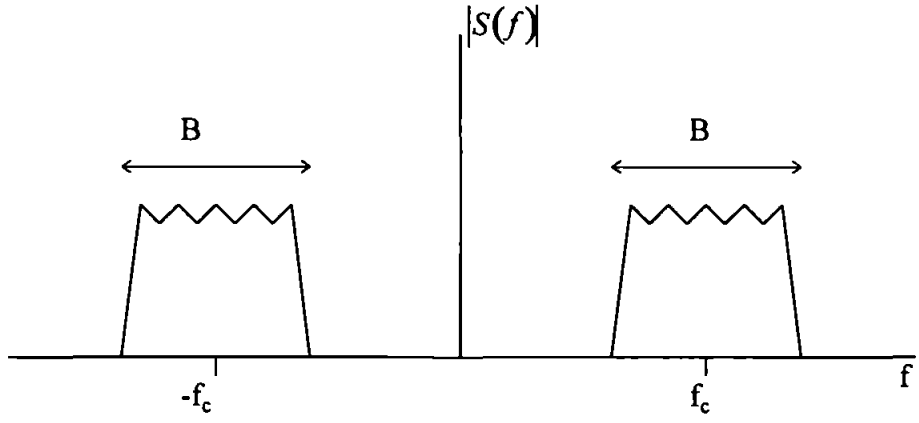

Figure 2-4. Amplitude spectrum of a chirp signal (approximate).

When we multiply this signal spectrum, S(f) , by the noise amplitude spectrum (equation 2.18), which is flat over the range where $|S(f)|$ is non zero, the magnitude of the resulting cross spectral density becomes

$$\sqrt{\frac{\eta T_s}{2}}\,|S(f)| \tag{2.28}$$

and the total energy of a **single** signal-noise cross correlation is therefore, by integrating under the cross energy spectral density

$$\int_{-\infty}^{\infty} \frac{\eta\, T_s}{2} |S(f)|^2\, df \;=\; \frac{\eta\, T_s}{2} E_p \tag{2.29}$$

If the signal pulse has a square r.m.s. envelope of length T_p then the amplitude of the r.m.s. envelope of the signal-noise cross correlation, found by considering the cross correlation of a rectangular pulse of length T_p with a rectangular pulse of length T_s, is of the form shown in figure 2-5, assuming that the signal is in the centre of sample.

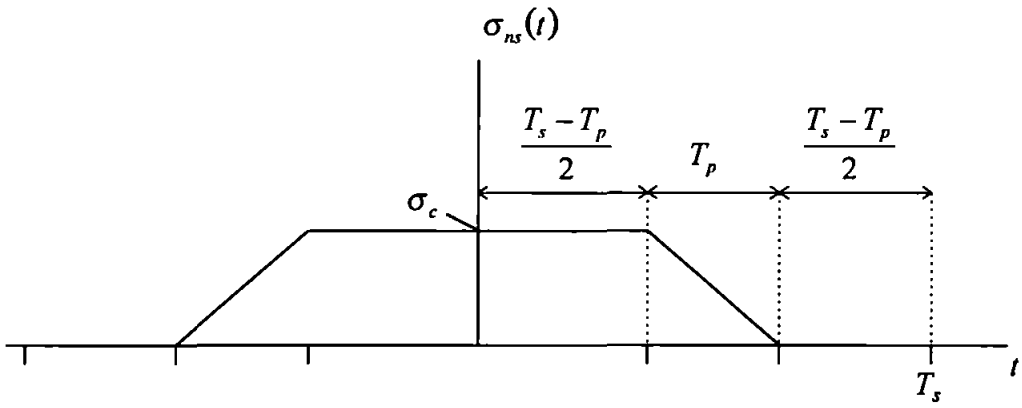

Figure 2-5. R.M.S. envelope of the signal-noise cross correlation.

The cross correlation will be noise-like within this r.m.s. envelope. The total energy of this signal-noise cross correlation is

$$\int_{-T_s}^{T_s} \sigma_{ns}^2(t)\, dt \;=\; 2\left\{ \frac{\sigma_c^2 \left(T_s - T_p\right)}{2} + \int_0^{T_p} \left(\frac{\sigma_c\, t}{T_p} \right)^2 \right\}$$

$$= \sigma_c^2 \left(T_s - T_p\right) \;+\; 2 \frac{\sigma_c^2}{T_p^2} \frac{T_p^3}{3}$$

$$= \sigma_c^2\left(T_s - \frac{T_p}{3}\right) \tag{2.30}$$

This must equal the total energy as calculated in the frequency domain and given by equation 2.29, and so we have:

$$\sigma_c^2\left(T_s - \frac{T_p}{3}\right) = \frac{\eta\, T_s}{2} E_p \tag{2.31}$$

Therefore the correlator output noise power at the centre of the correlation function is

$$\sigma_c^2 = \frac{3\eta\, T_s E_p}{2\left(3T_s - T_p\right)} \tag{2.32}$$

The total noise power in the output of the correlator arises from both signal-noise cross correlations and the total noise power is therefore (incoherent addition)

$$2\sigma_c^2 = \frac{3\eta\, T_s E_p}{\left(3T_s - T_p\right)} \tag{2.33}$$

Given that the peak output signal power is $\hat{S}_o = E_p^2$, using $2\sigma_c^2$ as given by equation 2.32 as total noise power gives an output peak signal to mean noise power ratio, for high input SNR

$$\left(\frac{\hat{S}}{N}\right)_o = \frac{E_p^2}{\left(\frac{3\eta\, T_s E_p}{\left(3T_s - T_p\right)}\right)} = \frac{\left(3T_s - T_p\right)E_p}{3\eta\, T_s} \tag{2.34}$$

Writing E_p as $S_i T_p$ and noting that ηB_n is the input noise power, we have the output peak SNR, for high input SNR

$$\left(\frac{\hat{S}}{N}\right)_o = \frac{\left(3T_s - T_p\right)T_p\, B_n}{3\, T_s} \left(\frac{S}{N}\right)_i \tag{2.35}$$

2.3.3 Total output SNR (finite sample time domain correlation).

The complete expression for the peak signal to mean noise power ratio in the time domain cross correlator output is, assuming that no noise is added by the correlator and using equations 2.25 and 2.32 respectively to substitute for σ_p^2 and $2\sigma_c^2$,

$$\left(\frac{\hat{S}}{N}\right)_o = \frac{\hat{S}_o}{\sigma_p^2 + 2\sigma_c^2} = \frac{E_p^2}{\frac{3}{4}\eta^2 B_n T_s + \frac{3\eta T_s E_p}{3T_s - T_p}} \tag{2.36}$$

The input SNR is

$$\left(\frac{S}{N}\right)_i = \frac{S_i}{\eta B_n} = \frac{E_p}{\eta B_n T_p} \tag{2.37}$$

and so

$$\left(\frac{\hat{S}}{N}\right)_o = \frac{T_p^2 B_n \left(\frac{S}{N}\right)_i^2}{\frac{3}{4}T_s + \frac{3T_s T_p}{(3T_s - T_p)}\left(\frac{S}{N}\right)_i} \tag{2.38}$$

Figure 2-6 shows how the processing gain in dB, given by the output peak signal to mean noise ratio in dB minus the input signal to noise ratio in dB, varies with input signal power for a time domain correlator. The signal bandwidth does not affect the processing gain provided that it falls entirely within the receiver bandwidth, as has been assumed to be the case here.

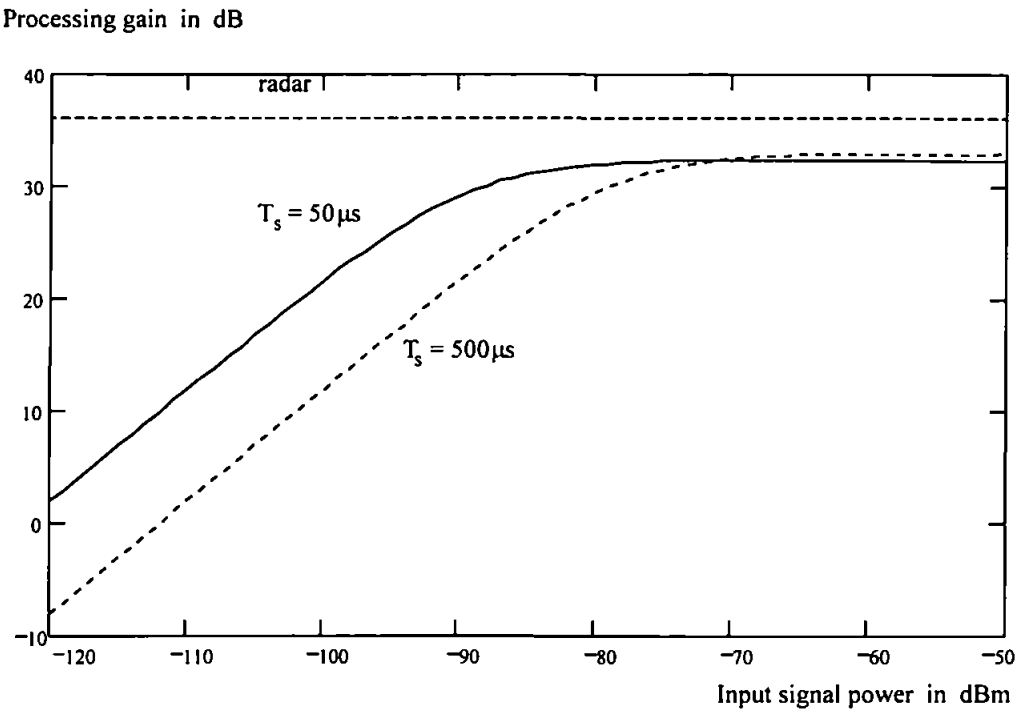

Figure 2-6. Variation of the processing gain of the correlator with input signal power for a time domain cross correlating ESM receiver for different sample lengths. The parameters used for this graph are: sample lengths, T_{s1} = 50 μs and T_{s2} = 500 μs , signal pulse length, T_p = 20 μs, system noise temperature, T_{sys} = 500 K, and receiver noise bandwidth, B_n = 100 MHz. The processing gain of the radar is shown as constant at 37 dB.

We can clearly see from figure 2-6, that although the longer sample length gives a slightly higher processing gain for high input SNR, it gives a much poorer performance at low input SNR, when the noise-noise cross correlation dominates the output. At first sight we would infer from this that increasing the integration time, beyond a length sufficient to have a good chance of including a whole pulse, would lead to a reduced SNR at the correlator output. This is certainly the case if we are dealing with just one isolated pulse: once T_s is large enough to take in the whole signal pulse then increasing T_s any further only takes in more noise. However, pulsed LPI radar signals are usually pulse chains with a relatively high duty cycle. A radar with a range of 75 km could have a pulse repetition interval (p.r.i.) as low as 500 μs. The radar in a missile homing head could well have a significantly higher pulse repetition frequency (p.r.f.), increasing with decreasing range. If the pulse length is 100 μs, the p.r.i. can be expected to be significantly less than 1 ms. Hence, if we use long sample lengths, we can expect our sample to include several pulses. The system will effectively achieve coherent pulse integration, something that it is normally assumed that only the radar can do! To account for this, when T_s is significantly greater than the p.r.i., we should replace T_p in

equation 2.29 by nT_p where n is the number of pulses falling within the ESM integration time, given by

$$n = \frac{T_s}{p.r.i.} \tag{2.39}$$

T_p will be replaced by nT_p, and E_p by nE_p, in all equations from this point on.

2.3.4 Output SNR for CW input signals (time domain correlator).

If the input signals are CW then the sample time will be the length of the signal sample in the correlator. i.e. $nT_p = T_s$. When this is the case, from equation 2.36 we obtain

$$\left(\frac{\hat{S}}{N}\right)_o = \frac{E_p^2}{\frac{3}{4}\eta^2 B_n T_s + \frac{3}{2}\eta E_p} \tag{2.40}$$

and from equation 2.38

$$\left(\frac{\hat{S}}{N}\right)_o = \frac{T_s^2 B_n \left(\frac{S}{N}\right)_i^2}{\frac{3}{4}T_s + \frac{3T_s^2}{(3T_s - T_s)}\left(\frac{S}{N}\right)_i} = \frac{\frac{4}{3} B_n T_s \left(\frac{S}{N}\right)_i^2}{1 + 2\left(\frac{S}{N}\right)_i} \tag{2.41}$$

Clearly detection is improved by using longer integration times, as is almost always the case.

2.4 True continuous and finite sample frequency domain correlation

2.4.1 Output SNR

Because any discrete Fourier transform process treats its signal samples as one time period of a periodic continuous signal, the output of a FSFD correlator is different from that of a FSTD correlator which treats its signal samples as isolated pulses. One difference of considerable importance is the shape of the amplitude envelopes of the noise-noise and signal-noise cross correlations. Since the noise signals are now treated as having continuous flat amplitude envelopes, any cross correlation with them will result in a function which has a

flat amplitude envelope over the output signal length of T_s. A true continuous correlation process will clearly produce the same amplitude envelope. Although the detailed structure of the output noise signal is different, it will have the same statistical properties. The detailed structure of the signal output may also differ (though for some conditions it will not), but it is the amplitude of the output ccf at the centre that is important , and this will be the same for both TC and FSFD correlation. Using the expressions derived earlier for the total energies of the noise-noise and signal noise correlations (equations 2.23 and 2.29) and noting that the noise power is now simply the total noise energy, given by equation 2.23, divided by T_s, we obtain the noise-noise cross correlation power as

$$\frac{\frac{1}{2}\eta^2 B_n T_s^2}{T_s} = \frac{\eta^2 B_n T_s}{2} \tag{2.42}$$

and, considering n pulses per sample, the power of each of the two signal-noise correlations from equation 2.29 as

$$\frac{\frac{1}{2}\eta\ T_s\ n E_p}{T_s} = \frac{\eta\, n E_p}{2} \tag{2.43}$$

Hence, the output peak signal to mean noise power ratio for the FSFD correlation, dividing the peak signal power, $\left(n E_p\right)^2$, by the sum of the noise-noise correlation power (equation 2.42) and twice the single signal-noise correlation power (equation 2.43), is

$$\left(\frac{\hat{S}}{N}\right)_o = \frac{2\ n^2\ E_p^2}{\eta^2\ B_n\ T_s\ +\ 2\,\eta\ n\ E_p} \tag{2.44}$$

or, in terms of the input SNR

$$\left(\frac{\hat{S}}{N}\right)_o = \frac{n^2\ T_p^2\ B_n \left(\frac{S}{N}\right)_i^2}{\frac{1}{2} T_s\ +\ n T_p \left(\frac{S}{N}\right)_i} \tag{2.45}$$

Comparing these with the equivalent expressions for the time domain correlator (equations 2.36 and 2.38), we see that the FSFD or TC correlators have an advantage. For high input SNR, when the second of the two noise terms in the denominator dominates, the advantage is $(3T_s - nT_p)/3T_s$. For large sample length, T_s, and low signal duty cycle, so that $3T_s >> nT_p$, this advantage becomes equal to one and the time domain correlator does as well as the FFT correlator. For low input SNR, when the noise-noise cross correlation dominates the output noise, the advantage is 3/2, or 1.76 dB.

2.4.2 Output SNR for CW signals (TC and FSFD correlators)

If the input signals are CW then the sample time will be the length of the signal sample in the correlator. i.e. $nT_p = T_s$. When this is the case, equation 2.45 becomes

$$\left(\frac{\hat{S}}{N}\right)_o = \frac{2\,T_s\,B_n\left(\frac{S}{N}\right)_i^2}{1 + 2\left(\frac{S}{N}\right)_i} \tag{2.46}$$

2.5 The radar correlation process.

In a radar receiver the correlation is a cross correlation of signal with signal plus noise giving the signal autocorrelation function and one signal-noise cross correlation. The signal-noise cross correlation is the same as in the ESM cross correlating receiver, but we only have one signal-noise cross correlation instead of two. There is no noise-noise cross correlation. Hence the radar will inevitably do better than the ESM system. For high input SNR, when the noise-noise cross correlation term can be neglected, if the ESM correlator is an FFT correlator or a time domain correlator with $T_s >> T_p$, the radar will only have a processing gain 3 dB greater than the ESM system. However, while the processing gain of the ESM cross correlating system falls off with decreasing input SNR, the processing gain of the radar is maintained at the same value regardless of input SNR.

The radar will usually perform the cross correlation using a matched filter, such as a SAW (surface acoustic wave) device, rather than by an explicit correlation process. Using a matched filter is effectively the same as performing a time domain correlation with an infinite sample length, T_s. We can see that this is so by looking at what happens to the envelope of the signal-noise cross correlation as the sample length becomes very large and comparing this to the noise at the output of a matched filter. The amplitude envelope of the signal-noise cross correlation was shown in figure 2-5. If T_s becomes large so that T_p is relatively very small then this trapezoid envelope will tend towards being a flat rectangular envelope of total width T_s, as for the signal-noise correlation at the output of an FFT correlation process. If we consider a rectangular envelope burst of noise passing through a SAW filter, which like any filter simply imposes different gains and phase shifts on different frequency components, the rectangular burst will have its leading and trailing edges reshaped to give a trapezoid envelope. However, if we have continuous white noise as is usually the case, then the output will clearly have a constant amplitude, as for the case in the time domain correlator when $T_s \rightarrow \infty$ and T_p can be neglected. In this case the power of the single signal-noise correlation is given by equation 2.32 as

$$\sigma_c^2 = \frac{3\eta T_s E_p}{2\left(3T_s - T_p\right)} = \frac{\eta E_p}{2} \tag{2.47}$$

Hence, the peak signal to mean noise power ratio at the output of the matched filter is

$$\left(\frac{\hat{S}}{N}\right)_o = \frac{E_p^2}{\frac{1}{2}\eta E_p} = \frac{2E_p}{\eta} \tag{2.48}$$

This agrees with the standard result for matched filter noise performance to be found in most undergraduate texts covering communication signal processing. (See e.g. [15]) Writing E_p as $S_i T_p$ and noting that ηB_n is the input noise power, this is, in terms of the input SNR

$$\left(\frac{\hat{S}}{N}\right)_o = 2\,B_n\,T_p\left(\frac{S}{N}\right)_i \tag{2.49}$$

i.e. the radar receiver processing gain is $2B_nT_p$. Radar processing gain is often thought of as simply B_nT_p, but if we consider peak signal to mean noise power ratio at the matched filter output, as we do here, there is an additional factor of 2. The above expression gives the radar

receiver output SNR for a single pulse, if the radar uses predetection pulse integration then this SNR should be multiplied be an integration gain factor, I. The variations in peak signal to mean noise power ratio with input signal power, at the outputs of both time domain and frequency domain cross correlating ESM receivers and a matched filter radar receiver, are shown in figure 2-7, for a CW signal.

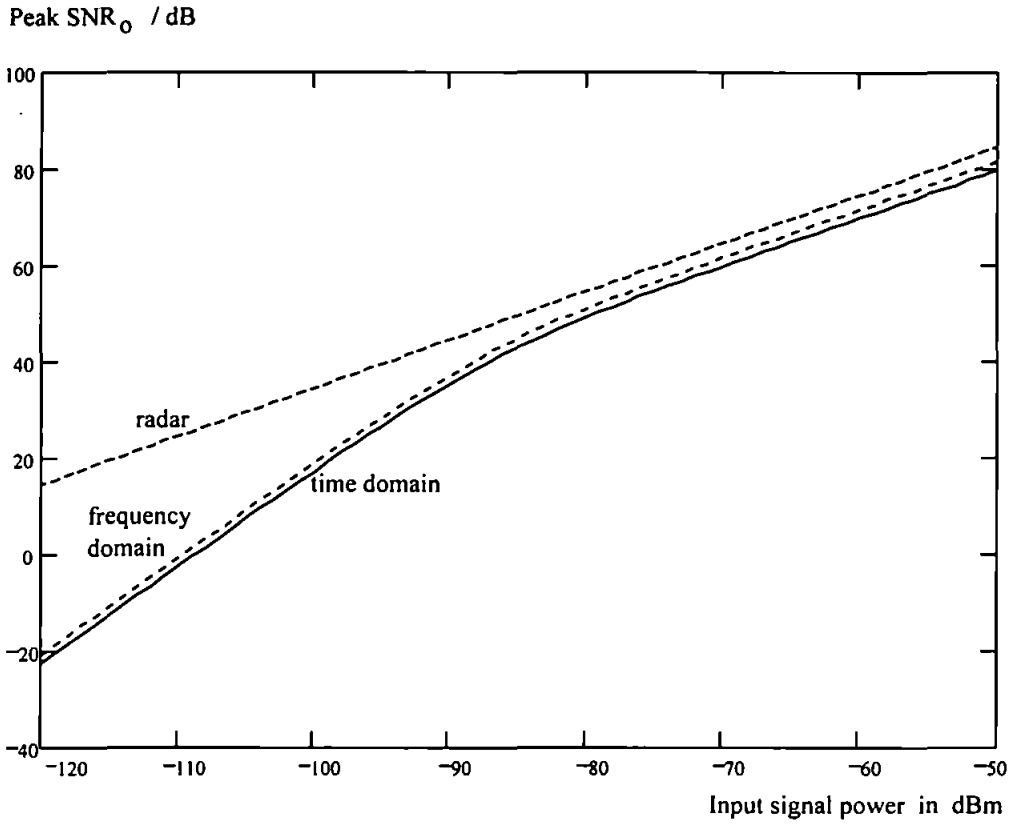

Figure 2-7. The variations in peak signal to mean noise power ratio with input signal power, at the outputs of both time domain and frequency domain cross correlating ESM receivers and a matched filter radar receiver. The signal is a CW signal with both ESM system and radar using an integration time of 100 μs. Both radar and ESM system are assumed to have a system noise temperature of 500 K and the ESM noise bandwidth is 500 MHz.

2.6 Simulation

The theoretical predictions of the preceding sections have been tested against a computer simulation. Limited signal bandwidths had to be used to allow computation (on a PC) within a reasonable time, but the bandwidths used were still large enough to allow

good comparisons to be made between the theoretical predictions and the results of the simulation. Complete displays of the Mathcad simulations, both program and results, are given in the appendices. Appendix A, for example shows a simulation for an FMCW signal using the following parameters:

T_s	B_n	B_s	SNR_i
500 μs	100 MHz	20 MHz	-15 B

The noise is additive white Gaussian noise (AWGN) created independently for each channel. Appendix B shows a simulation for a CW biphase signal coded by a maximal length sequence and appendix C shows a simulation with two separate FMCW signals and a high power interfering pulse. Results are shown here from a simulation for an FMCW signal using :

T_s	B_n	B_s	SNR_i
50 μs	80 MHz	10 MHz	-11 B

Figure 2-8 shows the first 1 μs of a typical pair of channel inputs. These are clearly two independent broadband noise signals.

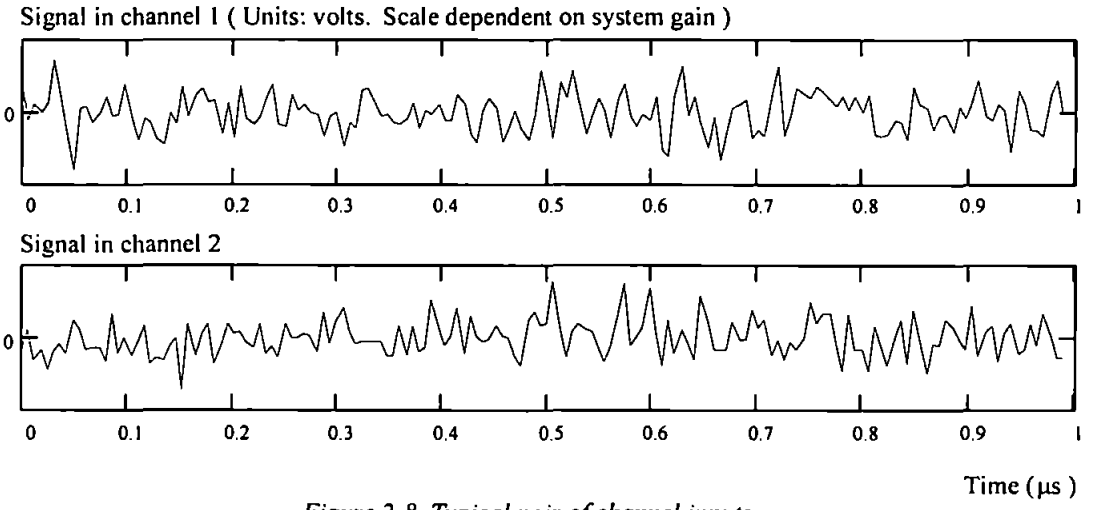

Figure 2-8. Typical pair of channel inputs.

At a SNR of -11 dB the common signal in both channels is predictably not apparent. The acf of one channel input, shown in figure 2-9, is dominated by a very large central peak, normal for the acf of broadband noise, masking the acf of any signal. Figure 2-10 shows the ccf of both inputs. In the ccf the noise-noise and signal-noise cross correlations are

spread out over the whole width of the correlation function so that the much smaller central peak is entirely due to the signal-signal cross correlation.

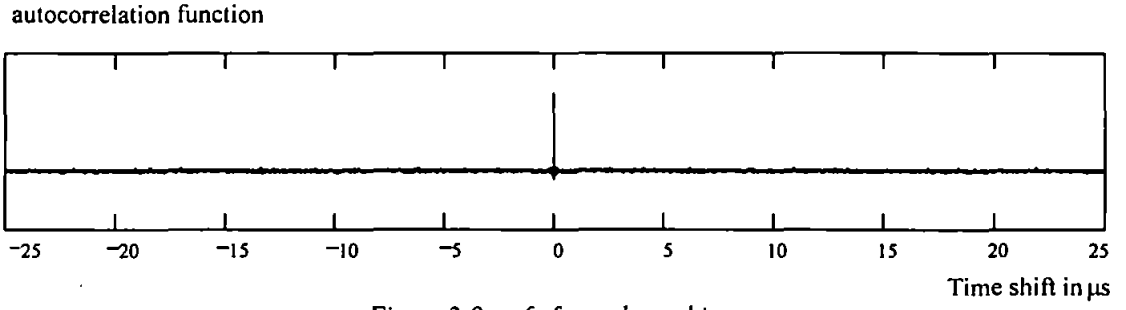

Figure 2-9. acf of one channel input

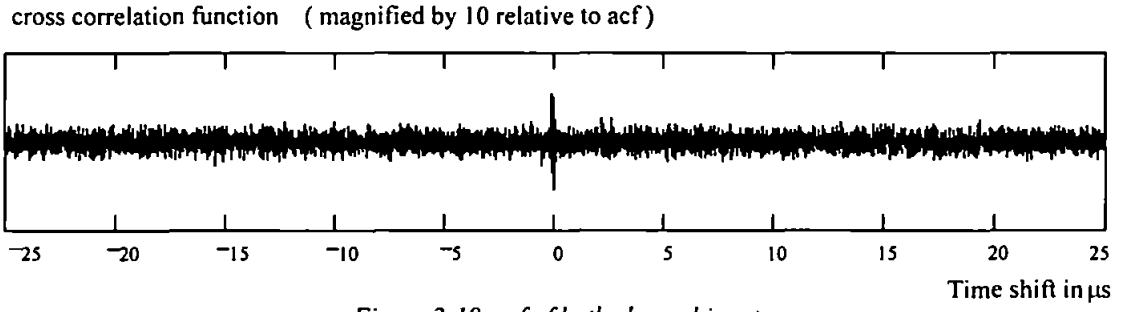

Figure 2-10. ccf of both channel inputs

The simulation was repeated 20 times (see Appendix D), using different noise seeds each time, for the following parameters:

T_s	B_n	B_s	SNR_i
500 μs	100 MHz	10 MHz	-16 B

The SNR in the ccf predicted by equation 2.46 is 17.8 dB. In the simulation, the SNR, calculated by dividing the peak signal power by the mean power as shown in appendix D, had a mean of 17.6 dB with a standard deviation of 0.7 dB. Therefore analysis and simulation show no disagreement.

2.7 Summary

The equations for the signal to noise ratios at the outputs of the correlators discussed above are:

Finite sample time domain cross (FSTD) correlation

$$\left(\frac{\hat{S}}{N}\right)_o = \frac{n^2 E_p^2}{\frac{3}{4}\eta^2 B_n T_s + \frac{3\eta T_s n E_p}{3T_s - nT_p}} = \frac{\frac{4}{3} n^2 T_p^2 B_n \left(\frac{S}{N}\right)_i^2}{T_s + \frac{4 T_s n T_p}{3T_s - nT_p}\left(\frac{S}{N}\right)_i} \tag{2.50}$$

Finite sample frequency domain (FSFD) and true continuous (TC) correlation

$$\left(\frac{\hat{S}}{N}\right)_o = \frac{n^2 E_p^2}{\frac{1}{2}\eta^2 B_n T_s + \eta n E_p} = \frac{2 n^2 T_p^2 B_n \left(\frac{S}{N}\right)_i^2}{T_s + 2 n T_p \left(\frac{S}{N}\right)_i} \tag{2.51}$$

Radar matched filter

$$\left(\frac{\hat{S}}{N}\right)_o = I\frac{2E_p}{\eta} = 2 I B_n T_p \left(\frac{S}{N}\right)_i \tag{2.52}$$

Expressions for CW signals are obtained by replacing nT_p by T_s.

3. The Time Domain Filtered Cross Spectral Density

3.1 SNR in the Cross Spectral Density

As will be shown, some signals may show up against a noise background better in the Fourier transform of the cross correlation function, the cross spectral density, than in the cross correlation function itself. Consider an FFT cross correlation process. We have shown that the total energy of the noise-noise cross correlation is $\frac{1}{2}\eta^2 B_n T_s^2$ (equation 2.23), and that the total combined energy of the two signal-noise cross correlations is $\eta E_p T_s$ (equation 2.29). We now assume a LFM pulse with an approximately rectangular energy spectral density, and consider the signal-signal cross correlation. Since this cross correlation is the signal acf with a time shift, the magnitude of the signal-signal CSD is the same as the signal pulse's energy spectral density. If we consider a pulse of energy E_p and bandwidth B_s, then the mean amplitude of this double sided energy spectral density, within the signal bandwidth, will be equal to $E_p/2B_s$. We now wish to find the relative powers of the signal and noise terms in the cross spectral density. The mean power of the signal term in the cross spectral density, where non-zero, is the square of the CSD amplitude

$$\left(\frac{nE_p}{2B_s}\right)^2 \tag{3.1}$$

where n is included to allow for n pulses within the sample period T_s. The mean power of the noise terms in the cross spectral density is obtained by dividing the total energy of all the noise terms in the cross correlation function (given by equations 2.23 and 2.29) by $2B_n$, to give, where non zero,

$$\frac{\frac{\eta^2 B_n T_s^2}{2} + 2\times\frac{\eta n E_p T_s}{2}}{2B_n} = \frac{\eta^2 T_s^2}{4} + \frac{\eta n E_p T_s}{2B_n} \tag{3.2}$$

Hence, the signal to noise ratio in the Cross Spectral Density, treating the CSD in the same way as we would a time domain signal, is

$$\left(\frac{S}{N}\right)_{CSD} = \frac{\left(\frac{nE_p}{2B_s}\right)^2}{\frac{\eta^2 T_s^2}{4} + \frac{\eta n E_p T_s}{2B_n}} \tag{3.3}$$

$$\left(\frac{S}{N}\right)_{CSD} = \frac{n^2 E_p^2}{\eta^2 B_s^2 T_s^2 + \frac{2\eta n E_p B_s^2 T_s}{B_n}} \tag{3.4}$$

In terms of the input signal power, S_i, and pulse length, T_p, this becomes

$$\left(\frac{S}{N}\right)_{CSD} = \frac{n^2 S_i^2 T_p^2}{\eta^2 B_s^2 T_s^2 + \frac{2\eta n S_i B_s^2 T_s T_p}{B_n}} \tag{3.5}$$

If the input signal is a CW signal, then $nT_p = T_s$ and we have

$$\left(\frac{S}{N}\right)_{CSD} = \frac{\left(\frac{S_i}{B_s}\right)^2}{\eta^2 + \frac{2\eta S_i}{B_n}} \tag{3.6}$$

3.2 Effect of time domain filtering on the cross spectral density

When we form the cross correlation of the outputs of two receivers, the signal-signal cross correlation is, for spread spectrum signals, concentrated almost totally in a small region in the centre while the noise terms are spread out over the full range of the of the total cross correlation function. The total noise energy can be significantly reduced by using a simple brick wall, low pass time domain filter. In practice, if the cross correlation function is held in sampled data form this simply involves taking only the centre portion of the cross correlation

function and throwing the rest away. If the cross correlation function occurs spatially in an optical system, this can be done by simple spatial filtering. The advantage gained by this time domain filtering depends on whether the cross correlation function has been formed by frequency domain techniques (i.e. by FFT and CSD) or by a time domain correlator.

3.2.1 SNR using a FSFD or TC correlator, LFM signals.

When the cross correlation function is formed by a frequency domain correlator the envelope of the noise terms is flat across the full width of the cross correlation function. If we window the centre portion of the cross correlation function, or "zoom in" by a factor γ, then the total noise energy is reduced by this factor γ. Provided γ is not too great the signal-signal cross correlation term is unaffected. The signal to noise ratio in the cross spectral density will then simply be increased by the factor γ from the expression given in equation 3.5.

$$\left(\frac{S}{N}\right)_{CSD} = \frac{\gamma n^2 T_p^2 S_i^2}{\eta^2 B_s^2 T_s^2 + \frac{2 n \eta S_i B_s^2 T_s T_p}{B_n}} \tag{3.7}$$

In terms of the input signal to noise ratio this is (using $N_i = \eta B_n$)

$$\left(\frac{S}{N}\right)_{CSD} = \frac{\gamma \left(\frac{B_n}{B_s}\right)^2 \left(\frac{S}{N}\right)_i^2}{\left(\frac{T_s}{n T_p}\right)^2 + 2\left(\frac{T_s}{n T_p}\right)\left(\frac{S}{N}\right)_i} \tag{3.8}$$

For a CW signal, when $nT_p = T_s$, this becomes

$$\left(\frac{S}{N}\right)_{TDFCSD} = \frac{\gamma \left(\frac{B_n}{B_s}\right)^2 \left(\frac{S}{N}\right)_i^2}{1 + 2\left(\frac{S}{N}\right)_i} \tag{3.9}$$

The maximum value of γ is determined by the degree of pulse compression achieved in the signal-signal cross correlation, or signal autocorrelation function. The main peak of the signal autocorrelation function will be approximately one over the signal bandwidth, and so as a rule of thumb, we set the criterion that the width of the section of the cross correlation function taken in the windowing process must be at least three times this value.

$$\text{i.e.} \quad \gamma \leq \frac{B_s T_s}{3} \tag{3.10}$$

3.2.2 SNR using a FSTD correlator, LFM signals

When we use a time domain correlator the advantage is a little less. If we assume a CW signal then the combined noise terms in the cross correlation function will have an amplitude envelope of the form shown in figure 3-1, from the cross correlation of two rectangular pulses of length T_s.

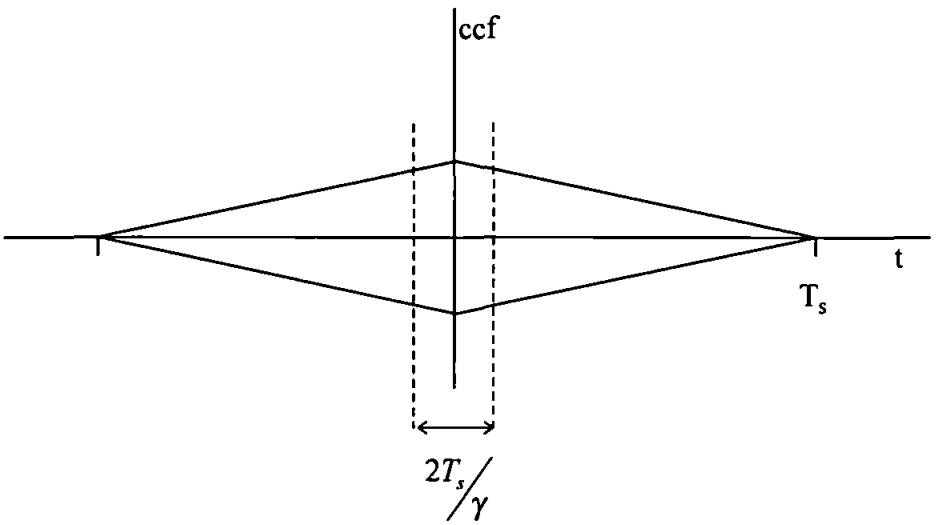

Figure 3-1 Envelope of combined noise terms in the output of a time domain correlator for a CW signal, showing section selected by time domain windowing.

By integrating over the square of this amplitude envelope we find that the factor by which the total noise energy is reduced by time domain filtering is now

$$\frac{\int_0^{T_s}\left(1-t/T_s\right)^2 dt}{\int_0^{T_s/\gamma}\left(1-t/T_s\right)^2 dt} = \frac{\gamma^3}{3\gamma^2-3\gamma+1} \tag{3.11}$$

For $\gamma > 1$ this approximates to $\frac{\gamma}{3}$ and so we have (from equation 3.5)

$$\left(\frac{S}{N}\right)_{CSD} = \frac{\frac{\gamma}{3} n^2 T_p^2 S_i^2}{\eta^2 B_s^2 T_s^2 + \frac{2n\eta S_i B_s^2 T_s T_p}{B_n}} \tag{3.12}$$

or for a CW signal we have (from equation 3.6)

$$\left(\frac{S}{N}\right)_{CSD} = \frac{\frac{\gamma}{3}\left(\frac{S_i}{B_s}\right)^2}{\eta^2 + \frac{2\eta S_i}{B_n}} \tag{3.13}$$

which is one third of the value obtained if a FSFD or TC correlator is used

3.3 Biphase coded signals

Since the exact form of the signal was irrelevant in calculating the equations for SNR in the ccf the equations developed in chapter 2 apply equally well to LFM and to biphase coded signals. However, the PSD of a biphase coded signal takes a *sinc*^{2} (see figure 1-1) rather than the approximately rectangular form of the LFM signal. As a result the SNR in the TDFCSD is not constant over the signal bandwidth as it is for the LFM signal. The processes of sections 3.1 and 3.2 can be repeated for the biphase coded signal PSD which takes the form

$$A\left\{\text{sinc}^2\left(\frac{f+f_c}{r_c}\right) + \text{sinc}^2\left(\frac{f-f_c}{r_c}\right)\right\} \tag{3.14}$$

where f_c is the centre frequency and r_c is the code chip rate. For a CW signal, the result, in terms of input SNR, by comparison with equation 3.9, is

$$\left(\frac{S}{N}\right)_{TDFCSD} = \frac{\gamma\left(\frac{B_n}{r_c}\right)^2\left(\frac{S}{N}\right)_i^2 \operatorname{sinc}^4\left(\frac{f'}{r_c}\right)}{1 + 2\left(\frac{S}{N}\right)_i} \tag{3.15}$$

where $f' = f - f_c$. The two main points to notice about this output are that it is not constant over the signal bandwidth and that the bandwidth is less clearly defined than for LFM signals. r_c , the code chip rate, replaces B_s as a clearly defined figure that can be used in predicting output SNR. The SNR required for reliable detection is easily defined for LFM signals with their rectangular spectra. For a biphase coded signals with its sinc^4 TDFCSD we must specify a bandwidth over which the threshold SNR is exceeded. At the 6 dB down points of the sinc^4 spectrum (the 3 dB down points of the sinc^2 spectrum) the output SNR is

$$\left(\frac{S}{N}\right)_{TDFCSD} = \frac{\frac{\gamma}{4}\left(\frac{B_n}{r_c}\right)^2\left(\frac{S}{N}\right)_i^2}{1 + 2\left(\frac{S}{N}\right)_i} \tag{3.16}$$

and this figure is exceeded over a bandwidth of $B_s = 0.886\, r_c$.

The maximum possible value of γ is found by considering the width of the acf. A maximal length sequence acf has a total width of $2/r_c$. Hence

$$\gamma_{\max} = \frac{r_c T_s}{2} \tag{3.17}$$

The rectangular form of the LFM PSD is ideal for the application of threshold detection to the TDFCSD. The sinc^4 form of the TDFCSD for the biphase coded signal is a little less convenient and detection performance will clearly not be quite as good.

3.4 Comparison of SNR in the ccf and the TDFCSD

The relative detection performances of the ccf and the TDFCSD depend on the ratio of the system noise bandwidth to the signal bandwidth and the integration time used. The performance of the ccf increases linearly with the integration time used. As we shall see, at relatively short integration times the situation can be a little more complicated for the TDFCSD. For LFM signals, if we use a FSFD or TC correlator, then the relevant equations for CW signals are (equations 2.51 and 3.9):

$$\left(\frac{\hat{S}}{N}\right)_{ccf} = \frac{2B_nT_s\left(\frac{S}{N}\right)_i^2}{1 + 2\left(\frac{S}{N}\right)_i} \quad \text{and} \quad \left(\frac{S}{N}\right)_{TDFCSD} = \frac{\frac{B_s T_s}{3}\left(\frac{B_n}{B_s}\right)^2\left(\frac{S}{N}\right)_i^2}{1 + 2\left(\frac{S}{N}\right)_i} \tag{3.18}$$

The above expression for the SNR in the TDFCSD applies if we can treat the signal bandwidth as constant and the SNR as constant across the full signal bandwidth. This is the case if the signal is a continuous or pulsed LFM signal and the integration time of the correlation is long enough to contain many frequency sweeps, or an integer number of sweeps of the signal. For very low values of input signal power, which are the values we are interested in, these expressions approximate to

$$\left(\frac{\hat{S}}{N}\right)_{ccf} = 2B_nT_s\left(\frac{S}{N}\right)_i^2 \quad \text{and} \quad \left(\frac{S}{N}\right)_{TDFCSD} = \frac{B_n^2 T_s}{3B_s}\left(\frac{S}{N}\right)_i^2 \tag{3.19}$$

This gives the ratio between the two signal to noise ratios as

$$\frac{\left(\frac{S}{N}\right)_{TDFCSD}}{\left(\frac{\hat{S}}{N}\right)_{ccf}} = \frac{B_n}{6B_s} \tag{3.20}$$

where B_s is the bandwidth of that part of the signal that falls within the sample. Figure 3-2 shows how both these output SNRs vary with input signal power and noise bandwidth.

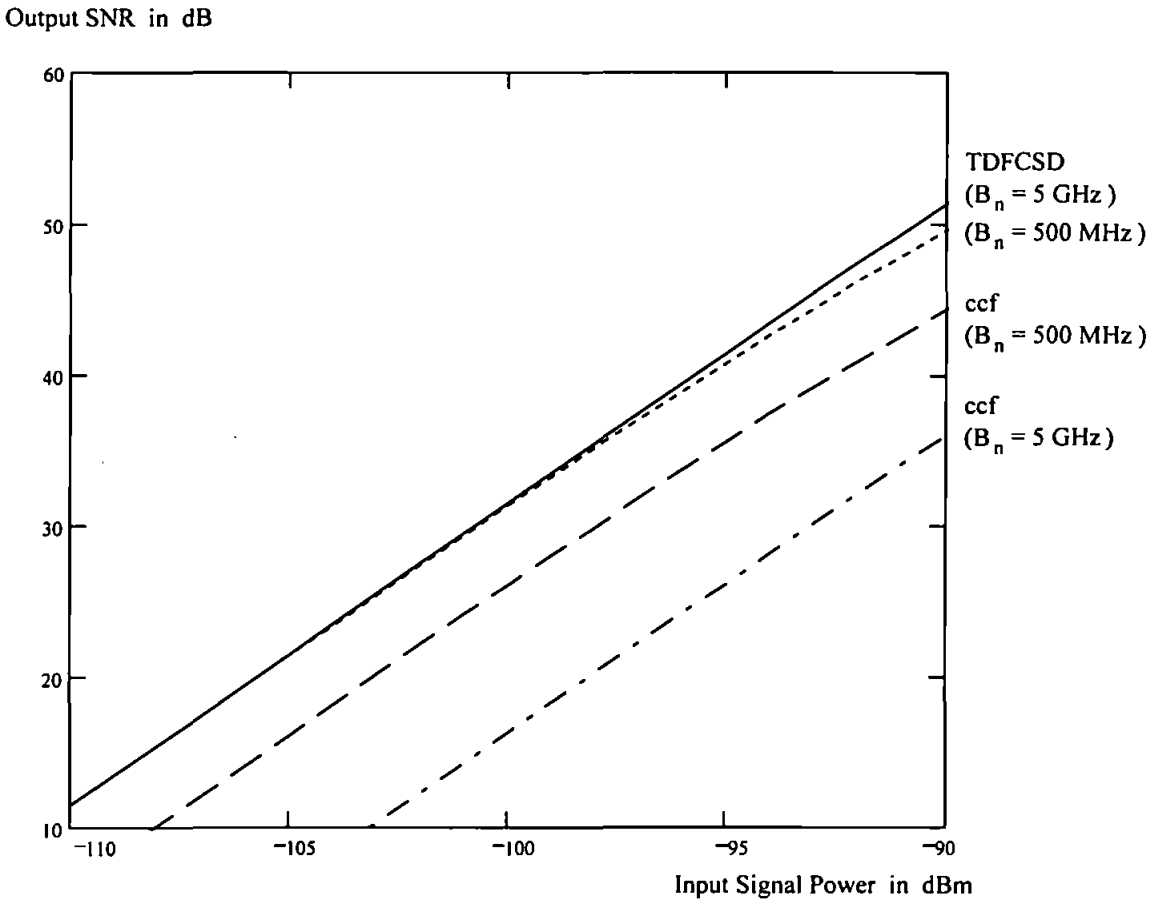

Figure 3-2. Variation, with input signal power, of the output SNR in the TDFCSD and the ccf derived from a FSFD or TC correlator for noise bandwidths of 500 MHz and 5 GHz. Fixed parameters: receiver system noise temp = 500 K, B_s = 25 MHz, T_s = 500 μs.

We can see very clearly that the TDFCSD gives a significantly higher output SNR than the ccf, for the parameters used. This advantage increases with the receiver noise bandwidth. The SNR in the TDFCSD is virtually unchanged as the noise bandwidth increases while that in the ccf decreases significantly. Comparison of the output SNRs does not give the full story however. The probability density functions (pdfs) for noise alone and signal plus noise are different in these two systems and the SNRs required to give the same detection performance therefore differ. This will be discussed in more detail in chapter 4, section 4.2. This advantage of the TDFCSD is illustrated again in figure 3-3, which shows how the SNRs in the TDFCSD and ccf vary with signal bandwidth for a fixed receiver noise bandwidth. In the ccf, the SNR is unaffected by signal bandwidth since it depends only on total signal input power and total noise input power which, for fixed noise bandwidth, does not vary. The SNR in the TDFCSD, however, does depend on signal bandwidth and decreases as that signal bandwidth increases. In figure 3-3 we see that, as B_s increases, the SNR in the TDFCSD drops below that in the ccf when B_s reaches one sixth of B_n.

However, it is not until the SNR in the TDFCSD has dropped more than 2.4 dB below that in the ccf that the TDFCSD stops giving the better detection performance.

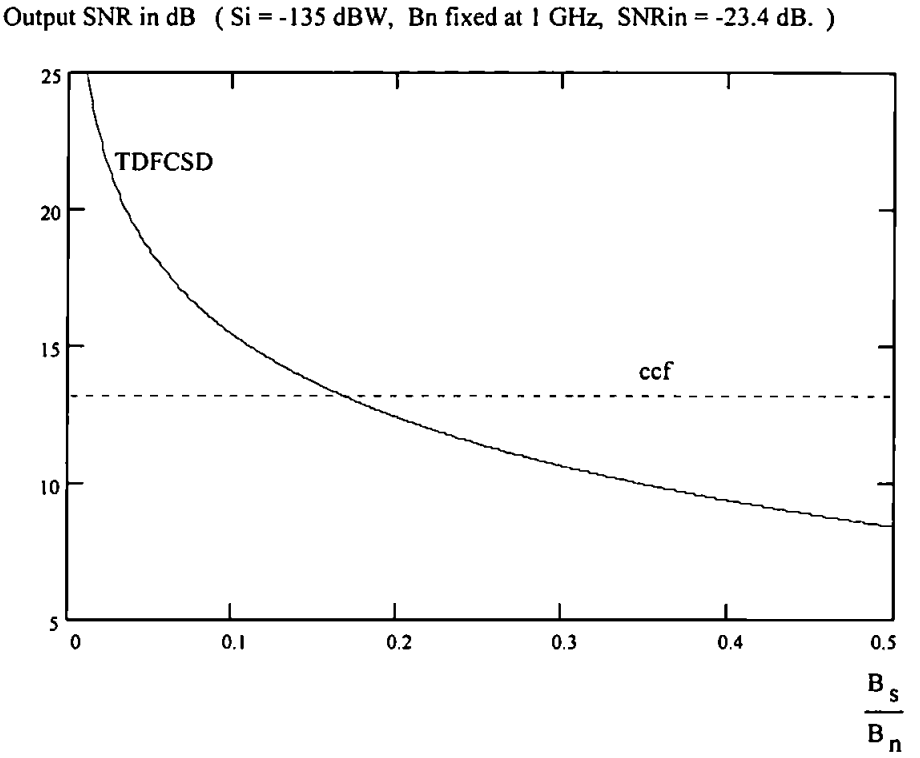

Figure 3-3. Variation, with signal bandwidth B_s, of output SNR in TDFCSD and ccf for a fixed receiver noise bandwidth of B_n = 1 GHz. Fixed parameters are: receiver system noise temp = 500 K and T_s = 500 μs.

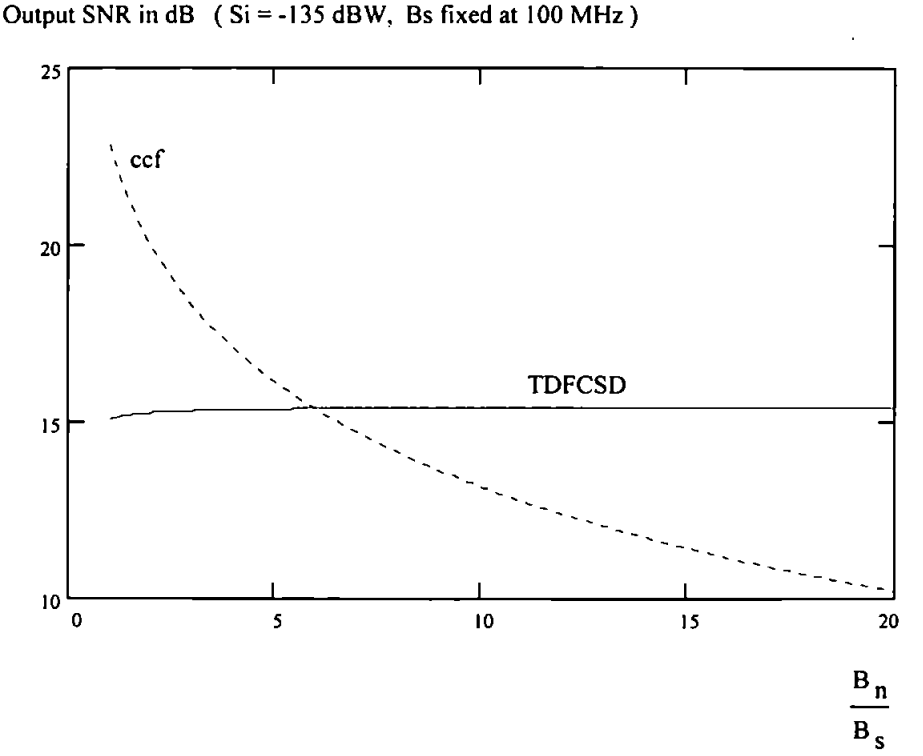

Figure 3-4. Variation, with receiver noise bandwidth B_n, of output SNR in TDFCSD and ccf for a fixed signal bandwidth B_s = 100 MHz. Fixed parameters: receiver system noise temp = 500 K and T_s = 500 μs.

Figure 3-4 shows how the SNRs vary with receiver noise bandwidth for a fixed signal bandwidth. This contains essentially the same information as figure 3-3 but emphasises the point that the receiver noise bandwidth can be increased indefinitely without affecting the SNR in the TDFCSD, since it is the noise spectral density and not the bandwidth that is important. In the ccf, an increase in the noise bandwidth causes an increase in the total noise power and a decrease in the output SNR.

To see the effect of integration time, consider an FMCW radar. An existing example is the PILOT (otherwise known as SCOUT) tactical navigation radar which operates at around 9 GHz. PILOT [6] employs a sawtooth frequency sweep of 50 MHz with a time period of 1 ms within a bandwidth of 1 GHz. An ESM system may have to work on samples significantly shorter than 1 ms. If our cross correlating system uses a sample time of 50 μs then it can only "see" a frequency sweep of 2.5 MHz. We can see very clearly that the TDFCSD gives a significantly higher output SNR than the ccf, and hence use of the TDFCSD will give increased detectability of the FMCW signal at lower powers. For the figures considered above, the output SNR in the TDFCSD exceeds 15 dB for input signal powers down to -108 dBm. It should be noted that the comparison has been made between the peak SNR of the cross correlation function and the mean SNR of the TDFCSD. If we were to use the peak signal power in analysing the TDFCSD then the TDFCSD would show another 3 dB advantage. An examination of the approximate expressions for these SNRs shows how their values change with the sample length, T_s. As long as T_s is less than the time period of the frequency sweep of the FMCW signal (1 ms for PILOT), then, for a linear frequency sweep, the SNR in the CSD will not vary with T_s, since the value of B_s within the sample taken will vary linearly with T_s. Once T_s exceeds the time period of the FMCW frequency sweep however, the SNR will start to increase. However this increase will not be a uniform increase. If the integration time is not an integer multiple of the signal sweep time then the TDFCSD system will "see" some parts of the signal sweep one more time than others, giving a higher SNR for those parts. Rather than rise linearly, the SNR for different parts of the signal sweep will rise as a step function of the integration time. The SNR in the cross correlation function clearly increases linearly with T_s for all values of T_s. This is illustrated in figure 3-5, which shows that, for detection of the PILOT radar, the time domain filtered cross spectral density is more useful than the

cross correlation function for all values of T_s and, not surprisingly, gives better detection the longer the integration time.

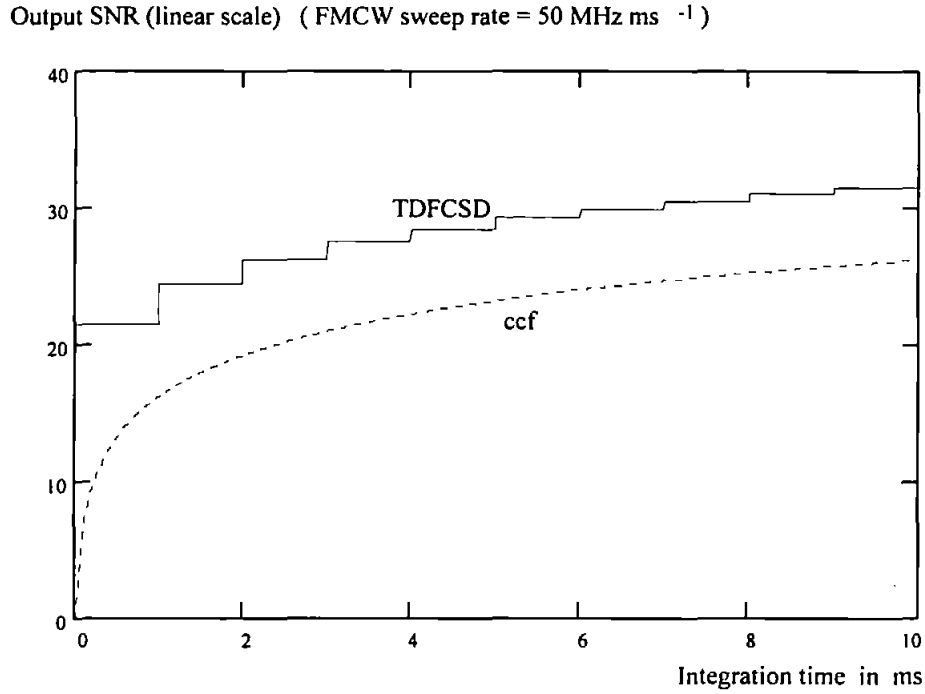

Figure 3-5. Variation, with receiver integration time, of output SNR for TDFCSD and ccf when input signal is an FMCW signal. Parameters given in the text.

3.5 Simulation

The mathcad simulation, described in section 2.6 and shown in full in appendix A, includes generation of the TDFCSD. Results are shown here for the following input parameters:

T_s	B_n	B_s	SNR_i
500 μs	100 MHz	20 MHz	-15 B

Figures 3-6 and 3-7 show the PSD of the channel 1 signal input and the CSD of both inputs respectively. We see that in the frequency domain, as well as the time domain, the signal has been buried in the noise. In fact the signal PSD to noise PSD ratio, within the signal bandwidth, is -8 dB. Even the CSD offers us no clear indication of the presence of a common signal; time domain filtering of the CSD is required to bring the signal out.

Power Spectral Density

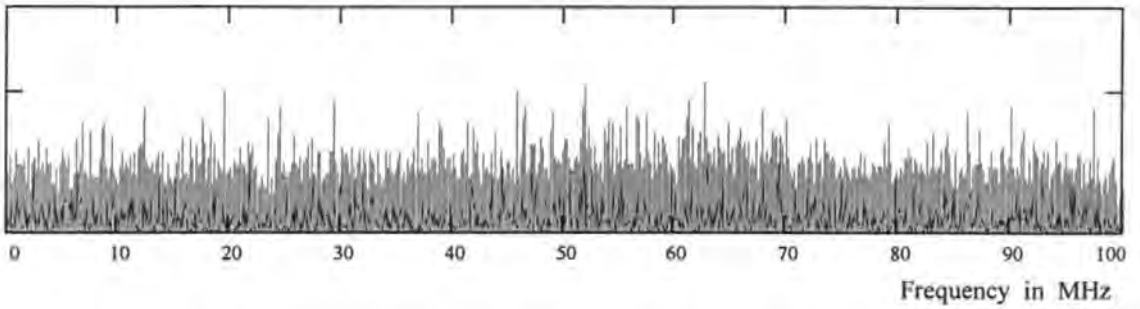

Figure 3-6. Unfiltered power spectral density of one channel input.

Cross Spectral Density

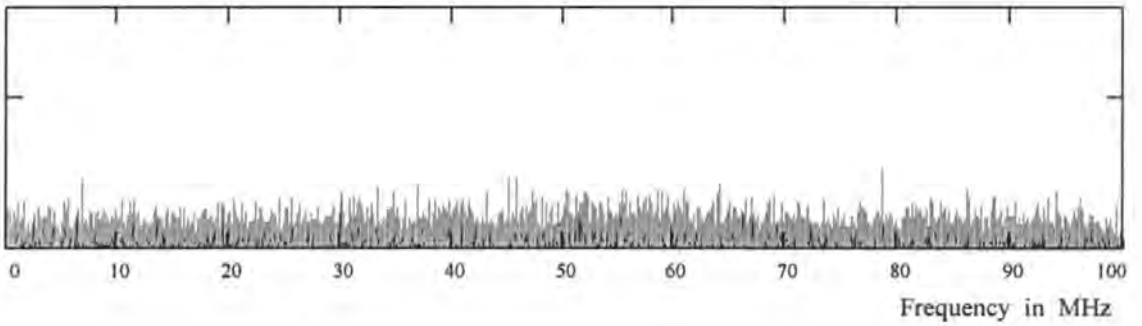

Figure 3-7. Unfiltered cross spectral density of both channel inputs..

Figure 3-8 shows the ccf as originally generated and illustrates the process of selecting the central portion and then "zooming in" by a factor of 2048. The Fourier transform of central portion of the ccf, the TDFCSD, is shown in figure 3-9, in which the large peak between 50 and 70 MHz now shows the presence of the signal very clearly and gives a good indication of its spectrum.

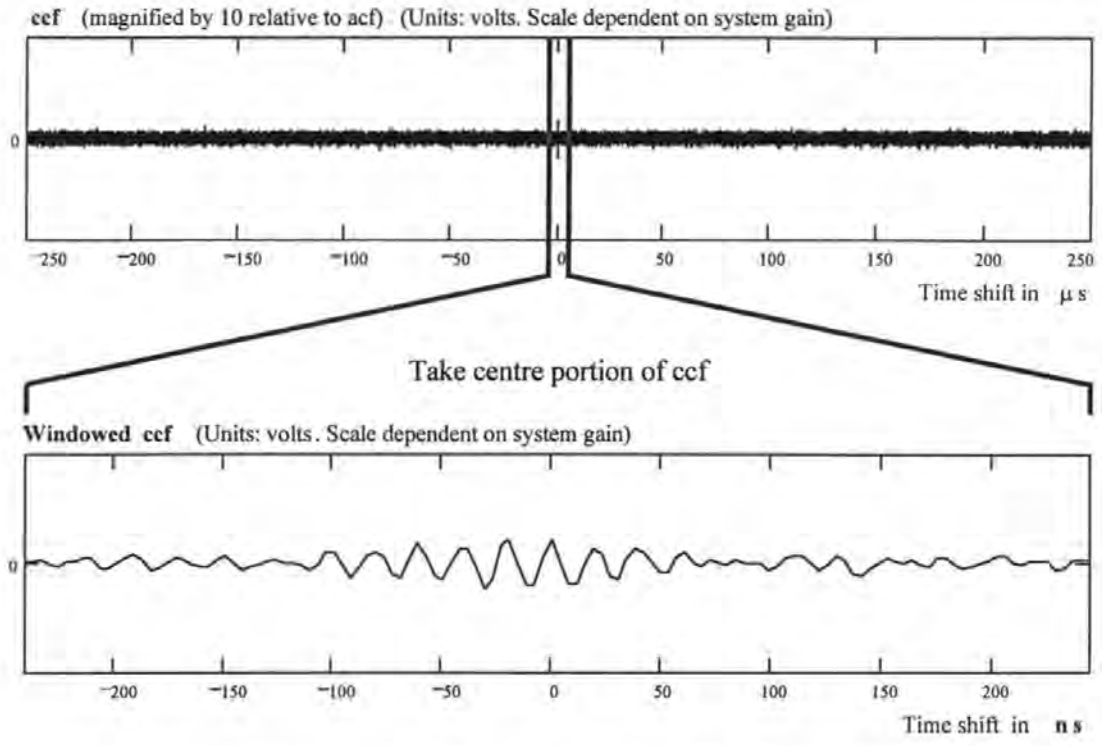

Figure 3-8. "Zooming in" on the centre of the ccf by a factor of 2048

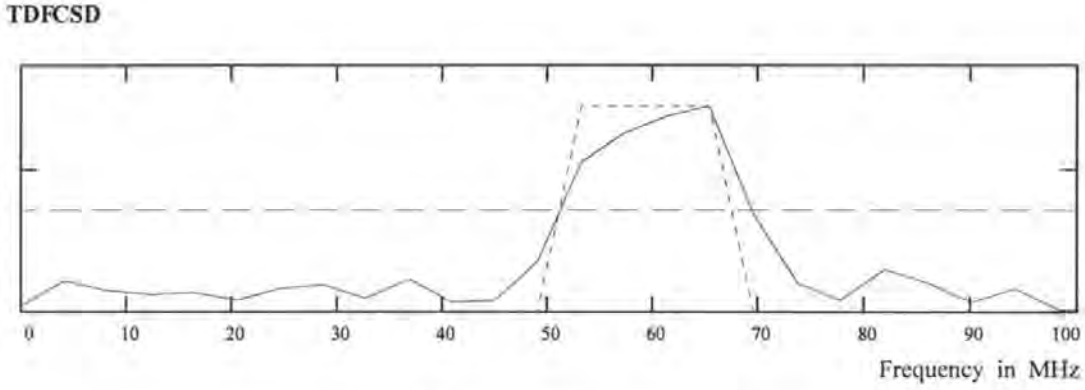

Figure 3-9. Magnitude of the TDFCSD, showing application of a threshold.

To compare the results of the simulation against the theoretical predictions, the SNR in the TDFCSD was estimated for 20 repeated simulations, using different noise seeds each time, for the following parameters:

T_s	B_n	B_s	SNR_i
500 μs	100 MHz	10 MHz	-16 B

This simulation and the results are shown in full in appendix D. The SNR in the TDFCSD predicted by equation 3.9, allowing for a γ of 1024 as used in the simulation, is 17.9 dB. In

the simulation the SNR, measured by dividing the mean power within the signal bandwidth by the mean power over an equally wide frequency range outside the signal bandwidth, had a mean of 17.4 dB with a standard deviation of 1.1 dB. As with the ccf, we see no disagreement between analysis and simulation.

4. ESM System Performance

4.1 Introduction

In chapters 2 and 3, expressions were developed, and compared against computer simulation, for the output SNRs that can be achieved in the ccf or the TDFCSD, at the output of an appropriate signal processing system, in terms of the input signal parameters. It is important to put these results into context by considering their implications for the overall system performance. In this chapter, these implications will be examined in some detail and comparisons will made with other types of surveillance receiver.

The important question is, "can LPI radars be detected when necessary?" The main parameter to consider is the range at which detection can be achieved. For radars of fixed output power, with a fixed detection range, it is highly desirable that the ESM system can detect the radar at a range greater than that at which the radar can detect the ESM platform. Expressions for the ESM range advantage are therefore extremely useful in evaluating ESM system performance. By using the expressions developed in chapters 2 and 3 to derive expressions for receiver sensitivity and considering the power transmission requirements of the radar, expressions will be derived for the range advantages of different ESM systems over both pulsed and CW radars. As will be shown, LPI radars can gain great advantages from using power management. When a radar does this, the power available to the ESM receiver will, if the ESM platform is the radar's target, actually decrease as the radar gets closer. The crucial parameter then becomes the signal to noise ratio at the required minimum detection range.

We are concerned with wide open ESM systems designed to achieve near 100% probability of interception. It would not be appropriate to repeat existing textbook theory to the extent of surveying all known types of ESM receiver. A limited range will be considered with existing theory only reproduced as required to support the subsequent discussion. Expressions will be developed for, and comparisons made between: a very basic ESM receiver with no processing gain comprising an RF amplifier followed by an envelope detector and a threshold detector, a crystal video receiver with a narrow video

bandwidth, a cross correlating receiver applying threshold detection directly to the ccf, and a cross correlating receiver applying threshold detection to the TDFCSD. Which provides greater sensitivity, the ccf or the TDFCSD, depends on the relative bandwidths of the signal and the ESM receiver. An operational system, designed to operate with no a priori knowledge of the signal, will need to use both. The performance of all these systems will be analysed for pulsed radar and, where relevant, for CW radar. The effects described by the equations developed in this chapter will be illustrated by a set of graphs (generated in Mathcad) using the parameters listed in table 4-1.

4.2 Threshold SNRs for signal detection

The sensitivity of a receiver, as defined in this thesis, is the minimum input signal power that can be detected with a specified reliability. This reliability is specified in terms of the probability of false alarm, P_{fa}, and the probability of detection, P_d. If we integrate over 1 ms in forming the ccf we make a threshold decision 1000 times per second. If we set P_{fa} to 10^{-5}, then we can expect a false alarm every 100 seconds. (This false alarm would normally be cancelled when the next threshold decision fails to confirm the detection.) If the ccf integration time is increased to 10 ms a P_{fa} of 10^{-4} might be acceptable. Once P_{fa} has been set the threshold level to be used in threshold detection is fixed and P_d then depends on the SNR. We can then determine the SNR required to give a specified P_d. For the purpose of comparing receiver sensitivities for different systems, we will use $P_{fa} = 10^{-5}$ and $P_d = 0.99$. Since there are many individual samples in any sample period we must specify a more stringent value of P_{fa} for each individual sample within a sample period. The ccf output has a bandwidth of B_n and must therefore be sampled at a frequency of at least $2B_n$. If the windowed centre portion of the ccf that we pass to our threshold detector is of the order of $4/B_s$ wide and B_n/B_s is of the order of 10 then the number of samples we must consider is of the order of 100. To achieve $P_{fa} = 10^{-5}$ for the whole sample period we must therefore specify $P_{fa} = 10^{-7}$ for each individual sample. We arrive at the same result for the TDFCSD. The above is standard radar detection theory based on the Neyman Pearson criterion. The reader who requires a general introduction is referred to any standard radar textbook, such as Skolnik [42].

Every value in the ccf output is the sum of a large number of independent contributions. The central limit theorem applies and the probability density function (pdf) for all values in the ccf will be Gaussian to a very close approximation. Probabilities of false alarm and detection are calculated and plotted in appendix F. For Gaussian statistics it is shown that, for a P_{fa} of 10^{-7} and a P_d of 0.99, the threshold L_T should be set at 5.12 σ (where σ is the standard deviation of the noise) and the required SNR is 17.53 dB.

Radar system noise temperature	500K
ESM system noise temperature	500K
Radar antenna gain	30 dB
ESM system antenna gain	6 dB
ESM platform radar cross section	3000 m^2
Threshold SNR at Radar threshold detector	20 dB
ESM probability of false alarm (P_{fa})	10^{-5}
ESM probability of detection (P_d)	0.99
Threshold SNR at ESM threshold detector (ccf)	17.5 dB
Threshold SNR at ESM threshold detector (TDFCSD)	15 dB
Signal carrier centre frequency	10 GHz
Radar pulse length	100 μs*
Radar p.r.i. (pulse repetition interval)	1 ms*
Radar integration gain	10
Radar signal bandwidth	100 MHz*
Integration time of CW radar	1 ms*

*unless stated otherwise

Table 4.1. Parameters used in Mathcad model generating all the figures in chapter 4.
(The system noise temperatures of both radar and ESM system are assumed to be equal [16].)

The statistics are different for the TDFCSD. These statistics will be examined in more detail in chapter 5 where the effect of noise on the phase terms of the TDFCSD will be discussed.

As will be shown, where the TDFCSD contains only noise the values of its magnitude are described by the Rayleigh pdf and where there is a signal the pdf is Ricean. Threshold detection under these conditions is descibed by most textbooks on radar detection theory (see e.g. [42]), and the relevant equations and calculations are shown in full in appendix F. The analysis in appendix F shows that, if the required detection performance for each sample is $P_{fa} = 10^{-7}$ and $P_d = 0.99$, the threshold L_T should be set at 5.68 σ and the required signal to noise ratio is 14.98 dB. The required threshold SNRs, 17.5 dB for the ccf and 15 dB for the TDFCSD, are listed in table 4-1.

4.3 Power Managed LPI Radars

CW radars that also make use of power management are likely to pose a major threat in the future. A radar mounted, for example, in a missile approaching a target will steadily reduce its transmitter power. As it gets closer the radar will use a feedback mechanism to keep the power returning to the radar at a level just sufficient to enable reliable detection and tracking. The power it needs to have reflected off the target reduces and hence the power arriving at the ESM receiver will reduce. The standard radar equation, using the simple free space model, gives the range of the radar as

$$R_r^4 = \frac{P_T G_r^2(0) \sigma \lambda^2}{(4\pi)^3 S_r} \tag{4.1}$$

where P_T is the radar transmit power, $G_r(0)$ is the main beam gain of the radar antenna, σ is the radar cross section of the ESM platform[1], λ is the wavelength of the radiation, and S_r is the sensitivity (minimum detectable signal power) of the radar receiver. From this we see that the transmitter power required to achieve a given range is

$$P_T = \frac{(4\pi)^3 R_r^4 S_r}{G_r^2(0) \sigma \lambda^2} \tag{4.2}$$

To derive an expression for the sensitivity we need to consider the processing gain achievable by the radar matched filter. This processing gain is $2I_r B_s T_p$, where I_r is the

[1] Note: we follow the standard notation in using σ for radar cross section. This should not be confused with signal standard deviation. Wherever σ is used for signal standard deviation in this thesis, it is always with a subscript.

integration gain, B_s the signal bandwidth and T_p the pulse length, for a pulsed radar, and $2B_sT_{srad}$, where T_{srad} is the radar integration time, for a CW radar (This processing gain is often, mistakenly, quoted as being simply B_sT_{srad} . A factor of 2 should be included since, for the threshold detection process involved, it is the peak signal power that is important rather than the mean signal power.) Hence, for the pulsed radar, the sensitivity is such that

$$SNR_{thrad} = 2I_r B_s T_p \frac{S_r}{\eta_r B_s} \tag{4.3}$$

The sensitivity of the radar receiver is therefore

$$S_r = \frac{\eta_r \, SNR_{thrad}}{2T_p \, I_r} \tag{4.4}$$

In the CW case this sensitivity is

$$S_r = \frac{\eta_r \, SNR_{thrad}}{2T_{s,radar}} \tag{4.5}$$

Hence, for the power managed CW radar, the transmitted power is

$$P_T = \frac{(4\pi)^3 R_r^4 \eta_r \, SNR_{thrad}}{2G_r^2(0)\sigma\lambda^2 T_{srad}} \tag{4.6}$$

The variation of radar transmitter power with range for different radar integration times is illustrated in figure 4-1. We see that as a power managed radar approaches its target the transmitter power can fall to microwatt and even nanowatt levels.

The signal power at the ESM receiver input, when the main lobe of the radar antenna is directed at the ESM system, is given (see e.g. [42]) by

$$S_i = \frac{P_T \, G_r(0) G_e \, \lambda^2}{(4\pi)^2 \, R_r^2} \tag{4.7}$$

Substituting for P_T gives

$$S_i = \frac{4\pi \, G_e \, R_r^2 \, \eta_r \, SNR_{thrad}}{2\sigma \, G_r(0) T_{srad}} \tag{4.8}$$

This expression for the signal power arriving at the ESM receiver input gives us the sensitivity requirement for an ESM system designed to detect the main lobe of a power

managed CW LPI radar. The variation of this signal power with range from radar to ESM platform is plotted in figure 4-2 for a selection of radar integration times.

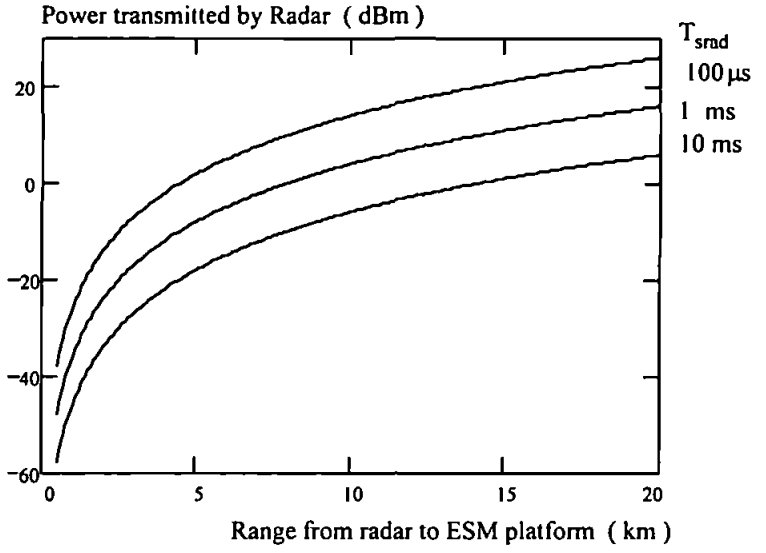

Figure 4-1. Variation of transmitter power with range, for a selection of radar integration times, for a power managed CW LPI radar. System and signal parameters are as in table 4-1

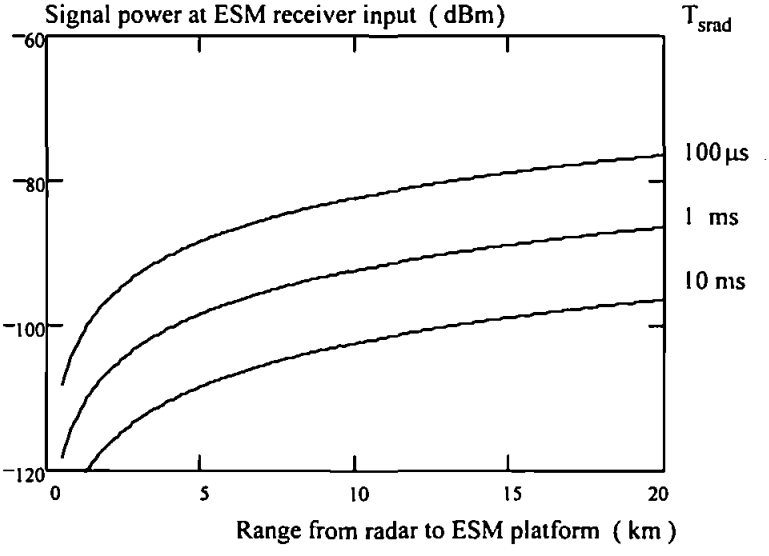

Figure 4-2. Variation of signal power at ESM receiver input with range from radar to ESM platform for a power managed CW LPI radar. System and signal parameters are as in table 4-1.

Although the radar transmitter power does contain a carrier frequency term (λ in equation 4.6) the value for signal power at the ESM receiver input is independent of carrier frequency and so equations 4.8 and figure 4-2 are valid for all frequencies. The radar antenna gain assumed in table 4-1 may seem a little high for the size of antenna that could realistically be mounted in a homing missile at a carrier frequency of 10 GHz, but it is

reasonable to expect future missiles to use mm wave radars. At 60 GHz a 30 dB gain can be realised with a parabolic dish diameter of 10 cm.

4.4 Range advantage of ESM systems

The concern here will be with the radar main lobe range advantage when $G_r(\theta) = G_r(0)$. The sidelobe range advantage, for which $G_r(\theta)$ is the gain of the the radar antenna sidelobe in question, will not be worth considering for any well designed LPI radar. ESM systems often make considerable use of radar sidelobes to form tracks and to characterise radars. As a result, the use of low sidelobe antennas is an LPI technique almost as important as the use of spread spectrum signals and it seems reasonable to assume that the future LPI radars being considered here will have very low sidelobes. It will be difficult enough to detect the main lobes; attempting detection of sidelobes transmitting at least 30 dB less power is likely to be a fruitless exercise. In the case of an ESM system attempting to detect a power managed LPI radar mounted in a missile targeted on the ESM platform sidelobe detection may well be irrelevant anyway. If the missile radar has locked onto and is tracking the ESM platform, it is only the main lobe that will be directed towards the ESM receiver. Henceforth, only the radar main lobe will be considered and both $G_r(\theta)$ and $G_r(0)$ will be replaced simply by G_r in all equations.

Before analysing the performance of the different types of receiver we will develop, in the standard way, the expression for range advantage in terms of the radar to ESM range sensitivity ratio. This initial analysis contains nothing new: it is simply presented to prepare the ground for analysis of the dual receiver ESM system. The sensitivity, S_e, of an ESM system with no processing gain is such that the threshold SNR at the threshold detector is

$$SNR_{thesm} = \frac{S_e}{\eta_e B_n} \tag{4.9}$$

where η_e is the input noise spectral density (given by kT_{sys}) and B_n is the noise bandwidth of the receiver. The radar will almost certainly have a different noise bandwidth, but it cancels out and does not appear in the final expression for the radar sensitivity. Not having the necessary a-priori information the conventional ESM system cannot integrate from

pulse to pulse. Hence, an ESM receiver that achieves no processing gain will have sensitivity

$$S_e = \eta_e B_n SNR_{thesm} \tag{4.10}$$

The variation of this sensitivity with receiver noise bandwidth is plotted in figure 4-3. Comparison with the required sensitivity, as shown by figure 4-2, makes it very clear that an ESM system with no processing gain has no hope of detecting LPI radars.

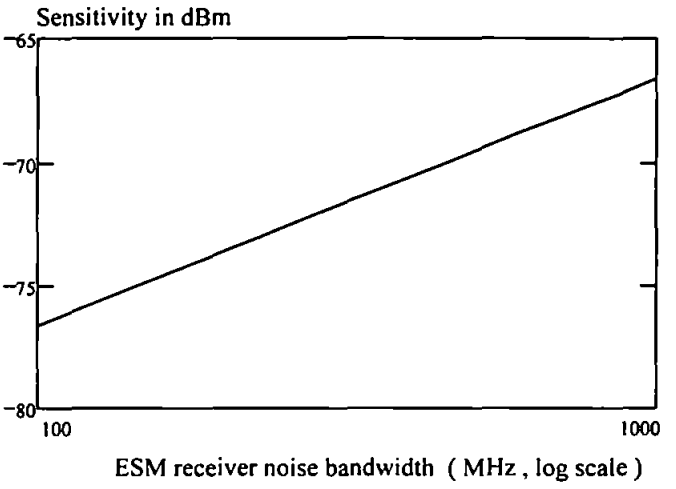

Figure 4-3. Variation of the sensitivity of a basic ESM receiver with no processing gain with receiver RF noise bandwidth. System and signal parameters are as in table 4-1.

To find an expression for range advantage we first need an expression for the detection range of the ESM system. This can be obtained by transposing equation 4.8 to give

$$R_e^2 = \frac{P_T G_r G_e \lambda^2}{(4\pi)^2 S_e} \tag{4.11}$$

Combining this with equation 4.1 (the radar equation) gives the range advantage

$$\frac{R_e}{R_r} = R_r \left\{ \frac{4\pi G_e}{G_r \sigma} \times \frac{S_r}{S_e} \right\}^{\frac{1}{2}} \tag{4.12}$$

The range advantage clearly increases with radar maximum range (power). Clearly, the important factor in calculating ESM range advantage and minimum detection range is the radar sensitivity advantage S_e/S_r . This sensitivity advantage is approximately equal to the ratio of the processing gains times any integration gain the radar might use. For an ESM

system with no processing gain the sensitivity advantage of the ESM system over a CW radar, from equations 4.5 and 4.10, is given by

$$\frac{S_r}{S_e} = \frac{\eta_r \, SNR_{thrad}}{2 \, B_n \, T_{srad} \, \eta_e \, SNR_{thesm}} \tag{4.13}$$

Given the approximations we have made, this approach and its results are in agreement with expressions for radar sensitivity advantage given by Wiley [16]: equation 4.13 above can be arrived at by inserting expressions for the individual terms into Wiley's general equation 2.9. Substituting equation 4.13 into 4.12 allows us to produce figure 4-4, a plot of ESM range advantage against radar maximum range for different ESM receiver noise bandwidths. Figure 4-4 shows very clearly that the ESM receiver with no processing gain can only achieve a range advantage if it uses a set of narrowband receivers and the radar is a very long range radar. This is obviously not very useful!

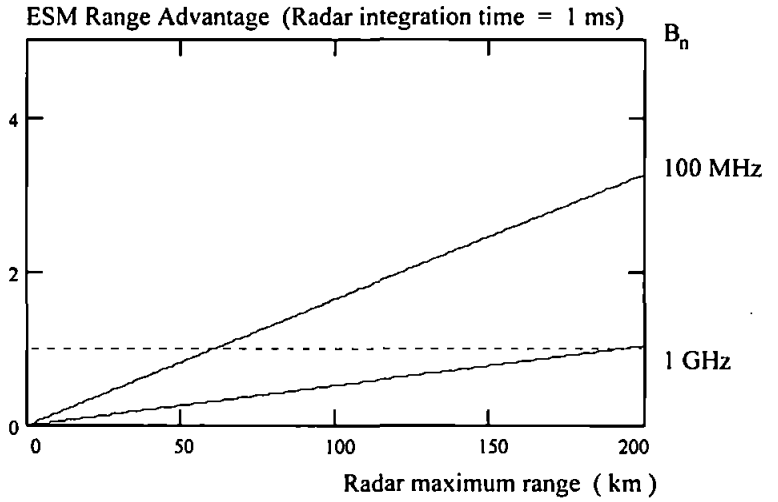

Figure 4-4. Variation of the ESM range advantage with radar maximum range for a basic ESM receiver with no processing gain, for two different ESM RF noise bandwidths. System and signal parameters are as in table 4-1.

4.5 Minimum Detection Range

Figure 4-2 shows that as a power managed LPI radar approaches an ESM platform the signal power at the ESM receiver input decreases. Contrary to normal expectations, the radar becomes increasingly difficult to detect as it gets closer. The ESM system may well detect the radar when it is at a long range and is transmitting high power, but will eventually lose it as it gets closer. The important parameter in this case is not range

advantage or maximum detection range, but minimum detection range - the range below which the radar is invisible to the ESM system. If the LPI radar is in the homing head of a missile it is clearly important to be able to track it until point defence systems can be locked onto it. If the minimum detection range is greater than the maximum range at which point defence systems can reliably engage the missile, then the ESM platform is clearly very vulnerable. If the minimum detection range for an ESM system against a particular radar is 30 km and the radar is not turned on until it is less than 30 km away, then the ESM system will never "see" it. A minimum detection range of the order of one or two kilometres is required, against wideband CW radars using power management and long integration times.

Taking equation 4.12 and setting the range advantage to one give the minimum detection range

$$R_{\min} = \left\{ \frac{G_r \, \sigma}{4\pi \, G_e} \frac{S_e}{S_r} \right\}^{\frac{1}{2}} \tag{4.14}$$

For an ESM system with no processing gain and a CW radar, by substituting equation 4.13 into 4.14, we have

$$R_{\min} = \left\{ \frac{G_r \, \sigma}{4\pi \, G_e} \frac{2 \, B_n \, T_{srad} \, \eta_e \, SNR_{thesm}}{\eta_r \, SNR_{thrad}} \right\}^{\frac{1}{2}} \tag{4.15}$$

The expression for a pulsed radar is obtained simply be substituting $I \times T_p$ for $T_{srad.}$ The variation of minimum detection range with ESM receiver noise bandwidth is plotted in figure 4-5 for a pulsed radar using different pulse lengths. If an ESM receiver has no processing gain it cannot detect the radar when it uses longer pulse lengths, even if the ESM system uses a set of narrowband receivers

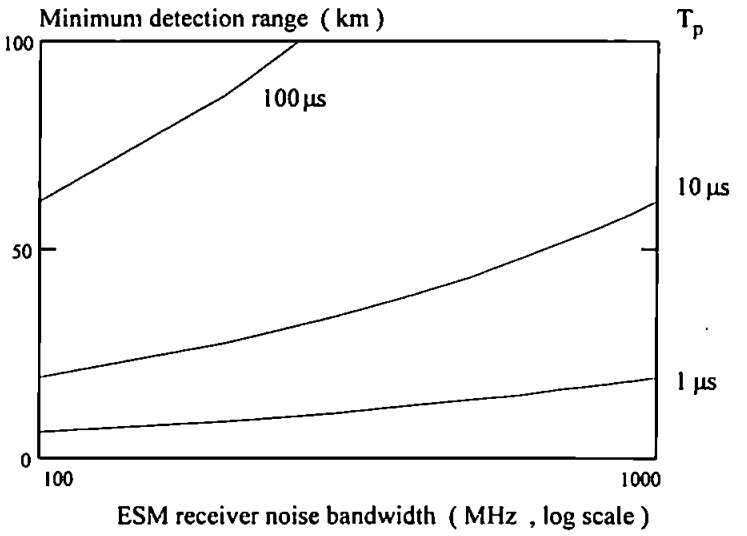

Figure 4-5. Variation of minimum detection range with ESM RF noise bandwidth for an ESM system with no processing gain against a power managed pulsed LPI radar. System and signal parameters are as in table 4-1.

4.6 The Crystal Video Receiver

One well known technique for obtaining processing gain in the ESM system while maintaining a reasonably wide RF bandwidth is to use a crystal video receiver with a narrow video bandwidth. It can be shown [17] that if the gain of the RF front end amplifier is sufficient to make the system noise limited rather than gain limited and the RF bandwidth, B_n, is very much greater than the video bandwidth, B_v, then the effective bandwidth of such a system is $\sqrt{2B_nB_v}$. Hence the sensitivity of a crystal video receiver is approximately

$$S_{e\_xstal} = \eta_e \sqrt{2\, B_n\, B_v}\; SNR_{thesm} \tag{4.16}$$

However, this does not so readily define the sensitivity since the required SNR at the threshold detector does not give itself to a simple definition. The probability density function of the signal at the output of an envelope detector following an the IF filter will be Rayleigh when the input is just AWGN and Ricean when the input is signal plus AWGN. The video filter will then have a very marked effect on these pdfs, compressing them around their mean values. The rather complicated expressions for these pdfs are quoted by Tsui [18]. These equations have been used, with some minor adaptation, to generate all the figures relating to crystal video receiver performance in this thesis. The variation of sensitivity of a crystal video receiver with RF and video bandwidth is shown in figure 4-6

for a number of different video bandwidths. These values for sensitivity must be applied with a little caution. If the video bandwidth is 10 kHz, for example, the equations are only valid for pulses shorter than 100 μs. Comparison with figure 4-3 shows an enormous increase in sensitivity over the ESM system with no processing gain, but comparison with figure 4-2 makes it clear that this increase in sensitivity may not be quite enough. The required sensitivity of significantly below -100 dBm can be approached using narrow RF or IF channels, but this has two major problems. A channellised receiver comprising the large number of channels required to cover a wide RF spectrum would be very expensive, and if the channels have bandwidths narrower than the spread spectrum signal then no channel can collect the whole signal.

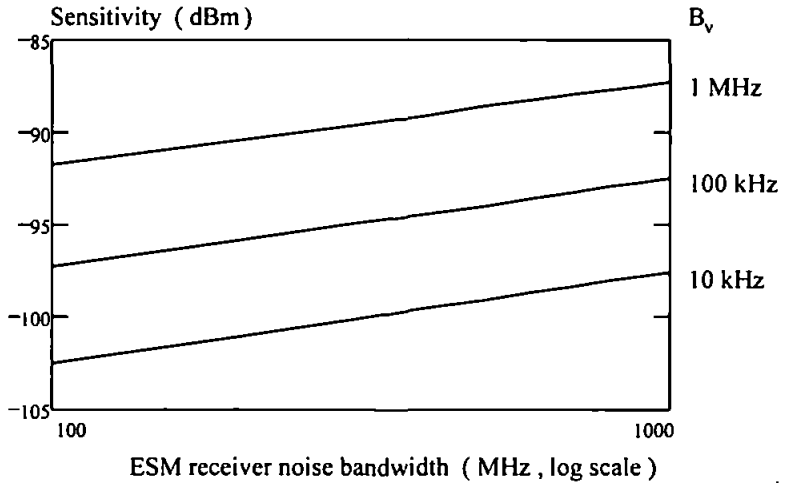

Figure 4-6. Variation of sensitivity with RF noise bandwidth for a crystal video receiver with different video bandwidths. System and signal parameters are as in table 4-1

Substituting equations 4.16 and 4.4 into 4.12 gives the range advantage of the crystal video receiver over a pulsed radar

$$\frac{R_e}{R_r} = R_r \left\{ \frac{4\pi G_e}{G_r \sigma} \times \frac{\eta_r SNR_{thrad}}{2 I_r T_p \eta_e \sqrt{2 B_n B_v SNR_{thesm}}} \right\}^{\frac{1}{2}} \qquad (4.17)$$

The variation of this range advantage with radar maximum range for a fixed video bandwidth, not matched to the pulse, and different RF bandwidths is plotted in figure 4-7.

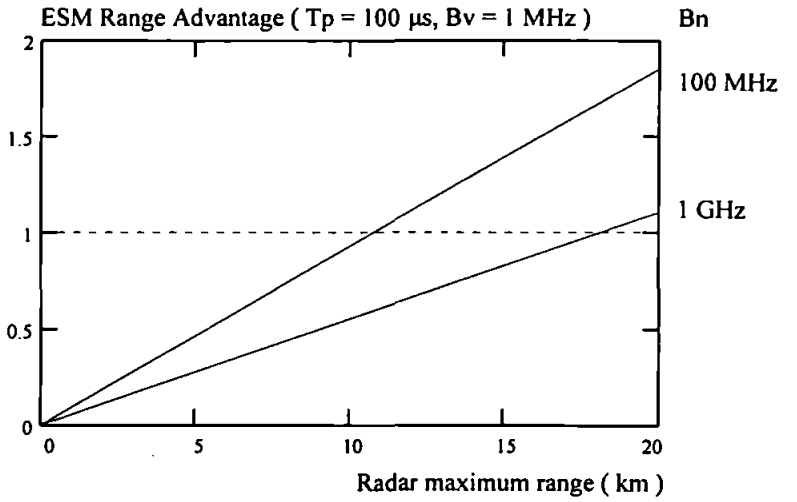

Figure 4-7. Variation of ESM range advantage with radar maximum range for a crystal video receiver of fixed video bandwidth and radar pulses of length 100 μs, for different ESM RF bandwidths. System and signal parameters are as in table 4-1.

Similarly, substituting equations 4.16 and 4.4 into 4.14 gives the minimum detection range against a power managed LPI radar

$$R_{\min} = \left\{ \frac{G_r\, \sigma}{4\pi\, G_e} \frac{2\, I_r\, T_p\, \eta_e \sqrt{2\, B_n\, B_v}\, SNR_{thesm}}{\eta_r\, SNR_{thrad}} \right\}^{\frac{1}{2}} \qquad (4.18)$$

The variation of minimum detection range with ESM receiver RF bandwidth is plotted in figure 4-8 for different radar pulse lengths and a fixed ESM video bandwidth of 1 MHz. We see that for relatively short 1 μs pulses the crystal video receiver can easily detect the radar but that as the pulses get longer the minimum detection range becomes unacceptably large: an incoming homing missile with a radar that cannot be detected once it is inside a radius of 15 km would pose a very serious threat.

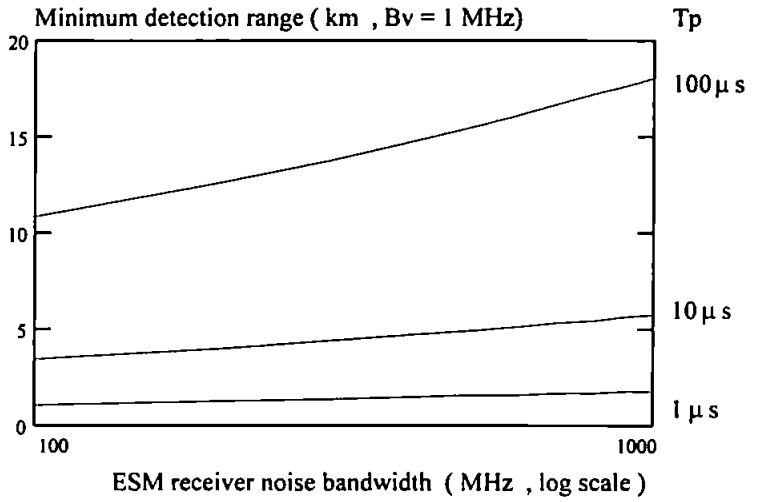

Figure 4-8. Variation of minimum detection range with ESM RF noise bandwidth for a crystal video receiver with a fixed video bandwidth of 1 MHz against a power managed pulsed LPI radar with different pulse lengths T_p. System and signal parameters are as in table 4-1.

Of course, the performance of the crystal video receiver can be improved by reducing the video bandwidth as far as possible. Optimum performance of the crystal video receiver is obtained if the video bandwidth is matched to the pulse by setting

$$B_v = \frac{1}{T_p} \tag{4.19}$$

This requires either a priori knowledge of the pulse length or a bank of different video filters and detectors attached to every RF receiver. The plots in figures 4-7 and 4-8 are repeated in figures 4-9 and 4-10 respectively for the cases where video bandwidth has been matched to the pulse length. We see a significant improvement in ESM system performance, but for longer radar pulses (100 μs) the ESM system is still not quite sensitive enough to provide adequate tracking of a power managed radar, especially if it has to have wide RF/IF channels and does not have the a priori information to match its video bandwidth perfectly to the pulse length.

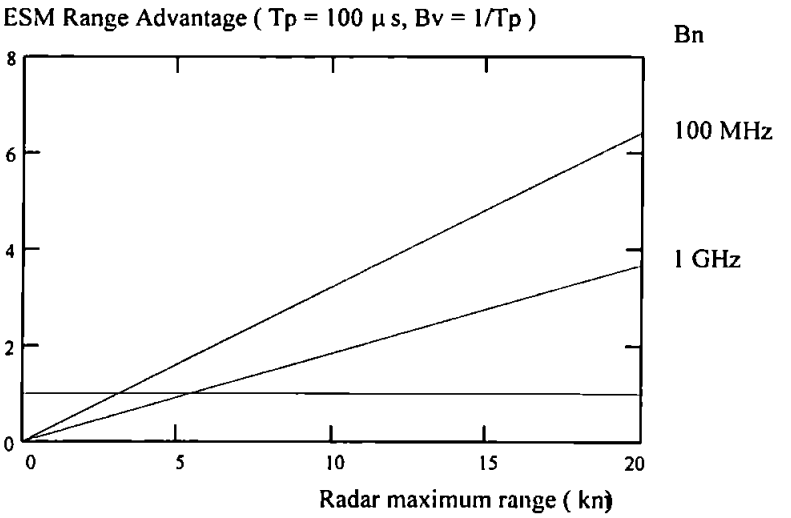

Figure 4-9. Variation of ESM range advantage with radar maximum range for a crystal video receiver with video bandwidth matched to the radar pulse length and radar pulses of length 100 μs, for different ESM RF bandwidths. System and signal parameters are as in table 4-1.

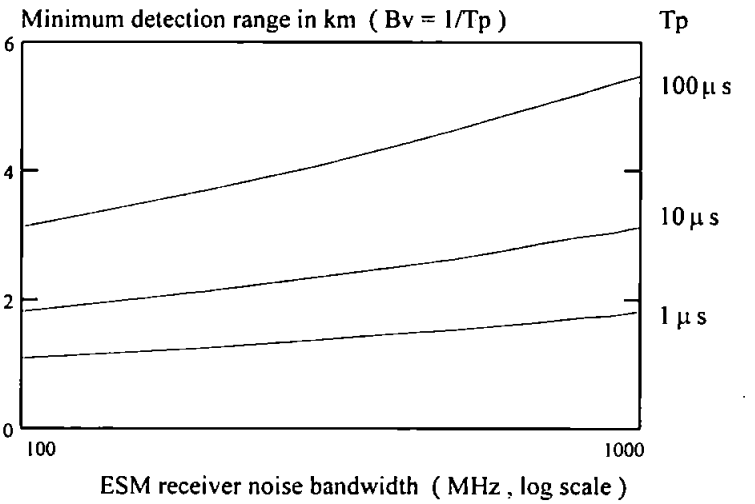

Figure 4-10. Variation of minimum detection range with ESM RF noise bandwidth for a crystal video receiver with video bandwidth matched to radar pulse length against a power managed pulsed LPI radar with different pulse lengths T_p. System and signal parameters are as in table 4-1.

4.7 The Cross Correlation Receiver

4.7.1 The ccf receiver and pulsed radar - advantage over the crystal video receiver

For the ccf, derived by continuous correlation, we have, from equation 2.45

$$\left(\frac{\hat{S}}{N}\right)_o = \frac{2n^2 T_p^2 B_n \left(\frac{S}{N}\right)_i^2}{T_{se} + 2n T_p \left(\frac{S}{N}\right)_i} \tag{4.20}$$

where n is the number of radar pulses of length T_p captured within the ESM integration period of length T_{se}. It should again be emphasised that the ccf receiver can perform coherent pulse integration (see section 2.3.3) and that this is enormously important. For low SNR_i, when $2n T_p \left(\frac{S}{N}\right)_i << T_{se}$, this simplifies to

$$\left(\frac{\hat{S}}{N}\right)_o = \frac{2n^2 T_p^2 B_n}{T_{se}} \left(\frac{S}{N}\right)_i^2 = \frac{2n^2 T_p^2 S_i^2}{T_{se} B_n \eta_e^2} \tag{4.21}$$

Hence, the sensitivity of the ccf receiver to pulsed signals is

$$S_{eccf} = \frac{\eta_e}{n T_p} \sqrt{\frac{B_n T_{se}}{2} SNR_{thccf}} \tag{4.22}$$

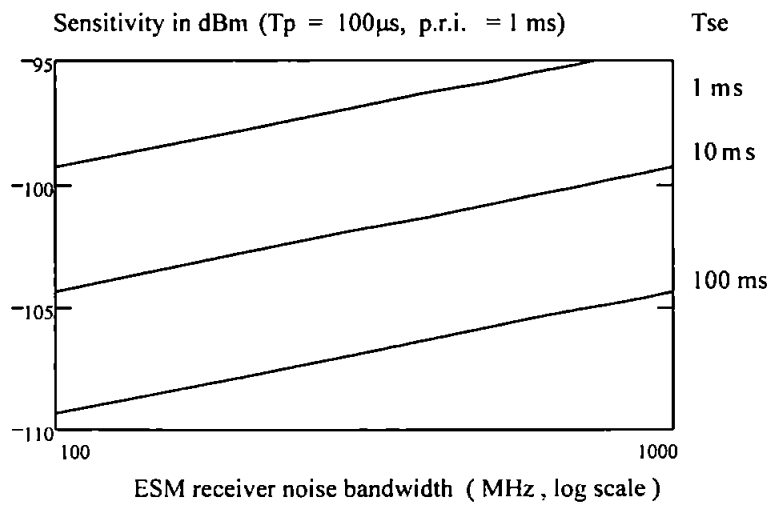

Figure 4-11. Variation of sensitivity, to pulsed radar signals, with RF noise bandwidth for a cross correlation receiver applying threshold detection to the ccf, using different integration times. System and signal parameters are as in table 4-1.

The variation of ccf ESM receiver sensitivity with RF bandwidth, for different ESM integration times is shown in figure 4-11. The radar pulse length and p.r.i. are fixed at 100 μs and 1 ms while different ESM integration times capture different numbers of pulses for coherent integration: a 1 ms integration time will include 1 pulse while a 100 ms integration time will coherently integrate 100 pulses. From equation 4.22, the sensitivity advantage of the ccf receiver over the crystal video is given by

$$\frac{S_{exstal}}{S_{eccf}} = \frac{n\,T_p\,S_{exstal}}{\eta_e}\sqrt{\frac{2}{B_n\,T_{se}\,SNR_{thccf}}} \qquad (4.23)$$

where S_{exstal} is obtained from the equations [18] used to plot figure 4-6. If the ESM integration time is very much greater than the radar pulse repetition interval, T_{pri} then the number of radar pulses included in the ESM sample is

$$n = \frac{T_{se}}{T_{pri}}. \qquad (4.24)$$

Then equation 4.23 becomes

$$\frac{S_{exstal}}{S_{eccf}} = \frac{T_p\,S_{exstal}}{T_{pri}\,\eta_e}\sqrt{\frac{2\,T_{se}}{B_n\,SNR_{thccf}}} \qquad (4.23)$$

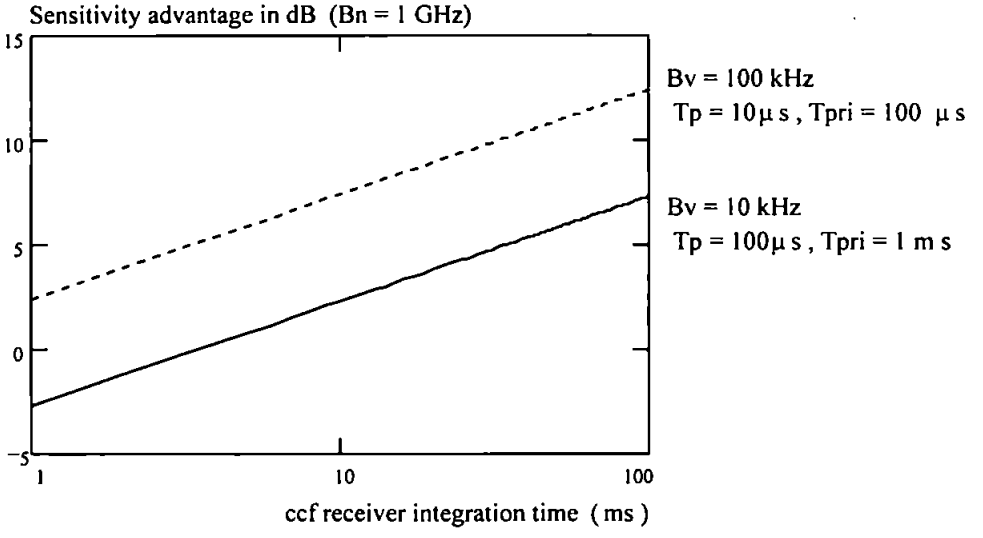

Figure 4-12. Variation with integration time of the sensitivity advantage of a cross correlating receiver applying threshold detection to the ccf over a crystal video receiver with video bandwidth matched to the pulse length, for different combinations of radar pulse length and p.r.i. such that the duty cycle is 1/10. System and signal parameters are as in table 4-1.

This sensitivity advantage is plotted against ESM receiver integration time, for two different combinations of radar pulse length and T_{pri}. (in both cases the duty cycle,

$\frac{T_p}{T_{pri}}$, is $\frac{1}{10}$) , in figure 4-12. We see that sensitivity advantages in excess of 5 dB are quite realistic and, as we shall see, this is sufficient to make the difference between detection and non detection of a power managed radar. It should be emphasised that this sensitivity advantage is plotted for the case where the video bandwidth of the crystal video receiver is matched to the pulse length. Hence figure 4-12 shows the minimum sensitivity advantage of the cross correlating system over the crystal video receiver. The higher the duty cycle, i.e. the closer the radar signal approaches the CW case, the greater the advantage of the ccf receiver. Figure 4-13 shows the effect of reducing T_{pri} so that the duty cycle is changed from 1/10 to 1/2.

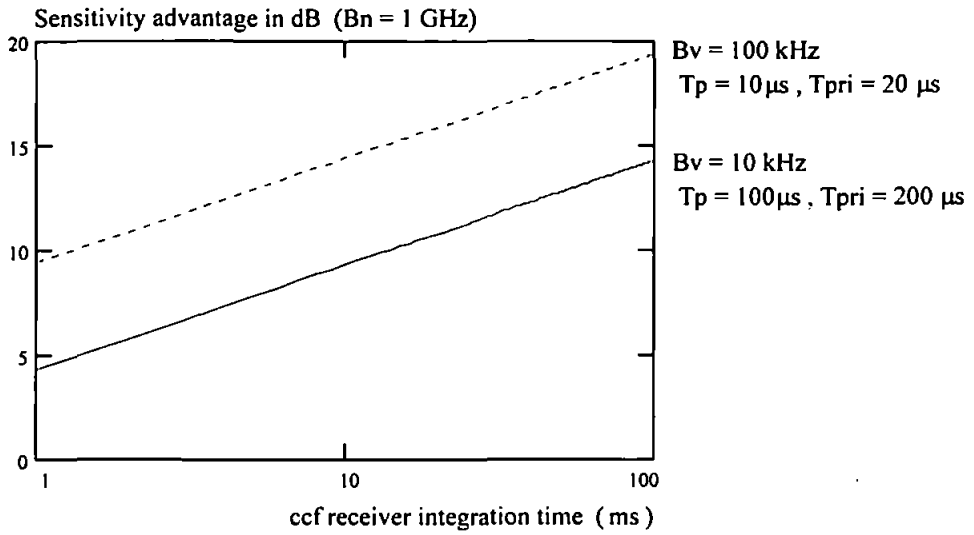

Figure 4-13. Variation with integration time of the sensitivity advantage of a cross correlating receiver applying threshold detection to the ccf over a crystal video receiver with video bandwidth matched to the pulse length, for different combinations of radar pulse length and p.r.i. such that the duty cycle is 1/2. System and signal parameters are as in table 4-1.

The range advantage of a ccf ESM receiver over a pulsed radar is found by combining equations 4.4, 4.12 and 4.22 to give

$$\frac{R_e}{R_r} = R_r \left\{ \frac{4\pi G_e n \eta_r \quad SNR_{1hrad}}{\sigma G_r I \eta_e \quad \sqrt{2 B_n T_{se} SNR_{1hccf}}} \right\}^{\frac{1}{2}} \tag{4.26}$$

Figure 4-14 shows the variation of this range advantage with radar maximum range for different ESM RF bandwidths and fixed values of radar pulse length (100 μs) and ESM sample length (1 ms). We see that, for the wide RF bandwidth that would be desirable, the

ccf ESM system still does not offer quite the sensitivity that is required, but this can now be improved by using longer ESM integration times, which are quite realistic.

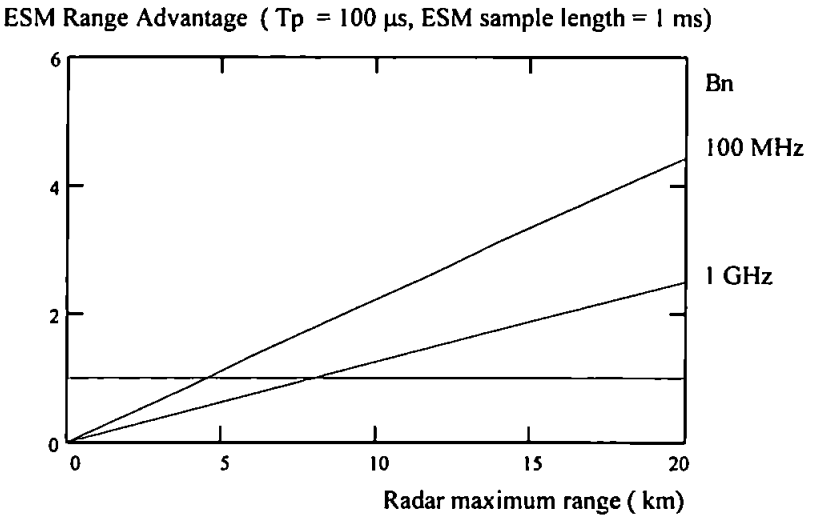

Figure 4-14. Variation, with radar maximum range, of the ESM range advantage of a cross correlating receiver applying threshold detection to the ccf, over a pulsed radar, for different RF noise bandwidths. System and signal parameters are as in table 4-1.

The minimum detection range for a ccf ESM receiver against a pulsed power managed radar is

$$R_{\min} = \left\{ \frac{\sigma G_r I_r \eta_e \sqrt{2 B_n T_{se} SNR_{thccf}}}{4\pi G_e n \eta_r SNR_{thrad}} \right\}^{\frac{1}{2}} \qquad (4.27)$$

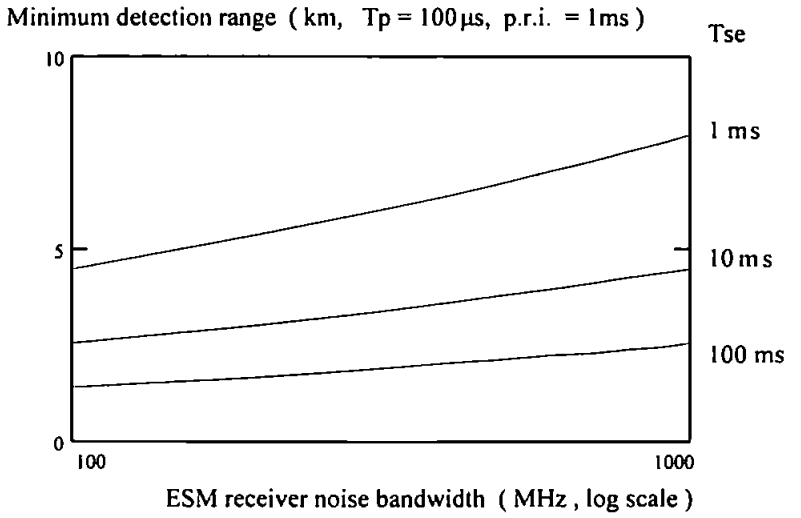

Figure 4-15. Variation, with receiver RF noise bandwidth, of the minimum detection range for a ccf receiver against a power managed pulsed radar, for different ESM integration times. System and signal parameters are as in table 4-1.

The variation of this minimum detection range with ESM receiver RF bandwidth is shown for different ESM integration times in figure 4-15. We see that, if we use sufficiently long integration times we can at last achieve small enough minimum detection ranges, even with large RF bandwidths.

4.7.2 The ccf receiver and CW radar

The performance of the ccf receiver is even better for CW signals. Replacing nT_p in equation 4.22 with T_{se} gives the sensitivity of the ccf receiver to CW signals

$$S_{eccf} = \eta_e \sqrt{\frac{B_n}{2\,T_{se}} SNR_{thccf}} \qquad (4.28)$$

The variation of this sensitivity with ESM receiver RF bandwidth is plotted in figure 4-16 for different ESM integration times. Comparing figure 4-16 with the sensitivity requirement, as shown in figure 4-2, we see that with longer integration times (10 ms or more) the required sensitivity (better than -110 dBm) can be achieved. The results obtained here can be compared with those of Torrieri [4] who also compares the ccf and crystal video receiver. Torrieri discusses a radiometer (similar to the crystal video receiver) designed to detect CW signals. Instead of a video filter, he talks in terms of an integrator integrating over a long period of time, and he presents a very full and rigorous analysis. An integrator with an integration time of 100 ms would be equivalent to a video bandwidth of 10 Hz. Substituting B_n = 1 GHz and B_v = 10 Hz into the equations for the crystal video receiver at appendix F gives, for a system noise temperature of 500 K, a sensitivity of -112.6 dBm for a probability of false alarm (P_{fa}) of 10^{-5} and probability of detection (P_d) of 0.99. Substituting B_n = 1 GHz, T_{se} = 100 ms and SNR_{thccf} = 17.53 dB (as required for $P_{fa} = 10^{-7}$ and P_d = 0.99 for each sample in the ccf) into equation 4.28 gives a sensitivity for the ccf receiver of -114.35 dBm. This is an advantage of 1.65 dB for the ccf receiver. Torrieri obtains a value of 1.5 dB ($\sqrt{2}$) by a different approach which involves considering the components of a DFT (discrete Fourier transform). The difference lies in the assumptions of how many samples in the ccf need to be considered in specifying P_{fa} for each sample. Torrieri considers all the samples in the ccf rather than just those in the windowed centre portion. By considering γ times fewer samples we can specify a higher P_{fa} for each sample and hence achieve the required detection performance with a slightly

lower SNR in the ccf output. Hence the sensitivity advantage of the ccf receiver over the radiometer will generally exceed 1.5 dB by an amount dependent on γ. Calculation of the precise value of this advantage is straightforward but it is never more than a few tenths of a dB greater than 1.5 dB.

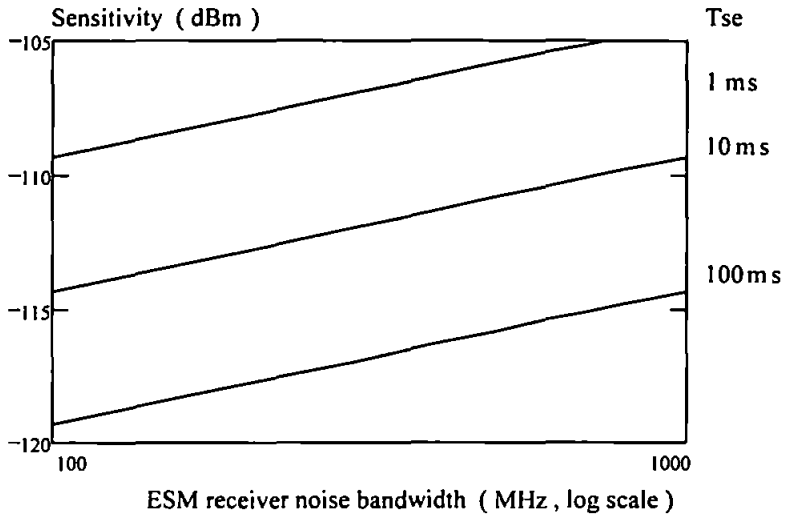

Figure 4-16 Variation, with receiver RF noise bandwidth, of the sensitivity of a cross correlating ESM receiver applying threshold detection to the ccf to CW LPI radar signals, for different ESM integration times. System and signal parameters are as in table 4-1.

Substituting equations 4.5 and 4.28 into equation 4.12 gives the range advantage of the ccf ESM receiver over a CW radar

$$\frac{R_e}{R_r} = R_r \left\{ \frac{4\pi G_e}{\sigma G_r} \frac{\eta_r}{\eta_e} \sqrt{\frac{T_{se} SNR_{thrad}^{\ 2}}{2 B_n T_{sr}^2 SNR_{thccf}}} \right\}^{\frac{1}{2}} \qquad (4.29)$$

The variation of this range advantage with radar maximum range, for two different ESM RF bandwidths, is shown in figure 4-17.

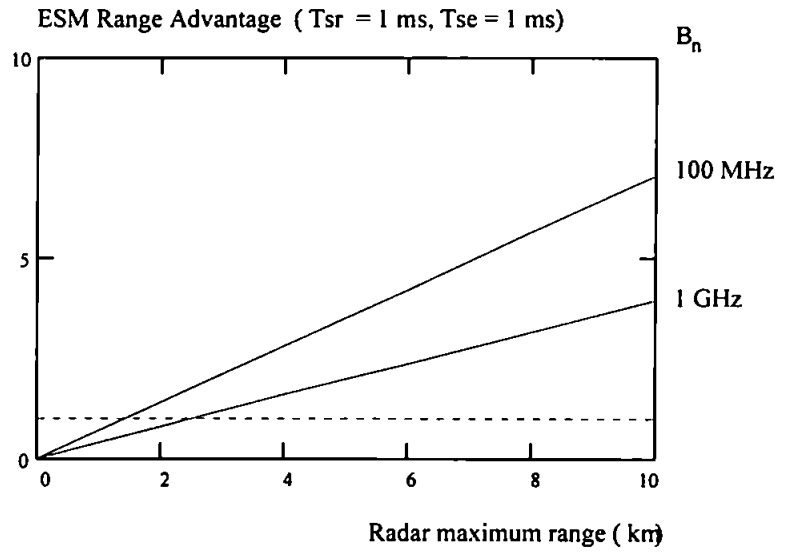

Figure 4-17. Variation, with radar maximum range, of ESM range advantage of a cross correlating ESM receiver applying threshold detection to the ccf over a CW LPI radar, for different ESM integration times. System and signal parameters are as in table 4-1.

By setting the range advantage to one in equation 4.29 we obtain the minimum detection range for the ccf ESM receiver against the power managed CW LPI radar.

$$R_{\min} = \left\{ \frac{\sigma G_r}{4\pi G_e} \frac{\eta_e}{\eta_r} \sqrt{\frac{2 B_n T_{sr}^2 SNR_{thccf}}{T_{se} SNR_{thrad}^2}} \right\}^{\frac{1}{2}} \tag{4.30}$$

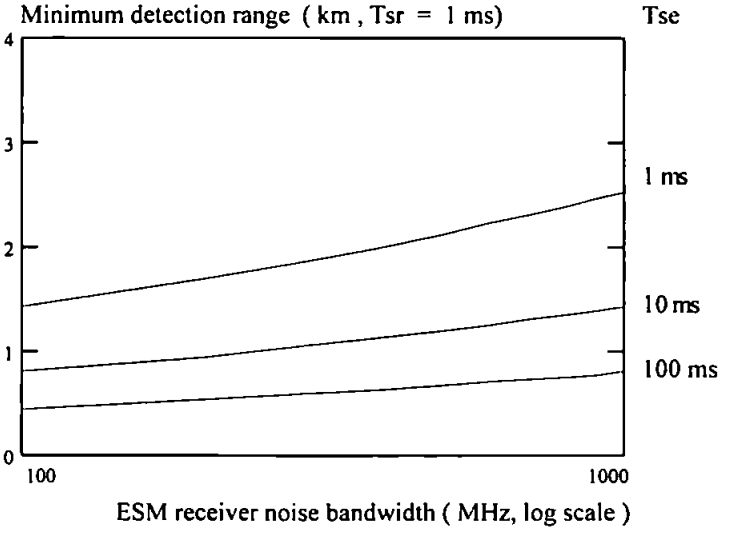

Figure 4-18. Variation, with ESM receiver RF noise bandwidth, of minimum detection range for a cross correlating ESM system applying threshold detection to the ccf against a power managed CW LPI radar, for different ESM integration times. System and signal parameters are as in table 4-1.

The variation of this minimum detection range with ESM receiver RF bandwidth, for different ESM integration times, is plotted in figure 4-18. We see that the minimum detection ranges are down at 2 km or less, particularly for longer ESM integration times. It is interesting to note that when we use a ccf ESM receiver CW signals become easier to detect than pulsed signals.

4.8 The TDFCSD receiver

4.8.1 The TDFCSD receiver and pulsed radar

For the time domain filter, assuming a "zoom factor" of $\gamma = \frac{B_s T_s}{3}$, we have, from equation 3.8

$$\left(\frac{S}{N}\right)_o = \frac{\left(\frac{B_n}{B_s}\right)^2 \left(\frac{S}{N}\right)_i^2}{\left(\frac{T_s}{n T_p}\right)^2 + 2\left(\frac{T_s}{n T_p}\right)\left(\frac{S}{N}\right)_i} \times \frac{B_s T_s}{3} \qquad (4.31)$$

For small input SNR this approximates to

$$\left(\frac{S}{N}\right)_o = \frac{n^2 T_p^2 S_i^2}{3 B_s T_s \eta_e^2} \qquad (4.32)$$

Hence, the sensitivity of the TDFCSD receiver to pulsed radar signals is

$$S_{ecsd} = \frac{\eta_e}{n T_p} \sqrt{3 B_s T_{se} SNR_{thcsd}} \qquad (4.33)$$

In figure 4-19 this sensitivity is plotted against receiver RF bandwidth for different integration times and fixed values of pulse length $T_p = 100$ μs, p.r.i. = 1 ms and signal bandwidth $B_s = 100$ MHz. The most obvious feature of figure 4-19 is that the sensitivity is independent of RF bandwidth. This means that, in principle, the RF bandwidth can be made arbitrarily large without reducing the sensitivity. This is extremely useful if we wish to build a relatively low cost ESM system giving wide band coverage with the minimum number of RF receivers. In practice we will find that the RF bandwidth that can be realised

will be limited by the bandwidth that the initial correlator can process. Figure 4-20 shows how this sensitivity varies with signal bandwidth.

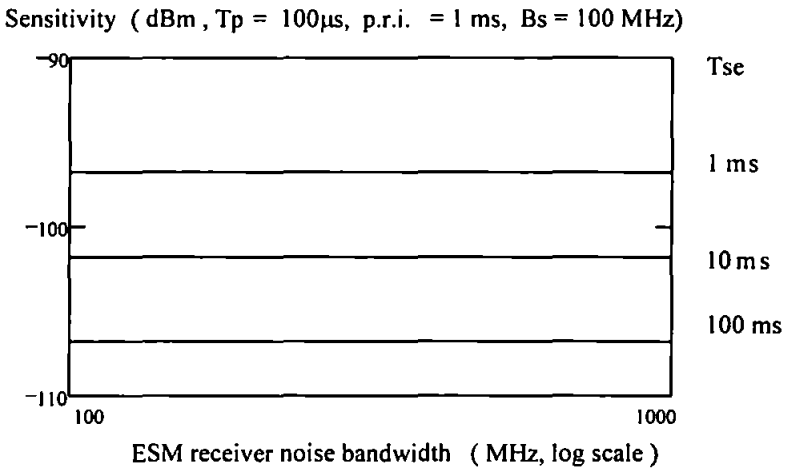

Figure 4-19. Variation (or in fact lack of variation!), with receiver RF noise bandwidth, of the sensitivity of a cross correlating ESM receiver applying threshold detection to the TDFCSD to pulsed LPI radar signals, for different ESM integration times. System and signal parameters are as in table 4-1.

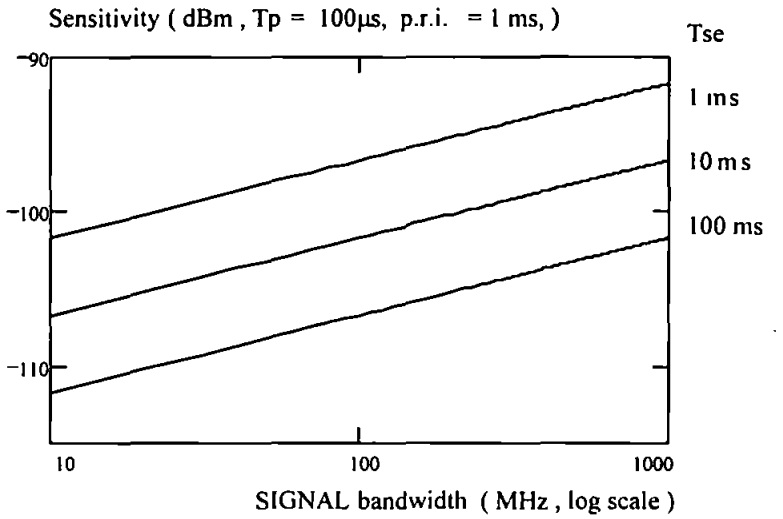

*Figure 4-20. Variation, with **signal** bandwidth, of the sensitivity of a cross correlating ESM receiver applying threshold detection to the TDFCSD to pulsed LPI radar signals, for different ESM integration times. System and signal parameters are as in table 4-1.*

Substituting equations 4.4 and 4.33 into 4.12 gives the range advantage of the TDFCSD ESM receiver over a pulsed radar

$$\frac{R_e}{R_r} = R_r \left\{ \frac{4\pi G_e}{\sigma G_r} \frac{n \eta_r}{2 I_r \eta_e} \sqrt{\frac{SNR_{thrad}^{\ 2}}{3 B_s T_{se}^2 SNR_{thcsd}}} \right\}^{\frac{1}{2}} \qquad (4.34)$$

This variation, with radar maximum range, of the ESM range advantage over a pulsed LPI radar, is plotted in figure 4-21 for different ESM integration times.

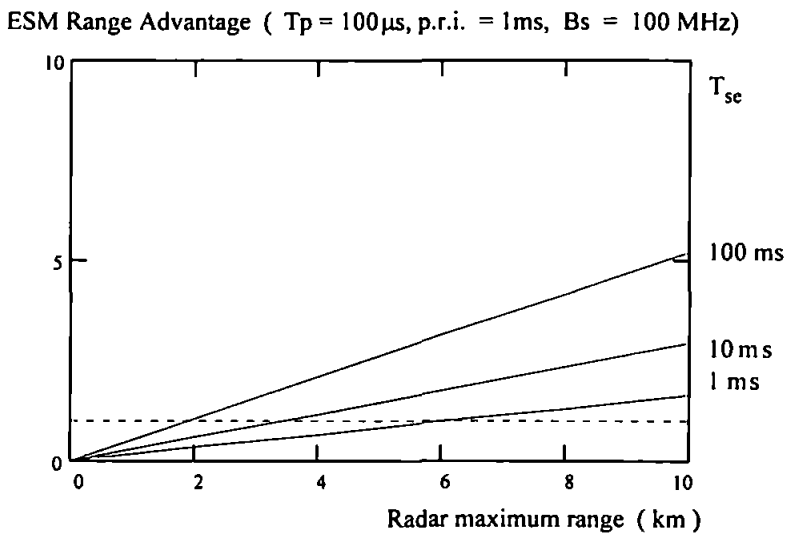

Figure 4-21. Variation, with radar maximum range, of ESM range advantage of a cross correlating ESM receiver over a pulsed LPI radar, for different ESM integration times. System and signal parameters are as in table 4-1.

Setting the range advantage to one in equation 4.34 gives the minimum detection range for the TDFCSD receiver against a power managed pulsed LPI radar.

$$R_{\min} = \left\{ \frac{\sigma G_r}{4\pi G_e} \frac{2 I_r \eta_e}{n \eta_r} \sqrt{\frac{3 B_s T_{se}^2 SNR_{thcsd}}{SNR_{thrad}^2}} \right\}^{\frac{1}{2}} \qquad (4.35)$$

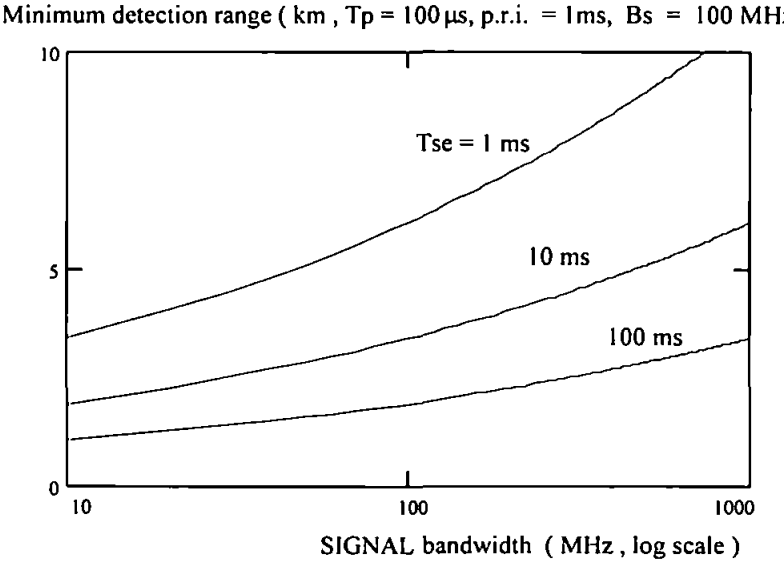

*Figure 4-22. Variation, with **signal** bandwidth, of minimum detection range for a cross correlating ESM system applying threshold detection to the TDFCSD against a power managed pulsed LPI radar, for different ESM integration times. System and signal parameters are as in table 4-1.*

4.8.2 The TDFCSD receiver and CW radar

Replacing nT_p by T_{se} in equation 4.33 gives the sensitivity of the TDFCSD to CW signals

$$S_{ecsd} = \eta_e \sqrt{\frac{3\,B_s}{T_{se}}\,SNR_{thcsd}} \tag{4.36}$$

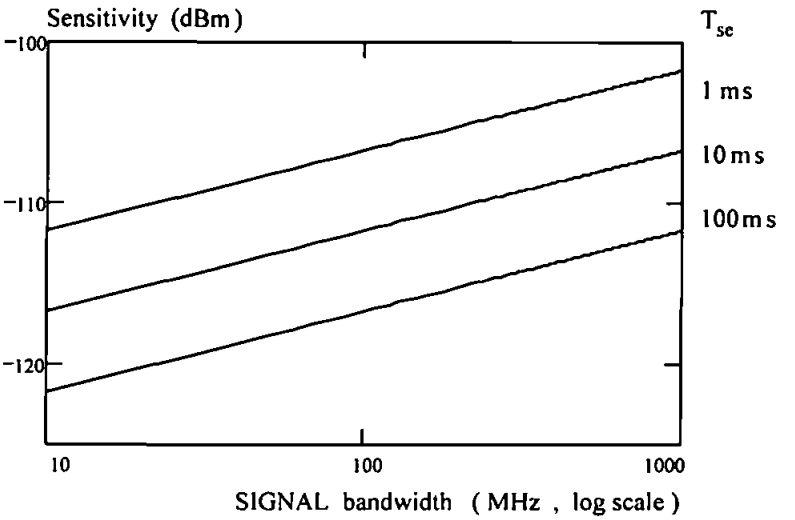

Figure 4-23. Variation, with signal bandwidth, of the sensitivity of a cross correlating ESM receiver applying threshold detection to the TDFCSD to CW LPI radar signals, for different ESM integration times. System and signal parameters are as in table 4-1.

Substituting equations 4.5 and 4.36 into equation 4.12 gives the range advantage of the TDFCSD ESM receiver over a CW radar

$$\frac{R_e}{R_r} = R_r \left\{ \frac{4\pi\,G_e}{\sigma\,G_r}\,\frac{\eta_r}{\eta_e} \sqrt{\frac{T_{se}\,SNR_{thrad}{}^2}{12\,B_s\,T_{sr}^2\,SNR_{thcsd}}} \right\}^{\frac{1}{2}} \tag{4.37}$$

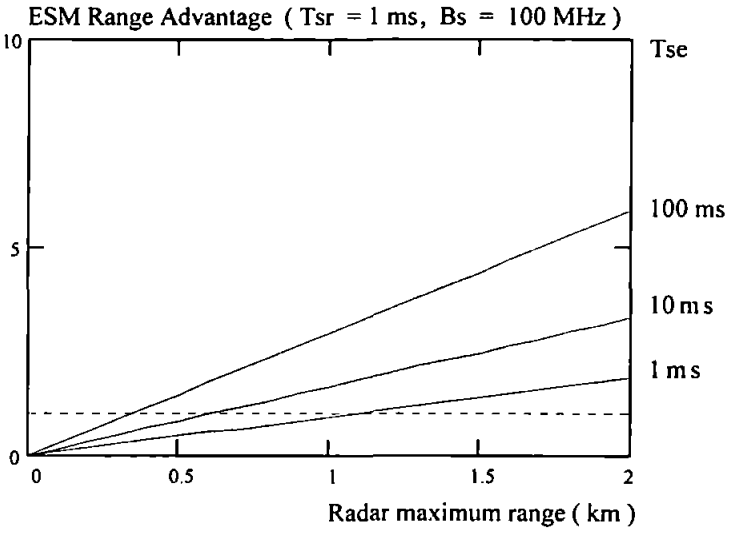

Figure 4-24. Variation, with radar maximum range, of ESM range advantage of a cross correlating ESM receiver applying threshold detection to the TDFCSD over a CW LPI radar, for different ESM integration times. System and signal parameters are as in table 4-1.

Setting the range advantage to one in equation 4.37 gives the minimum detection range for a TDFCSD ESM receiver against a power managed CW LPI radar

$$R_{\min} = \left\{ \frac{\sigma G_r}{4\pi G_e} \frac{\eta_e}{\eta_r} \sqrt{\frac{12\, B_s\, T_{sr}^2\, SNR_{thccf}}{T_{se}\, SNR_{thrad}^{\,2}}} \right\}^{\frac{1}{2}} \tag{4.35}$$

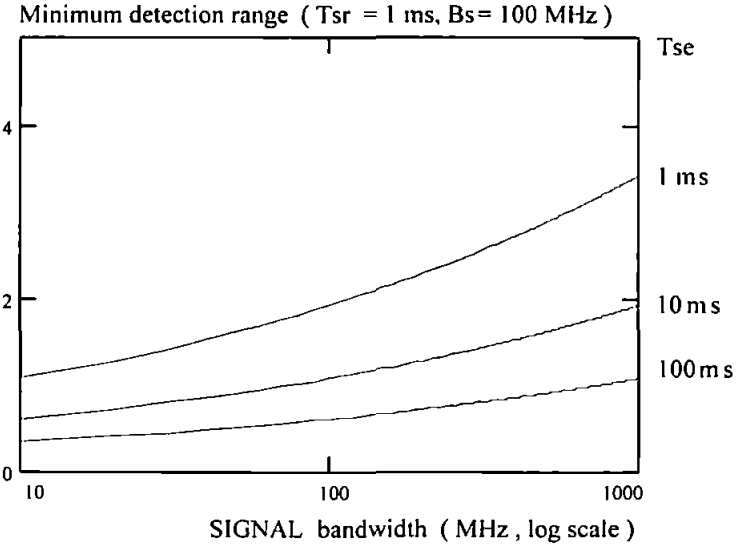

*Figure 4-25. Variation, with **signal** bandwidth, of minimum detection range for a cross correlating ESM system applying threshold detection to the TDFCSD against a power managed CW LPI radar, for different ESM integration times. System and signal parameters are as in table 4-1.*

4.9 Conclusions

The cross correlation receiver offers greater ability to counter the future threat of the power managed CW, or pulsed, LPI radar than crystal video receiver or radiometer. If the receiver noise is assumed to be stationary, the theoretical sensitivity of the cross correlation receiver applying threshold detection directly to the ccf is only about 1.5 dB better than for the radiometer, as is shown by Torrieri [4] and confirmed here. However the assumption of stationarity is a major one that will not be valid in many real situations. The internal receiver noise may well be stationary, but the external noise picked up by the antenna may vary significantly. The total noise at the receiver input is $kT_{sys}B_n$.The system noise temperature $T_{sys} = T_A + T_R$ where T_A is the antenna noise temperature and T_R the internal receiver noise temperature. If a low noise high gain front end preamplifier is used its noise temperature forms the major part of the total internal receiver noise temperature. At 10 GHz, broadband low noise amplifiers with noise temperatures better than 170 K (equivalent to a noise figure of 2 dB) can be seen to be readily available by consulting the commercial adverts in, e.g., any recent issue of "Microwaves and RF". Antenna noise temperature varies with elevation. Blake [18] plots the noise temperature for an idealized antenna. He shows that, at 10 GHz the minimum antenna noise temperature varies from about 150 K at 0° elevation through 35 K at 5° elevation to 6 K at 90° elevation. For a real antenna mounted in close proximity to many other metal structures the noise temperatures will be somewhat larger. Hence we can expect antenna noise to account for about half the total receiver noise, at 0° elevation. The variation in noise power will be considerable for a system mounted on a mobile platform. For a ship, e.g., a roll of 10° or more is quite normal and there are many nearby structures incuding other antennas, some of them rotating. The total receiver noise temperature can be expected to be in the region of 400 to 500 K and to vary by more than 100 K over time periods of the order of a few seconds. Under these conditions, a radiometer attempting to detect CW signals by looking for changes in total input signal power level cannot be expected to detect a signal at a negative input SNR causing an apparent change in receiver noise temperature of only a few K. The cross correlation receiver does not suffer from this problem. Each sample can be handled without any prior knowledge of the input noise level, and a threshold set independently. Variations in receiver noise temperature will inevitably cause small variations in sensitivity, of the

order of 1 dB, but that is all. The cross correlation receiver detects signals on a totally different basis from the radiometer or crystal video receiver. The radiometer measures total signal power while the cross correlation receiver picks out coherent point sources from an incoherent background.

We now consider the choice of whether to apply threshold detection to the ccf or the TDFCSD. From equations 4.22 and 4.33, which give sensitivities to pulsed signals, we can obtain the sensitivity advantage of the TDFCSD over the ccf

$$\frac{S_{eccf}}{S_{ecsd}} = \sqrt{\frac{B_n\ SNR_{thccf}}{6\ B_s\ SNR_{thcsd}}} = \sqrt{0.3\frac{B_n}{B_s}} \qquad (4.36)$$

where the required SNRs at the threshold detector for the ccf and the TDFCSD are 17.53 dB and 14.98 dB respectively. The same result can be obtained by considering equations 4.28 and 4.36, which give sensitivities to CW signals. It can also be obtained from equation 3.16. In section 3.3, relatively short integration times were considered and it was shown that, for FMCW signals, use of the TDFCSD could provide greater sensitivity because of the narrow signal bandwidth within the sample taken. In the case where maximum sensitivity is required, however, ESM integration times will be much longer and the fine detail discussed in section 3.3 ceases to be relevant. Only when the signal power reaches a relatively large level will it be worth switching the system into a mode where it takes short samples in order to characterise the frequency sweeping characteristics of the signal in detail. Whether the ccf or the TDFCSD provides the greater sensitivity simply depends on the relationship between the signal bandwidth and the RF noise bandwidth of the cross correlating receiver. If B_s is greater than $0.3B_n$ the ccf offers the greater sensitivity, otherwise the TDFCSD offers the greater sensitivity. If a channellised ESM system using a large number of narrow RF channels is considered affordable and desirable, then direct threshold detection applied to the ccf could lead to the most sensitive system possible. However, a rather more realistic and cheaper approach is to opt for a much smaller number of broadband RF receivers applying threshold detection to the TDFCSD. Since the sensitivity is independent of RF noise bandwidth, large bandwidths offer no disadvantage. There are two great advantages of using the TDFCSD. The LPI signal can be characterised spectrally within the RF bandwidth (the frequency resolution is $\frac{\gamma}{T_{se}}$), and as

will be discussed in detail in chapter 5, high resolution direction finding becomes possible. In short, use of the TDFCSD offers the possibility of obtaining much more information while only being less sensitive in the case of an expensive system comprising many narrow RF channels, or in the case of a signal with such a wide spectrum that it occupies most or all of the receiver bandwidth.

5. Direction Finding

5.1 Introduction

The angle of arrival (AOA) is obtained by estimating the time difference of arrival (TDA) of the LPI signal at the two receivers. The AOA is calculated simply as

$$\theta = \sin^{-1}\left(\frac{c\,t_d}{d}\right) \tag{5.1}$$

where c is the speed of light, d is the spatial separation of the two receiver antennas, t_d is the TDA and θ is the AOA measured from the normal to the line joining the two antennas. The TDA is estimated from the phase slope of the TDFCSD. A time shift in the time domain corresponds to a linear phase slope in the frequency domain given by

$$\frac{d\theta}{df} = 2\pi t_d \tag{5.2}$$

If the TDFCSD has been obtained in digital form, the phase slope can be estimated by using a least squares algorithm to fit a straight line to the set of points representing the phase terms of the complex TDFCSD. The decision as to which part or parts of the TDFCSD should be considered is made by applying a threshold to the magnitude terms. If there is one CW signal then a single block of TDFCSD elements must be considered. For a frequency hopping signal the components containing signal and those containing just noise will be mixed up - there will be many components we do not wish to include in the phase slope estimation, mixed in with those we do wish to consider, within the total signal bandwidth. If a threshold is applied separately to each component of the TDFCSD then direction finding can be carried out on frequency hopping signals by taking all those components for which the magnitude exceeds the threshold and fitting a straight line to them. If there are more than one signal then two or more separate or overlapping blocks will have to be considered, and more than one straight line will have to be fitted to the phase data.

5.2 Effect of noise on the phase of the TDFCSD

Any small error in the AOA measurement is given by

$$\Delta\theta = \frac{c\,\Delta t_d}{d\cos\theta} \tag{5.2}$$

Where Δt_d is the error in the TDA estimation. To estimate the error in the AOA measurement we must therefore estimate the error in the TDA measured from the phase slope of the TDFCSD. To determine the error in this phase slope we proceed in two stages. First we must obtain the statistics of the noise induced errors in the values of the phase of each data point in the TDFCSD, and then we must determine the effect that these phase errors have on the process of fitting a straight line to the points.

Implicit in the process is the requirement to phase unwrap the phase values held digitally for the TDFCSD. The FFT process used to obtain the TDFCSD from the windowed ccf will have produced wrapped phase values between $-\pi$ and $+\pi$. To fit a straight line to the phase values, within the signal bandwidth, requires that we first unwrap the phase. Clearly, this can only be done if the errors in the phase values are small enough not to cause the phase unwrap algorithm to fail. As we shall see, this translates into a requirement for an adequate SNR in the TDFCSD - a condition which will be shown to be satisfied whenever the SNR in the TDFCSD is sufficient to enable detection in the first place. i.e. if an LPI signal can be detected then the direction finding process will always be possible, even though it may not always be particularly accurate.

To estimate the error in the phase of each sample in the TDFCSD we consider the effect of the noise on the phase. The k^{th} sample in the TDFCSD can be written as

$$TDFCSD_k = A_k + n_k \tag{5.3}$$

where A_k and n_k are both complex and A_k represents the signal, n_k the noise. The SNR in the TDFCSD can then be written as

$$\left(\frac{S}{N}\right)_{TDFCSD} = \frac{E\left\{|A_k|^2\right\}}{E\left\{|n_k|^2\right\}} \tag{5.4}$$

The complex value n_k can be written, using the standard representation for narrowband noise, as

$$n_k = r_k\, e^{j\phi_k} \tag{5.5}$$

where r_k , the magnitude of n_k , has a Rayleigh pdf of the form

$$p_R(r) = \frac{r}{\sigma^2} e^{-\frac{r^2}{2\sigma^2}} \tag{5.6}$$

and ϕ has a uniform pdf equal to $1/2\pi$ between $-\pi$ and $+\pi$. n_k can alternatively be represented, in the quadrature form, as

$$n_k = c_k + j\, s_k \tag{5.7}$$

c_k and s_k are real and have Gaussian pdfs of the form

$$p_G(x) = \frac{1}{\sqrt{2\pi\sigma^2}} e^{-\frac{x^2}{2\sigma^2}} \tag{5.8}$$

where σ is the same for c_k, s_k and r_k. The power of the noise in the TDFCSD, N, is given by

$$N = E\left\{|n_k|^2\right\} = E\left\{r_k^{\,2}\right\} = \int_{-\infty}^{+\infty} r^2\, p_R(r)\, dr = 2\sigma^2 \tag{5.9}$$

The error in phase caused by this noise is shown by figure 5-1.

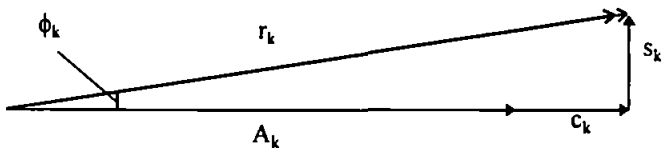

Figure 5-1. Vector representation of kth component of TDFCSD plus noise represented in quadrature form.

If the signal to noise ratio in the TDFCSD is greater than 14 dB, which it must be to allow signal detection in the first place, then the phase error caused by the noise in each sample is approximately

$$\phi_k = \frac{|s_k|}{|A_k|} \tag{5.10}$$

and has a Gaussian pdf. The validity of this approximation is proved in appendix F, where it is shown that if the signal to noise ratio is greater than 14 dB, the error incurred by this approximation is less than 2.2%. The mean of ϕ_k is zero but its variance is given by

$$\sigma_\phi^{\,2} = \frac{\sigma^2}{A_k^{\,2}} = \frac{1}{2\left(\frac{S}{N}\right)_{TDFCSD}} \tag{5.11}$$

For a TDFCSD derived from a ccf obtained using a FFT based or true continuous correlator, and a CW signal, we have, from equation 3.9

$$\left(\frac{S}{N}\right)_{TDFCSD} = \frac{\gamma\left(\frac{B_n}{B_s}\right)^2\left(\frac{S}{N}\right)_i^2}{1 + 2\left(\frac{S}{N}\right)_i} \tag{5.12}$$

Hence we have

$$\sigma_\phi = \sqrt{\frac{1 + 2\left(\frac{S}{N}\right)_i}{2\gamma\left(\frac{B_n}{B_s}\right)^2\left(\frac{S}{N}\right)_i^2}} \tag{5.13}$$

This theoretical prediction has been compared against values extracted from the Mathcad simulation. The Mathcad program used to generate these results is at appendix E. The integration time T_s was 500 μs, the receiver noise bandwidth was 100 MHz and the signal

was a FMCW signal with a sawtooth frequency scan ramping up through 50 MHz in 500 μs. A range of values of input signal to noise ratios were used from -17 dB to +30 dB, with several different values of "zoom factor" for each value of input signal to noise ratio. The direction of arrival was set to zero so that all phase values should be zero. The standard deviation of the phases of the data points were calculated, as were the values predicted by equation 5.13 above. The results are tabulated it appendix E, and plotted graphically in figure 5-1.

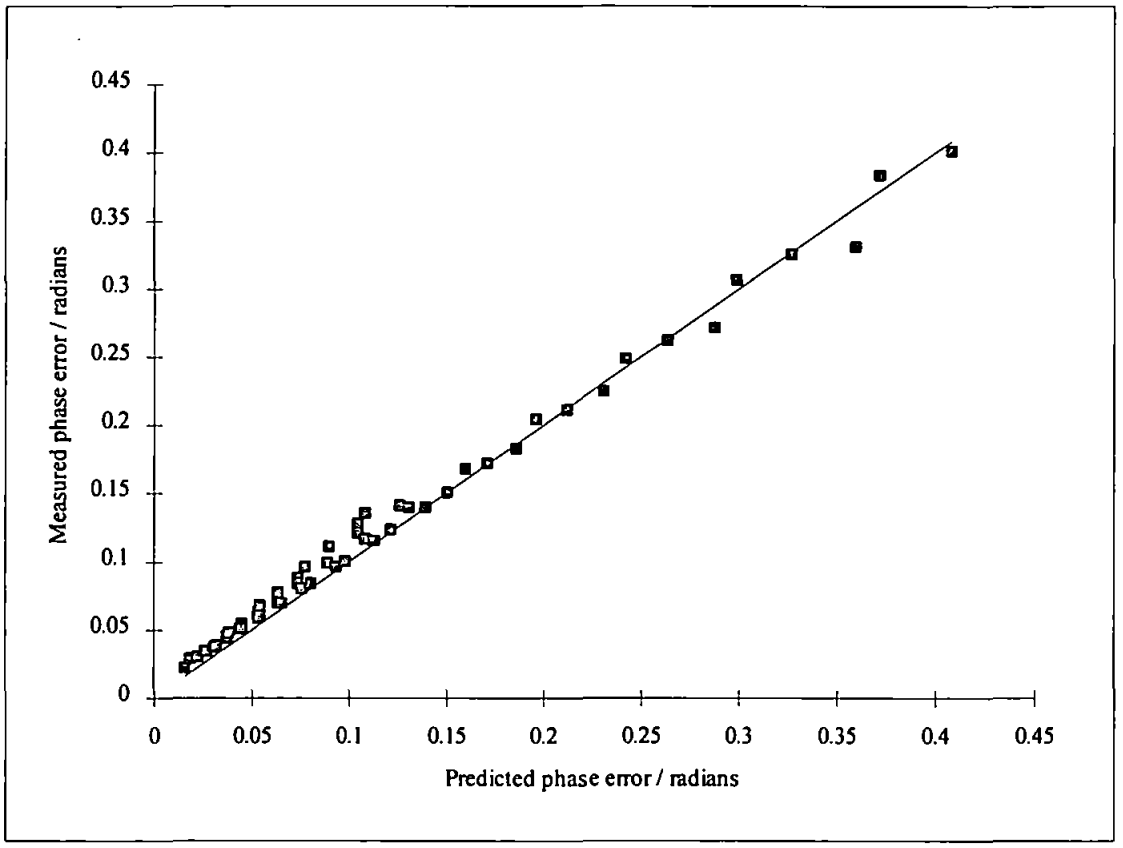

Figure 5-2. Phase errors measured in Mathcad simulation against theoretical prediction.

At very low phase errors, when the signal to noise ratio is high, rounding/quantisation errors within the Mathcad simulation will become relatively more important and the measured errors can be expected to be greater than the predicted errors, as is seen to be the case. The area of interest is where the input signal to noise ratio is relatively low and phase errors are relatively large. In this area the results of the Mathcad simulation are seen to be in excellent agreement with the theoretical prediction.

5.3 Condition for phase unwrap without error

The phase unwrap process examines the phase of each sample relative to the previous one and decides whether a wrap has occurred. If the change is more than $\pm\pi$ (e.g. from greater than $\pi/2$ to less than $-\pi/2$) then 2π is added to or subtracted from the phase of that sample and all subsequent samples. If the phase change that should occur between samples is small, then a phase difference of π caused by noise is sufficient to cause an error in the unwrap process and hence a discontinuity in the "unwrapped" phase plot. If there is a signal phase difference of $\Delta\phi_s$, then an additional phase difference of $\pi - \Delta\phi_s$ will be enough to cause an error in the unwrap process.

The phase difference between two adjacent samples due to noise is equal to the phase error in one sample minus the phase error in the other. The phase difference due to noise will be Gaussian and have variance given by

$$\sigma_\Delta^2 = 2\sigma_\phi^2 \tag{5.14}$$

The probability that the phase difference due to noise, $\Delta\phi_n$, exceeds $\pi - \Delta\phi_s$ is given by

$$P(\Delta\phi_n > \pi - \Delta\phi_s) = Q\left(\frac{\pi - \Delta\phi_s}{\sigma_\Delta}\right) = Q\left(\frac{\pi - \Delta\phi_s}{\sqrt{2\sigma_\phi^2}}\right) \tag{5.15}$$

But $2\sigma_\phi^2 = \dfrac{1}{\left(\frac{S}{N}\right)_{TDFCSD}}$ and so we have

$$P(\Delta\phi_n > \pi - \Delta\phi_s) = Q\left((\pi - \Delta\phi_s)\sqrt{\left(\frac{S}{N}\right)_{TDFCSD}}\right) \tag{5.16}$$

Now $\Delta\phi_s = 2\pi\,\Delta f\, t_d$ where t_d is the TDA and Δf is the frequency spacing between samples in the TDFCSD given by $\Delta f = \dfrac{\gamma}{T_{se}}$. Hence

$$\Delta\phi_s = \frac{2\pi\gamma\, t_d}{T_{se}} \tag{5.17}$$

There is a limit on the size of the zoom factor γ of: $\gamma \leq \dfrac{T_{se}}{4\,t_d}$ (5.18)

Hence $$\left(\pi - \Delta\phi_s\right) \geq \frac{\pi}{2} \tag{5.19}$$

If it is assumed that the SNR in the TDFCSD is greater than 13 dB, as it must be if reliable detection of the signal is to occur in the first place, then

$$\sqrt{\left(\frac{S}{N}\right)_{TDFCSD}} \geq \sqrt{20} \tag{5.20}$$

and hence

$$\left(\pi - \Delta\phi_s\right)\sqrt{\left(\frac{S}{N}\right)_{TDFCSD}} \geq \frac{\pi}{2}\sqrt{20} \tag{5.21}$$

$$Q\left(\left(\pi - \Delta\phi_s\right)\sqrt{\left(\frac{S}{N}\right)_{TDFCSD}}\right) \leq Q\left(7.02\right) \tag{5.22}$$

or $$P\left(\Delta\phi_n > \pi - \Delta\phi_s\right) \leq 10^{-12} \tag{5.23}$$

i.e. if the signal can be detected, the probability of an error in the phase unwrap process is negligible.

5.4 Error in estimation of phase slope

It has been shown (equation 5.13) that the phase error in each sample can be adequately approximated as having variance

$$\sigma_\phi^{\,2} = \frac{1}{2\left(\frac{S}{N}\right)_{TDFCSD}} = \frac{1 + 2\left(\frac{S}{N}\right)_i}{2\gamma\left(\frac{B_n}{B_s}\right)^2\left(\frac{S}{N}\right)_i^2} \tag{5.24}$$

where the phase error has Gaussian statistics. In this section we determine the effect that these errors have on the slope of the straight line fitted to the points. If the straight line is fitted, by a least mean squares approximation, to N points with coordinates (x_i, y_i) the slope, m, of the line is given by

$$m = \frac{\sum_i (x_i - \bar{x})(y_i - \bar{y})}{\sum_i (x_i - \bar{x})^2} \tag{5.25}$$

If the values x_i are assumed not to have significant errors and the values y_i have errors δy_i causing an error, δm, in m, then we have

$$\begin{aligned} m + \delta m &= \frac{\sum_i (x_i - \bar{x})(y_i + \delta y_i - \bar{y})}{\sum_i (x_i - \bar{x})^2} \\ &= \frac{\sum_i (x_i - \bar{x})(y_i - \bar{y})}{\sum_i (x_i - \bar{x})^2} + \frac{\sum_i (x_i - \bar{x})\,\delta y_i}{\sum_i (x_i - \bar{x})^2} \end{aligned} \tag{5.26}$$

i.e.
$$\delta m = \frac{\sum_i (x_i - \bar{x})\,\delta y_i}{\sum_i (x_i - \bar{x})^2} \tag{5.27}$$

If δy_i are zero mean random Gaussian variables with variance σ_y^2, then δm is a zero mean random Gaussian variable with variance

$$\sigma_m^2 = \frac{\sum_i (x_i - \bar{x})^2\ \sigma_{y_i}^2}{\left(\sum_i (x_i - \bar{x})^2\right)^2} \tag{5.28}$$

$$\sigma_m^2 = \frac{\sigma_{y_i}^2}{\sum_i (x_i - \bar{x})^2} \tag{5.29}$$

In this application, the x axis is the frequency axis and the y axis represents phase. σ_y is the standard deviation of the phase errors.

Now, if the number of points, N, is odd

$$\sum_{i=0}^{N-1}(x_i-\bar{x})^2 = 2\sum_{i=1}^{\frac{N-1}{2}}(i\,\Delta f)^2 \qquad \text{where} \quad \Delta f = x_{i+1}-x_i$$

$$= 2\Delta f^2 \sum_{i=1}^{\frac{N-1}{2}} i^2$$

$$= 2\Delta f^2 \frac{\left(\frac{N-1}{2}\right)}{6}\left(\frac{N-1}{2}+1\right)\left(2\left(\frac{N-1}{2}\right)+1\right) \qquad (5.30)$$

$$= \frac{\Delta f^2}{12} N\left(N^2-1\right) \approx \frac{\Delta f^2 N^3}{12} \qquad \text{for large N}$$

The same result is obtained for even N. Hence, for N > 10, we have

$$\sigma_m^2 = \frac{12\,\sigma_\phi^2}{\Delta f^2 N^3} \qquad (5.31)$$

The number of points used, $$N = \frac{B_s}{\Delta f} \qquad (5.32)$$

where B_s is the signal bandwidth as estimated from the magnitude of the TDFCSD. Δf, the separation between samples on the frequency axis is given by

$$\Delta f = \frac{\gamma}{T_{se}} \qquad (5.33)$$

and hence we obtain $$\sigma_m^2 = \frac{12\,\gamma}{B_s^3\,T_{se}}\sigma_\phi^2 \qquad (5.34)$$

Substituting for σ_ϕ^2 from equation 5.13 gives, after simplification

$$\sigma_m^2 = \frac{6\left(1 + 2\frac{S_i}{\eta_e B_n}\right)}{B_s T_{se}\left(\frac{S_i}{\eta_e}\right)^2} \tag{5.35}$$

5.5 Accuracy of direction finding

Since $m = 2\pi t_d$ where t_d is the TDA, and from equation 5.2 we have

$$\sigma_\theta^2 = \frac{c^2 \sigma_{t_d}^2}{d^2 \cos^2\theta} \tag{5.36}$$

we obtain the variance in the AOA estimation as

$$\sigma_\theta^2 = \frac{3c^2\left(1 + 2\frac{S_i}{\eta_e B_n}\right)}{2\pi^2 d^2 \cos^2\theta \; B_s T_{se}\left(\frac{S_i}{\eta_e}\right)^2} \tag{5.37}$$

For small inputs SNR, where $2\frac{S_i}{\eta_e B_n} << 1$, this simplifies to

$$\sigma_\theta^2 = \frac{3c^2 \eta_e^2}{2\pi^2 d^2 \cos^2\theta \; B_s T_{se} \; S_i^2} \tag{5.38}$$

For $d = 1$ m and $\theta = 0$ (broadside), this can be simplified to give

$$\sigma_\theta = \sqrt{\frac{3}{2 B_s T_{se}}}\left(\frac{c \eta_e}{\pi S_i}\right) \tag{5.39}$$

This error in AOA estimation is plotted against receiver input signal power in figures 5-3 and 5-4. In figure 5-3 the signal bandwidth is kept constant and the effect of varying the ESM integration time is shown, in figure 5-4 the ESM integration time is kept constant and the effect of varying the signal bandwidth is shown. In both figures the points where the plots go vertical as input signal power decreases indicate the sensitivity of the system. For input signal powers below the sensitivity reliable detection cannot be achieved by a threshold detector applied to the magnitude of the TDFCSD, and hence the information

necessary to select the correct part of the TDFCSD for phase slope estimation is not available. All parameter values not explicitly stated here and for the remainder of this section are as given in table 4-1. Values of error in AOA estimation for antenna spacings, d, other than one metre and non zero AOA can be obtained simply by dividing the values plotted by $d \cos \theta$.

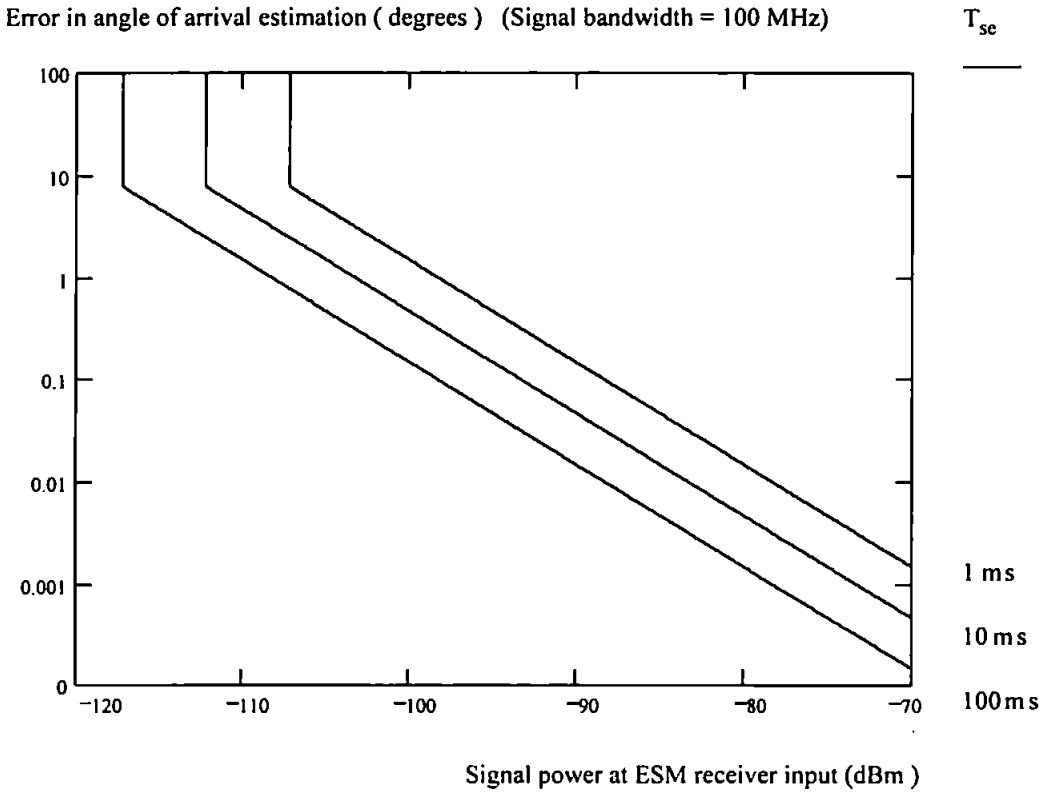

Figure 5-3. AOA estimation error as a function of ESM receiver input signal power for a fixed signal bandwidth of 100 MHz and different ESM integration times. Parameter values not explicitly stated here are as in table 4-1. (The points where the plots go vertical as input signal power decreases indicate the sensitivity of the system. For input signal powers below the sensitivity reliable detection cannot be achieved by a threshold detector applied to the magnitude of the TDFCSD, and hence the information necessary to select the correct part of the TDFCSD for phase slope estimation is not available.)

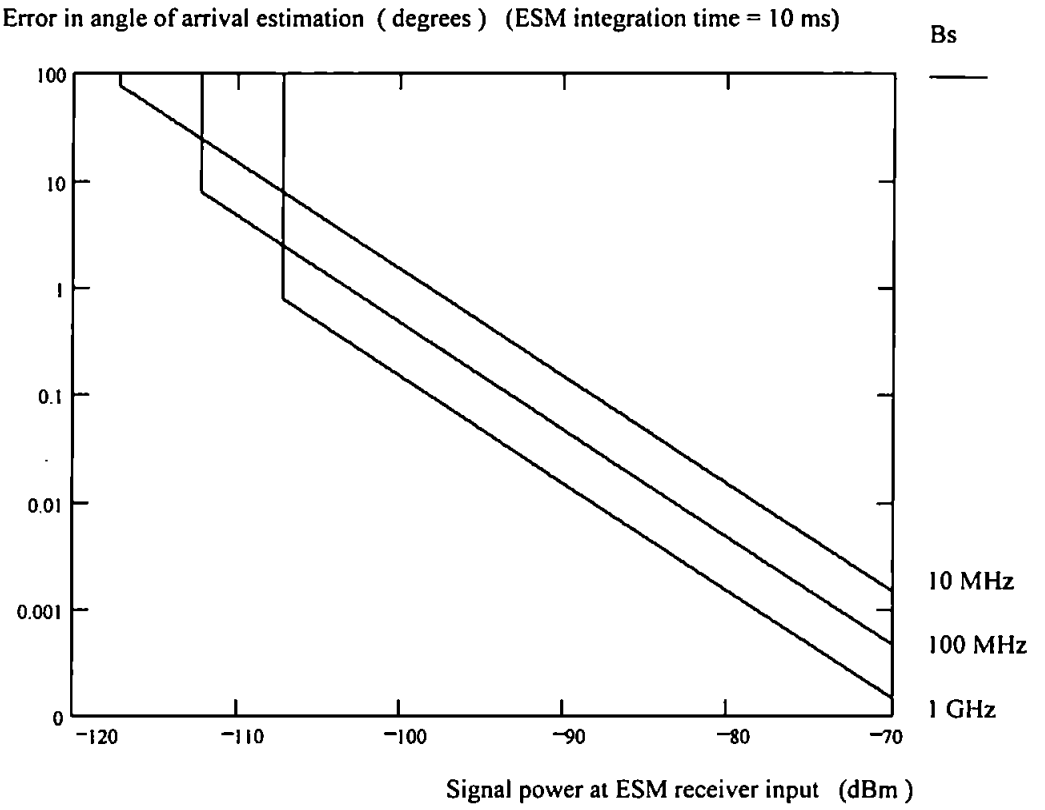

Figure 5-4. AOA estimation error as a function of ESM receiver input signal power for a fixed ESM integration time of 10 ms and different signal bandwidths. Parameter values not explicitly stated here are as in table 4-1.

Combining equation 5.39 with equation 4.8, which gives the ESM system input signal power from a power managed CW LPI radar, gives us an expression for the AOA estimation error as a function of the distance such a radar is from the ESM platform.

$$\sigma_\theta = \sqrt{\frac{3}{2\,B_s\,T_{se}}}\left(\frac{c\,\sigma\,G_r\,T_{sr}}{2\,\pi^2\,G_e\,SNR_{thrad}\,R_r^2}\right) \qquad (5.40)$$

This AOA estimation error is plotted as a function of range of radar from ESM platform in figures 5-5 to 5-8. Figures 5-5 and 5-6 show the effects of varying the ESM integration time and varying the signal bandwidth respectively, for a fixed radar integration time of 1 ms. The effect shown by figure 5-6 represents something of a dilemma for the radar designer. Increasing the signal bandwidth does reduce the probability of intercept, as is well known, but it does make direction finding on the signal significantly more accurate, once the signal has been detected.

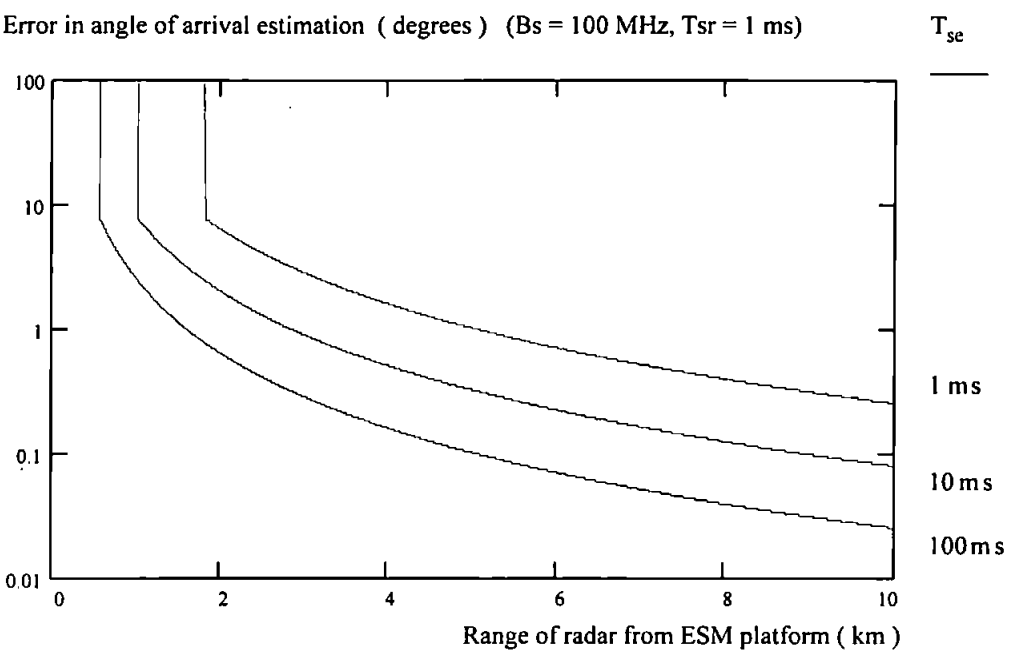

Figure 5-5. AOA estimation error as a function of range of radar from ESM platform, against a power managed CW LPI radar with a radar integration time of 1 ms and fixed signal bandwidth 100 MHz, for different ESM integration times. Parameter values not explicitly stated here are as in table 4-1.

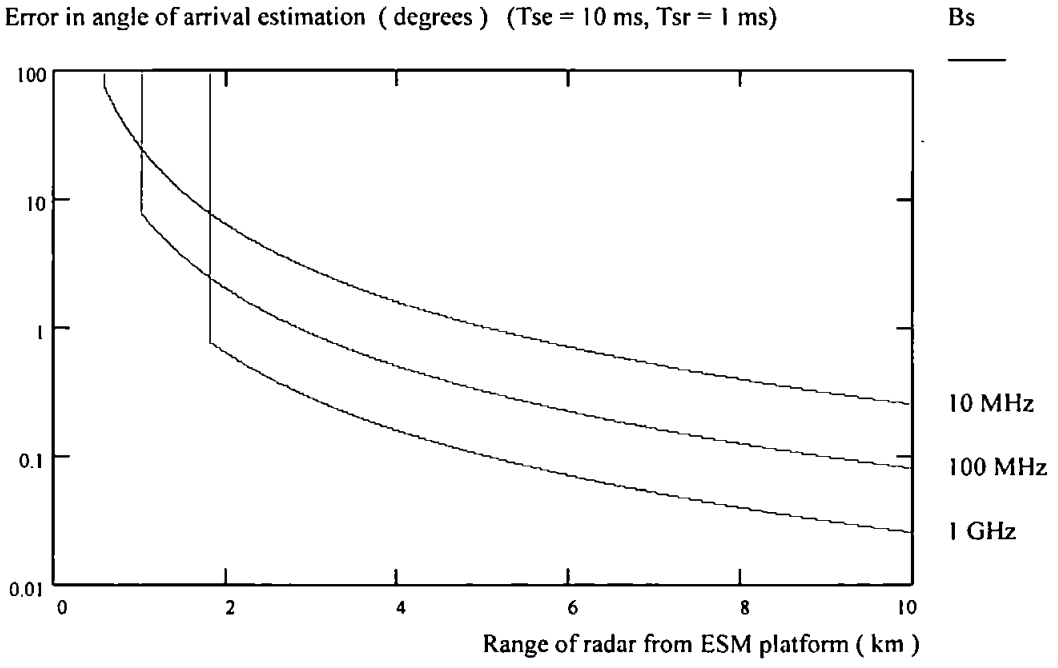

Figure 5-6. AOA estimation error as a function of range of radar from ESM platform, against a power managed CW LPI radar with a radar integration time of 1 ms for a fixed ESM integration time of 10 ms and different radar signal bandwidths. Parameter values not explicitly stated here are as in table 4-1.

Figures 5-7 and 5-8 are simply repeats of 5-5 and 5-6, but with a longer radar integration time of 10 ms. Comparison of figures 5-7 and 5-8 with figures 5-5 and 5-6 very clearly shows the impact of increasing the radar integration time, both in increasing the all important minimum ESM detection range and in increasing the AOA estimation error.

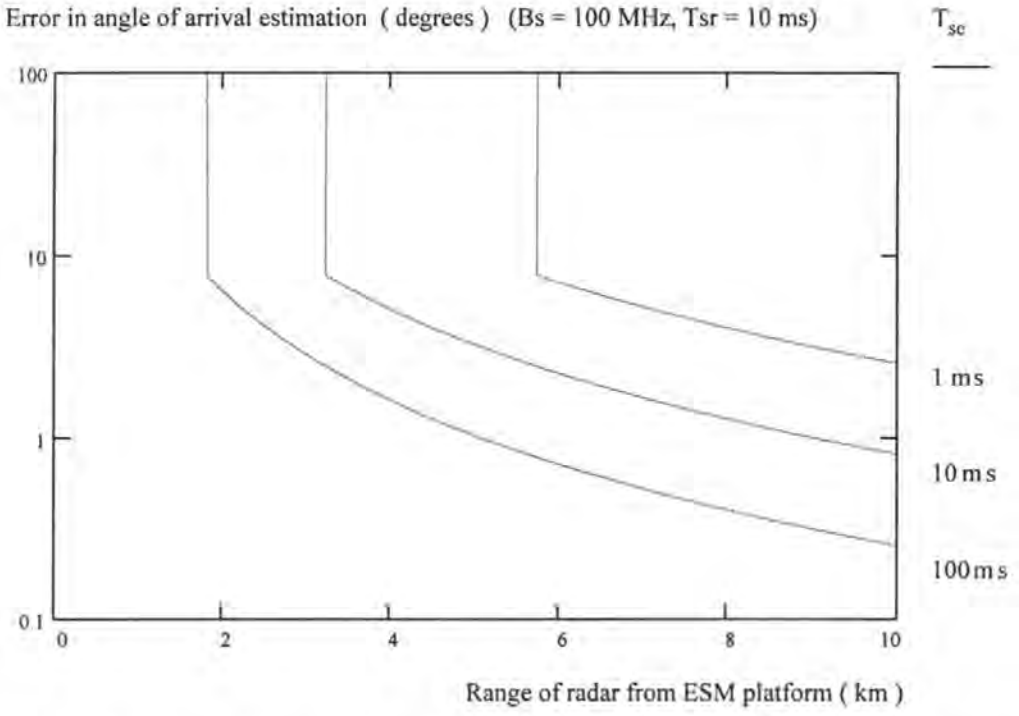

Figure 5-7. AOA estimation error as a function of range of radar from ESM platform, against a power managed CW LPI radar with a radar integration time of 10 ms and fixed signal bandwidth 100 MHz, for different ESM integration times. Parameter values not explicitly stated here are as in table 4-1.

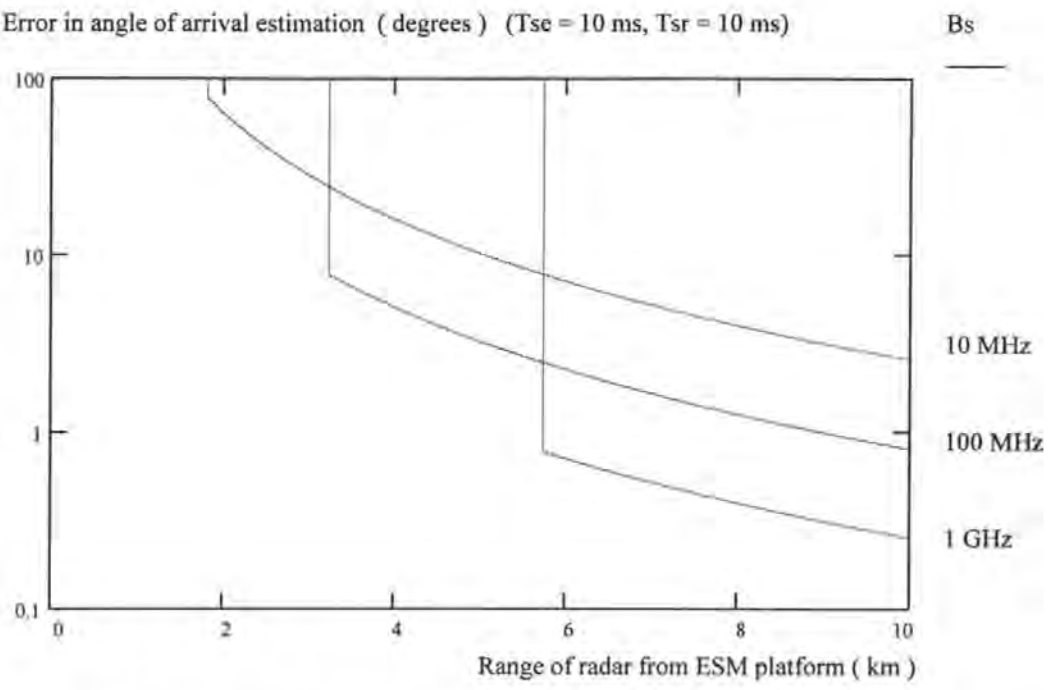

Figure 5-8. AOA estimation error as a function of range of radar from ESM platform, against a power managed CW LPI radar with a radar integration time of 10 ms for a fixed ESM integration time of 10 ms and different radar signal bandwidths. Parameter values not explicitly stated here are as in table 4-1.

5.6 Simulation

The Mathcad simulation, described in sections 2.6 and 3.5 and shown in full in appendix A, includes estimation of the phase slope of the TDFCSD. Results are shown here for the following input parameters

T_s	B_n	B_s	SNR_i
500 μs	100 MHz	20 MHz	-15 B

Threshold detection applied to the magnitude of the TDFCSD (see figure 3.10) tells us that the portion that should have a straight line fitted to its phase terms lies between 50 and 70 MHz. The phase terms for the whole receiver bandwidth are shown in figure 5-9. With a sample time of 500 μs, the frequency separation between elements in the unfiltered CSD is 2 kHz. However, after time domain filtering with a "zoom factor" of 2048, the frequency separation between elements in the TDFCSD is 4.096 MHz. This means that there will only be 5 data points in the TDFCSD within the signal bandwidth of 20 MHz. Figure 5-9

shows that the phase terms of the TDFCSD lie approximately on a straight line within the signal bandwidth while being more random elsewhere. Figure 5-10 shows just the phase terms lying within the signal bandwidth, enabling a closer view of how well the terms fit a straight line.

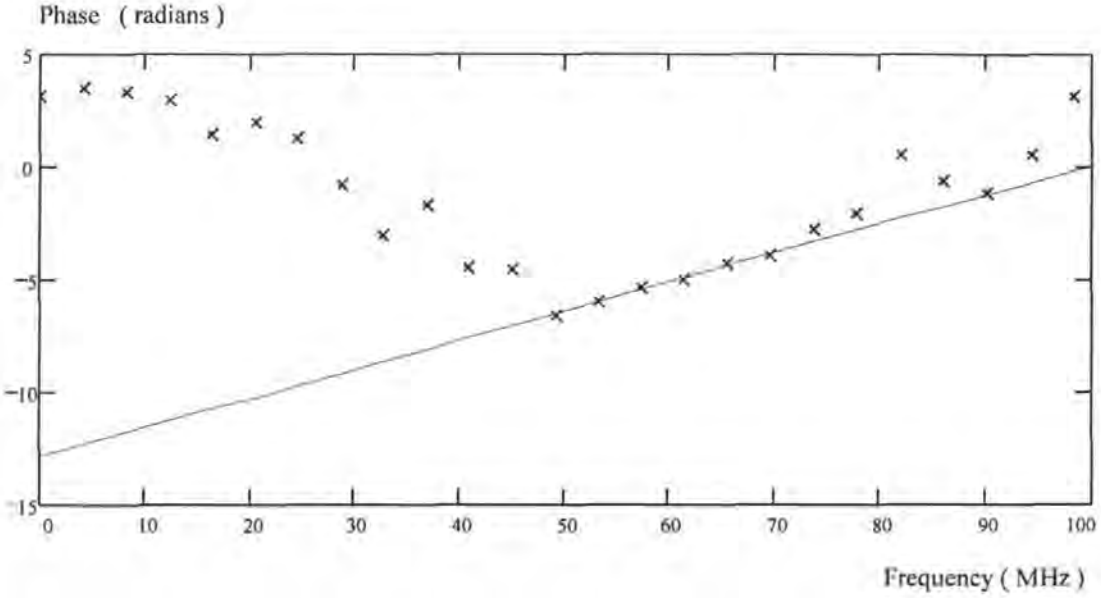

Figure 5-9. Phase terms for whole receiver bandwidth, showing straight line fitted to terms within signal bandwidth

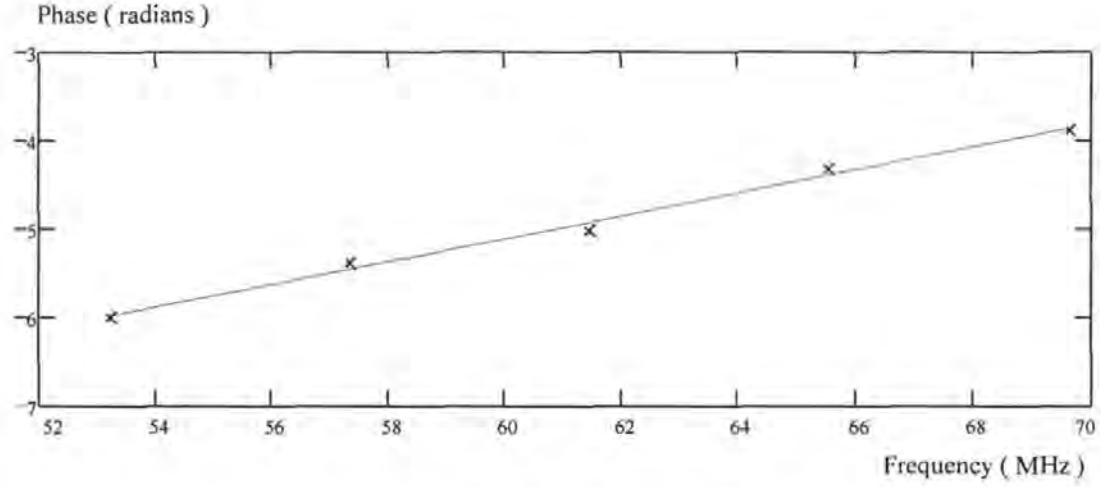

Figure 5-10. Phase terms for just the signal bandwidth, showing fitting of straight line.

The fitting of a straight line to the phase terms shown in figure 5-10 gives a phase slope of 0.1295 radians MHz^{-1}, corresponding to a time delay of 20.61 ns (see appendix A for full details). The time delay between the original signal inputs was 20 ns, corresponding to an

AOA of 36.9 degrees for a 10 m antenna separation. The error in TDA estimation is therefore 0.61 ns. The AOA estimation is 38.19 degrees - an error of 1.32 degrees which is well within the AOA estimation standard deviation error of 3.14 degrees given by equation 5.38.

5.7 Separation of multiple sources

This thesis concentrates on the detection and direction finding of a single spread spectrum signal source. It would obviously be useful to be able to detect and direction find on a number of sources simultaneously. There are two ways of separating multiple signals. If a large enough antenna separation can be used then, rather than extracting just one small central section of the ccf, a number of small contiguous, or even overlapping, sections can be extracted, each one corresponding to an arc of the antenna pair's field of view. Signals detected in different sections of the ccf will then be identified as separate and subsequent TDFCSD phase slope measurement will provide a finer estimate of AOA within the corresponding arc. A land based system with a large baseline (maybe of the order of km) could obviously detect and direction find on a large number of sources simultaneously. Achieving the required baseline for this on a mobile platform is unlikely to be feasible. Even if signals cannot be separated in the time domain, however, it may still be possible to separate them in the frequency domain, provided that they do not overlap in frequency. If the signals do not overlap in frequency, they can be identified as different blocks in the magnitude of the TDFCSD, and as giving different slopes in the phase of the TDFCSD. This is demonstrated in the Mathcad simulation in appendix C. The simulation in appendix C considers two simultaneous low power FMCW signals, chirping up from 15 to 35 MHz and from 60 to 70 MHz in 50 μs, and a high power 1 μs interfering pulse at 30 MHz. The receiver bandwidth is 80 MHz and the input SNRs are -7 dB and -10 dB for the FMCW signals and +30 dB for the interfering pulse. The pulse is detected by a crystal video system and its frequency obtained by FFT analysis. A notch filter is then programmed and applied to the input signals for the duration of the pulse. After clipping at three times the noise standard deviation to eliminate the remaining "rabbit's ears"[1], the large pulse has

[1] "Rabbit's ears" are remnants of the pulse occurring at either end where the sharp leading and trailing edges of the pulse lead to brief periods when the spectrum is spread outside the range of the notch filter. The

been effectively removed. Cross correlation and time domain filtering then continue as normal to produce the TDFCSD whose magnitude and phase terms are shown in figures 5-11 and 5-12. It is quite clearly possible to identify the two signals, to determine their spectra and to direction find on them independently and simultaneously. Predicting the accuracy of this direction finding is clearly more complicated than for single sources. There is obvoiously considerable scope for further work in the investigation of system performance for multiple signals.

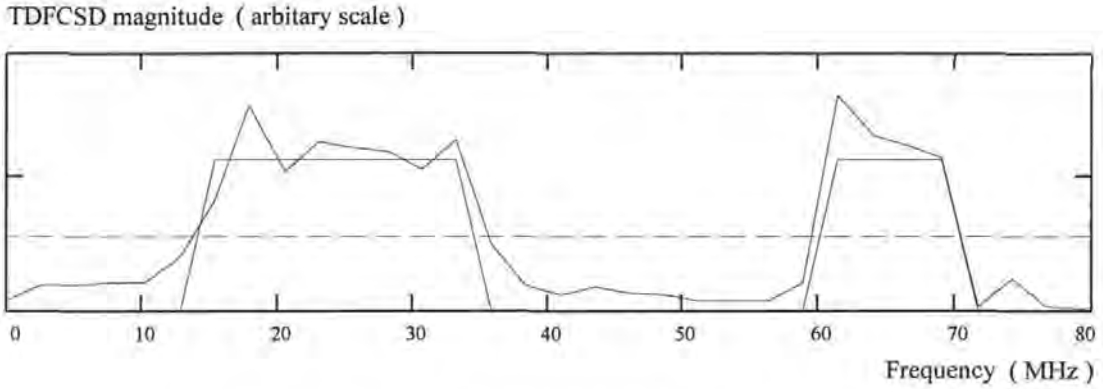

Figure 5-11. Magnitude of TDFCSD for two simultaneous FMCW signals.

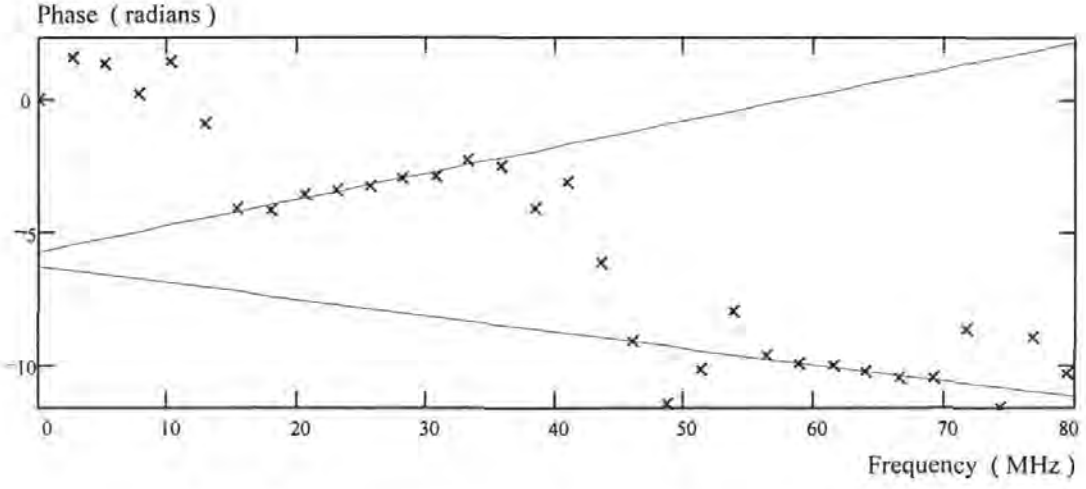

Figure 5-12. Phase of TDFCSD for two simultaneous FMCW signals

notch filter cannot filter out all the pulse energy at the start and finish of the pulse, and so two short pulses of energy are left which look, in the time domain, a little like a rabbit's ears.

6. Implementation using acousto-optic correlators

6.1 Introduction

To sample the signals from the two receivers and perform the necessary cross correlations digitally in real time may not be feasible, especially if we wish to design a system with large channel bandwidths and long sample lengths. For example: a channel bandwidth of 1 GHz and a sample length of 50 μs would require analogue to digital conversion at a sampling frequency of 2 GHz and data sets of 50,000 points. Acousto-optic correlators may provide the answer to the problem of forming the initial cross correlation function. The fact that we then only want to sample a relatively small centre portion of the cross correlation function is then very convenient since this means that the number of data points we have to extract for further processing is very much reduced. One commonly quoted disadvantage of acousto-optic signal processing systems is that they have a limited dynamic range. This need not be a problem here. Since we are looking for signals below the noise level, the system would be set up with RF and IF gains such that the standard deviation of the noise is approximately one third of the amplitude range of the correlator inputs. Short high power pulses will be severely clipped. This goes some way towards eliminating the non LPI pulses that would be detected by a conventional system, although they would of course be better excluded by the use of notch filters to block known signals as demonstrated in appendix D. There are three main types of acousto-optic correlator: space integrating, time integrating and joint transform.

6.2 Space integrating correlation

There are many forms of space integrating correlator, producing the correlation function as a time domain signal from a single photodetector which spatially integrates all the light diffracted by an acousto-optic cell. Some do not produce a true correlation function. Rather than producing the true ccf of the form

$$\int_{-\infty}^{+\infty} s_1(t-\tau)\, s_2(t+\tau)\, dt \tag{6.1}$$

they produce functions of the form

$$\int_{-\infty}^{+\infty} \left| s_1(t-\tau)\, s_2(t+\tau) \right|^2 dt \quad \text{or} \quad \left| \int_{-\infty}^{+\infty} s_1(t-\tau)\, s_2(t+\tau)\, dt \right|^2 \tag{6.2}$$

This is useful if we are simply looking for a correlation peak in the time domain, but useless if we wish to form the CSD, since all the phase information is lost. Heterodyning correlators which produce the true correlation function are described by Rhodes[9], but these are more complicated in both their optical architecture and the processing required to extract the correlation function from the photodetector output. Non heterodyning correlators which also produce the true correlation function employing a simpler optical architecture have been built at RNEC[10, 20]. Unfortunately, space-integrating correlators still suffer from a number of disadvantages. One of the signal inputs must be time reversed. This requires that the input signals be broken up into frames and cross correlated one frame at a time. The time reversal can be done, either by the use of digital RF memory or by an analogue technique, involving mixing with a chirp signal and using dispersive delay lines, known as "Stretch"[21], but any such time reversal introduces an additional time delay into the system and adds considerably to the complexity of the system. Another problem is that as the input signal bandwidth is increased the angular spread of the diffracted light from the acousto-optic cell increases. The photodetector is normally positioned in the Fourier transform plane of an acousto-optic cell. As the signal bandwidth increases then the active area required of the photodetector increases. However, as the bandwidth increases the speed at which the photodetector must be able to respond increases, requiring that the active area of the photodetector be made smaller to reduce the junction capacitance (assuming the detector is a photodiode). These two requirements are clearly incompatible. It may be possible to extend the bandwidths at which a space-integrating correlator can be used up to a useful value by the use of imaging optics to focus the required diffracted light onto a small active area photodiode, but even if diffraction limits do not make this totally impossible the cost, size and complexity of the system make it very impractical.

The work discussed in this thesis started with the zeroth order space-integrating correlator. Subsequent work, on the application of cross correlation receivers to the detection

of spread sectrum signals, led in another direction. Considerable work was carried out, however, leading to a unified general theory of space-integrating correlators. This general theory succesfully explains the operation of some new architectures as well as those already described in the literature. This work is presented in the next two chapters.

6.3 Time-integrating correlation

The time-integrating correlator seems to be ideally suited to use in a cross correlation receiver. Both input signals can be inserted without reversal, a true correlation can be extracted and very long integration times are possible. The time-integrating correlator due to Sprague and Koliopoulos [19], shown in figure 6-1, is described by Vanderlugt [22]

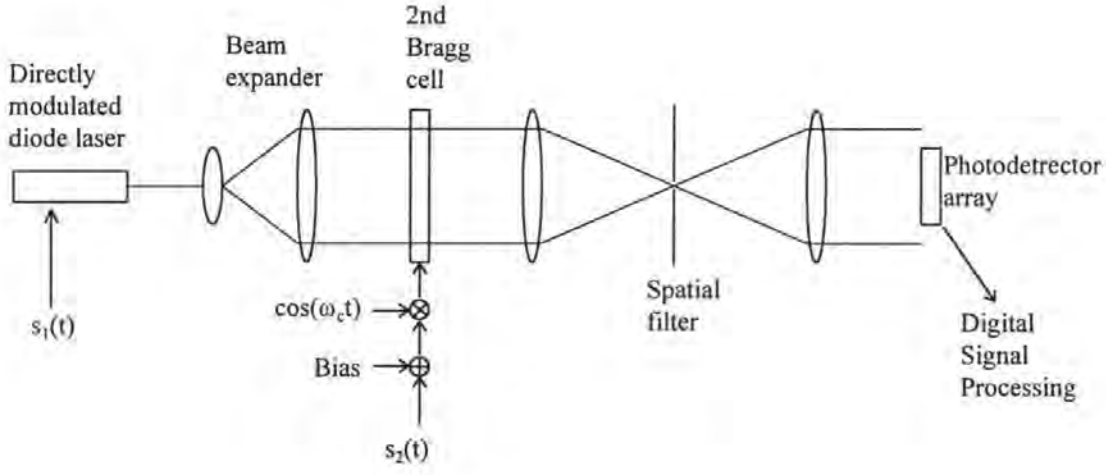

Figure 6-1. Time-integrating correlator.

VanderLugt shows that the time-integrated light intensity at the plane of the photodetector array contains a spatially invariant term which is proportional to the integration time and the cross correlation function of the two input signals imposed as double sideband suppressed carrier modulation of a spatial carrier. This correlator gives itself ideally to the required process of windowing the centre portion of the cross correlation function. The spatial dimensions of the cross correlation function are controlled by adjustment of the imaging optics so that the required centre portion falls on to the photodetector array. The spatial function is then sampled by the array and all further processing performed digitally, including demodulating the spatial signal to recover the correlation function from the carrier. This is a

particularly elegant system in that it combines and makes the best use of both optical and digital signal processing techniques. It takes advantage of the speed of optical signal processing for the correlation and the flexibility of digital signal processing once the sets of data points has been reduced to manageable numbers. Since this time-integrating correlator, and a variant known as the electronic reference correlator can perform the required signal processing, it is discussed in detail in chapter 9. A demonstrator correlator has been built using a Fairchild 2048 element CCD linescan camera controlled by, and delivering its data to, a TMS320C30 based framegrabber and digital signal processing board mounted in a host PC. Results from experiments with this correlator are presented in chapter 10.

6.4 Joint transform correlation

The joint transform correlator, which combines space-integrating and time-integrating attributes, does not suffer from the main drawbacks of either. Time-integrating correlators do not require time reversal of signals but they suffer from unwanted bias terms which tend to saturate the detector array and limit integration time. For the joint transform correlator no time reversal is required and unwanted terms are easily separated from the required correlation. A schematic diagram of the system is shown in figure 6-2. [23, 24]

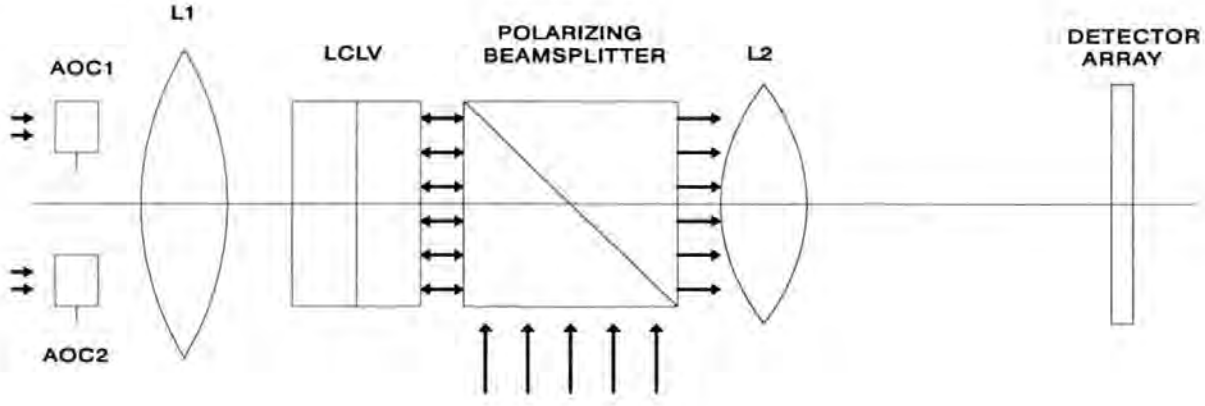

Figure 6-2. Schematic diagram of a joint transform correlator. AOC = Acousto-optic cell, L = Lens, LCLV = Liquid Crystal Light Valve (Spatial Light Modulator)

This is a standard joint transform correlator in which the inputs are provided by the first order diffracted light from two identical acousto-optic cells. The lenses and spatial filters

required to extract the first order light from the cells have been omitted in order to keep the diagram simple and concentrate on the features specific to this correlator. The input function for a joint transform correlator, with two input acousto-optic cells separated by a distance 2a, is of the form

$$o(x,t) \;=\; s_1(x-a-Vt) \;+\; s_2(x+a-Vt) \tag{6.3}$$

where V is the acoustic velocity in the cells. It is straightforward to show that if, at any given time, the Fourier transforms of $s_1(x)$ and $s_2(x)$ are written as $|S_1(u)|\exp\{j\phi_1(u)\}$ and $|S_2(u)|\exp\{j\phi_2(u)\}$ respectively then the response of the square law detector of the spatial light modulator (liquid crystal light valve) will be

$$|O(u)|^2 \;=\; |S_1(u)|^2 + |S_2(u)|^2 + |S_1(u)|\cdot|S_2(u)|\cos\{2ua + \phi_1(u) - \phi_2(u)\} \tag{6.4}$$

The final term in equation 6.4 represents a set of sinusoidal fringes of spatial frequency 2a, amplitude modulated by the amplitude of the cross spectral density of $s_1(x)$ and $s_2(x)$ and phase modulated by the phase of the cross spectral density. The Fourier transform of this function is formed by lens L2 and contains the required cross correlation function spatially shifted by an amount corresponding to the spatial frequency of the final term in equation 6.4, which in turn depends purely on the spatial separation of the input acousto-optic cells plus any relative time shift. The only other component is the sum of the autocorrelation functions of the input signals which are not spatially shifted. The fact that the cross correlation function is spatially shifted, whereas the autocorrelation functions are not makes it very easy to extract by straightforward spatial filtering. The photodetector array is a square law device and hence the output of this correlator is the square of the cross correlation function. The advantages of this correlator are that it requires no time reversal of the input signals, can use long integration times and the output cross correlation function is not cluttered by other terms. There are two significant disadvantages. The joint transform correlator is more complex and expensive than the time-integrating correlator. Secondly, and more importantly, since the output is the **square** of the cross correlation function the phase information, crucial for accurate direction finding, is lost. In view of these disadvantages and the promise offered by the time-integrating correlator, the joint transform correlator will not be considered further.

7. The acousto-optic interaction

7.1 Introduction

The central component of acousto-optic signal processing systems is the acousto-optic cell, sometimes referred to as a Bragg cell. A piezoelectric transducer is used to convert an electronic signal into an acoustic one and launch it as a bulk or surface wave into a crystal, typically of lead molybdate, tellurium dioxide, lithium niobate or gallium phosphide. A collimated light beam illuminates the acousto-optic cell as shown in figure 7-1.

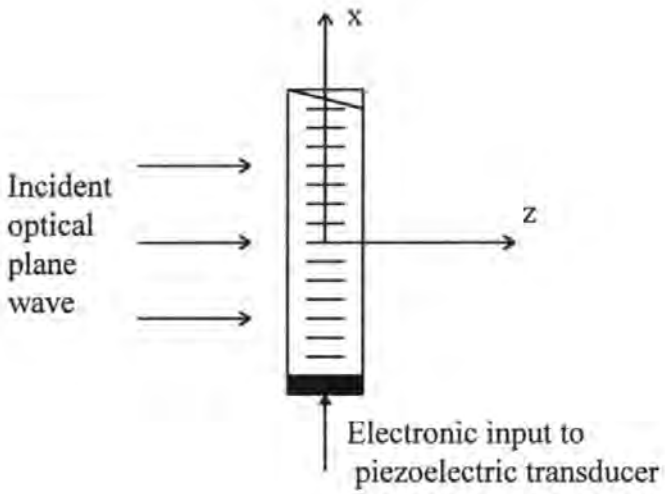

Figure 7-1. Acousto-optic cell showing directions of optic and acoustic waves

The acousto-optic interaction has been the subject of an enormous amount of investigation, both experimental and theoretical. Early work considered the acousto-optic interaction in fluids and started in 1921 with Brillouin's theoretical description of what is generally referred to as the Bragg mode of interaction [25, 26]. In 1932 Debye and Sears tested Brillouin's predictions and discovered that diffraction occurs under wider conditions than the strict Bragg condition, and observed higher diffraction orders, but were unable to give a satisfactory explanation. In 1935/36 Raman and Nath published a series of papers based initially on considering the acoustic wave as a thin non-moving phase grating

[27,28,29,30,31]. Many further papers [25] have analysed the acousto-optic interaction in more detail, clarifying the distinction between the Raman-Nath and Bragg modes of interaction, and developing techniques for the analysis of the general case which is neither. In spite of the more detailed descriptions available, most descriptions of acousto-optic correlators start by considering operation of the acousto-optic cell in either the Raman-Nath or the Bragg mode. In general, the assumption of Raman -Nath operation is particularly suspect, but the approximation is a very useful one in that it does enable a very good qualitative prediction of correlator operation, and will usually enable an approximate prediction of output signal levels. Unfortunately, some papers approximate the Raman-Nath mode (an approximation of an approximation!) to a point that does not even lead to a qualitative description of some correlator architectures [9, 32]. The mathematical treatment involves an approximation leading to the assumption that the zeroth diffraction order contains no information. This suggests that the zeroth order cannot be used in creating a correlator.

After an explanation of the difference between Raman-Nath and Bragg diffraction, this chapter develops the equations for Raman-Nath diffraction from first principles. The purpose of this is to provide a clear description of the fine structure of the diffraction orders. When the input to the acousto-optic cell is a modulated carrier even the zeroth order has sub-orders that carry information and can be used in a correlator. After the development of this theory it will be possible to develop a general unified theory of space integrating correlators, and in particular to explain the operation of the zeroth order correlator described by Houghton and Reeve [14]

7.2 Bragg diffraction

There are two fundamental differences between pure Raman-Nath and pure Bragg diffraction. Pure Raman-Nath diffraction requires that the directions of propagation of the optical wave is normal to the axis of the acousto-optic cell and that $Q \ll 1$. (The value Q will be discussed in more detail below.) For pure Bragg diffraction, the light must be incident on the cell at the "Bragg angle", typically one or two degrees from normal, and $Q \gg 1$. Bragg diffraction is, as the name suggests, much the same as used in X-ray crystallography and can be analysed in a number of ways. A simple geometric argument, treating wavefronts as

reflecting surfaces and considering interference between reflections in sufficient to calculate the Bragg angle, but does not account for the doppler shift observed in the diffracted light. A common approach, used by many authors (see e.g. Vanderlugt [11], page 292) is to consider the diffraction as being caused by a photon-phonon interaction as shown in figure 7-2.

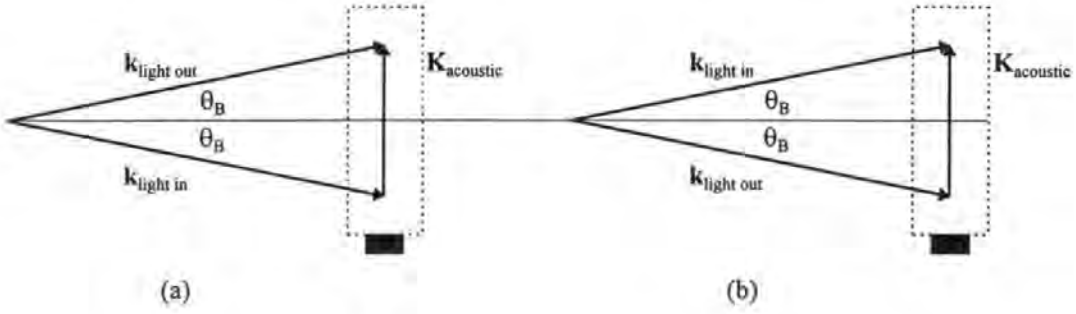

Figure 7-2. Bragg diffraction: (a) upshift mode and (b) downshift mode

If we note that the energy of a photon or phonon is given by $\hbar\omega$, and apply energy conservation to the interaction, we have, for the upshift and downshift modes shown in figure 7-2,

$$\omega_{+1} = \omega_o + \omega_A \tag{7.1a}$$

and

$$\omega_{-1} = \omega_o - \omega_A \tag{7.1b}$$

where ω_{+1}/ω_{-1} and ω_o are the angular frequencies of the diffracted and incident photons and ω_A is the angular frequency of the phonon. Equations 7.1a and 7.1b describe Doppler shifts, whch are important in heterodyning acousto-optic systems. Applying $\omega = c|\mathbf{k}|$ to equation 7.1a gives

$$|\mathbf{k}_{+1}| = |\mathbf{k}_o| + \frac{V_A}{c}|\mathbf{K}_A| \tag{7.2}$$

where V_A and c are the acoustic and optical velocities, $\mathbf{k}_{+1}$ and $\mathbf{k}_0$ are the wave vectors of the diffracted and incident photons and $\mathbf{K}_A$ is the wave vector of the phonon. Since $V_A << c$, we have $|\mathbf{k}_{+1}| \approx |\mathbf{k}_o|$ and the momentum diagrams in figure 7-2 can be treated as isoceles triangles. We therefore obtain the optimum illumination angle, the Bragg angle given by

$$\sin\theta_B = \frac{|\mathbf{K}|}{2|\mathbf{k}|} = \frac{\lambda}{2\Lambda} \tag{7.3}$$

where λ and Λ are the optical and acoustic wavelengths respectively. This analysis of the acousto-optic interaction is only valid if the active thickness, d, of the acousto-optic cell is large enough for the incident optical wave to be deflected sideways by at least one acoustic wavelength as it passes through. This condition is generally described in terms of the parameter Q given by [33]

$$Q = \frac{2\pi \lambda d}{n_o \Lambda^2} \tag{7.4}$$

where n_o is the refractive index of the interaction medium. Opinions as to the precise value of Q at which the Bragg and Raman-Nath regions start vary, as discussed by Klein and Cook [34]. Klein and Cook conclude that the equations describing Bragg diffraction are valid for $Q > 10$, and that equations describing Raman-Nath diffraction are valid for $Q < 0.5$.

7.3 Raman-Nath diffraction

For Raman-Nath diffraction we assume that the acousto-optic cell, carrying the acoustic wave, acts as a moving phase grating. That is, we assume that the optical path length across the cell is short enough to neglect any deviations in the direction of propagation of the light from its incident direction, and so the cell simply imposes a phase term, $\theta(x,t)$, onto the incident plane wave, $cos(kz - \omega_o t)$, where k is the wave vector of the incident light, ω_o is the angular frequency of the incident light, and x and z represent distances along the axis of the co-ordinate frame shown in figure 7-1. If a signal, $v(T-t) = v\left(\frac{W}{V} - t\right)$, where W is the length of the acousto-optic cell and V is the acoustic velocity, is applied to the piezoelectric transducer of the acousto-optic cell, this will give rise to a strain wave travelling up through the cell crystal proportional to $v(x-Vt)$, where V is the acoustic velocity. If $v(t)$ is a simple unmodulated carrier of the form $sin(\omega_c t)$, then $v(x-Vt)$ takes the form $sin(K_c x - \omega_c t)$, where K_c is the acoustic wave vector of amplitude $\frac{\omega_c}{V}$. If an optical plane wave, of the form $cos(kz - w_o t)$, is incident on this cell, then the light experiences a phase delay dependent on the refractive index and the thickness of the cell. The refractive index, n, will depend on the strength of the strain field, $S(x,t)$. For small amplitude signals we assume

that this relationship is linear (it is not linear for large signals). If we also assume that n has no z dependence we have:

$$n(x,t) = n_o + \Delta n(x,t) = n_o + const \times v(x - Vt) \tag{7.5}$$

and the phase delay

$$\theta(x,t) = \theta_o + \Delta\theta(x,t) = (n_o + \Delta n(x,t))\, k\, d \tag{7.6}$$

where d is the thickness of the acousto-optic cell. Hence we have:

$$\Delta\theta(x,t) = \beta\, v(x - V t) \tag{7.7}$$

where β is a constant that can be thought of as a modulation index.

Therefore, if the optical plane wave incident on the acousto-optic cell is described by the function $cos(kz - w_o t)$, then the optical wave leaving the acousto-optic cell on the "output" side can be expressed as

$$u(x,t) = \cos(kz - \omega_o t + \theta(x,t))\, rect\left(\frac{x}{W}\right) \tag{7.8}$$

where W is the width of the acousto-optic cell window, or, in analytic complex form, the incident plane wave can be written as

$$Re\{ e^{j(kz - \omega_o t)} \} \tag{7.9}$$

and the output wave can be described by

$$\begin{aligned} u(x,t) &= Re\{ e^{j(kz - \omega_o t)}\ e^{j\Delta\theta(x,t)} \} \\ &= Re\{ e^{j(kz - \omega_o t)}\ e^{j\beta v(x - Vt)} \} \end{aligned} \tag{7.10}$$

7.4 Derivation of diffraction orders

We now need to consider the form of $v(t)$ in more detail. The electrical signal applied to the acousto-optic cell must occupy a frequency band to which it will respond. The usual technique for placing a signal of interest onto the acousto-optic cell is to insert it as modulation of a carrier sinusoid at its centre frequency. Both amplitude and angle modulation techniques are used. We will concentrate on amplitude modulation. Under the heading of amplitude modulation we have double sideband suppressed carrier (DSBSC) modulation and double sideband large carrier (DSBLC) modulation. Rhodes [9] assumes DSBSC, and this seems to be a fairly common assumption. Work at RNEC has concentrated on the use of DSBLC. If we use DSBSC, then $v(t)$ takes the form $a(t)\sin(w_c t)$ where $a(t)$ is the modulating signal of interest. If we use DSBLC modulation, then $v(t)$ takes the form $[1 + m\,a(t)]\sin(w_c t)$ where m is the AM modulation index, and $a(t)$ is suitably normalised. In the following development $v(t)$ will be taken to be $s(t)\sin(w_c t)$ where $s(t)$ is equal to $a(t)$ for DSBSC and $[1 + m\,a(t)]$ for DSBLC. We therefore have

$$u(x,t) = Re\left\{ e^{j(kz-\omega_o t)}\, e^{j\beta s(x-Vt)\sin(K_c x-\omega_c t)} \right\} rect\left(\frac{x}{W}\right) \tag{7.11}$$

Using the Fourier series expansion, in terms of Bessel functions,

$$e^{j\zeta\sin(\xi)} = \sum_{n=-\infty}^{+\infty} J_n(\zeta)\, e^{jn\xi} \tag{7.12}$$

this expression becomes

$$u(x,t) = Re\left\{ e^{j(kz-\omega_o t)} \sum_{n=-\infty}^{\infty} J_n\big(\beta\, s(x-Vt)\big)\, e^{jn(K_c x-\omega_c t)} \right\} rect\left(\frac{x}{W}\right) \tag{7.13}$$

$$= \sum_{n=-\infty}^{\infty} J_n\big(\beta\, s(x-Vt)\big)\cos\left[(kz + nK_c x) - (\omega_o + n\omega_c)t \right] rect\left(\frac{x}{W}\right)$$

This represents a set of plane waves that can be focused into diffraction orders such that the n^{th} diffraction order has coefficient

$$J_n\left(\beta\, s(x - Vt)\right) \tag{7.14}$$

and propagates at an angle to the z direction given by

$$\phi_n = \tan^{-1}\left(\frac{nK_c}{k}\right) \tag{7.15}$$

with a Doppler shifted optical frequency given by

$$\omega_n = \omega_o + n\omega_c \tag{7.16}$$

The direction of propagation of these plane waves, that will focus into diffraction orders, are illustrated in figure 7-3. A positive diffraction order is taken as one in which the Doppler shift is positive. For an acoustic wave propagating in the negative x direction a positive diffraction order will, therefore, involve deflection in the negative x direction.

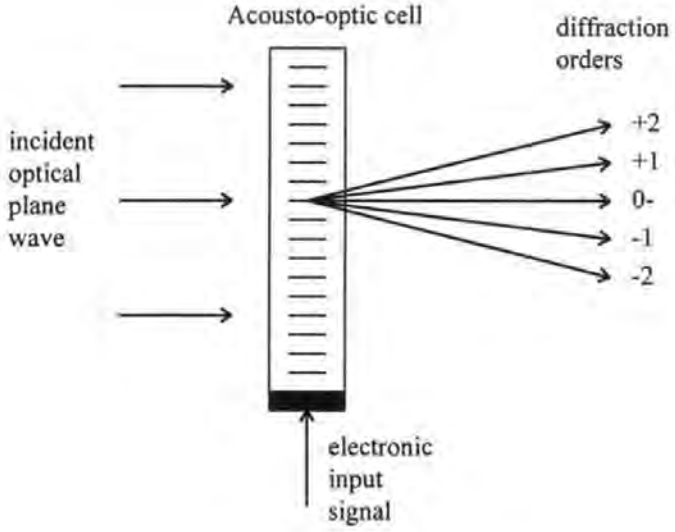

Figure 7-3. Acousto-optic cell showing directions of propagation of diffraction orders.

The approximation mentioned in the introduction is to use the expansion:

$$e^{jx} = 1 + jx - \frac{x^2}{2!} + \ldots \tag{7.17}$$

and disregard second and higher order terms. This leads to the result:

$$u(x,t) = Re\left\{ e^{j(kz-\omega_o t)}\left(1 + j\beta\, s(x-Vt)\sin(K_c x - \omega_c t)\right)\right\}$$

$$= \cos(kz - \omega_o t) \qquad (7.18)$$

$$+ \tfrac{\beta}{2} s(x-Vt)\left[\cos\left(kz + K_c x - (\omega_o + \omega_c)t\right) - \cos\left(kz - K_c x - (\omega_o - \omega_c)t\right)\right]$$

On first inspection the three terms in this expression appear to describe the zeroth, +1 and -1 diffraction orders, and the zeroth order appears to have a constant amplitude independent of $s(x-Vt)$. However, when the form of $s(x-Vt)$ is taken into account and the expression expanded further it can be seen that the true picture is not so simple and that parts of what appears to be the first diffraction orders actually make a contribution to the zeroth order. Inclusion of the second and higher order terms of the original exponential expansion will also alter the zeroth order terms. The full picture can, of course, be arrived at by writing down the full (infinite) exponential expansion and then expanding out all the terms that arise. When all the terms belonging to each diffraction order are gathered together, the result is the expansion as a series of Bessel functions used in equation 13.

7.5 Focusing of the diffraction pattern

If a lens is placed so that the acousto-optic cell lies in its front focal plane, then it can be shown that the Fourier transform of u(x,t) will be formed in its back focal plane, as shown in figure 7-4. i.e. U(x',t) in this back focal plane is given by

$$U(x',t) = \text{const} \times \int_{-\infty}^{\infty} u(x,t)\, \exp\left(-j\frac{k\,x'x}{f}\right) dx \qquad (7.19)$$

where f is the focal length of the lens and x' is the x co-ordinate in the FT (Fourier transform) plane.

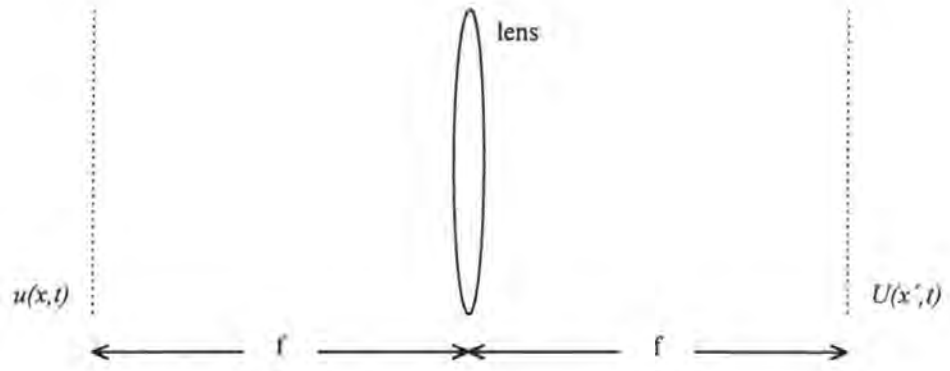

Figure 7-4. Formation of the Fourier transform by a lens

In practical terms, all the light propagating away from the acousto-optic cell at a given angle to the optic axis will be focused onto the same point in the FT plane, as shown in figure 7-5.

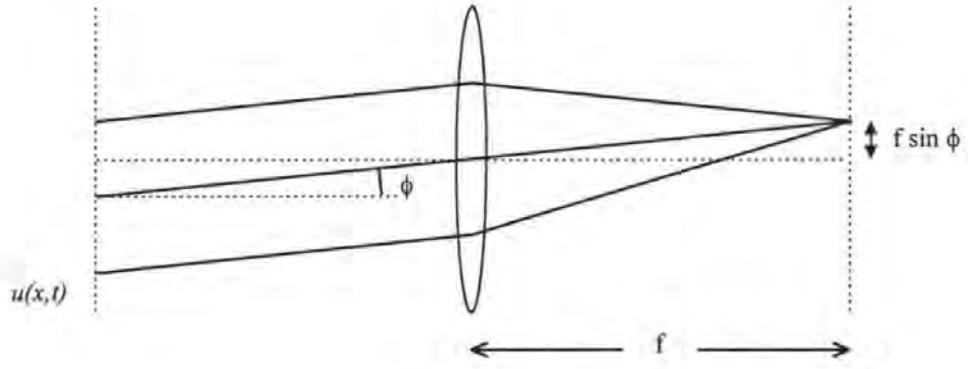

Figure 7-5. Focusing of a diffraction order in the FT plane

A plane wave with an x component k_x in its wave vector, propagating away from the acousto-optic cell at an angle to the optic axis given by

$$\phi = \frac{k_x}{k} \quad \text{for small } \phi \tag{7.20}$$

will be focused to a point in the FT plane, the position of this point being given by

$$x' = \frac{f\,k_x}{k} \quad \text{for small } \phi \tag{7.21}$$

The effect of the aperture function in u(x,t) is, of course, that the diffraction orders will not be perfect points, but have a $\mathrm{sinc}^2(x')$ type intensity profile. If we examine this in more detail we see that, because of the Gaussian profile of the original laser beam, the intensity profile is actually a $\mathrm{sinc}^2(x')$ function convolved with a Gaussian function. The important point here is that we can place a spatial filter in the FT plane to select whatever terms in *u(x,t)* we want. A second lens placed one focal length beyond this filter will transform the selected term back into the image plane. Because this whole process involves taking the Fourier transform twice, rather than the Fourier transform followed by the inverse Fourier transform, the result is a spatially reversed version of the selected component(s) of *u(x,t)*.

7.6 Fine structure of the principal diffraction orders

When the carrier injected into the acousto-optic cell is modulated, the diffraction orders have a fine structure. We can gain a feel for the form of this fine structure by considering the case of simple sinusoidal modulation. Both DSBSC and DSBLC modulation will be considered. Taking DSBSC first, the zeroth diffraction order is

$$^0u(x,t) = J_o\left(\beta a(x - Vt)\right) \cos(kz - \omega_o t)\, rect\left(\tfrac{x}{W}\right) \tag{7.22}$$

if $a(t) = \cos(w_m t)$ then this becomes

$$^0u(x,t) = J_o\left(\beta \cos(K_m x - \omega_m t)\right) \cos(kz - \omega_o t)\, rect\left(\tfrac{x}{W}\right) \tag{7.23}$$

using the approximation, valid for $\xi < 1$,

$$J_o(\xi) \approx 1 - \frac{\xi^2}{4} \tag{7.24}$$

we obtain

$$
\begin{aligned}
{}^{0}u(x,t) &= \left[\, 1 - \tfrac{\beta^2}{4}\cos^2(K_m x - \omega_m t) \,\right] \cos(kz - \omega_o t)\, rect\left(\tfrac{x}{W}\right) \\
&= \left\{ \begin{array}{l} \left(1 - \tfrac{\beta^2}{8}\right)\cos(kz - \omega_o t) \\ \\ -\ \tfrac{\beta^2}{16}\left[\, \cos\left(kz + 2K_m x - (\omega_o + 2\omega_m)t\right) \,\right] \\ \\ -\ \tfrac{\beta^2}{16}\left[\, \cos\left(kz - 2K_m x - (\omega_o - 2\omega_m)t\right) \,\right] \end{array} \right\} rect\left(\frac{x}{W}\right)
\end{aligned}
\tag{7.25}
$$

These three terms represent the 0,0, the 0,+1, and the 0,-1 diffraction sub-orders. Similarly, the first diffraction order is

$$
{}^{+1}u(x,t) = J_1\left(\beta\cos(K_m x - \omega_m t)\right)\cos(kz - \omega_o t)\, rect\left(\tfrac{x}{W}\right) \tag{7.26}
$$

which, using the approximation

$$
J_1(\xi) \approx \frac{\xi}{2} \qquad \text{for small } \xi \tag{7.27}
$$

becomes

$$
{}^{+1}u(x,t) = \tfrac{\beta}{2}\left\{ \cos\left(kz + K_m x - (\omega_o + \omega_m)t\right) + \cos\left(kz - K_m x - (\omega_o - \omega_m)t\right) \right\} rect\left(\tfrac{x}{W}\right) \tag{7.28}
$$

These two terms represent the +1,+1 and the +1,-1 diffraction sub-orders. From this we can see that, when we use DSBSC modulation, the first diffraction order will focus in the FT plane to give the Fourier transform of the modulating signal centred on the position of the first diffraction order due to the unmodulated carrier. It is worth noting that small Doppler shifts are associated with these diffraction sub-orders just as for the principle orders. If we consider DSBLC modulation, then for the zeroth diffraction order we have

$$
{}^{0}u(x,t) = J_o\left(\beta\left[1 + ma(x - Vt)\right]\right)\cos(kz - \omega_o t)\, rect\left(\tfrac{x}{W}\right) \tag{7.29}
$$

For $a(t) = cos(w_m t)$, this becomes

$$ {}^{0}u(x,t) \approx \left\{ 1 - \frac{\beta^2}{4} \left[1 + m \cos(K_m x - \omega_m t) \right]^2 \right\} \cos(kz - \omega_o t)\, rect\left(\frac{x}{W}\right) \tag{7.30} $$

$$ = \left\{ \begin{array}{l} \left(1 - \dfrac{\beta^2}{4} - \dfrac{\beta^2 m^2}{8} \right) \cos(kz - \omega_o t) \\ \\ - \dfrac{\beta^2 m}{4} \left[\cos\left(kz + K_m x - (\omega_o + \omega_m)t\right) + \cos\left(kz - K_m x - (\omega_o - \omega_m)t\right) \right] \\ \\ - \dfrac{\beta^2 m^2}{16} \left[\cos\left(kz + 2K_m x - (\omega_o + 2\omega_m)t\right) + \cos\left(kz - 2K_m x - (\omega_o - 2\omega_m)t\right) \right] \end{array} \right\} rect\left(\frac{x}{W}\right) \tag{7.31} $$

These terms represent the diffraction sub-orders $0,n$ where $n = 0, \pm 1, \pm 2$ as shown in figure 7-6.

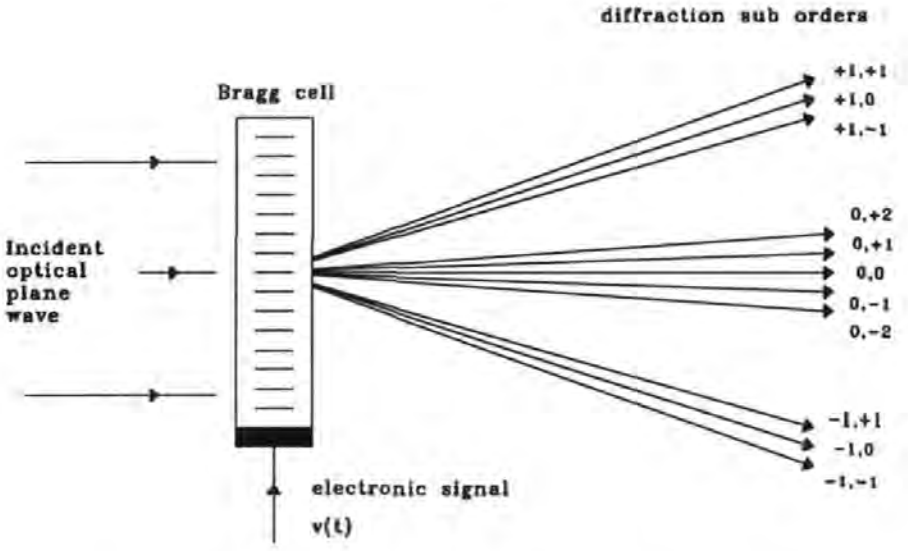

Figure 7-6. Fine structure of principal diffraction orders for sinusoidal modulation of carrier injected into acousto-optic cell.

The angle to the optic axis at which these sub-orders propagate is given by

$$ \phi_{o,n} = \tan^{-1}\left(\frac{n K_m}{k}\right) \approx \frac{n K_m}{k} \tag{7.32} $$

If we return to considering the structure of the zeroth order for a general $a(t)$, we have

$$^{0}u(x,t) = J_0\left(\beta\left[1 + ma(x - Vt)\right]\right)\cos(kz - \omega_0 t)\, rect\left(\frac{x}{W}\right)$$

(7.33)

$$= \left\{\left(1 + \frac{\beta^2}{4}\right) - \frac{\beta^2 m}{2}\, a(x - Vt) - \frac{\beta^2 m^2}{4}\, a^2(x - Vt)\right\}\cos(kz - \omega_0 t)\, rect\left(\frac{x}{W}\right)$$

and we can see that the zeroth order contains three significant terms that can be spatially separated provided *a(t)* contains no zero frequency component and has a frequency spectrum extending over less than one octave. (The $a^2(x-Vt)$ term gives rise to dc and double frequency components.) If these conditions are satisfied, then a spatial filter in the *FT* plane can, in principal, isolate the Fourier transform of *a(t)*. The ability of the spatial filter to isolate this term in any real system is limited by the spatial spreading in the Fourier transform plane caused by spatial windowing at the acousto-optic cell.

7.7 Experimental evidence

To test the predictions of the preceding sections an experiment was carried out to demonstrate that the power spectral density of a chirp pulse can be formed in the 0,+1 diffraction order. The experimental set-up is shown in figure 7-7. A chirp pulse was generated using an Analogic D2045 polynomial waveform synthesiser. This was then used to apply double sideband large carrier modulation to a 45 MHz carrier in an Isomet acousto-optic modulator driver (model no. 231A-1-45). Modulation depth can be set using gain and bias adjustments on the modulator module or by altering the programming of the D2045. Using the D2045 to set the modulation depth gives more accurate and consistent results. This modulated signal was then applied to an Isomet OPT1 TeO_2 acousto-optic cell. The input signal power was approximately 0.5 W. A lens, placed one focal length from the a-o cell was then used to focus the diffraction pattern onto a K series Reticon 256 element photodiode array placed in the focal plane of the lens. The output of the photodiode array was captured using an Analogic Data 6100 Waveform Analyser (digital oscilloscope with internal signal processing capability) and plotted out using an HP plotter. Outputs were obtained for a range of different parameters and results are shown here, alongside the predictions created in using the equation (obtained from equation 7.33)

$$u(x) = J_o\left(\beta\left[1 + m\, a(x)\right]\right) \mathrm{rect}\left(\frac{x}{W}\right) \qquad (7.34)$$

In both cases the input signal was a chirp pulse of length 20 μs. Figure 7-8 shows the results for the first set, in which a very large amplitude modulation index of m = 0.9. With this large value of m, the 0,+2 diffraction sub-order just become significant enough to be seen. This second order term is more pronounced in the experimental results than in the simulation. Since the acousto-optic cell used has a value of Q of the order of 60, it comes as no surprise to observe that the theoretical predictions based on the Raman-Nath approximation, while giving a good qualitative indication of what to expect, underestimate second order terms. Figure 7-9 shows the 0,+1 diffraction sub-order in greater detail for a more moderate modulation index. Figure 7-10 illustrates the absence of diffraction sub-orders when double sideband suppressed carrier modulation (DSBSC) is used.

7.8 Conclusions

Some recent literature makes the assumption that the zeroth diffraction order, from an acousto-optic cell operating in the Raman-Nath mode, contains no information and is therefore of little use in optical signal processing systems such as correlators. This view is neither true nor supported by the papers offering a more rigorous analysis of the acousto-optic interaction. The reality is that the zeroth diffraction order contains as much fine structure and information, available in its sub-orders, as all the other orders put together. This can be seen to be obviously true by noting that any light diffracted into the first and higher orders must be removed from the zeroth order; a reduction in light intensity contains as much information as an increase. Although the 0,0 order cannot usually be directed usefully onto a photodetector because of the probability of driving it into saturation, the sub-orders of the zeroth order can be detected to extract the information they contain. This means that it is possible to use the zeroth order in systems such as acousto-optic correlators. Obvious advantages are that such systems should be easier to set up since the optical signal being used will be on the optical axis of the system, and that more optical power is available.

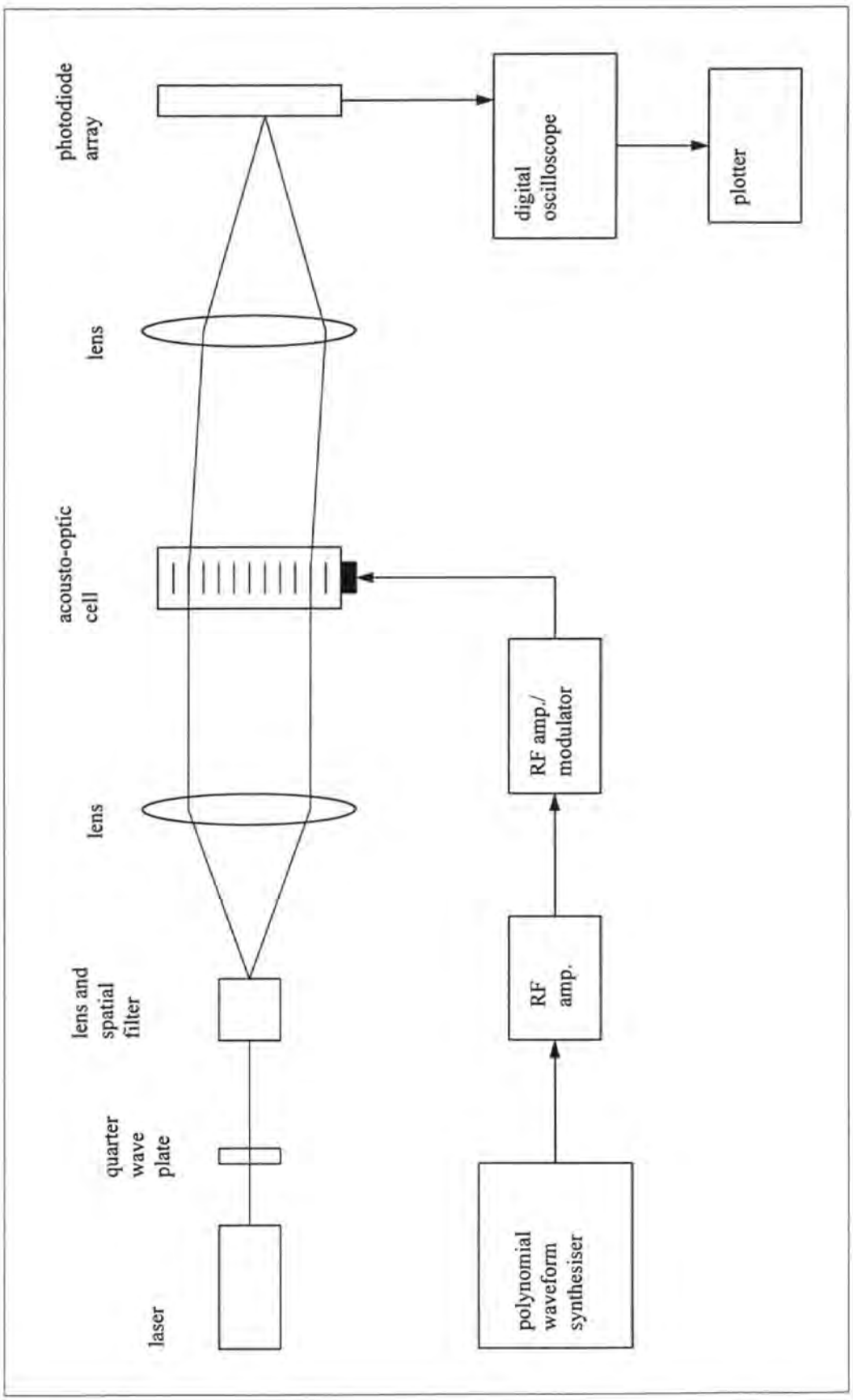

Figure 7-7. Experimental arrangement for measuring the form of the zeroth diffraction order

Pulse length	Centre frequency	Chirp bandwidth	mod. index m	mod. index β
20 μs	9 MHz	2 MHz	0.9	0.35

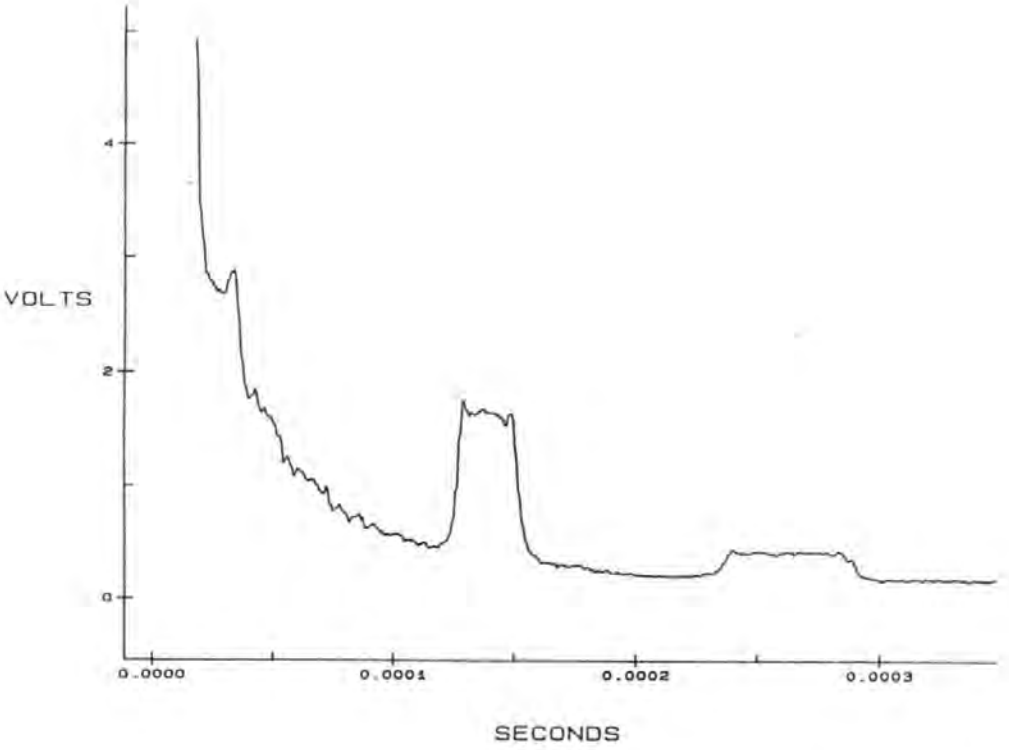

Predicted amplitude of photodiode array output (Volts - arbitrary scale)

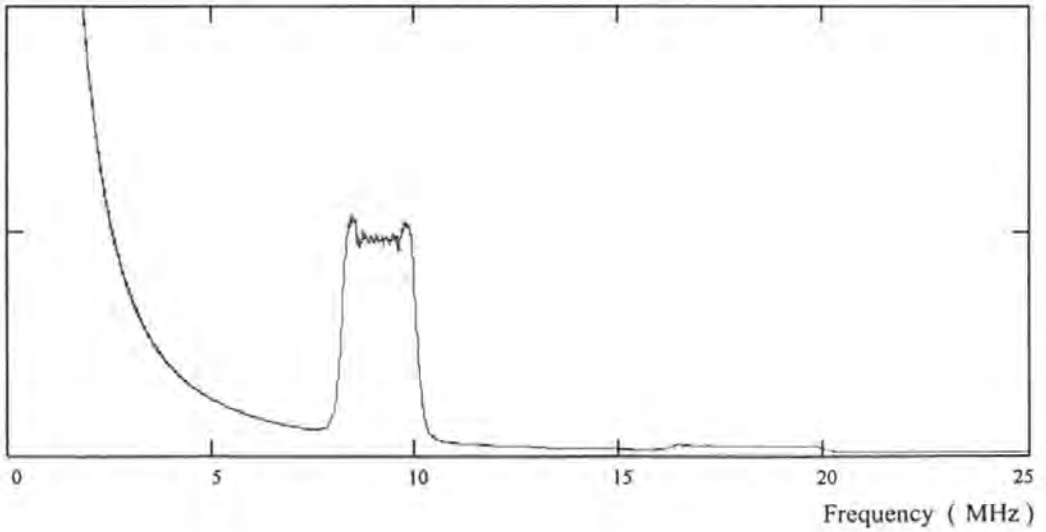

Figure 7-8. Actual output from photodiode array (top) and theoretical prediction (bottom) - large m.

Pulse length	Centre frequency	Chirp bandwidth	mod. index m	mod. index β
20 μs	12 MHz	8 MHz	0.5	0.2

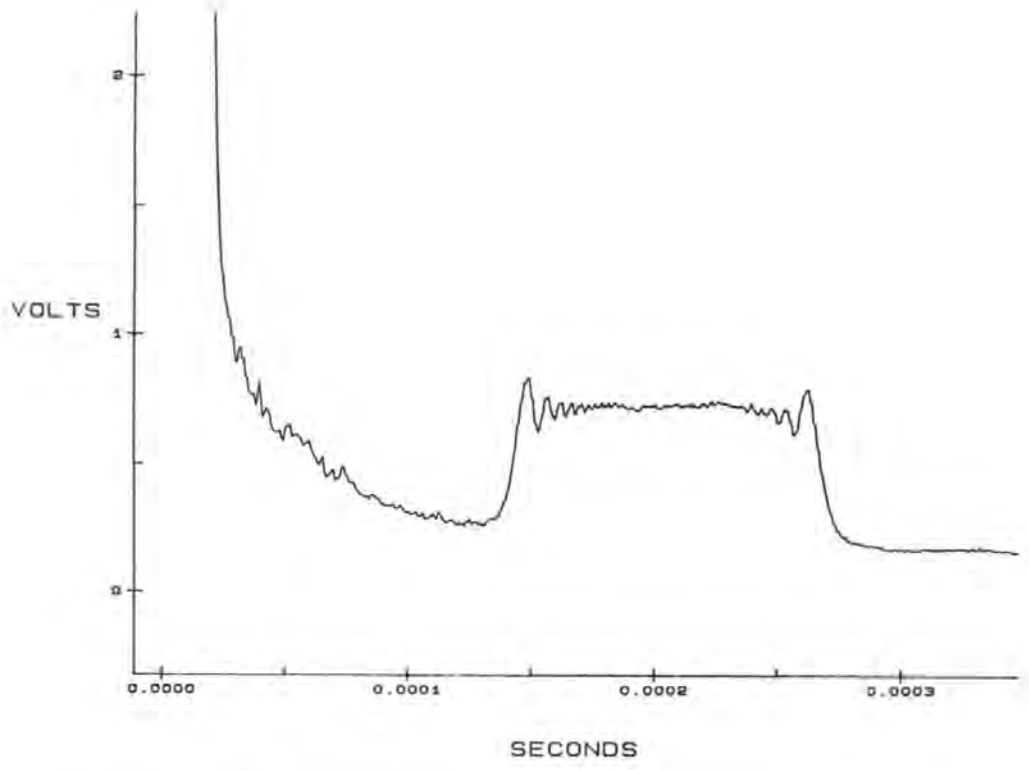

Predicted amplitude of photodiode array output (Volts - arbitrary scale)

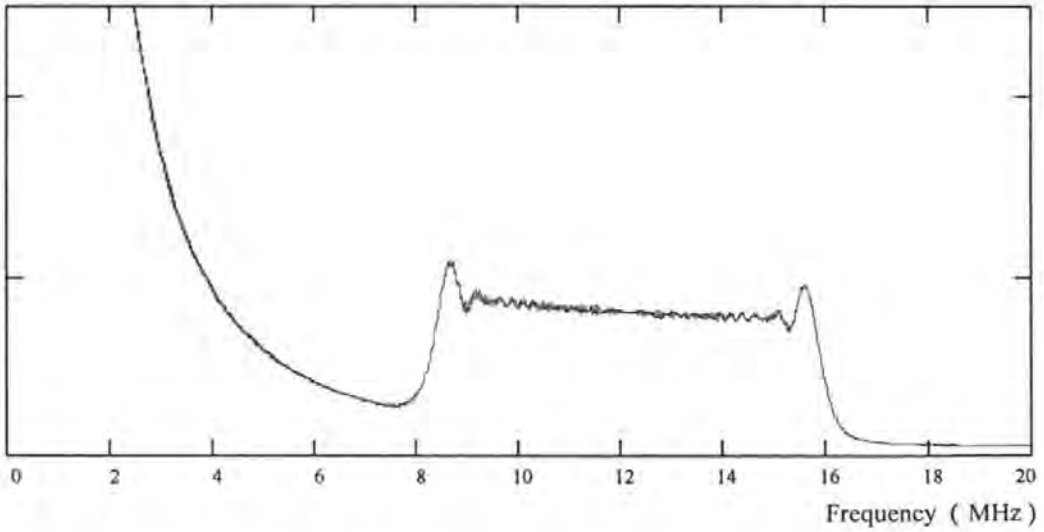

Figure 7-9. Actual output from photodiode array (top) and theoretical prediction (bottom) - moderate m.

Pulse length	Centre frequency	Chirp bandwidth	mod. index m	mod. index β
20 μs	10 MHz	4 MHz	NA: DSBSC	0.2

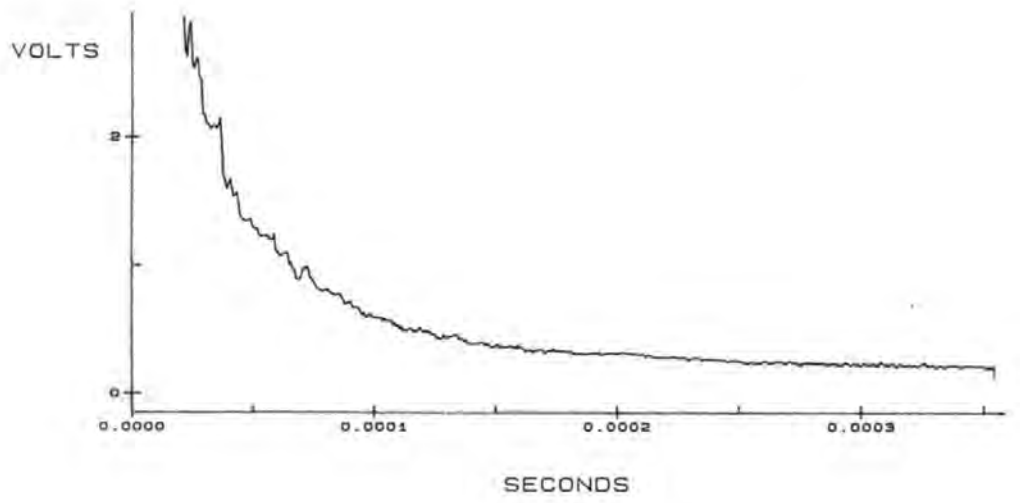

Predicted amplitude of photodiode array output (Volts - arbitrary scale)

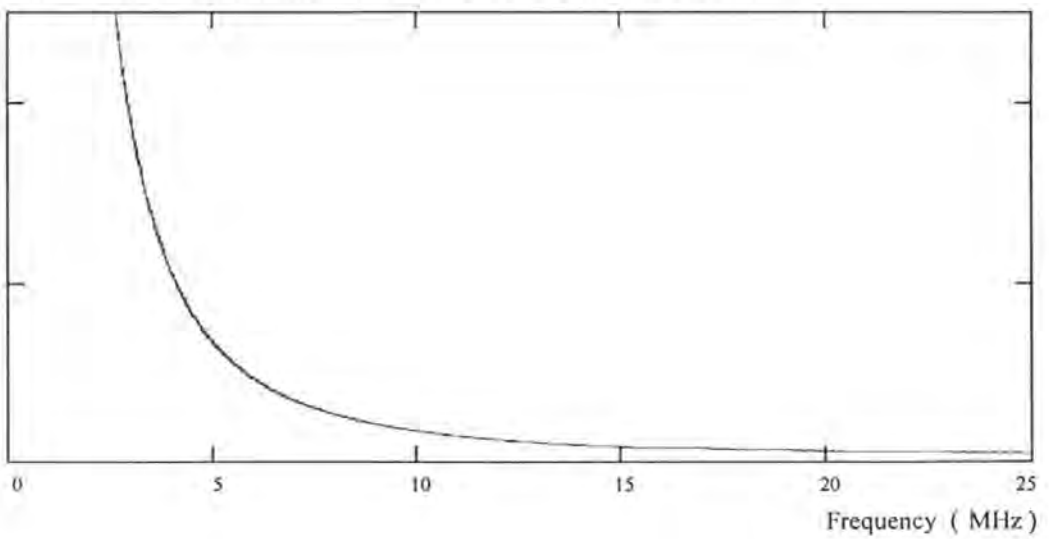

Figure 7-10. Actual output from photodiode array (top) and theoretical prediction (bottom) - moderate m.

8. Space integrating acousto-optic correlators

8.1 Introduction

Many different space integrating acousto-optic correlators have been described in the literature since the basic concept was first suggested by Cutrona in 1960 [32]. The one dimensional architectures tried have fallen into 3 main categories: heterodyning, non-heterodyning and chirp. Then heterodyning and non-heterodyning structures are similar and it will be shown that they are related as special cases of a generalised correlator. The chirp correlator is a separate highly specific device designed to detect one specific chirp signal and requires separate analysis.

For the general acousto-optic correlator the two signal inputs are inserted either by two acousto-optic "Bragg" cells or by one acousto-optic cell and one transparency. Electronic temporal input signals $s_1(t)$ and $s_2(t)$ appear as spatial signals of the form $s_1(x-Vt)$ and $s_2(x+Vt)$ when applied via acousto-optic cells. Permanently stored signals can appear in the form $s(x)$ if applied via a transparency. In the acousto-optic cell the signal usually appears as modulation of a higher frequency carrier. In either case the resulting spatial input signal causes modulation of an optical wavefront, either in amplitude (transparency) or in phase (acousto-optic cell).

Various architectures for correlating two signals have been investigated. All involve creating a collimated beam of monochromatic light and using one input device to impose one of the signals as modulation of the wavefront. The optical output, after spatial filtering in the Fourier transform plane, is imaged onto the second input device. Correlation is performed by integrating light diffracted from all parts of the signals which are simultaneously present in the input devices. The desired correlation function is of the form

$$\int_{-\infty}^{+\infty} s_1(x-Vt)\, s_2(x+Vt)\, dx \tag{8.1}$$

or
$$\int_{-\infty}^{+\infty} s_1(x-Vt)\, s_2(x)\, dx \tag{8.2}$$

However, some correlators lose phase information and give outputs of the form

$$\int_{-\infty}^{+\infty} \left| s_1(x-Vt)\, s_2(x+Vt) \right|^2 dx \tag{8.3}$$

or

$$\left| \int_{-\infty}^{+\infty} s_1(x-Vt)\, s_2(x+Vt)\, dx \right|^2 \tag{8.4}$$

The correlation, or pseudo correlation, function appears as a time varying signal at a photodetector output.

All early correlator designs seem to involve blocking the zeroth diffraction order from the first acousto-optic cell on the assumption that it contains no information. If a signal *v(t)* is injected into an acousto-optic cell then the optical wave function at the cell output, assuming Raman-Nath diffraction, takes the form (equation 7.10)

$$u(x,t) = \mathrm{Re}\left\{ e^{j(kz-\omega_o t)}\, e^{j\beta v(x-Vt)} \right\} \tag{8.5}$$

where k is the optical wave vector, z is distance along the optic axis, ω_o is the optical angular frequency, β is a constant that can be thought of as a modulation index, x is distance in the direction of acoustic propagation, and V is the velocity of acoustic propagation. The commonly offered mathematical analysis, eg. [9], approximates this as

$$\begin{aligned} u(x,t) &= Re\left\{ e^{j(kz-\omega_o t)} \left[1 + j\beta\, v(x-Vt) \right] \right\} \\ &= \cos(kz-\omega_o t) - j\, v(x-Vt)\, \sin(kz-\omega_o t) \end{aligned} \tag{8.6}$$

representing a zeroth undiffracted and a diffracted term. This approximation leads to the assumption that the zeroth order contains no information and should be rejected by a block in the Fourier transform plane to leave the Fourier transform of *v(x-Vt)*. If *v(t)* is a simple sinusoidal test tone, then this gives rise to +1 and -1 diffraction orders. Thus this analysis describes the optical output of the acousto-optic cell as comprising no more than a zeroth order containing no information and +1 and -1 diffraction orders containing all the information. As was shown in chapter 7, this model is very misleading. In the Raman-Nath

mode we can expect to observe 2nd and 3rd diffraction orders; higher orders will be too faint to observe easily. Also, there is as much information in the zeroth order, albeit in sub-orders of the zeroth order, as in all the other diffraction orders put together. Indeed the zeroth order can be used to produce a very effective correlator. The approximation described above can be used to justify the operation of some correlator architectures: see for example Rhodes [9]. It does not, however, explain the operation of the zeroth order correlator.

The analysis will start with a general all order space integrating correlator in which no spatial filtering whatsoever is carried out in the Fourier transform plane of the first of two acousto-optic cells. This will be followed by an analysis of how adjusting the acousto-optic cells to operate in the Bragg mode can be accounted for. Several other architectures, both heterodyning and non-heterodyning will then be described as special cases of this general correlator in which different diffraction orders are selected at the Fourier transform plane.

8.2 The general all order space integrating correlator

Consider the correlator shown in figure 8-1.

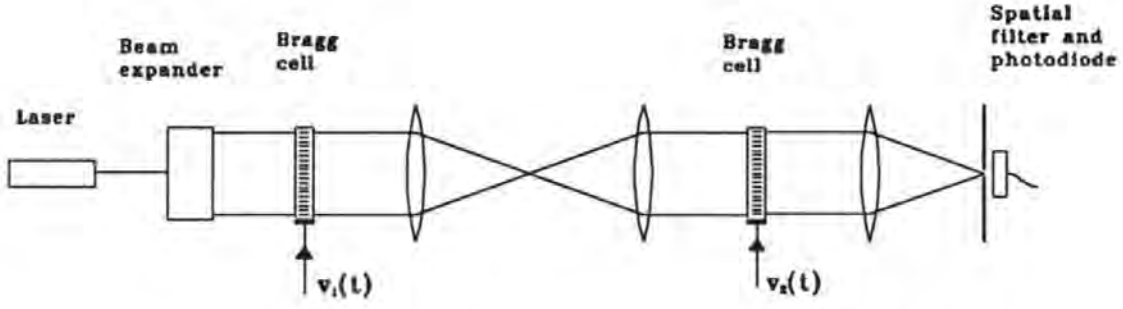

Figure 8-1. *General all order space-integrating acousto-optic correlator.*

8.2.1 Analysis based on Raman-Nath diffraction theory

To perform a correlation the signals in the two acousto-optic cells must counter propagate. The imaging process spatially reverses the first signal and so if the second signal is injected from the same direction as the first the counter propagation is achieved. However for this counter propagation to occur with the signal in the correct orientation one of the

signals must be time reversed before injecting into the acousto-optic cell. This requirement for time reversal adds an extra complication to the space integrating correlator, not present in time integrating correlators. If the first signal, $v_1(t)$, is time reversed so that the signal actually delivered to the transducer of the acousto-optic cell is $v_1(T-t)$ where $T = \frac{W}{V}$ and W is the acoustic length of the acousto-optic cell and V is the acoustic velocity, then if the x axis is defined as having its origin at the transducer and having its positive sense in the direction of acoustic propagation, the traveling wave in the first acousto-optic cell can be described as proportional to $v_1(x-Vt)$. If the second signal, $v_2(t)$, is not time reversed, but the sense of the x axis is reversed while maintaining its origin at the transducer of the second cell, then the travelling wave in the second acousto-optic cell can be described as proportional to $v_2(x+Vt)$. The optical wave incident on the first acousto-optic cell has the function

$$Re\{ e^{j(kz-\omega_o t)} \} \tag{8.7}$$

The output from the first cell can, assuming Raman-Nath diffraction, be written as

$$u_1(x,t) = Re\left\{e^{j(kz-\omega_o t)}\ e^{j\beta v_1(x-Vt)}\right\} rect\left(\frac{x}{W}\right) \tag{8.8}$$

This is imaged onto the second acousto-optic cell. The optical output from the second cell is therefore

$$u_2(x,t) = Re\left\{ e^{j(kz-\omega_o t)}\ e^{j\beta v_1(x-Vt)} e^{j\beta v_2(x+Vt)} \right\} rect\left(\frac{x}{W}\right) \tag{8.9}$$

If the signals $v(t)$ are generated by imposing signals of interest $a(t)$ by means of double sideband large carrier (DSBLC) or double sideband suppressed carrier (DSBSC) amplitude modulation then we have

$$v_1(x-Vt) = s_1(x-Vt)\ \sin\left(K_c x - \omega_c t\right) \tag{8.10}$$

$$v_2(x+Vt) = s_2(x+Vt)\ \sin\left(K_c x + \omega_c t\right) \tag{8.11}$$

where ω_c is the angular frequency and K_c is the acoustic wave vector of the carrier. $s(t) = a(t)$ for DSBSC and $s(t) = [1+ma(t)]$ for DSBLC modulation, where $a(t)$ is the information signal. The optical output of the second acousto-optic cell is then

$$u_2(x,t) = Re\left\{ e^{j(kz-\omega_o t)}\ e^{j\beta s_1(x-Vt)\sin(K_c x-\omega_c t)}\ e^{j\beta s_2(x+Vt)\sin(K_c x+\omega_c t)} \right\} rect\left(\frac{x}{W}\right) \tag{8.12}$$

Expanding this out in terms of Bessel functions (see equation 7.13) gives

$$u_2(x,t) = Re\left\{ e^{j(kz-\omega_o t)} \sum_{p=-\infty}^{+\infty} J_p\left(\beta s_1(x-Vt)\right) e^{jp[K_c x-\omega_c t]} \sum_{q=-\infty}^{+\infty} J_q\left(\beta s_2(x+Vt)\right) e^{jq[K_c x+\omega_c t]} \right\} rect\left(\frac{x}{W}\right) \quad (8.13)$$

$$= Re\left\{ \sum_{p=-\infty}^{+\infty} \sum_{q=-\infty}^{+\infty} J_p\left(\beta s_1(x-Vt)\right) J_q\left(\beta s_2(x+Vt)\right) e^{j\{kz+(p+q)K_c x-[\omega_o+(p-q)\omega_c]t\}} \right\} rect\left(\frac{x}{W}\right) \quad (8.14)$$

$$= \sum_{p=-\infty}^{+\infty} \sum_{q=-\infty}^{+\infty} J_p\left(\beta s_1(x-Vt)\right)\ J_q\left(\beta s_2(x+Vt)\right)\ \cos\{kz+(p+q)K_c x\ -\ [\omega_o+(p-q)\omega_c]t\}\ rect\left(\frac{x}{W}\right) \quad (8.15)$$

All the p terms relate to the first input and the q terms relate to the second input. A spatial filter at the Fourier transform plane of the first acousto-optic cell effectively limits the allowed values of p. A spatial filter in the Fourier transform plane of the second cell, the photodetector plane, limits the allowed values of $p+q$. Almost all practical correlators described in the literature, and analysed later in this paper, do involve spatial filtering at the first Fourier transform plane. Equation 8.15 provides a common starting point for the analysis of all these correlators. However, with certain limitations, a correlator with no spatial filtering in the first Fourier transform plane can operate very effectively and has the advantage of simplicity. An analysis of this "all order" correlator, in which all values of p are allowed, is therefore presented first, before returning to the range of correlators in which p is restricted to specific values. If the final spatial filter before the photodetector selects the zeroth order components of this function then the only terms of interest are those for which the x component of the wave vector is zero. i.e. we are only interested in those terms for which

$$p = -q \quad (8.16)$$

If DSBLC modulation is used so that $s(t) = [1+ma(t)]$, the relevant part of the wave function simplifies to

$$u_2(x,t) = \sum_{n=-\infty}^{+\infty} (-1)^n\ J_n\left(\beta[1+ma_1(x-Vt)]\right) J_n\left(\beta[1+ma_2(x+Vt)]\right) \cos(2n\omega_c t) \cos(kz-\omega_o t)\, rect\left(\frac{x}{W}\right) \quad (8.17)$$

If the spatial filter were to pass the whole of this zeroth order then the output of the photodetector would take the form

$$\int_{-\infty}^{+\infty} \left| {}^{o}u_2(x,t) \right|^2 rect\left(\frac{x}{W}\right) dx \tag{8.18}$$

In reality the whole of the zeroth order is not usually used in this form. The zeroth order breaks down into a number of sub orders. The 0,0 sub order in this expression is very bright and even if it does not saturate the photodetector, the temporal variation in intensity will be so small in comparison to the average optical power that the signal to noise ratio of the electronic signal at the photodetector output will be very low. The sensible practice is to avoid using this 0,0 order either by spatial filtering at the photodetector to use one of the sub orders or by spatial filtering in the Fourier transform plane of the first acousto-optic cell to block diffraction orders including the zeroth order. All terms other than the $n = 0$ term produce temporal electronic outputs which are modulations of a $\cos^2(2n\omega_c t)$ carrier. If a low pass filter is used to eliminate these terms, then only the $n = 0$ term is relevant. There is a limitation here: the highest frequency in the correlation function at the photodetector output must be significantly less than twice the carrier frequency ω_c. If this is the case and a low pass filter is used, then the zeroth order is effectively

$${}^{o}u_2(x,t) = J_o\left(\beta[1 + m\, a_1(x-Vt)]\right) J_o\left(\beta[1 + m\, a_2(x+Vt)]\right) \cos\left[kz - \omega_o t\right] rect\left(\frac{x}{W}\right) \tag{8.19}$$

using the approximation, valid for $x < 1$,

$$J_o(\xi) \approx 1 - \frac{\xi^2}{4} \tag{8.20}$$

equation 8.19 becomes

$${}^{o}u_2(x,t) = \left\{ 1 - \frac{\beta^2}{4}[1 + m\, a_1(x-Vt)]^2 \right\} \left\{ 1 - \frac{\beta^2}{4}[1 + m\, a_2(x+Vt)]^2 \right\} \times \cos\left[kz - \omega_o t\right] rect\left(\frac{x}{W}\right) \tag{8.21}$$

$$
{}^{o}u_2(x,t) = \left\{ \begin{array}{l} \left(1 - \frac{\beta^2}{2} + \frac{\beta^4}{16}\right) \\ + \left(\frac{\beta^4 m}{8} - \frac{\beta^2 m}{2}\right)\left(a_1(x-Vt) + a_2(x+Vt)\right) \\ + \frac{\beta^4 m^2}{4}\, a_1(x-Vt)\, a_2(x+Vt)) \\ + \left(\frac{\beta^4 m}{16} - \frac{\beta^2 m^2}{4}\right)\left(a_1^2(x-Vt) + a_2^2(x+Vt)\right) \\ + \frac{\beta^4 m^3}{8}\left(a_1^2(x-Vt)\, a_2(x+Vt) + a_1(x-Vt)\, a_2^2(x+Vt)\right) \\ + \frac{\beta^4 m^4}{16}\, a_1^2(x-Vt)\, a_2^2(x+Vt) \end{array} \right\} \cos\left[kz - \omega_o t\right] rect\left(\frac{x}{W}\right) \qquad (8.22)
$$

i.e. ${}^{o}u_2(x,t)$ contains a d.c. term plus the first order terms $a_1(x-Vt)$ and $a_2(x+Vt)$, plus higher order terms. The third lens in the system forms the Fourier transform of ${}^{o}u_2(x,t)$ in the photodetector plane where the final spatial filter is used to isolate the required sub diffraction order terms. If we look at the optical intensity of the whole zeroth diffraction order in the final spatial filter plane, it will take the form shown in figure 8-2, assuming that $a_1(t)$ and $a_2(t)$ have no d.c. components and that signal bandwidths occupy less than 1 octave, and ignoring for the moment the effect of the limited aperture of the acousto-optic cells.

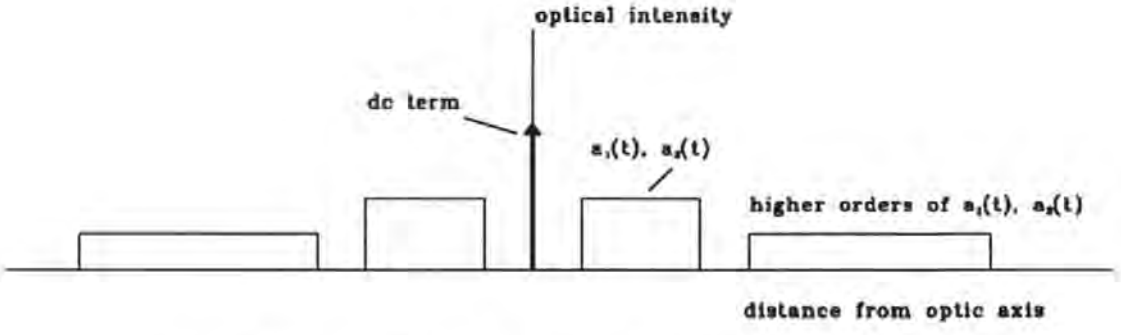

Figure 8-2. *Form of zeroth diffraction order at photodetector plane*

The effect of the limited aperture of the Bragg cell, described in the above equations by the term $rect\left(\frac{x}{W}\right)$, is to cause the above intensity profile to be convolved with a $sinc^2$ function.

We will observe a strong central spot with extended sidelobes containing considerable fine structure. A simple spatial filter (i.e. a slit or hole) can be used to select one of the first order sidelobes. If the photodiode placed behind this filter is of sufficient area to receive the whole of this sidelobe, then the spatially integrated intensity of the light incident on the photodiode will be

$$I(t) = \frac{1}{2}\int_{-\infty}^{+\infty}\left(\frac{\beta^2 m}{4}\right)^2 \left| a_1(x-Vt) + a_2(x+Vt)\right|^2 rect\left(\frac{x}{W}\right) dx \qquad (8.23)$$

Equation 8.23 represents a major approximation. The spatial windowing term, $rect\left(\frac{x}{W}\right)$, at the second acousto-optic cell (see figure 8-1) will cause spreading of all the terms in equation 8.22 in the photodetector plane, by convolution with a sinc function. This effect can be seen by comparing figure 8-2, which ignores it, with figure 7-8, which shows the light intensity distribution that can be expected at the photodetector plane in reality. The dimensions of the spatial filter being used in the photodetector plane, to select out the second term in equation 8.22, are clearly very important. The aim of this filter is to include most of the required 0,±1 diffraction sub-order while excluding as much of the other terms as possible. Unfortunately, it is inevitable that all the diffraction sub-orders will be spread so that they suffer some degree of overlap. Hence, equation 8.23 should contain all the other terms in equation 8.22, multiplied by small weighting factors. The higher order terms will have a relatively small effect, but the first, zeroth order, term will have a major effect. Examination of figure 7-8 makes it clear that the amount of light that will pass through the spatial filter at the photodetector due to the zeroth order is of the same order of magnitude as, and may, for small input signal powers, be much greater than, the amount due to the required first order terms. This background light, even though it may vary very little, will cause shot noise in the photodetector so that the dynamic range of the correlator will be severely limited. The dynamic range will depend on the values of β and m, the dimensions of the spatial filter at the photodetector, the size, W, of the acousto-optic cell window, and the frequency band occupied by the correlator input signals. The higher the frequency of the signals, the further out from the central zeroth order the required first order terms are in the photodetector plane, and the smaller the amount of light from the central zeroth order passing through the spatial filter at the photodetector. If the signal frequency range occupies more than one octave, then the higher order terms will overlap the first order terms, even without spreading due to windowing. It is tempting to attempt a prediction of the dynamic range from a more detailed

analysis of equation 8.22, but it should be remembered that the whole of the analysis leading up to equation 8.22 is based on the Raman-Nath approximation in the first place and does not give us a reliable quantitative guide to the amplitudes of the various diffraction orders. As was pointed out in section 7.7, the approximations used here lead to a useful qualitative indication of what to expect from a practical system. Having noted that equation 8.23 is a major approximation, we proceed on the basis that it is a useful one that leads to a prediction of correlator output that is borne out by experiment.

Expanding equation 8.23 gives

$$I(t) = \frac{1}{2}\left(\frac{\beta^2 m}{4}\right)^2 \int_{-\infty}^{+\infty} \left[a_1^2(x-Vt) + a_2^2(x+Vt) + 2a_1(x-Vt)a_2(x+Vt)\right] rect\left(\tfrac{x}{W}\right) dx \tag{8.24}$$

$$= \frac{1}{2}\left(\frac{\beta^2 m}{4}\right)^2 \left\{ \begin{array}{l} \int_{-\infty}^{+\infty} a_1^2(x-Vt)\, rect\left(\tfrac{x}{W}\right) dx + \int_{-\infty}^{+\infty} a_2^2(x+Vt)\, rect\left(\tfrac{x}{W}\right) dx \\ \quad + 2\int_{-\infty}^{+\infty} a_1(x-Vt)\, a_2(x+Vt)\, rect\left(\tfrac{x}{W}\right) dx \end{array} \right\}$$

Provided that the lengths of the pulses $a_1(t)$ and $a_2(t)$ are less than the time window of the acousto-optic cells (this is an essential requirement for the space integrating correlator anyway) the $\int a^2(x \pm Vt)\, rect\left(\tfrac{x}{W}\right) dx$ terms will give a time varying function of the form shown in figure 8-3.

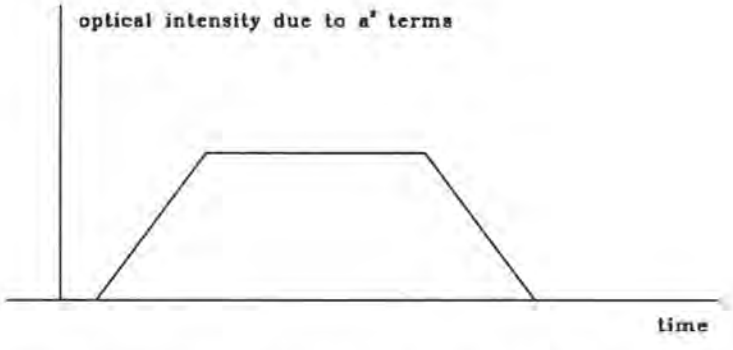

Figure 8-3. *Component of photodetector output due to a^2 terms.*

Once the function $a(x \pm Vt)$ is totally within the acousto-optic cell window described by $rect\left(\tfrac{x}{W}\right)$ the integral of $a^2(x \pm Vt)$ will remain at a constant positive value. As it enters and leaves the window, the integral will rise and fall as shown. The width of the flat part of this function depends on the relative lengths of the signals $a(t)$ and the time window of the Bragg

cells. This slowly varying or constant function at the output of the photodiode can be removed by a high pass filter to leave the desired cross correlation function

$$\left(\frac{\beta^2 m}{4}\right)^2 \int_{-\infty}^{+\infty} a_1(x-Vt)\ a_2(x+Vt)\ rect\left(\frac{x}{W}\right) dx \tag{8.25}$$

There are a few points to note about this cross correlation function. Because both signals are moving, we are obtaining a correlation function of the form

$$r_{12}(\tau) = \int_{-\infty}^{+\infty} a_1(t-\tau)\ a_2(t+\tau)\ dt \tag{8.26}$$

rather than the usual

$$r_{12}(\tau) = \int_{-\infty}^{+\infty} a_1(t)\ a_2(t+\tau)\ dt \tag{8.27}$$

The time axis of the output correlation function will be compressed by a factor of two. Because of the windowing term, $rect\left(\frac{x}{W}\right)$, the correlation function can only be formed if the functions $a_1(t)$ and $a_2(t)$ are shorter than the time window of the acousto-optic cells, so that all the overlap between $a_1(t)$ and $a_2(t)$ will lie within the time window at all times. As mentioned earlier, this system can only operate in the ideal way described if the input signals have bandwidths of less than one octave and no dc component, and the highest frequency component of the correlation function is significantly less than twice the carrier frequency used in the acousto-optic cells. Subject to these conditions, this system produces the complete correlation function giving both amplitude and phase.

8.2.2 Bragg diffraction

The assumption of Raman-Nath diffraction is only valid if the Q factor of the acousto-optic cell is less than 1 [35]. The Q factor is given by equation 7.4, which can be rewritten as

$$Q = \frac{K^2 d}{n k} \tag{8.28}$$

where K is the acoustic wave vector, d is the thickness of the cell, n is the refractive index and k is the optical wave vector. Q is often greater than 1. Indeed, the TeO_2 cells used in the

experimental work have a Q of the order of 100. If Q > 10, then the cell is usually considered to operate in the Bragg mode [35]. A cell with a high Q factor operating in a pseudo Raman-Nath mode will exhibit something approximating to true Raman-Nath diffraction for very low input RF power, but as the power is turned up the amplitudes of the diffraction orders will very rapidly cease to be given by the Bessel functions as described above. A proper prediction of the performance of an acousto-optic correlator using cells operating in this pseudo Raman-Nath mode would more realistically be based on empirical measurements of the characteristics of the cells being used. (This is analogous to basing the design of an amplifier on the actual characteristics of the transistors rather than h-parameter models.)

Where possible, it is more efficient to use high Q cells operating in the Bragg mode. Clearly, the all order correlator relies upon a symmetry in its diffraction that requires the cells to be operated in the Raman-Nath or pseudo Raman-Nath mode. Other correlators, such as a heterodyning correlator using both +1 and -1 diffraction orders, have the same requirement. However, for many correlators the slight adjustment to operate in the Bragg mode is very easy and can be shown to offer very considerable advantages. Korpel [33] gives expressions for the amplitudes of the zeroth and first diffraction orders, for pure Bragg diffraction. that can be rewritten as

$$ {}^{0}u(x,t) = \cos\left[\frac{\beta}{2}s(x-Vt)\right]\cos\left(kz-\omega_o t\right) \tag{8.29} $$

$$ {}^{\pm 1}u(x,t) = \sin\left[\frac{\beta}{2}s(x-Vt)\right]\sin\left(kz \pm K_c x - (\omega_o \pm \omega_c)t\right) \tag{8.30} $$

where β is the same quantity as used in describing Raman-Nath diffraction. If *s(t)* is normalised so that its peak value is 1, β represents the peak variation in optical phase shift caused by the acousto-optic cell. These expressions can be compared directly with the equivalent terms for Raman-Nath diffraction

$$ {}^{0}u(x,t) = J_o\left[\beta\, s(x-Vt)\right]\cos\left(kz-\omega_o t\right) \tag{8.31} $$

$$ {}^{\pm 1}u(x,t) = J_{\pm 1}\left[\beta\, s(x-Vt)\right]\cos\left(kz \pm K_c x - (\omega_o \pm \omega_c)t\right) \tag{8.32} $$

Comparing the approximations for the diffraction order amplitudes given by these two sets of expressions, we compare

$$J_0(\xi) \approx 1 - \frac{\xi^2}{4} \quad \text{with} \quad \cos(\xi) \approx 1 - \frac{\xi^2}{2}$$

and

$$J_1(\xi) \approx \frac{\xi}{2} \quad \text{with} \quad \sin(\xi) \approx \xi \tag{8.33}$$

where $\xi = \beta\, s(x - Vt)$ for Raman-Nath diffraction and $\xi = \frac{\beta}{2}\, s(x - Vt)$ for Bragg diffraction. Clearly the results from expanding out the appropriate expressions using these approximations will be very similar and all the results obtained using Raman-Nath diffraction theory can, where applicable, be adjusted to give the result to be expected in the case of Bragg diffraction simply by replacing $\frac{\beta^2}{4}$ by $\frac{\beta^2}{8}$ for zeroth order diffraction terms. For first order diffraction terms the approximation remains unchanged.

In the analysis of the following correlators, the photodetector output will first be predicted on the assumption of Raman-Nath diffraction and then the results adjusted by the above substitution, if required, to give the prediction based on Bragg diffraction. In some cases the output signal will appear to be smaller when Bragg diffraction is assumed. However it should be remembered that β, the peak variation in phase shift across the acousto-optic cell is proportional to the thickness of the cell. A high Q cell, designed for use in the Bragg mode will therefore be able to achieve much higher values of β than a thin cell designed for Raman-Nath diffraction. Although photodetector output levels are often lower in terms of β, they are generally higher in absolute terms when the acousto-optic cells are operated in the Bragg mode. The approximations for the amplitudes of the diffraction orders given above for Bragg diffraction hold for $\beta < 2$.

8.3 Zeroth order non-heterodyning correlator

The zeroth order correlator is very similar to the all order correlator and its analysis has effectively been covered already. Consider the architecture shown in figure 8-4.

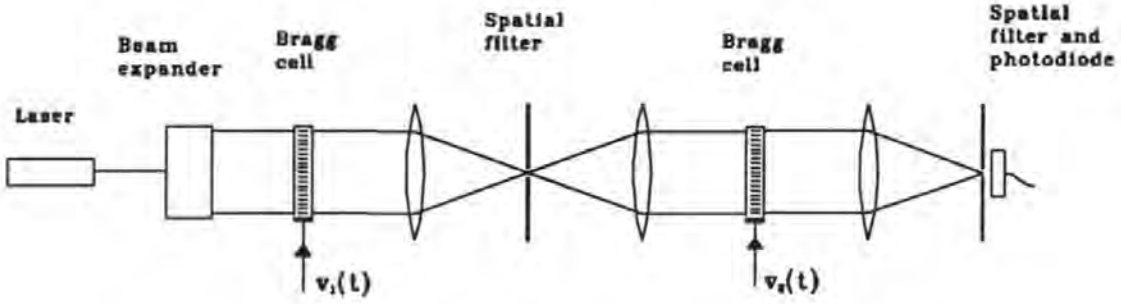

Figure 8-4. *Zeroth order, non-heterodyning, space integrating correlator*

8.3.1 Operation in the Raman-Nath mode

The effect of the first spatial filter on equation 8.15 is to restrict p to taking one value: zero. The second filter restricts $p+q$ similarly to being zero and therefore q can only be zero. This leads directly to the relevant output from the second acousto-optic cell being given by equation 8.19, the spatially integrated intensity of the light incident on the photodetector being given by equation 8.25. The analysis therefore continues exactly as for the all order correlator. The difference is that, whereas the all order correlator required a low pass filter on the photodetector output to eliminate signal components comprising modulated carrier multiples, in the zeroth order correlator these terms are prevented from arising by the first spatial filter. No low pass filter is required and the restriction on the highest frequency component of the output correlation function is therefore removed. The zeroth order correlator can therefore, for example, be used to generate the autocorrelation functions of pulses with much higher time bandwidth products.

8.3.2 Operation in the Bragg mode

Since the zeroth diffraction order is used at each stage, equation 8.25, which effectively gives the photodetector output for Raman-Nath diffraction, is modified by replacing $\frac{\beta^2}{4}$ by $\frac{\beta^2}{8}$ to give

$$\left(\frac{\beta^2 m}{8}\right)^2 \int_{-\infty}^{+\infty} a_1(x-Vt)\; a_2(x+Vt)\; rect\left(\frac{x}{W}\right) dx \qquad (8.34)$$

This appears to be one quarter of the amplitude of the output when the acousto-optic cells are operated in the Raman-Nath mode, but it should be remembered that much larger values of β are possible in high Q cells which are designed to be operated in the Bragg mode.

8.4 Experimental results for a zeroth order non-heterodyning correlator

The work discussed in this thesis started with a study of the zeroth order non heterodyning space integrating correlator (ZOSIAC). All the other correlators discussed in this chapter have been previously described in the literature, but the zeroth order correlator was not described prior to presentation by Houghton and Reeve [14]. Results of experimental work, confirming the predicted operation, are therefore presented here.

The arrangement for experiments with the ZOSIAC is shown in figure 8-5. This correlator was used to generate the acf of a number of different chirp pulses and results for 15 μs pulses of BT products of 22.5, 45, 67.5 and 90 are shown in figures 8-6 to 8-9. One polynomial waveform synthesiser was programmed to produce the chirp pulse and the other to produce a time reversed version of the same pulse. Both synthesisers were triggered externally by a pulse generator which also supplied the trigger for the digital oscilloscope.

The results displayed in figures 8-6 to 8-9 show that this correlator clearly produces the predicted ccf for limited signal bandwidths. For higher bandwidths the performance is limited by the performance of the photodiode. Unfortunately the requirements of this correlator put conflicting pressures on the choice of photodiode, as discussed in section 6.2, and this type of correlator is therefore not appropriate for the processing of signals with wide bandwidths.

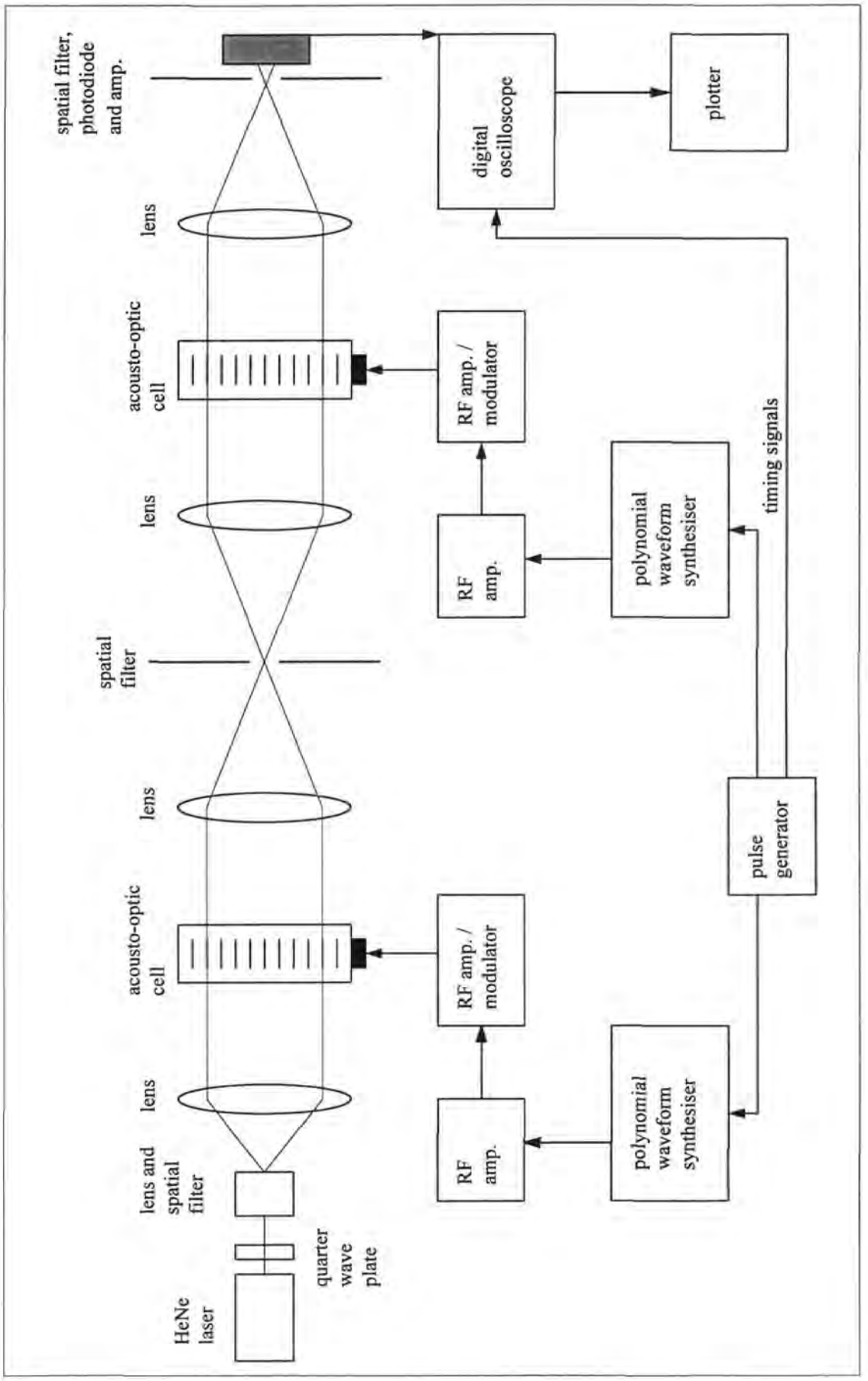

Figure 8-5. Experimental arrangement of zeroth order non-heterodyning space integrating correlator.

Chirp from 4.25 to 5.75 MHz in 15 μs. (Bandwidth = 1.5 MHz, BT product = 22.5)

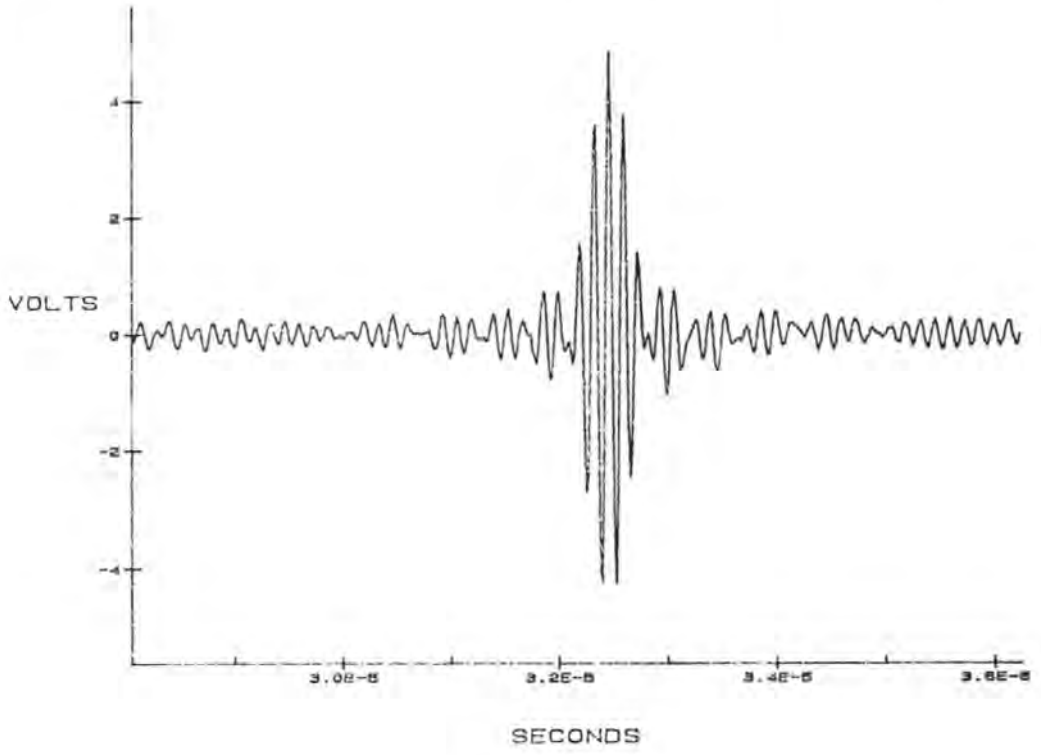

Theoretical acf amplitude (volts - arbitrary scale)

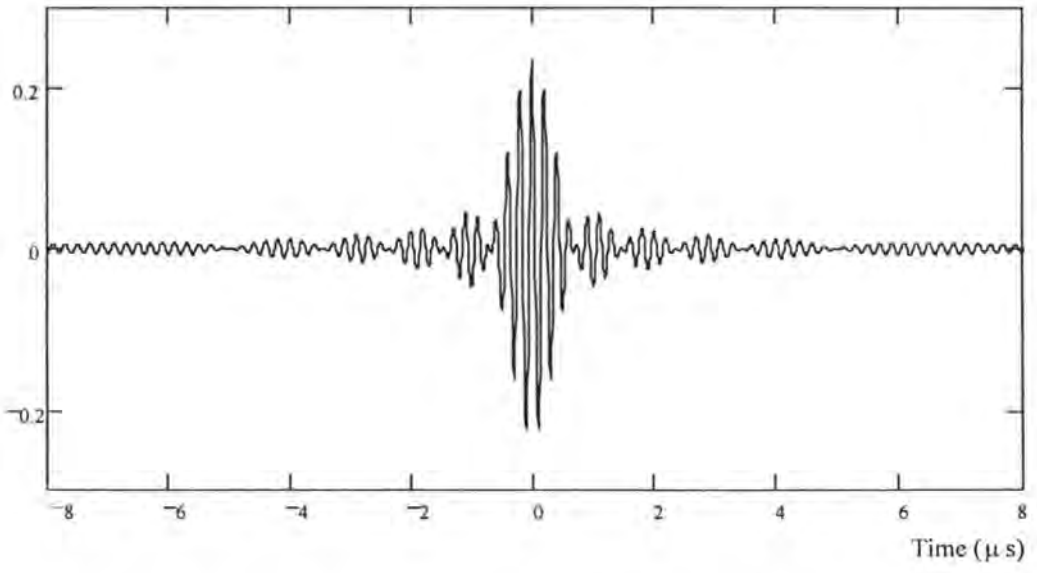

Figure 8-6. Experimental correlator output and theoretical form of the acf for a chirp pulse from 4.25 to 5.75 MHz in 15 μs . (BT = 22.5)

Chirp from 3 to 6 MHz in 15 μs. (Bandwidth = 3 MHz, BT product = 45)

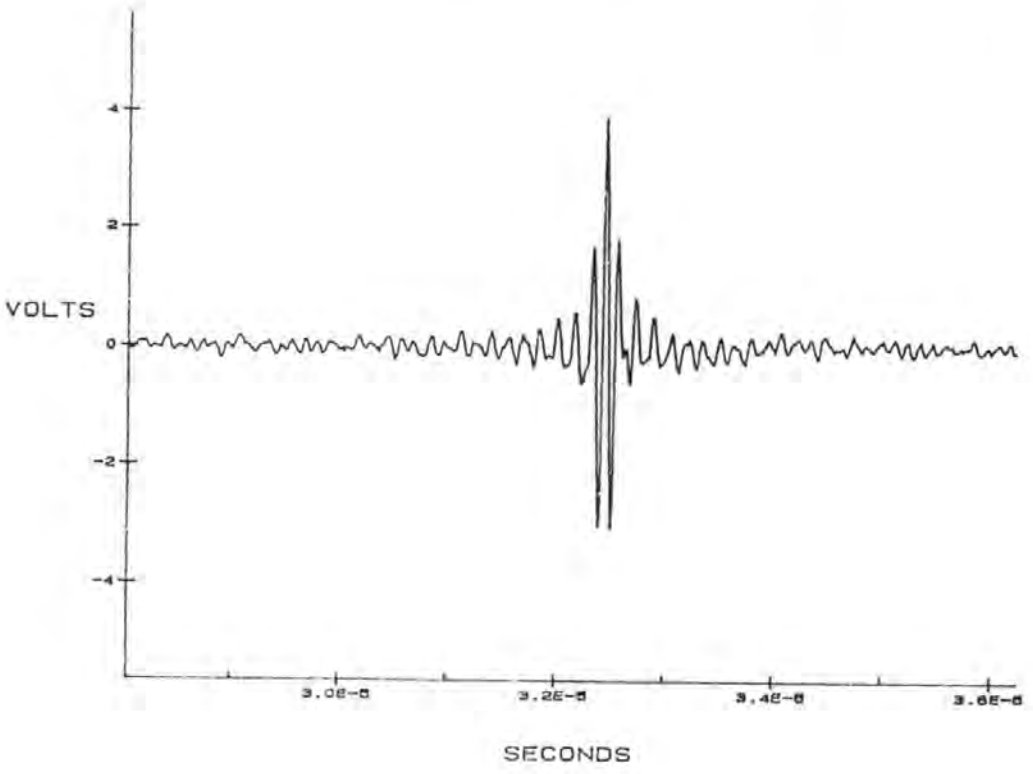

Theoretical acf amplitude (volts - arbitrary scale)

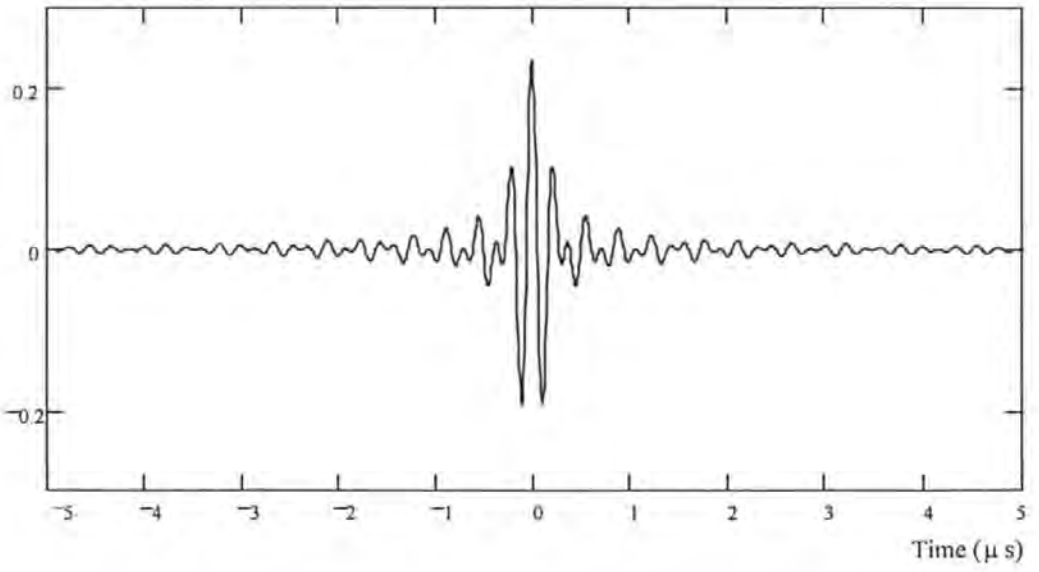

Figure 8-7. Experimental correlator output and theoretical form of the acf for a chirp pulse from 3 to 6 MHz in 15 μs. (BT = 45)

Chirp from 3 to 7.5 MHz in 15 μs. (Bandwidth = 4.5 MHz, BT product = 67.5)

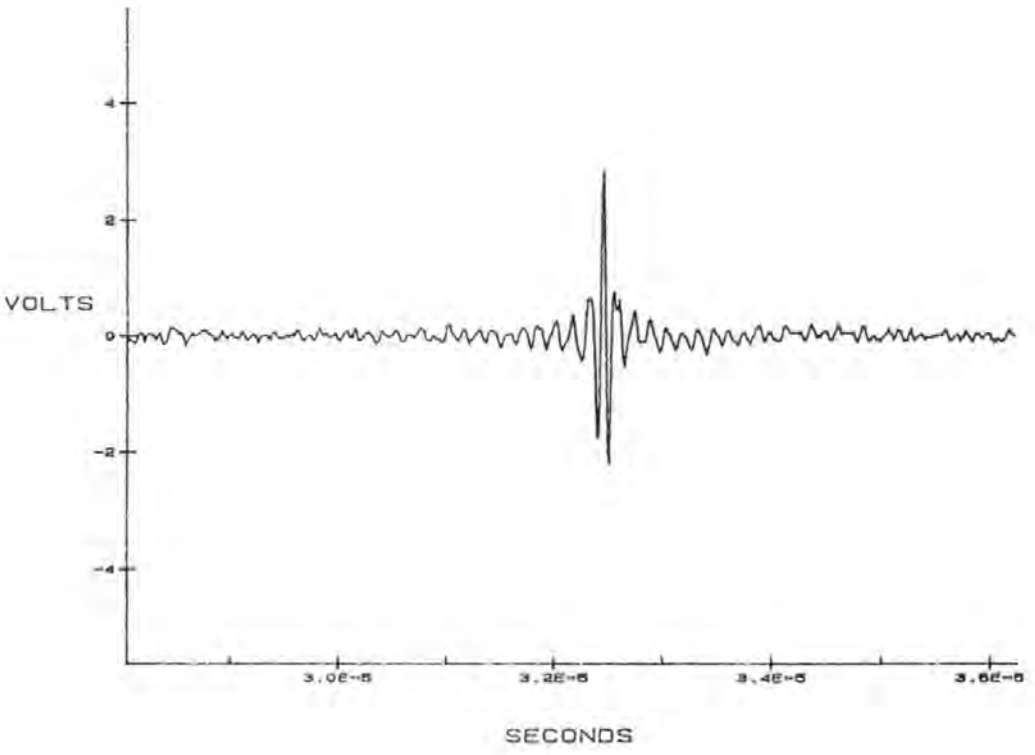

Theoretical acf amplitude (volts - arbitrary scale)

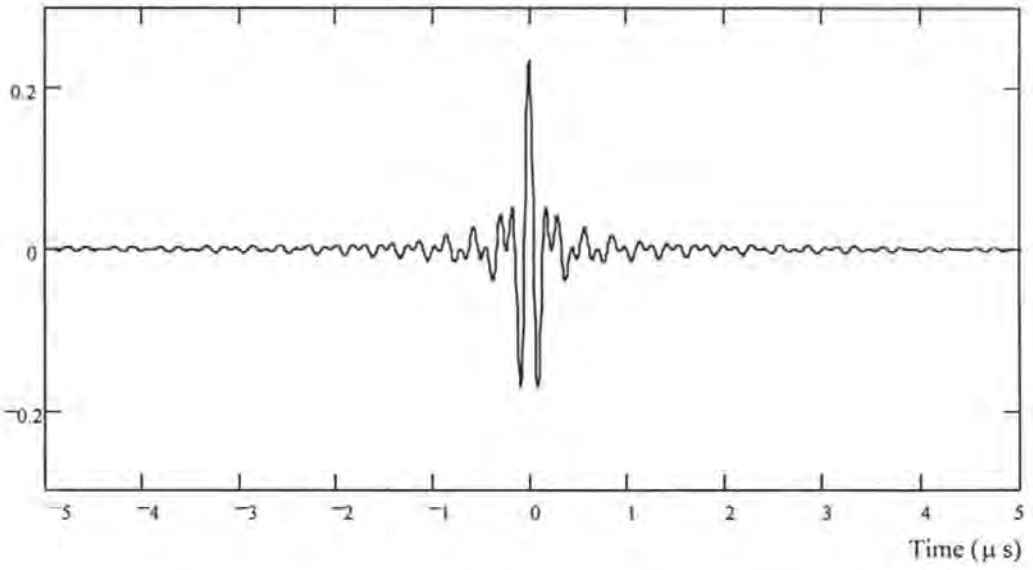

Figure 8-8. Experimental correlator output and theoretical form of the acf for a chirp pulse from 3 to 7.5 MHz in 15 μs . (BT = 67.5)

Chirp from 2 to 8 MHz in 15 μs. (Bandwidth = 6 MHz, BT product = 90)

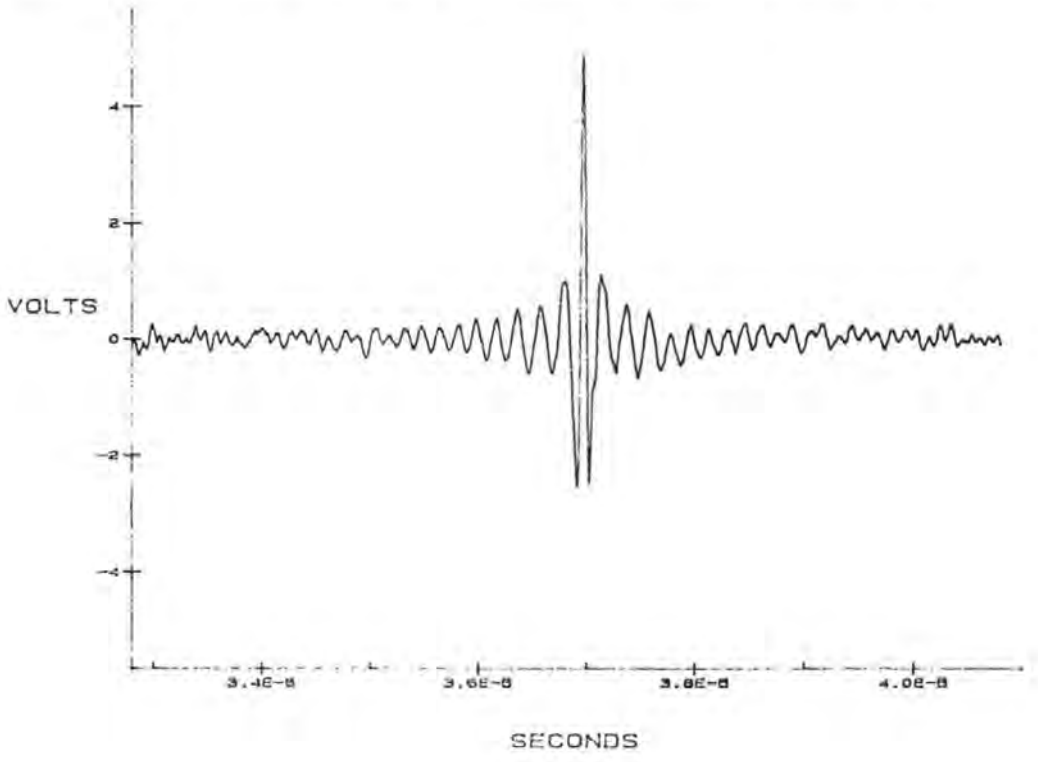

Theoretical acf amplitude (volts - arbitrary scale)

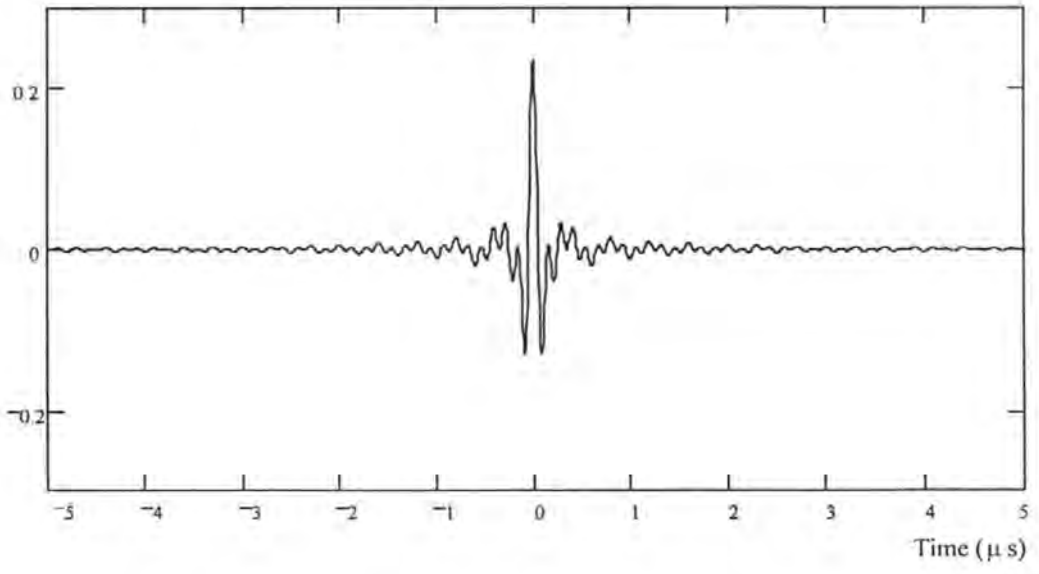

Figure 8-9. Experimental correlator output and theoretical form of the acf for a chirp pulse from 2 to 8 MHz in 15 μs (BT = 90)

8.5 Zeroth order non-heterodyning correlator using a photographic mask for second input

8.5.1 Operation in the Raman-Nath mode

If the second cell is replaced by a photographic mask, or transparency of power transmittance

$$t_2(x,t) = s_2(x) = [1 + a_2(x)]^2 \tag{8.35}$$

then the optical wave function at the output of this mask is, assuming DSBLC modulation of the signal inserted into the acousto-optic cell, obtained by modifying equation 8.19 to give

$$u_2(x,t) = J_o\left(\beta[1 + m\ a_1(x - Vt)]\right)\left(1 + a_2(t)\right)\cos(kz - \omega_o t)\,rect\left(\tfrac{x}{W}\right) \tag{8.36}$$

Actually, this system can be greatly simplified: the architecture shown in figure 8-10 will produce exactly the same result.

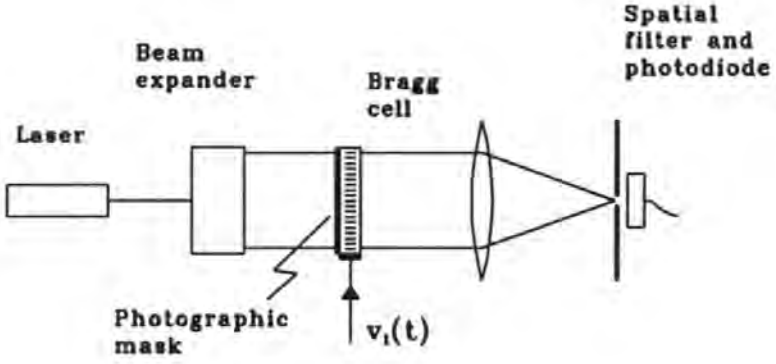

Figure 8-10. *Zeroth order correlator using photographic mask for one input.*

Expanding the Bessel function term in equation 8.36 gives

$$u_2(x,t) = \left\{1 - \tfrac{\beta^2}{2}[1 + m\ a_1(x - Vt)]^2\right\}\left\{1 + a_2(t)\right\}\cos(kz - \omega_o t)\,rect\left(\tfrac{x}{W}\right) \tag{8.37}$$

$$= \left\{1 - \frac{\beta^2}{4}\left[1 + 2m\ a_1(x - Vt) + m^2 a_1^2(x - Vt)\right]\right\}\left\{1 + a_2(x)\right\} \cos(kz - \omega_o t)\ rect\left(\frac{x}{W}\right) \tag{8.38}$$

$$= \left\{\begin{array}{l} \left(1 - \frac{\beta^2}{4}\right) - \frac{\beta^2 m}{2} a_1(x - Vt) - \frac{\beta^2 m^2}{4} a_1^2(x - Vt) + \left(1 - \frac{\beta^2}{4}\right) a_2(x) \\ \\ \quad - \frac{\beta^2}{2} a_1(x - Vt) a_2(x) - \frac{\beta^2 m^2}{4} a_1^2(x - Vt) a_2(x) \end{array}\right\} \cos(kz - \omega_o t) \tag{8.39}$$

The terms of interest are the first order terms $-\frac{\beta^2 m}{2} a_1(x - Vt) + \left(1 - \frac{\beta^2}{4}\right) a_2(x)$. If either the 0,+1 or the 0,-1 sub order is selected by the spatial filter at the photodetector, then the spatially integrated intensity of the light incident on the photodetector is given by

$$I(t) = \frac{1}{2} \int_{-\infty}^{+\infty} \left| \left(1 - \frac{\beta^2}{4}\right) a_2(x) - \frac{\beta^2 m}{2} a_1(x - Vt) \right|^2 \text{rect}\left(\frac{x}{W}\right) dx \tag{8.40}$$

$$I(t) = -\frac{\beta^2 m}{4}\left(1 - \frac{\beta^2}{4}\right) \int_{-\infty}^{+\infty} a_1(x - Vt)\, a_2(x)\, rect\left(\frac{x}{W}\right) dx$$

$$+ \frac{1}{2}\left(1 - \frac{\beta^2}{4}\right)^2 \int_{-\infty}^{+\infty} a_2^2(x)\, rect\left(\frac{x}{W}\right) dx \tag{8.41}$$

$$+ \frac{\beta^4 m^2}{8} \int_{-\infty}^{+\infty} a_1^2(x - Vt)\, rect\left(\frac{x}{W}\right) dx$$

The first term in equation 8.41 is the required correlation function, the second term is a constant term, and the third term produces a temporal plinth similar to that shown in figure 8-3. This correlator is simple and relatively easy to set up and use. There is no need for time reversal of one input signal. However, it is obviously limited to comparing an input signal with a fixed reference, performing the function of a matched filter. Clearly there are other ways of doing this, such as with a SAW matched filter. A possible use could be found by stacking a series of masks on top of each other (i.e. separated in the y direction), and using cylindrical optics to focus the light onto an array of photodetectors, also distributed in the y direction. This could provide a compact system for comparing an input signal with several references simultaneously.

8.5.2 Operation in the Bragg mode

Replacing $\frac{\beta^2}{4}$ by $\frac{\beta^2}{8}$ in the first term in equation 8.41 gives

$$I(t) = \frac{\beta^2 m}{8}\left(1-\frac{\beta^2}{8}\right)\int_{-\infty}^{+\infty} a_1(x-Vt)\,a_2(x)\,rect\left(\frac{x}{W}\right)dx \qquad (8.42)$$

8.6 First order non-heterodyning correlator

If we take the +1 diffraction order at the first cell and the on-axis diffraction order at the second Bragg cell we have the correlator, built at RNEC, described by Reeve and Wombwell [10], and shown in figure 8-11. As far as the whole system is concerned this on axis diffraction order is a zeroth order; as far as the second cell is concerned it is the -1 diffraction order, and this is how it is usually described.

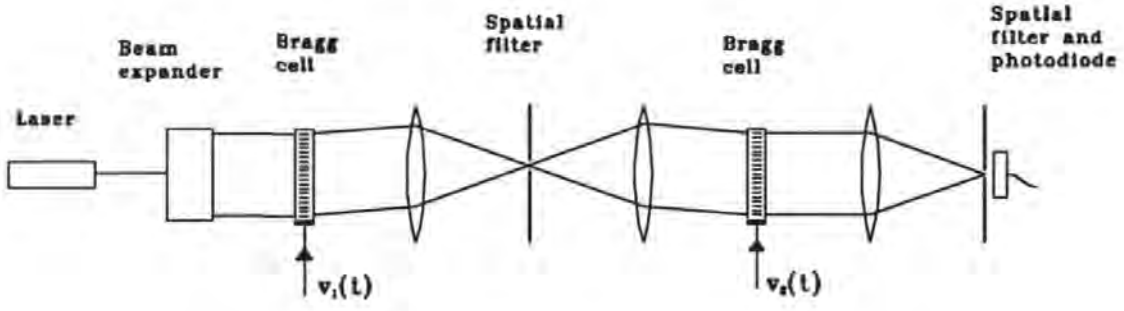

Figure 8-11. *First order, non-heterodyning, space integrating correlator.*

8.6.1 Operation using DSBLC modulation and Raman-Nath diffraction

In equation 8.15 the allowed value of p is +1, the allowed value of $p+q$ is 0, and so the allowed value of q is -1. Equation 8.15 therefore simplifies to

$$u_2(x,t) = J_1\left(\beta[1+m\,a_1(x-Vt)]\right)\,J_{-1}\left(\beta[1+m\,a_2(x+Vt)]\right)\cos\left(kz-(\omega_o+2\omega_c)t\right)rect\left(\frac{x}{W}\right) \qquad (8.43)$$

To a first approximation the first order Bessel function term is simply

$$\frac{\beta}{2}\left[1+m\,a(x-Vt)\right] \qquad (8.44)$$

The effective optical output from the second acousto-optic cell therefore approximates to

$$u_2(x,t) = \frac{\beta^2}{4}\left[1+ma_1(x-Vt)\right]\left[1+ma_2(x+Vt)\right]\cos(kz-\omega_o t)\,rect\left(\frac{x}{W}\right)$$

$$= \frac{\beta^2}{4}\left\{1+ma_1(x-Vt)+ma_2(x+Vt)+m^2 a_1(x-Vt)\,a_2(x+Vt)\right\}\cos(kz-\omega_o t)\,rect\left(\frac{x}{W}\right) \quad (8.45)$$

As in the zeroth order correlator, this expression includes terms in $a_1(x-Vt)$ and $a_2(x+Vt)$. These terms can be spatially selected at a photodiode placed in the Fourier transform plane of the second acousto-optic cell and the cross correlation function can be produced. However, it should be noticed that these terms are multiplied by $\frac{\beta^2 m}{4}$ rather than $\frac{\beta^2 m}{2}$ as in the case of the zeroth order correlator. Squaring by the photodiode will therefore produce an output correlation function with an amplitude which is four times smaller than that produced by the zeroth order correlator. The spatially integrated intensity of the light incident on the photodetector will be given by

$$I(t) = \left(\frac{\beta^2 m}{8}\right)^2 \int_{-\infty}^{+\infty} a_1(x-Vt)\; a_2(x+Vt)\; rect\left(\frac{x}{W}\right) dx \quad (8.46)$$

8.6.2 Operation in the Bragg mode

Since it is the first diffraction order being used at each cell, and from equation 8.33 we know that the approximation in terms of β is the same for both Raman-Nath and Bragg modes, the expression for $I(t)$, given in equation 8.46, remains unchanged.

8.6.3 Operation using DSBSC modulation and Raman-Nath diffraction

The first order non-heterodyning space integrating correlator is described by Rhodes [9]. The architecture of the optical system described by Rhodes is similar to that shown in figure 8-6, except that Rhodes uses just one acousto-optic cell, the second signal input being provided by a reference mask, or transparency, generated photographically. This limits the correlator to comparing an input signal with one reference signal, which may, in some applications be more appropriate. However the use of two Bragg cells offers a system of more general flexibility and is therefore analysed here. The following analysis can easily be

adapted for the replacement of the second cell by a photographic mask. A much more important difference is that Rhodes assumes the use of double sideband **suppressed** carrier modulation for imposing the signal of interest onto the carrier to be injected into the acousto-optic cell.

If the form of modulation used to insert the electronic signals is DSBSC then, in equations 8.15 and 8.43, the expressions $\left[1+ma_1(x-Vt)\right]$ and $\left[1+ma_2(x+Vt)\right]$ are replaced by $a_1(x-Vt)$ and $a_2(x+Vt)$. Equation 8.43 therefore becomes

$$u_2(x,t) = J_1\left(\beta a_1(x-Vt)\right) J_1\left(\beta a_2(x+Vt)\right) \cos\left[kz - (\omega_o+2\omega_c)t\right] rect\left(\tfrac{x}{W}\right) \tag{8.47}$$

If we then use the approximation

$$J_1(\xi) \approx \frac{\xi}{2} \tag{8.48}$$

the on axis diffraction order from the second acousto-optic cell approximates to

$$u_2(x,t) = \tfrac{\beta^2}{4}\, a_1(x-Vt)\, a_2(x+Vt) \cos\left[kz - (\omega_o+2\omega_c)t\right] rect\left(\tfrac{x}{W}\right) \tag{8.49}$$

If all of this diffraction order is passed onto the photodetector by the second spatial filter then the output of the photodetector will be a current of instantaneous amplitude proportional to the integrated intensity of the light incident on the photodetector given by

$$I(t) = \int_{cell} \tfrac{1}{2} \left| \tfrac{\beta^2}{4}\, a_1(x-Vt)\, a_2(x+Vt) \right|^2 rect\left(\tfrac{x}{W}\right) dx \tag{8.50}$$

This term is different from that obtained by Rhodes. The difference is that the above assumes that the whole of the on axis diffraction order is collected and spatially integrated by the photodetector whereas Rhodes uses a pinhole. To understand the effect of using a pinhole, we need to consider the spatial structure of the propagating wave at the photodetector plane. The optical wave function at the photodetector plane is the Fourier transform of the wave function at the output of the second Bragg cell. Therefore, considering the on axis diffraction order only, the wave function at the photodetector is given by

$$u_3(x',t') = \text{const} \times \int_{-\infty}^{+\infty} u_2(x,t)\, e^{-j\frac{kx'x}{f}}\, dx$$

$$= \text{const} \times \int_{-\infty}^{+\infty} a_1(x-Vt)\; a_2(x+Vt)\; \cos(kz-\omega_o t)\; Rect\left(\tfrac{x}{W}\right)\; e^{-j\frac{kx'x}{f}}\, dx \tag{8.51}$$

If we use a pinhole on the optical axis we are only interested in the value of this function at $x' = 0$, where

$$u_3(0,t') = \text{const} \times \int_{-\infty}^{+\infty} a_1(x-Vt)\; a_2(x+Vt)\; rect\left(\tfrac{x}{W}\right)\, dx\;\; \cos(kz-\omega_o t) \tag{8.52}$$

If we assume that the pinhole is small enough to treat $u_3(x',t)$ as constant across the width of the pinhole, then the intensity of the light passing through the pinhole is

$$I(t) = \text{const} \times \left| \int_{-\infty}^{+\infty} a_1(x-Vt)\; a_2(x+Vt)\; rect\left(\tfrac{x}{W}\right)\, dx \right|^2 \tag{8.53}$$

Comparing this with the term obtained with a large hole, passing all of the on axis diffraction order

$$I(t) = \text{const} \times \int_{-\infty}^{\infty} \left| a_1(x-Vt)\; a_2(x+Vt) \right|^2 rect\left(\tfrac{x}{W}\right)\, dx \tag{8.54}$$

we see how crucial the size of the spatial filter, at the photodetector, is. It is, of course, impossible to achieve the pinhole result exactly. If the hole was made small enough for the approximation used to be totally valid then the amount of light incident on the photodiode would become too small for a detectable electronic signal to be produced.

Clearly, neither of these outputs is a true correlation function. The true correlation function contains both amplitude and phase information. In both variations of this correlator the phase information is totally lost. In the limit as the spatial filter at the photodetector tends to a pinhole the output is the amplitude squared of the correlation function. As the hole becomes larger the function becomes something quite different. This correlator enables us to compare two signal in order to find out if they are the same but does not give us the wealth of information available from a true correlation function. To obtain the true correlation function other architectures must be used.

8.6.4 Operation in Bragg mode

It was shown earlier that for the first diffraction order the approximations for Raman-Nath and Bragg diffraction give rise to exactly the same expressions. The result of using Bragg diffraction and passing the whole of the on axis diffraction order from the second cell onto the photodetector is therefore given by equation 8.50. Again, the output will be larger when Bragg diffraction is used because of the larger value of β.

8.7 Heterodyning correlator using 0 and +1 diffraction orders

As the name suggests, the heterodyning correlator achieves its purpose by mixing two light waves of different frequencies. The two light waves are diffraction orders that are at different optical frequencies due to their Doppler shifts. The arrangement of the Bragg cells and lenses is basically the same as for the non-heterodyning correlator: the difference lies in the spatial filters used at the Fourier transform planes. Rhodes describes two such correlators. For the first heterodyning correlator, the 0 and +1 diffraction orders from the first cell are passed to the second cell. The -1 and 0 diffraction orders from the second cell due to the 0 and +1 diffraction orders respectively, from the first cell, will coincide and are selected in their entirety (i.e. the spatial filter used is not a pinhole) for spatial integration by the photodetector. This arrangement is shown in figure 8-12.

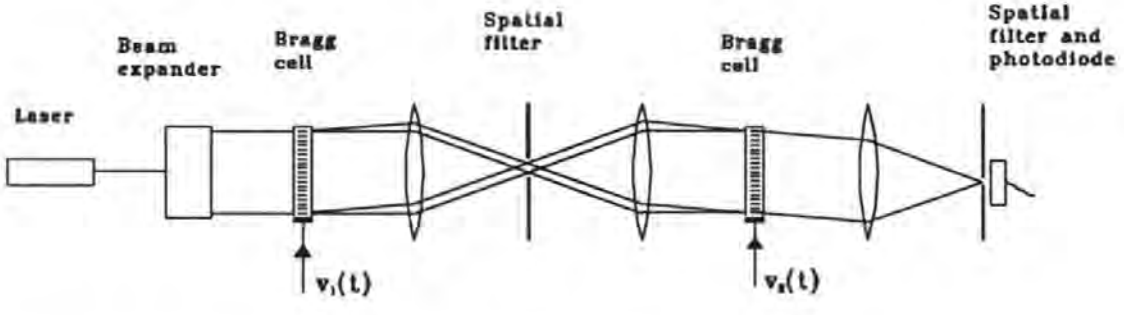

Figure 8-12. *Heterodyning correlator/convolver using 0 and +1 diffraction orders from first Bragg cell.*

There are some minor differences between the system depicted in figure 8-12 and that described by Rhodes. Rhodes introduces a 90° phase shift into the +1 diffraction order "for analytic convenience". We do not find this necessary. Rhodes uses just one Bragg cell, the

second signal input being provided by a reference mask generated photographically. As before, we analyse a two Bragg cell system.

8.7.1 Operation in the Raman-Nath mode using DSBSC modulation

Referring to equation 8.15, the allowed value of p+q is +1 (remembering the reversal of the positive x direction defined at the second acousto-optic cell). The allowed values of p and q are therefore p=+1, q=0 and p=0, q=+1. Hence, selecting the appropriate terms from equation 8.15, the wave function at the optical output of the second acousto-optic cell is given by

$$\begin{aligned} u_2(x,t) &= J_1\left(\beta s_1(x-Vt)\right) J_o\left(\beta s_2(x+Vt)\right) \cos\left(kz + K_c x - (\omega_o+\omega_c)t\right) \\ &+ J_o\left(\beta s_1(x-Vt)\right) J_1\left(\beta s_2(x+Vt)\right) \cos\left(kz + K_c x - (\omega_o-\omega_c)t\right) \end{aligned} \tag{8.55}$$

The optical signal incident on the photodetector is the sum of these two terms, which are at different optical frequencies due to their opposite Doppler shifts. To see how these two terms add, consider

$$\begin{aligned} A\cos(\omega_o+\omega_c)t + B\cos(\omega_o-\omega_c)t &= (A+B)\cos(\omega_c t)\cos(\omega_o t) - (A-B)\sin(\omega_c t)\sin(\omega_o t) \\ &= R(t)\cos(\omega_o t + \theta(t)) \end{aligned}$$

$$\text{where } R^2(t) = (A+B)^2\cos^2(\omega_c t) + (A-B)^2\sin^2(\omega_c t)$$

$$= A^2 + B^2 + 2AB\cos(2\omega_c t) \tag{8.56}$$

Using this result, and recalling that the photodetector will perform a spatial integration of the intensity of the incident light, we obtain the output current from the photodetector as proportional to

$$\begin{aligned} I(t) &= \tfrac{1}{2}\int_{-\infty}^{+\infty} \left[J_1\left(\beta s_1(x-Vt)\right) J_o\left(\beta s_2(x+Vt)\right)\right]^2 rect\left(\tfrac{x}{W}\right) dx \\ &+ \tfrac{1}{2}\int_{-\infty}^{+\infty} \left[J_o\left(\beta s_1(x-Vt)\right) J_1\left(\beta s_2(x+Vt)\right)\right]^2 rect\left(\tfrac{x}{W}\right) dx \\ &+ \left[\int_{-\infty}^{+\infty} J_1\left(\beta s_1(x-Vt)\right) J_o\left(\beta s_2(x+Vt)\right) J_o\left(\beta s_1(x-Vt)\right) J_1\left(\beta s_2(x+Vt)\right) rect\left(\tfrac{x}{W}\right) dx\right] \cos(2\omega_c t) \end{aligned} \tag{8.57}$$

The third term in this expression contains the required information as DSBSC modulation of a carrier which is twice the frequency of the carriers used in the acousto-optic cells. It can therefore be separated out using a bandpass filter and then demodulated to give

$$\int_{-\infty}^{+\infty} J_1\left(\beta s_1(x-Vt)\right)\, J_0\left(\beta s_2(x+Vt)\right)\, J_0\left(\beta s_1(x-Vt)\right)\, J_1\left(\beta s_2(x+Vt)\right) rect\left(\tfrac{x}{W}\right) \tag{8.58}$$

using the approximations

$$J_0(\xi) \approx 1 - \tfrac{\xi^2}{4} \quad \text{and} \quad J_1(\xi) \approx \tfrac{\xi}{2}$$

and, in order to avoid the expressions becoming too cluttered, writing $s(x-Vt)$ simply as s, this term approximates to

$$\int_{-\infty}^{+\infty} \tfrac{\beta s_1}{2}\left(1 - \tfrac{\beta^2 s_2^2}{4}\right)\left(1 - \tfrac{\beta^2 s_1^2}{4}\right)\tfrac{\beta s_2}{2}\, rect\left(\tfrac{x}{W}\right) dx$$

$$= \tfrac{\beta^2}{4}\int_{-\infty}^{+\infty}\left[\, s_1 s_2 - \tfrac{\beta^2}{4}\left(s_1^3 s_2 + s_1 s_2^3\right) + \tfrac{\beta^4}{16} s_1^3 s_2^3 \,\right] rect\left(\tfrac{x}{W}\right) dx \tag{8.59}$$

$$\approx \tfrac{\beta^2}{4}\int_{-\infty}^{+\infty} s_1(x-Vt)\, s_2(x+Vt)\, rect\left(\tfrac{x}{W}\right) dx$$

If DSBSC modulation is used, so that $s(t) = a(t)$, then the output of the system is

$$\tfrac{\beta^2}{4}\int_{-\infty}^{+\infty} a_1(x-Vt)\, a_2(x+Vt)\, rect\left(\tfrac{x}{W}\right) dx \tag{8.60}$$

which is the true correlation function of the input signals in both amplitude and phase. However this correlator suffers from the disadvantages of requiring very accurate alignment to ensure full coincidence of the two wave functions at the photodetector and additional electronic circuitry to extract the correlation function. The zeroth order non-heterodyning correlator produces this true correlation function much more easily.

8.7.2 Operation in the Bragg mode

The Bragg mode equivalent to expression 8.58 is

$$\int_{-\infty}^{+\infty} \sin\left(\tfrac{\beta}{2} s_1(x-Vt)\right) \cos\left(\tfrac{\beta}{2} s_2(x+Vt)\right) \cos\left(\tfrac{\beta}{2} s_1(x-Vt)\right) \sin\left(\tfrac{\beta}{2} s_2(x+Vt)\right) rect\left(\tfrac{x}{W}\right) \tag{8.61}$$

using the approximations

$$\cos(\xi) \approx 1 - \frac{\xi^2}{2} \quad \text{and} \quad \sin(\xi) \approx \xi$$

and again writing $s(x-Vt)$ simply as s, this becomes

$$\begin{aligned} &\int_{-\infty}^{+\infty} \tfrac{\beta s_1}{2} \left(1 - \tfrac{\beta^2 s_2^2}{8}\right)\left(1 - \tfrac{\beta^2 s_1^2}{8}\right) \tfrac{\beta s_2}{2} rect\left(\tfrac{x}{W}\right) dx \\ &\approx \tfrac{\beta^2}{4} \int_{-\infty}^{+\infty} s_1(x-Vt)\, s_2(x+Vt)\, rect\left(\tfrac{x}{W}\right) dx \end{aligned} \tag{8.62}$$

i.e. the expression is exactly the same as for the Raman-Nath mode.

8.8 Heterodyning correlator using both first diffraction orders

The second heterodyning correlator described by Rhodes (derived from a description by Sprague [32]) makes use of the +1 and -1 diffraction orders from the first cell, and uses a pinhole at the photodetector. The optical output, selected by a spatial filter on the system axis, is the -1 order from the 2nd cell due to the +1 order from the first cell plus the +1 order from the second cell due to the -1 order from the first cell. (Remember the reversal of the x axis due to the imaging process from the first to the second cell.) Since this correlator uses both the +1 and -1 diffraction orders at each stage, the acousto-optic cells will be adjusted normal to the optical axis so as to make them equal in amplitudes. The cells can therefore only be operated in Raman-Nath mode.

Referring to equation 8.15, the allowed value of $p+q$ is 0. The allowed values of p and q are $p = +1$, $q = -1$ and $p = -1$, $q = +1$. Hence, selecting the appropriate terms from equation 8.15, the component of $u_2(x,t)$ propagating along the optical axis is

$$u_2(x,t) = \left\{ \begin{array}{l} \left[J_1(\beta s_1(x - Vt))\ J_1(\beta s_2(x + Vt)) \right] \cos(kz - (\omega_o + 2\omega_c)t) \\ \\ + \left[J_1(\beta s_1(x - Vt))\ J_1(\beta s_2(x + Vt)) \right] \cos(kz - (\omega_o - 2\omega_c t)) \end{array} \right\} rect\left(\frac{x}{W}\right) \qquad (8.63)$$

$$= -2\ J_1(\beta s_1(x - Vt))\ J_1(\beta s_2(x + Vt)) \cos(2\omega_c t)\ \cos(kz - \omega_o t)\ rect\left(\frac{x}{W}\right)$$

How this signal can then be used depends on the type of modulation used in generating the input signals.

8.8.1 Operation using DSBLC modulation

If we use double sideband large carrier modulation (s(t) = [1+ma(t)]) and use a spatial filter that passes a whole diffraction sub order (i.e. not a pinhole), then equation 8.63 becomes

$$u_2(x,t) = \frac{-\beta^2}{2}[1 + ma_1(x - Vt)][1 + ma_2(x + Vt)] \cos(2\omega_c t)\ \cos(kz - \omega_o t)$$

$$= \frac{-\beta^2}{2}\left\{1 + m[a_1(x - Vt) + a_2(x + Vt)] + m^2 a_1(x - Vt)\, a_2(x + Vt)\right\} \cos(2\omega_c t)\ \cos(kz - \omega_o t) \qquad (8.64)$$

A spatial filter can then select the appropriate sub-order of this zeroth diffraction order to leave

$$\frac{-\beta^2 m}{4}\left[a_1(x - Vt) + a_2(x + Vt)\right] \cos(2\omega_c t)\ \cos(kz - \omega_o t) \qquad (8.65)$$

Spatial integration at the photodetector then gives an expression similar to equation 8.23

$$I(t) = \frac{1}{2}\int_{-\infty}^{+\infty} \left(\frac{\beta^2 m}{4}\right)^2 \left| a_1(x - Vt) + a_2(x + Vt) \right|^2 \cos^2(2\omega_c t)\ rect\left(\frac{x}{W}\right) \qquad (8.66)$$

the difference being the $\cos^2(2\omega_c t)$ term which can be written as $\frac{1}{2}(1 + \cos(4\omega_c t))$. Just as with the general all order correlator and the zeroth order non-heterodyning correlator, this can be low pass filtered to leave the true correlation function

$$I(t) = \frac{1}{2}\left(\frac{\beta^2 m}{f}\right)^2 \int_{-\infty}^{+\infty} a_1(x-Vt)\; a_2(x+Vt)\; rect\left(\frac{x}{W}\right) dx \tag{8.67}$$

8.8.2 Operation using DSBSC modulation

Rhodes assumes the use of double sideband suppressed carrier modulation and a pinhole at the photodetector. The wave function at the photodetector plane is the Fourier transform of $u_2(x,t)$, given by

$$u_3(x',t) = const \times \int_{-\infty}^{+\infty} u_2(x,t)\; e^{-j\frac{k x x'}{f}}\; dx \tag{8.68}$$

Then, making the same approximations for sampling of this by the pinhole as before, we find that the output current from the photodetector is given by

$$I(t) = \left(\frac{\beta^2}{f}\right)^2 \left| \int_{cell} 2\; J_1\left(\beta s_1(x-Vt)\right)\; J_1\left(\beta s_2(x+Vt)\right) dx \right|^2 \cos^2(2\omega_c t) \tag{8.69}$$

$$\approx \left(\frac{\beta^2}{f}\right)^2 \left| \int_{cell} s_1(x-Vt)\; s_2(x+Vt)\; dx \right|^2 \left(1 + \cos(4\omega_c t)\right)$$

and by use of a low pass filter we can extract the term

$$\left| \int_{cell} s_1(x-Vt)\; s_2(x+Vt)\; dx \right|^2 \tag{8.70}$$

This contains the amplitude information present in the correlation function but, unlike the first heterodyning correlator described above, it contains no phase information.

8.9 Summary

There are many different space-integrating correlators described in the literature and differing accounts have been offered to explain their operation. This chapter has developed a general framework for the analysis of any one dimensional space-integrating correlator for which the diffraction process at the acousto-optic cell(s) can be described by Raman-Nath or

Bragg diffraction. The most important expression in this chapter is equation 8.15, from which the operation of all the various possible correlators can be derived as special cases. This has been illustrated by applying equation 8.15 to a representative, though not exhaustive, selection of different correlators. The analysis offered here is significantly different from that offered by some papers, such as [9,32]. These more recent papers made approximations that lead to ignoring the zeroth diffraction order and a theoretical model that could not explain the operation of all possible correlators. The experimental work presented clearly demonstrates that a zeroth order correlator does produce the true correlation function as predicted, although the signal bandwidth is limited by the speed of response of the large area photodiode required to capture all of the diffraction sub-orders containing the signal information.

As far as the correlator output is concerned, the difference between Raman-Nath and Bragg diffraction is simply one of output signal amplitude, and hence output signal to noise ratio. Where possible, using high Q cells operating in the Bragg mode can be expected to give better results than operating low Q cells in the Raman-Nath mode. The type of modulation used to impose the information signal onto the carrier input to the acousto-optic cells is more critical. The results achieved when double sideband large carrier (DSBLC) modulation is used will not be obtained when double sideband suppressed carrier (DSBSC) modulation is used and vice versa. The zeroth order correlator, for example, only works if DSBLC modulation is used. Rhodes [9] describes only heterodyning correlators as giving the true correlation function. This is because he assumes DSBSC modulation throughout his paper.

9. Time-integrating correlators - theory

9.1 Introduction

Time-integrating acousto-optic correlators can form the true correlation function without the requirement for time reversal of one of the input signals that is such a drawback in space integrating correlators. In time-integrating systems, the correlation function is formed as a spatial function at a photodetector array which integrates the light incident on it over a period of time. If the time taken to transfer the information off the array and clear the integrating elements is short relative to the integration time then successive integrations can be added to give longer effective integration times. It can give a true continuous correlation function over an indefinitely long integration time. This is an extremely important advantage over both space integrating acousto-optic and FFT based digital correlators, as discussed in section 2.2.

A number of different time-integrating correlators have been described in the literature. This chapter discusses three different correlators. The material presented here is based mainly on Vanderlugt's descriptions ([11] - chapter 14), but with some significant additions and with some differences of approach to the analysis introduced in order to bring out points important to the concluding discussion.

9.2 Correlator due to Montgomery

The first time-integrating correlator described was due to Montgomery [9,11,36]. This uses either two acousto-optic cells positioned one after the other (optical sequence) as close together as possible, or one cell with two transducers causing acoustic waves propagating in opposite directions so that a broad collimated laser beam interacts with first one acoustic signal and then the other, as shown in figure 9-1. It can be shown [32] that the required cross correlation function is formed by time integration at the photodetector array as the amplitude modulation (DSBSC) envelope of a spatial carrier. It is possible to filter out this modulated carrier and then recover the required correlation function by demodulation. However, this

makes the system more complicated and requires a larger number of elements in the array to sample the modulated carrier rather than just the baseband ccf.

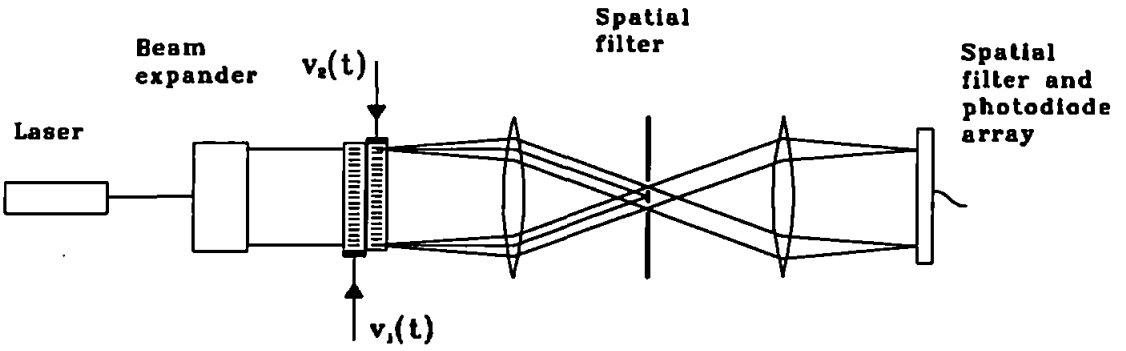

Figure 9-1. Time-integrating correlator due to Montgomery.

Another disadvantage is that the acousto-optic cells must be aligned normal to the incident light, in the Raman-Nath mode, since the correlator works by summing the composite plus one and minus one diffractions orders from the acousto-optic cell combination. This offers much lower diffraction efficiency than the Bragg mode.

9.3 Correlator due to Sprague and Koliopoulos

The second time-integrating correlator architecture described is that due to Sprague and Koliopoulos [19] and also described by VanderLugt [11] and Rhodes [9]. It is shown in figure 9-2.

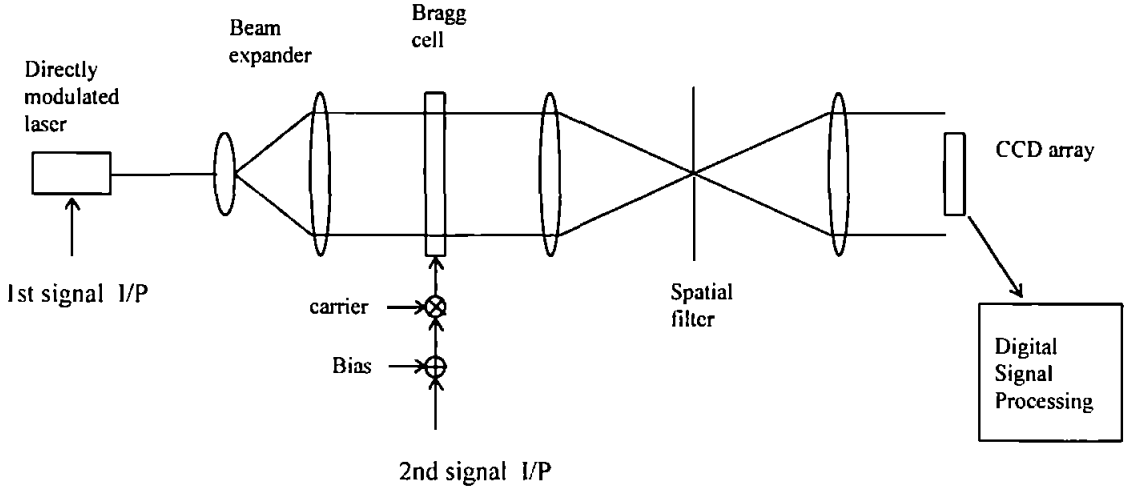

Figure 9-2. Time-integrating correlator due to Sprague and Koliopoulos.

9.3.1 Use of an acousto-optic cell for the first signal input

The original description given by Sprague and Koliopoulos uses an acousto-optic cell for the first signal input as shown in figure 9-3.

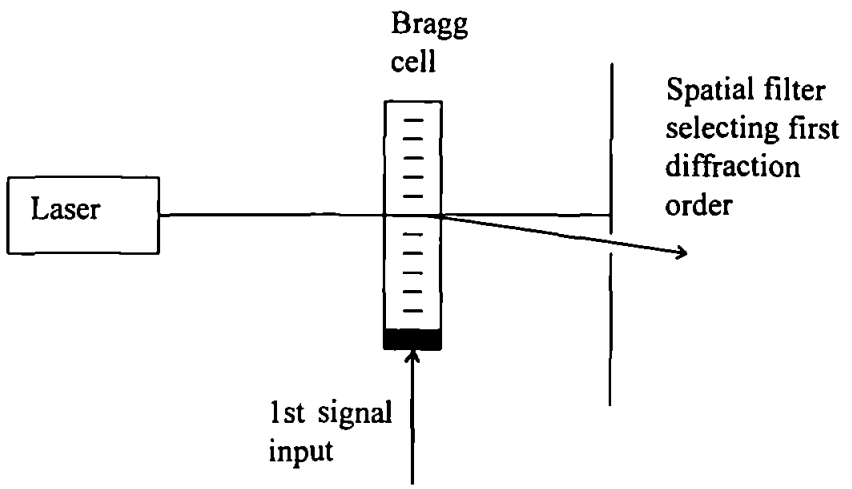

Figure 9-3. Use of Bragg cell for first signal input.

The signal bandwidth is severely limited if this method is used. For this method to be effective the width of the laser and the acoustic wavelength in the acousto-optic interaction medium must be such that the laser beam is sampling a small part of a cycle of the baseband signal. Young and Yao ([35] - figure 4) give a theoretically derived graph of normalised output intensity in the first diffraction order against modulation frequency. This graph shows the 3 dB modulation bandwidth to be such that $f_{3dB}\,\tau \approx 0.75$, where f_{3dB} is the modulation bandwidth and τ is the transit time of the acoustic signal through the Gaussian optical beam, found by dividing the $\frac{1}{e^2}$ intensity diameter of the optical beam by the acoustic velocity. For a HeNe laser with a $\frac{1}{e^2}$ intensity diameter of 0.75 mm and a TeO_2 acousto-optic cell with an acoustic velocity of 617 m/s this gives a modulation bandwidth of 617 kHz. Brooks [37] plots experimental results for the modulation frequency response of a TeO_2 cell showing a 3 dB modulation bandwidth of 800 kHz, using a slightly narrower laser beam with a $\frac{1}{e^2}$ intensity diameter of 0.5 mm. This bandwidth can be improved by focusing the laser to a smaller spot size and by using an acousto-optic interaction medium with a higher acousto-optic velocity. However, the narrowness of the spot to which the laser beam can be focused is

limited by diffraction, especially since it is the average spot size over the full thickness of the active part of the acousto-optic cell that is important. Using a GaP cell, with an acoustic velocity of 6320 ms^{-1} could, in principle, increase the bandwidth by a factor of 10, but, as will be shown later, the limited diffraction efficiency of GaP cells is such that it may not be possible to impose the correct type of modulation (intensity modulation as opposed to amplitude modulation) onto the laser beam. It is therefore clear that this technique cannot provide for the bandwidths of the order of 1 GHz that we ultimately need to achieve. Further disadvantages are waste of the laser output due to the limited diffraction efficiency of the acousto-optic cell and the considerable increase in complexity size and cost of attempts to increase the bandwidth. Introducing the first signal by means of an acousto-optic cell is not a viable option. It is not surprising that, as laser diodes capable of direct intensity modulation have become available, VanderLugt and Rhodes both describe much simpler and cheaper systems using direct intensity modulation of the laser.

9.3.2 Analysis of operation

We now demonstrate that the correlator shown in figure 9-2 will produce the required ccf of two signal $s_1(t)$ and $s_2(t)$. The laser is intensity modulated and so its output intensity is

$$I_1(t) = \alpha\left(B_1 + s_1(t)\right) \tag{9.1}$$

where B_1 is a bias term and α is a gain term. This modulated beam is expanded out and forms the input to the acousto-optic cell. At the acousto-optic cell, adjusted to operate in the Bragg mode, we use the first diffraction order. The amplitude of this first diffraction order is given by [11,33]

$$A_2(x,t) = \sqrt{I_1(t)}\sin\left(\beta\left[B_2 + s_2\left(t-\frac{x}{V}\right)\right]\right)\sqrt{W(x)} \tag{9.2}$$

where B_2 is a bias term and β is a gain term or modulation index, x is measured from the centre of the illuminated portion of the acousto-optic cell, V is the acoustic velocity and $W(x)$ is an intensity window function due principally to the profile of the laser beam. It is assumed that the signal to the laser has been delayed by the time taken by $s_2(t)$ to propagate across the acousto-optic cell to the centre of the illuminated portion. The intensity of the first diffraction order is therefore

$$I_2(x,t) = I_1(t)\,\sin^2\left(\beta\left[B_2 + s_2\left(t-\frac{x}{V}\right)\right]\right) W(x) \qquad (9.3)$$

To achieve the required correlation we need $I_2(t)$ to be a linear function of $s_2\left(t-\frac{x}{V}\right)$. i.e. we need the first diffraction order to be intensity modulated by the acousto-optic cell. The d.c. bias must be adjusted so that $\sin^2\left(\beta\left[B_2 + s_2\left(t-\frac{x}{V}\right)\right]\right)$ is a linear function of $s_2\left(t-\frac{x}{V}\right)$. If we consider the d.c. bias condition, in the absence of the ac signal, we have, omitting the spatial windowing term for the sake of clarity

$$I_2 = I_1 \sin^2(\beta B_2) \qquad (9.4)$$

By considering the shape of the $\sin^2$ function we see that I_2 is a linear function of the input signal amplitude at 50% diffraction efficiency, when $\beta B_2 = \frac{\pi}{4}$. 50% diffraction efficiency is usually the most that can be achieved in practice. (Taking the drive power to the acousto-optic cell above this point will usually destroy the cell.) This means that, in practice, we want to drive the cell at its maximum power rating, obtaining the highest available diffraction efficiency. This is easy to set up as, at 50% diffraction efficiency the intensity of the first diffraction order is the same as that of the zeroth order. Now, equation 9.3 can be rewritten as

$$I_2(x,t) = \frac{I_1(t)}{2}\left\{1-\cos\left(2\beta\left[B_2 + s_2\left(t-\frac{x}{V}\right)\right]\right)\right\} W(x) \qquad (9.5)$$

Expanding out further

$$I_2(x,t) = \frac{I_1(t)}{2}\left\{1-\cos(2\beta B_2)\cos\left(2\beta s_2\left(t-\frac{x}{V}\right)\right) + \sin(2\beta B_2)\sin\left(2\beta s_2\left(t-\frac{x}{V}\right)\right)\right\} W(x) \qquad (9.6)$$

Now, if $\beta B_2 = \frac{\pi}{4}$, then $2\beta B_2 = \frac{\pi}{2}$, $\cos(2\beta B_2) = 0$, $\sin(2\beta B_2) = 1$, and

$$I_2(x,t) = \frac{I_1(t)}{2}\left\{1+\sin\left(2\beta s_2\left(t-\frac{x}{V}\right)\right)\right\} W(x) \tag{9.7}$$

Substituting equation 9.1 into equation 9.7

$$I_2(x,t) = \frac{1}{2}\alpha\left(B_1+s_1(t)\right)\left\{1+\sin\left(2\beta s_2\left(t-\frac{x}{V}\right)\right)\right\} W(x) \tag{9.8}$$

or

$$I_2(x,t) = \frac{\alpha W(x)}{2}\left\{B_1 + s_1(t) + B_1\sin\left(2\beta s_2\left(t-\frac{x}{V}\right)\right) + s_1(t)\sin\left(2\beta s_2\left(t-\frac{x}{V}\right)\right)\right\} \tag{9.9}$$

This first diffraction order is imaged onto the photodetector array. The sense of x is reversed and the scale of x is changed according to the ratio of the focal lengths of the two imaging lenses. The incident light intensity is integrated over a period of time ΔT by the array. The total light energy stored by the array in time ΔT is

$$E_{\Delta T}(x) = \int_{\Delta T} I_2(x,t)\,dt \tag{9.10}$$

Now, the first of the four terms in the large brackets on the right hand side of equation 9, B1, integrates over time to give a spatially invariant term

$$\int_{\Delta T} B_1\,dt = B_1\,\Delta T \tag{9.11}$$

The second and third terms integrate to zero, if ΔT contains many cycles of $s_1(t)$ and $s_2(t)$ and they have zero means. Hence

$$E_{\Delta T}(x) = \frac{1}{2}\alpha\,B_1\,\Delta T\,W(x) + \frac{1}{2}\alpha\,W(x)\int_{\Delta T} s_1(t)\sin\left(2\beta s_2\left(t-\frac{x}{V}\right)\right)dt \tag{9.12}$$

If $\beta s_2(t)$ is small relative to βB_2 , so that variations in the intensity of the first diffraction order stay in the linear part of the $\sin^2$ curve, then

$$\sin\left(2\beta s_2\left(t-\frac{x}{V}\right)\right) \approx 2\beta s_2\left(t-\frac{x}{V}\right) \tag{9.13}$$

and

$$E_{\Delta T}(x) = \frac{1}{2}\alpha B_1 \Delta T W(x) + \alpha\beta W(x)\int_{\Delta T} s_1(t)\, s_2\left(t-\frac{x}{V}\right) dt \tag{9.14}$$

The first term is a spatially invariant d.c. level proportional to the integration time, that can easily be subtracted in post processing. The second term is the required ccf.

9.4 The electronic reference correlator

One disadvantage of the correlator due to Sprague and Koliopoulos is that if the two received signal are reduced to baseband, then two correlators are required to handle the I (in phase) and Q (quadrature) channels. A variant is possible, however, in which both signals are left on low frequency carriers, preserving both amplitude and phase information in both signals. One electronic reference correlator can then perform a single complex correlation, the output of which is the same as that achieved by summing the outputs of the I and Q baseband correlator outputs. Consider the signal arriving at one receiver input. If the receiver bandwidth is small relative to its centre frequency then it can be shown (see e.g. [13]) that the received signal can be described as

$$s_I(t)\cos(\omega_r t) - s_Q(t)\sin(\omega_r t) \tag{9.15}$$

where $s_I(t)$ and $s_Q(t)$ are baseband signals and ω_r is the centre angular frequency. If two baseband correlators are to be used, then splitting the signal and multiplying by $\cos(\omega_r t)$ in the I channel and $\sin(\omega_r t)$ in the Q channel will yield the baseband signals $s_I(t)$ and $s_Q(t)$. If one electronic reference correlator is to be used then the received signal, which can also be expressed as $s(t)\cos[\omega_r t + \theta(t)]$, can be downconverted to some IF frequency, ω_o, by multiplying by $\cos(\omega_L t)$, where $\omega_L = \omega_r - \omega_o$, and low pass filtering to give $s(t)\cos[\omega_o t + \theta(t)]$. For the electronic reference correlator, the IF frequencies used for the two inputs differ by a frequency ω_c. If the IF frequency used for the laser input is ω_o, the IF frequency used for the acousto-optic cell input is $\omega_o + \omega_c$. A d.c. bias is added to the laser

input and a carrier tone bias component, at frequency ω_c is added to the acousto-optic cell input. Hence the input to the laser is

$$B_1 + s_1(t)\cos\left[\omega_o t + \theta_1(t)\right] \tag{9.16}$$

and the input to the acousto-optic cell is

$$B_2\cos(\omega_c t) + s_2(t)\cos\left[(\omega_o + \omega_c)t + \theta_2(t)\right] \tag{9.17}$$

A second major difference between the baseband correlator and this correlator lies in the signal power input to the acousto-optic cell. For the baseband correlator the acousto-optic cell must be *intensity* modulated by the input signal, requiring that it be operated at 50% diffraction efficiency. For the electronic reference correlator the acousto-optic cell must be *amplitude* modulated, requiring operation at 10 to 20% diffraction efficiency. Following the operation of the correlator through as before, we obtain the intensity of the laser output

$$I_1(t) = \alpha\left\{B_1 + s_1(t)\cos\left[\omega_o t + \theta_1(t)\right]\right\} \tag{9.18}$$

The expression given above for the input to the acousto-optic cell can be expanded out to

$$B_2\cos(\omega_c t) + s_2(t)\cos\left[\omega_o t + \theta_2(t)\right]\cos(\omega_c t) - s_2(t)\sin\left[\omega_o t + \theta_2(t)\right]\sin(\omega_c t)$$

$$= \left\{B_2 + s_2(t)\cos\left[\omega_o t + \theta_2(t)\right]\right\}\cos(\omega_c t) - s_2(t)\sin\left[\omega_o t + \theta_2(t)\right]\sin(\omega_c t)$$

$$= R(t)\cos\left[\omega_c t + \phi(t)\right] \tag{9.19}$$

where $R^2(t) = \left\{B_2 + s_2(t)\cos\left[\omega_o t + \theta_2(t)\right]\right\}^2 - s_2^2(t)\sin^2\left[\omega_o t + \theta_2(t)\right]$

The amplitude of the first diffraction order from the acousto-optic cell is therefore

$$A_2(x,t) = \sqrt{I_1(t)}\sin\left[\beta R\left(t-\frac{x}{V}\right)\right]\sqrt{W(x)} \tag{9.20}$$

For low diffraction efficiency (small β) this approximates to

$$A_2(x,t) = \sqrt{I_1(t)}\ \beta R\left(t-\frac{x}{V}\right)\sqrt{W(x)} \tag{9.21}$$

Hence, the intensity of the first diffraction order output from the acousto-optic cell is

$$I_2(x,t) = I_1(t)\ \beta^2\ R^2\left(t-\frac{x}{V}\right)W(x) \tag{9.22}$$

$$= \alpha\beta^2 W(x)\left\{B_1 + s_1(t)\cos\left[\omega_o t + \theta_1(t)\right]\right\}$$

$$\times \left\{\left(B_2 + s_2\left(t-\frac{x}{V}\right)\cos\left[\omega_o\left(t-\frac{x}{V}\right)+\theta_2\left(t-\frac{x}{V}\right)\right]\right)^2 - s_2^2\left(t-\frac{x}{V}\right)\sin^2\left[\omega_o\left(t-\frac{x}{V}\right)+\theta_2\left(t-\frac{x}{V}\right)\right]\right\}$$

$$= \alpha\beta^2 W(x)\left\{B_1 + s_1(t)\cos\left[\omega_o t + \theta_1(t)\right]\right\}$$

$$\times \left\{B_2^{\,2} + s_2^{\,2}\left(t-\frac{x}{V}\right) + 2B_2 s_2\left(t-\frac{x}{V}\right)\cos\left[\omega_o\left(t-\frac{x}{V}\right)+\theta_2\left(t-\frac{x}{V}\right)\right]\right\}$$

$$I_2(x,t) = \alpha\beta^2 W(x)\left\{\begin{array}{l} B_1 B_2^{\,2} \\ + B_1 s_2^{\,2}\left(t-\frac{x}{V}\right) \\ + 2B_1 B_2 s_2\left(t-\frac{x}{V}\right)\cos\left[\omega_o\left(t-\frac{x}{V}\right)+\theta_2\left(t-\frac{x}{V}\right)\right] \\ + B_2^{\,2} s_1(t)\cos\left[\omega_o t + \theta_1(t)\right] \\ + s_1(t) s_2^{\,2}\left(t-\frac{x}{V}\right)\cos\left[\omega_o t + \theta_1(t)\right] \\ + 2B_2 s_1(t) s_2\left(t-\frac{x}{V}\right)\cos\left[\omega_o t + \theta_1(t)\right]\cos\left[\omega_o\left(t-\frac{x}{V}\right)+\theta_2\left(t-\frac{x}{V}\right)\right] \end{array}\right\} \tag{9.23}$$

$I_2(x,t)$ is then integrated over a period of time ΔT at the photodetector array. This time integration has different effects on the six terms making up the above expression. The first term will give a "d.c." spatially invariant term proportional to ΔT . The second will also produce a spatially invariant term proportional to the power of $s_2(t)$ as well as ΔT. The third, fourth and fifth terms are sinusoidal functions of time and will integrate to zero. The final term expands out to give

$$B_2\, s_1(t) s_2\left(t-\frac{x}{V}\right)\left\{\cos\left[\frac{\omega_o x}{V}+\theta_1(t)-\theta_2\left(t-\frac{x}{V}\right)\right] + \cos\left[2\omega_o t-\frac{\omega_o x}{V}+\theta_1(t)+\theta_2\left(t-\frac{x}{V}\right)\right]\right\} \quad (9.24)$$

the second part of which will again integrate to zero. Hence, the photodetector array output is

$$E_{\Delta T}(x) = \int_{\Delta T}\alpha\,\beta^2\, W(x)\left\{B_1\, B_2^{\,2}+B_1\, s_2^{\,2}\left(t-\frac{x}{V}\right)+B_2\, s_1(t) s_2\left(t-\frac{x}{V}\right)\cos\left[\frac{\omega_o x}{V}+\theta_1(t)-\theta_2\left(t-\frac{x}{V}\right)\right]\right\} dt \quad (9.25)$$

or

$$E_{\Delta T}(x) = C\, W(x)\,\Delta T + \alpha\,\beta^2\, B_2\, W(x)\int_{\Delta T} s_1(t) s_2\left(t-\frac{x}{V}\right)\cos\left[\frac{\omega_o x}{V}+\theta_1(t)-\theta_2\left(t-\frac{x}{V}\right)\right] dt \quad (9.26)$$

where C is a constant. Hence, the required complex correlation function, the second term in the above expression, appears as DSBSC amplitude modulation of a spatial carrier of spatial angular frequency $\frac{\omega_o}{V}$. This can be separated from the constant background terms by bandpass filtering. Demodulation, by multiplication by $\cos\left(\frac{\omega_o x}{V}\right)$ and low pass filtering, then yields

$$\int_{\Delta T} s_1(t) s_2\left(t-\frac{x}{V}\right)\cos\left[\theta_1(t)-\theta_2\left(t-\frac{x}{V}\right)\right] dt \quad (9.27)$$

By considering the complex signals

$$\begin{aligned} \mathbf{s}_1(t) &= s_1(t)e^{j\theta_1(t)} \\ \mathbf{s}_2(t) &= s_2(t)e^{j\theta_2(t)} \end{aligned} \tag{9.28}$$

we have

$$\begin{aligned} Re\left\{\mathbf{s}_1(t)\mathbf{s}_2^*\left(t-\tfrac{x}{V}\right)\right\} &= Re\left\{s_1(t)e^{j\theta_1(t)}\, s_2\left(t-\tfrac{x}{V}\right)e^{-j\theta_2\left(t-\frac{x}{V}\right)}\right. \\ &= Re\left\{\, s_1(t)s_2\left(t-\tfrac{x}{V}\right)e^{-j\left[\theta_1(t)-\theta_2\left(t-\frac{x}{V}\right)\right]}\right\} \end{aligned} \tag{9.29}$$

Hence, the complex correlation function (equation 9.27) can also be written as

$$Re\left\{\int_{\Delta T}\mathbf{s}_1(t)\mathbf{s}_2^*\left(t-\tfrac{x}{V}\right)dt\right\} \tag{9.30}$$

By writing $s(t) = s_I(t) + j\, s_Q(t)$, so that

$$\begin{aligned} Re\left\{\mathbf{s}_1(t)\mathbf{s}_2^*\left(t-\tfrac{x}{V}\right)\right\} &= Re\left\{\left(s_{I1}(t)+ js_{Q1}(t)\right)\left(s_{I2}\left(t-\tfrac{x}{V}\right)- js_{Q2}\left(t-\tfrac{x}{V}\right)\right)\right\} \\ &= s_{I1}(t)\, s_{I2}\left(t-\tfrac{x}{V}\right) + s_{Q1}(t)\, s_{Q2}\left(t-\tfrac{x}{V}\right) \end{aligned} \tag{9.31}$$

we see that the real part of this complex correlation function is equal to the sum of the I and Q correlations obtained in a system using 2 baseband correlators.

9.5 Discussion

The use of a time-integrating acousto-optic correlator for detecting and analysing wide bandwidth spread spectrum signals has recently been described by an American team working jointly in the Electro-optics Department, Dynetics, Inc., Hunstville, AL, USA and the US Army Research Laboratory (The Harry Diamond Laboratory), Adelphi, MD, USA. [39,40,41] This team describes a system in which a time-integrating acousto-optic correlator is used to generate the acf of a single receiver channel. They have not, so far, considered cross correlation of two receiver outputs or the signal processing involving the TDFCSD described here. However, the correlator described is exactly what is required to generate the initial time windowed ccf. The correlator described is the electronic reference correlator and

while neither this American team nor VanderLugt spell them out, there are a number of very good reasons why the electronic reference correlator is preferable to the baseband correlator.

It has already been pointed out that, since it performs a complex correlation, one electronic reference correlator can be used where two baseband time-integrating correlators would be required. The electronic reference correlator is a little more complicated and requires more sophisticated post detection processing but the baseband correlator system requires two channels. In terms of complexity the two systems do not differ greatly. A much more important advantage lies in the achievable bandwidth. For the baseband correlator, the acousto-optic cell must be *intensity* modulated - it must be operated at around 50% diffraction efficiency. This can readily be achieved with TeO_2 cells, but these only have bandwidths of the order of a few tens of MHz. To achieve wider bandwidths we need to consider other materials such as GaP. GaP cells with bandwidths of the order of 2 GHz are advertised, but even the most optimistic of manufacturers claims for diffraction efficiency do not exceed 30%. A good baseband time-integrating acousto-optic correlator cannot therefore be built using GaP cells. The electronic reference correlator, however, relies on *amplitude* modulation and 10 to 20% diffraction efficiency is therefore perfectly acceptable. It is therefore possible to build an electronic reference correlator with a bandwidth of the order of 1 GHz. Anderson et. al. [39,40,41] give a detailed description of the system to be built with specifications of the various components, but no practical results. The design presented is for a "brassboard" system with a bandwidth of 500 MHz and the specifications are very high. The acousto-optic cell, a shear GaP cell with a bandwidth of 1 GHz has been custom designed and fabricated, and a high laser power of 100 mW is required because of the low diffraction efficiency of the acousto-optic cell. The team's 1994 [41] paper states that "an acousto-optic correlator has been designed and will be fabricated." An interim proof-of-concept demonstration of the correlator was planned for summer 1994 with a modularised demonstration scheduled for 1995. No results have been published to date, but they will be of considerable interest when they are. The work of this American team clearly compliments the work described in this thesis.

10. Experimental results from a time-integrating acousto-optic correlator

10.1 Introduction

Two similar time-integrating correlators, of the type described in section 9.3, were built. They are shown in figures 10-1 and 10-2. They both used the same TeO_2 Optilas OPT1 acousto-optic cell with a centre frequency of 45 MHz and a bandwidth of approximately 30 MHz. Since double sideband modulation is used in the acousto-optic cell this limits the effective bandwidth of the correlator to approximately 15 MHz. The input signals were generated using 2 Analogic D2045 polynomial waveform synthesisers, one triggered off the other. They generated identical FMCW signals, by repeating an up chirp, but with the signal fed to the laser delayed by the time taken for the signal fed to the acousto-optic cell to travel across the acousto-optic cell to the centre of the laser beam. This delay was achieved by using a marker pulse from the D2045 driving the acousto-optic cell to trigger the D2045 driving the laser. Noise was added to both input signals using the D2045 software noise generator. By selecting different noise seeds the two sets of noise at the correlator inputs can be made different and independent. The repeat time for both signals and noise was 100 μs. The actual integration time of the CCD array was somewhat longer, at 2.5 to 5 ms, taking in 25 to 50 repeats of the input, but since the noise in the synthesiser outputs repeated every 100 μs, then the effective integration time of the correlator is still 100 μs. This is discussed further in section 10.4

Both correlators used a directly modulated diode laser for one signal input, but the lasers used were different. Principles were first tested using a Uniphase diode laser with a modulation bandwidth of approximately 20 MHz. This diode has a narrow output beam, with a $1/e^2$ diameter of 0.37 mm, and therefore a beam expansion stage had to be included. This correlator is shown in figure 10-1. A second correlator was then built using fewer, but higher quality, lenses and a Spectra Diode Laboratory laser supplied by Melles Griot.

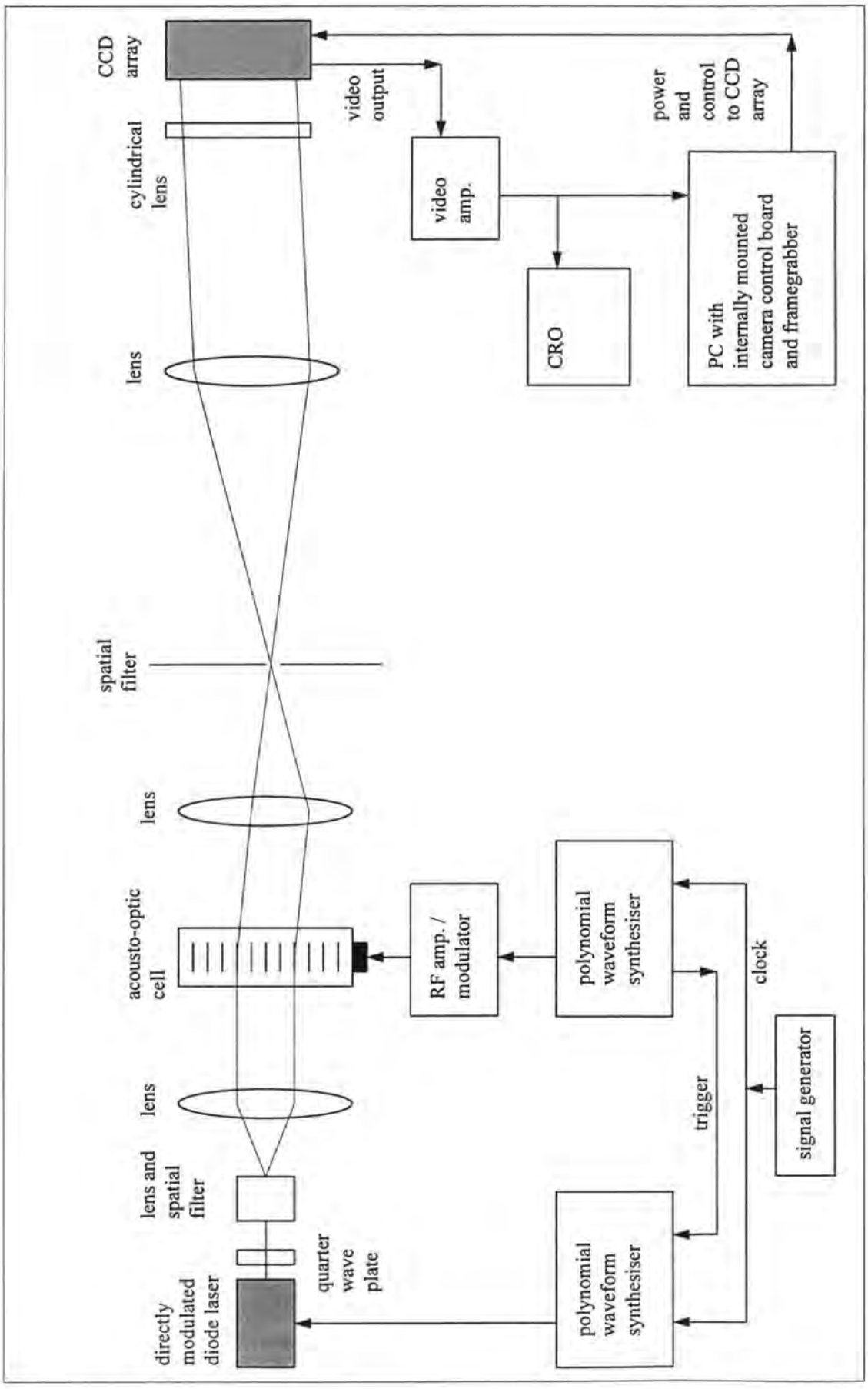

Figure 10-1. Experimental time-integrating correlator using narrow beam laser with external beam expansion.

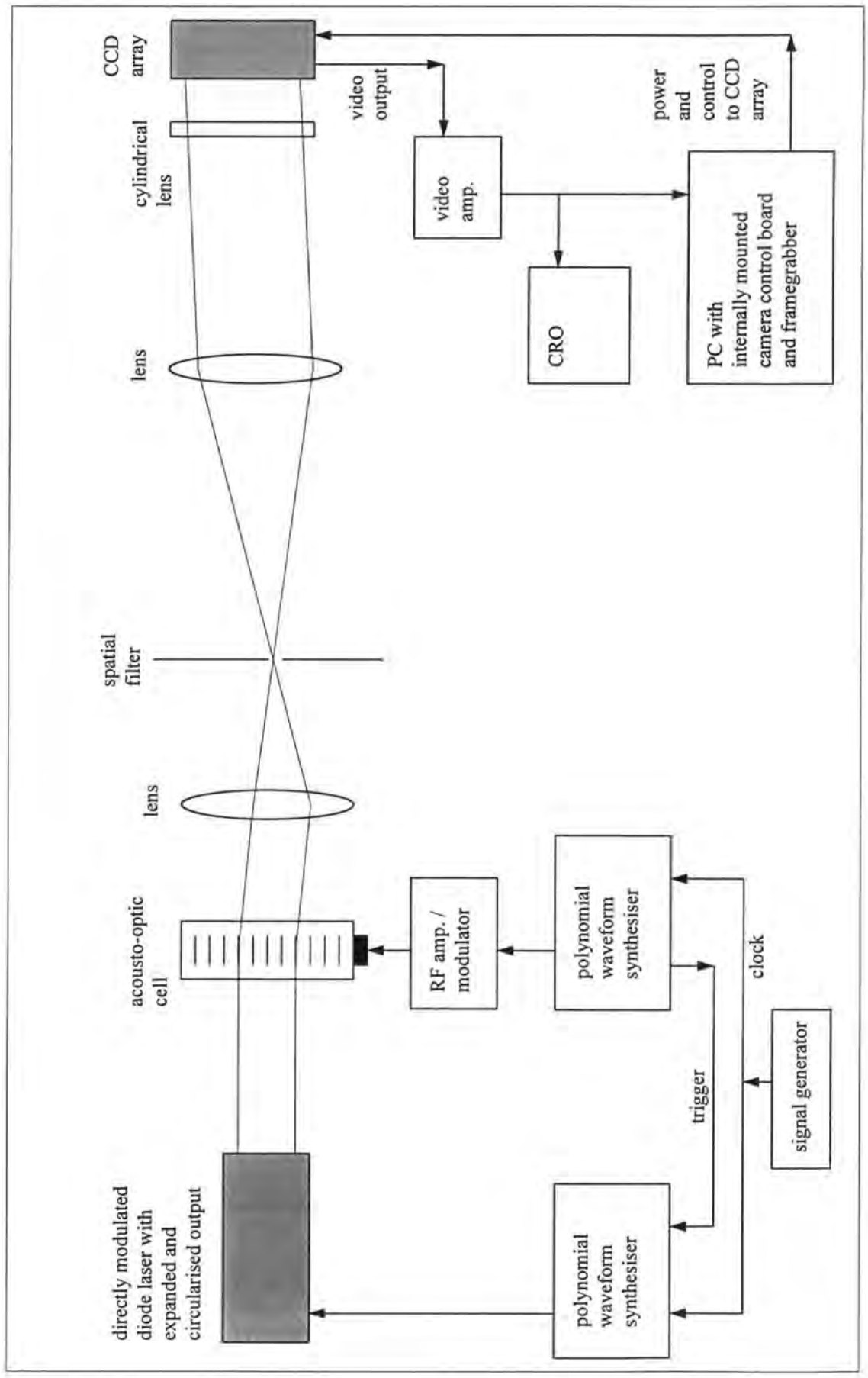

Figure 10-2. Experimental time-integrating correlator using laser with internal beam expansion.

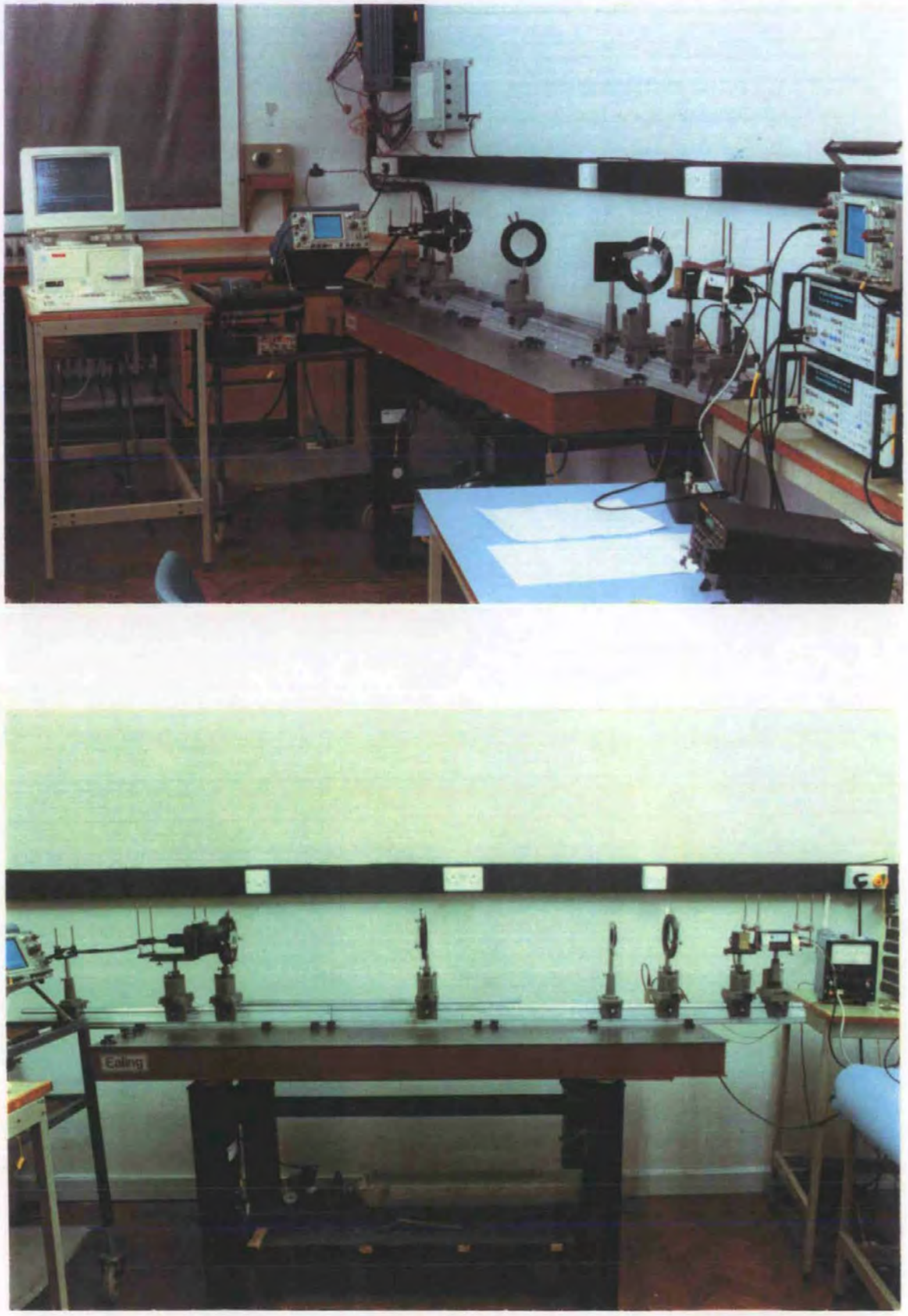

Figure 10-3. Photographs of the time-integrating correlator using laser with internal beam expansion

This laser has a modulation bandwidth of approximately 300 MHz and was supplied in a package including controllable thermoelectric cooling, dc current or output power control and beam cicularisation and expansion. The output beam has a maximum power of 15 mW and a $1/e^2$ diameter of 7 mm. Hence further beam expansion was not required, enabling a simpler system with fewer lenses. This correlator is shown in figures 10-2 and 10-3. The lenses were chosen with focal lengths of 200 and 600 mm to give a magnification of 3, so that the beam diameter at the CCD array was 21 mm.

The CCD array, and all the other components, were the same for both correlators. The CCD array comprises 2048 elements with a pitch of 10 μm. Hence, the beam diameter at the array (21 mm) just exceeds the array length of 20.48 mm. Since the acoustic velocity in the acousto-optic cell is 617 ms^{-1}, the time shift range covered by the array can readily calculated to be nominally 11.06 μs. Signals with bandwidths of the order of 1 MHz will have acfs of the order of 1 μs wide and hence this range of 11 μs will comfortably include such acfs, with some scope for further zooming in if wider bandwidth signals are used.

The CCD array camera was controlled by the PC via the installed Dipix P360F framegrabber board. This enabled the CCD array to be "read" at fixed, software controllable, integration periods. A programme written in the framegrabber system interpreter language grabbed and stored a number of frames from the CCD array on demand. A qbasic programme was then used to convert the data so that it could be imported into a Mathcad file for presentation and analysis. A sample printout of the Mathcad file is shown in appendix G. It is the results from the second correlator, using the higher modulation bandwidth laser with integral beam expansion, which are presented here, and in appendix H.

10.2 Removal of background from ccf

Equation 9.14 shows that the CCD array output is a spatially invariant dc. level, proportional to the integration time plus the required ccf. This assumed uniform illumination of the acousto-optic cell. The laser beam incident on the acousto-optic cell has a Gaussian profile and hence this background level has a Guassian profile. In order to subtract it, this background was recorded before inserting test signals into the correlator. This is illustrated in figure 10-4. The upper and middle plots shows a ccf and the pre-recorded background, as

taken in by the Mathcad file. The lower plot shows the ccf after subsequent subtraction of the background. (The "wobbly" nature of this plot is a function of the print quality of the Mathcad output, rather than the data.)

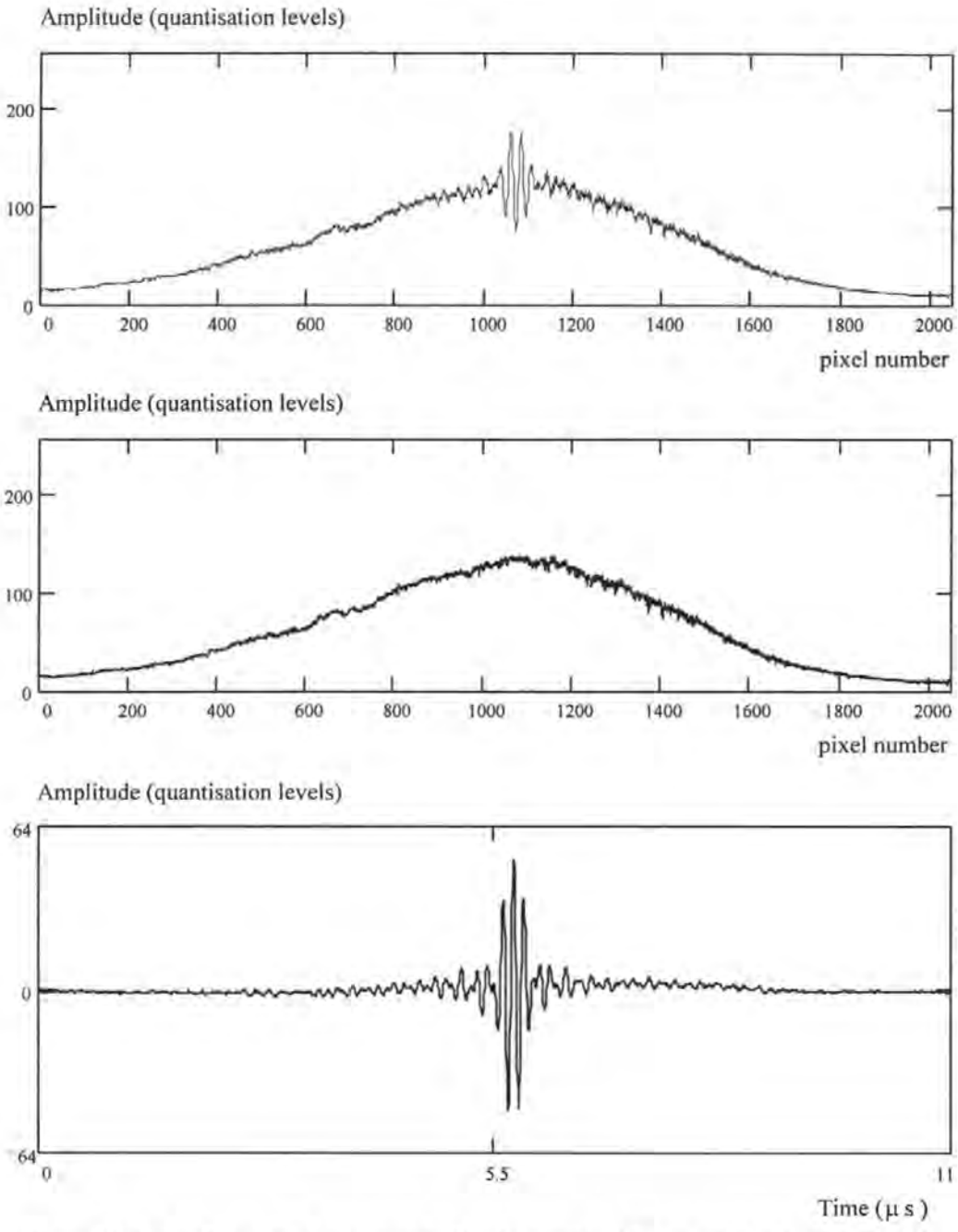

Figure 10-4. A ccf (top) and pre-recorded background(middle) as taken in by Mathcad file and the ccf after subtraction of the background (bottom).

In order to ensure that the power levels were approximately the same while recording the background, signals were inserted with the same power levels as for the subsequent test signals. The signal part of the D2045 outputs were replaced by two non-harmonically related

tones and two different noise seeds were chosen, which were different from those used for the subsequent test signals. The tones would not correlate, but the noise inputs did create a noise-noise cross correlation term equal in power to the noise-noise correlation in the subsequent correlation of test signals. When the background is subtracted from the ccf this means that the noise-noise correlation power in the output is effectively doubled. For this experiment, equation 3.9, which gives the SNR at the TDFCSD output in terms of the correlator input SNR, must be modified to give

$$\left(\frac{S}{N}\right)_{TDFCSD} = \frac{\gamma\left(\frac{B_n}{B_s}\right)^2\left(\frac{S}{N}\right)_i^2}{2 + 2\left(\frac{S}{N}\right)_i} \qquad (10.1)$$

Clearly, this doubling of the noise-noise cross correlation power is undesirable. In a production system the background would be obtained by averaging over a large number of frames making the noise-noise cross correlation term in the recorded background as small as required.

There was considerable spatial noise in the background, as can be seen from the centre plot of figure 10-4. This spatial noise is time invariant and arises from the imperfections of the optical components of the correlator. The output of the laser assembly itself had considerable spatial noise, possibly introduced by the anamorphic prism pair used to expand the beam. The lenses introduced very little noise. The largest source of spatial noise was the acousto-optic cell. This spatial noise varied significantly with the position of the cell, and the horizontal and vertical position of the cell was adjusted to minimise it. In principle, since this spatial noise is time invariant it will be removed completely when the background is subtracted. However, the experimental correlator described here was a little temperamental. It was constructed on an optical table and its physical length was such that it overhung the table at both ends (see figure 10-3). The mounts used for all the components had some "play" in them. In order to get sufficient power onto the CCD array a cylindrical lens was used to focus the laser beam onto the array. Since the array pixel size is 10 μm this tended to make the output extremely sensitive to the slightest movement or drift in the parameters of any component in the system. Care and continual adjustment were required to obtain consistent results. Hence, any recording of the background had to be made just before

recording the ccf with test signals. A more compact and robust brassboard version should not suffer these problems.

10.3 Frequency response

10.3.1 Calibration of time and frequency scales in the output

Each data set pulled into the Mathcad file comprises a sampled time domain signal of 2048 points. Both time and frequency scales can be established from the temporal length of this data set. This time was calculated above at 11.06 μs. This value was checked by inserting a 10 MHz test tone into the correlator and adjusting the scale in the Mathcad file so that the peak in the TDFCSD did indeed occur at 10 MHz. This calibration was also checked at a range of other frequencies from 1 MHz to 16 MHz. As a result of this calibration process the temporal length of the captured signal was estimated to be 11.00 μs, a difference of 0.5% from the value calculated above.

10.3.2 Measurement of frequency response

The frequency response of the correlator was obtained by measuring the rms. amplitude of the output ccf for input tones, from 2 to 21 MHz. The ccf output was processed using a slightly modified version of the Mathcad file shown in appendix G. The output was bandpass filtered using a brickwall filter with a bandwidth of 2 MHz centred on the frequency of the input tone, and the rms. value of the whole, 11 μs long, ccf was then calculated. The results are shown in figure 10-5. The 3 dB bandwidth was approximately 16 MHz. The quoted, double sided, bandwidth of the acousto-optic cell is 30 MHz, and so it would seem that the limiting component as regards bandwidth is the acousto-optic cell, as expected.

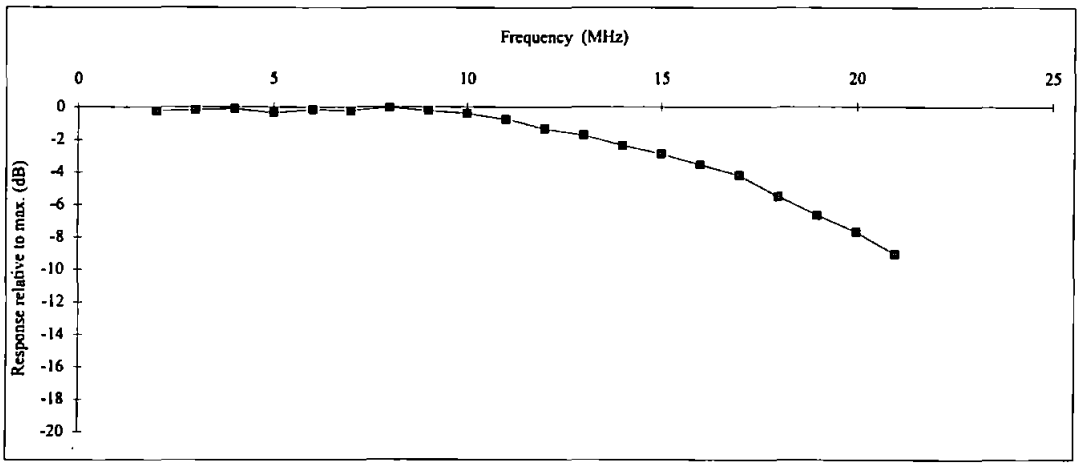

Figure 10-5. Frequency response of experimental time-integrating correlator.

10.4 Quantisation noise at the framegrabber

There are a number of points at which noise is added by the correlator itself, so that the final output SNRs will be less than those predicted for a perfect correlator in chapters 2 and 3. The amount of temporal noise introduced by the laser and the acousto-optic cell is negligible, for a receiver system that includes sufficient gain to be front end noise limited. Noise can be expected at the CCD array itself but if the array approaches saturation before being read, the SNR at the CCD is quoted as 70 dB (see appendix I). This condition was ensured by integrating over sufficient repeats of the basic 100 μs outputs from the waveform synthesiser. The actual integration time used for the CCD array varied between 2.5 and 5 ms, including 25 to 50 repeats of the input. Integrating over a longer period of time reduced the effect of background light in the laboratory entering the array, and ensured that the array approached saturation before reading. This made the making of adjustments and measurements easier since some laboratory lights could be left on, and ensured that the SNR at the array output approached its quoted value of 70 dB. In a brassboard version, outside light would be eliminated by enclosing the correlator in a lightproof box, and the laser and optics would be chosen to ensure that the CCD array approached saturation after the required integration time. Hence, the CCD array is not a major source of noise in either the experimental correlator described here or in a brassboard version.

One significant source of noise in the experimental correlator described here arises from the time invariant spatial noise introduced by the optical components of the system. As

discussed earlier, perfect elimination of this spatial noise was not possible. The amount of noise this introduced into the output could not be quantified and was variable. Fortunately, it was obvious, from inspection of the ccf output after subtraction of the background, when drift in the correlator had led to a very poor subtraction. Results badly affected in this way could then be rejected. In a brassboard version, this type of noise should be negligible.

By far the largest source of noise in the correlator is that arising from the quantisation involved in digitising the video signal from the CCD array in the framegrabber. The video signal is quantised into 256 levels, but because of the large background light level the output ccf signal spans no more than 50 levels (and often less). Thus, the effect of quantisation noise is considerable and dominates all other noise sources in the correlator. The expressions for the SNRs in the correlator output and in the TDFCSD can be modified to account for this. Signal values are passed out from the framegrabber and imported into a Mathcad worksheet for processing in digital form, such that the difference between quantisation levels (the significance of the least significant bit) is one (arbitrary) quantisation unit. The peak to peak range of the system is 256 quantisation units. It is readily shown that the mean square value (variance) of the random error due to quantisation is $\frac{\Delta^2}{12}$ where Δ is the size of a quantisation unit. The SNR depends on the size of the output signal. The theoretical peak output signal power of a perfect correlator with unit gain is $(S_i\, T_s)^2$. If the peak amplitude of the output ccf as measured in the Mathcad worksheet is measured as $\hat{S}_o$ qauntisation units, then the power gain of the correlator can be defined as

$$G = \frac{\hat{S}_0^2}{(S_i\, T_s)^2} \tag{10.2}$$

We know that for a perfect correlator of unit gain the total energy of the noise-noise and signal-noise correlation terms (from equations 2.23 and 2.29) is, for a CW signal,

$$\frac{\eta^2\, B_n\, T_s^2}{2} + \eta\, T_s^2\, S_i \tag{10.3}$$

The total energy in a correlation section of length $\frac{T_s}{\gamma}$ in the actual time-integrating correlator output is

$$\frac{G}{\gamma}\left(\frac{\eta^2 B_n T_s^2}{2} + \eta T_s^2 S_i\right) \tag{10.4}$$

The energy of the quantisation noise contribution in the same ccf section is

$$\frac{T_s}{12\gamma} \tag{10.5}$$

Following the approach taken at the start of chapter 3, we obtain the mean power of the noise terms in the TDFCSD by dividing by $2 B_n$, to give

$$\frac{G}{\gamma}\frac{\eta^2 T_s^2}{4} + \frac{G}{\gamma}\frac{\eta T_s^2 S_i}{2 B_n} + \frac{T_s}{24\gamma B_n} \tag{10.6}$$

while the mean power of the signal terms in the TDFCSD is given by

$$G\frac{S_i^2 T_s^2}{4 B_s^2} \tag{10.7}$$

so that the SNR in the TDFCSD is

$$\left(\frac{S}{N}\right)_{TDFCSD} = \frac{G\frac{S_i^2 T_s^2}{4 B_s^2}}{\frac{G}{\gamma}\frac{\eta^2 T_s^2}{4} + \frac{G}{\gamma}\frac{\eta T_s^2 S_i}{2 B_n} + \frac{T_s}{24\gamma B_n}} \tag{10.8}$$

$$= \frac{\gamma\left(\frac{B_n}{B_s}\right)^2\left(\frac{S}{N}\right)_i^2}{1 + 2\left(\frac{S}{N}\right)_i + \frac{B_n}{6 G T_s N_i^2}}$$

Now $$\frac{B_n}{6 G T_s N_i^2} = \frac{B_n}{6 T_s N_i^2}\frac{S_i^2 T_s^2}{\hat{S}_o^2} = \frac{B_n T_s}{6\hat{S}_o^2}\left(\frac{S}{N}\right)_i^2 \tag{10.9}$$

and hence we have

$$\left(\frac{S}{N}\right)_{TDFCSD} = \frac{\gamma\left(\frac{B_n}{B_s}\right)^2\left(\frac{S}{N}\right)_i^2}{1 + 2\left(\frac{S}{N}\right)_i + \frac{B_n T_s}{6\hat{S}_o^2}\left(\frac{S}{N}\right)_i^2} \tag{10.10}$$

where $\hat{S}_o$ is obtained by measurement of the output ccf. If we take into account the doubling of the power of the noise-noise cross correlation discussed earlier, this becomes

$$\left(\frac{S}{N}\right)_{TDFCSD} = \frac{\gamma\left(\frac{B_n}{B_s}\right)^2\left(\frac{S}{N}\right)_i^2}{2 + 2\left(\frac{S}{N}\right)_i + \frac{B_n T_s}{6\hat{S}_o^2}\left(\frac{S}{N}\right)_i^2} \qquad (10.11)$$

The variation in output SNR with the height of the signal acf peak, measured in number of quantisation levels, is shown in figure 10-6. The noise and signal bandwidths, sample length and zoom factor, used in figure 10-6 are as used in the experimental work. (B_n = 16 MHz, B_s = 4 MHz, T_s = 100 μs and γ = 32)

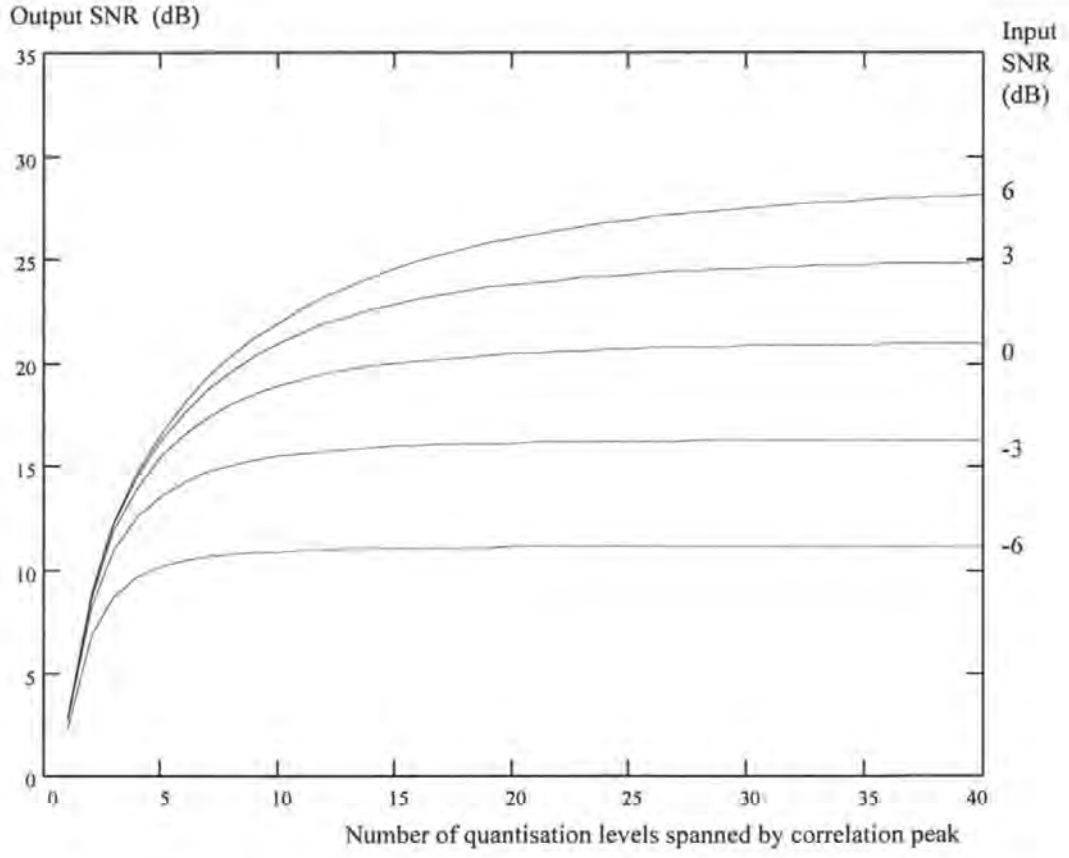

Figure 10-6. Variation of SNR in output TDFCSD with number of quantisation levels spanned by the correlation peak, for a range of input SNRs

The framegrabber used, in the experimental work, to quantise the video signal from the CCD array used 8-bit quantisation (256 levels). Since the ccf lies on top of a large background level this means that the number of quantisation levels spanned by the signal

acf peak may be fairly small. Experimentation showed that the largest acf peak amplitude that could realistically be obtained, even when the inputs contained no noise, is about one fifth of the full quantisation range. i.e. the number of qauntisation levels spanned by the signal acf peak generally less than 50 and less than 10 for lower input SNRs. Quantisation noise can therefore be expected to reduce the output SNR in the TDFCSD be an amount of the order of 1 dB

10.5 Results: variation of SNR_o with SNR_i

10.5.1 Generation of inputs with specified SNR

The Analogic D2045 arbitrary waveform generators used to generate the correlator inputs, have the facility to add noise of specified power and bandwidth to the output signal. (The settings required are explained in detail on page D-4 of the user's manual.) The spectrum of the noise is not flat and takes the form

$$P_{nn}(f) = \frac{V_{rms}^2}{ENBW}\left|\frac{1}{D-(D-1)e^{-j2\pi fT}}\operatorname{sinc}(fT)\right|^2 \qquad (10.12)$$

where V_{rms} is the rms amplitude, *ENBW* is the "effective noise bandwidth", T is the sample period of the generator, and D is an integer constant. Setting T, V_{rms} and the noise bandwidth (NBW - different from *ENBW*) automatically fixes the other values including D. A noise bandwidth of 22 MHz was used (D = 2, *ENBW* = 23.2 MHz) and values of V_{rms} were calculated so as to give the same noise power spectral density, at the centre frequency of the signal, as would arise from bandpass white noise with a bandwidth of 16 MHz. In practice this meant that for (e.g.) an effective input SNR of 0 dB the value of V_{rms} was set so that the total SNR

$$\frac{A^2}{2V_{rms}^2} = 0.686 = -1.637\,\text{dB} \qquad (10.13)$$

where A is the signal amplitude. i.e. since some of the noise fell outside the correlator bandwidth, the synthesisers were programmed to produce more noise than required so that the correct amount would fall within the correlator bandwidth.

10.5.2 Measurements taken

In total 25 sets of data were recorded, using the time-integrating correlator shown in figure 10-2, each set enabling a measurement of the SNR in the output TDFCSD. Input SNRs used were 10, 6, 3, 0, -3, and -6 dB, with 4 sets of data taken at each value (and an extra set obtained for $SNR_i = 0$ dB) The laser dc drive current was 45 mA, and the input signals were based on a repeated up chirp rising in frequency from 6 to 10 MHz in 100 μs (BT product = 400). The signal amplitudes set on the D2045 waveform generators were set to the maximum values that could be used to drive the correlator without being significantly distorted in the input devices (laser and acousto-optic cell). For example, the levels used to provide an input SNR of 10 dB were: to the laser, a signal amplitude of 1 V peak and an r.m.s. noise voltage of 0.27 V and, to the RF modulator driving the acousto-optic cell, a signal amplitude of 0.1 V and an r.m.s. noise voltage of 0.027 V. The CCD integration time (line sync. period) was 2.5 ms when the input SNR was 10 dB and 4 ms for all other values of input SNR. In all measurements taken 2 successive frames were added so that the effective integration times of the CCD array were 5 and 8 ms.

One set of graphical results is shown in appendix H for each value of input SNR - 6 sets in all. One set is shown here for an input SNR of 10 dB. Each data set comprised 3 pairs of 2048 point frames "grabbed" from the array. First the background CCD array output was recorded (ccf0) with the waveform generators set to produce noise using different noise seeds. Then the generators were set to produce the repeated up chirp, with a different pair of different noise seeds, and the CCD array output recorded (ccf1). Then the noise seeds were changed again, a length of coaxial cable causing a delay of approximately 60 ns was inserted into the acousto-optic cell input, and the CCD array output recorded again (ccf2). The two recorded ccfs should then have a 60 ns difference in their positions, which should be measurable from the slope of the differences between the phase terms of their associated TDFCSDs. All three pairs of CCD output frames were then converted into ASCII format and imported into the Mathcad file shown in appendix G. A typical set of outputs, as imported into the Mathcad file is shown in figure 10-7.

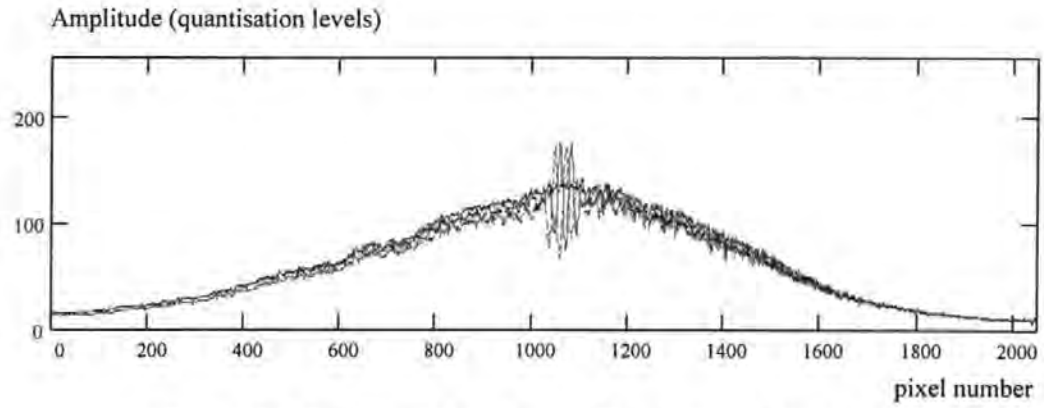

Figure 10-7. Raw outputs from framegrabber as imported into Mathcad file.

The background (ccf0) was subtracted from the two ccfs (ccf1 and ccf2). The two ccfs were already windowed but were windowed further to achieve a zoom factor of $\gamma = 32$. The results of these two stages are shown in figures 10-8 and 10-9.

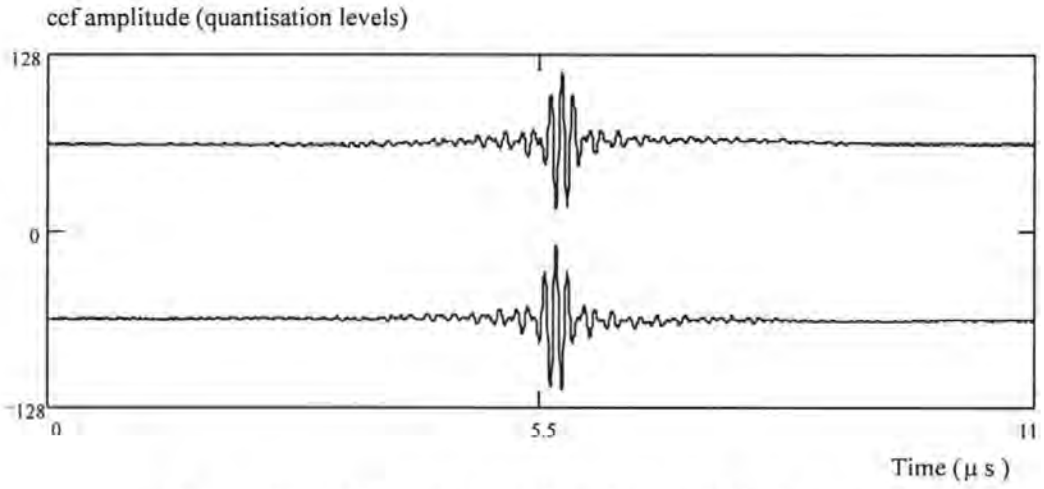

Figure 10-8. CCD array outputs after subtraction of background.

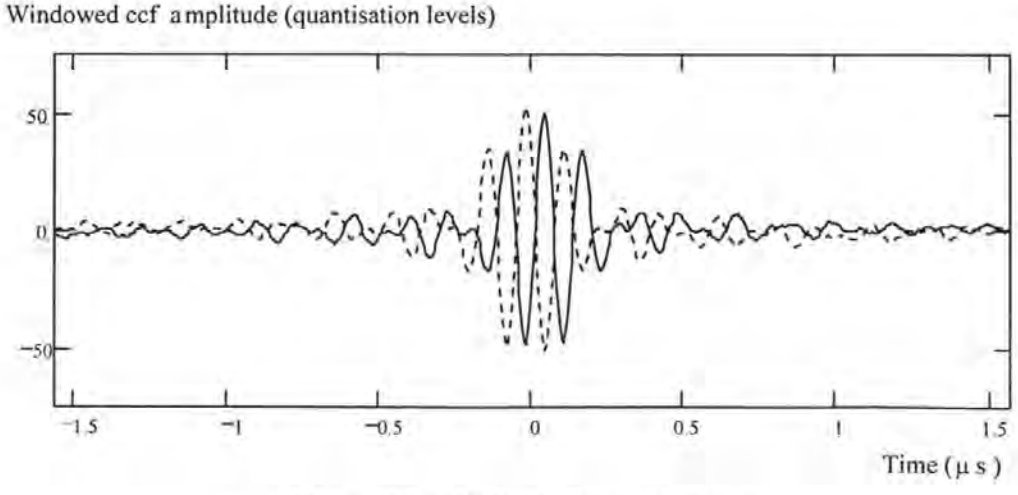

Figure 10-9. ccfs after further windowing.

The TDFCSDs were then obtained by FFT and bandpass filtered between 1 and 20 MHz. The magnitudes of these TDFCSDs are illustrated in figure 10-10.

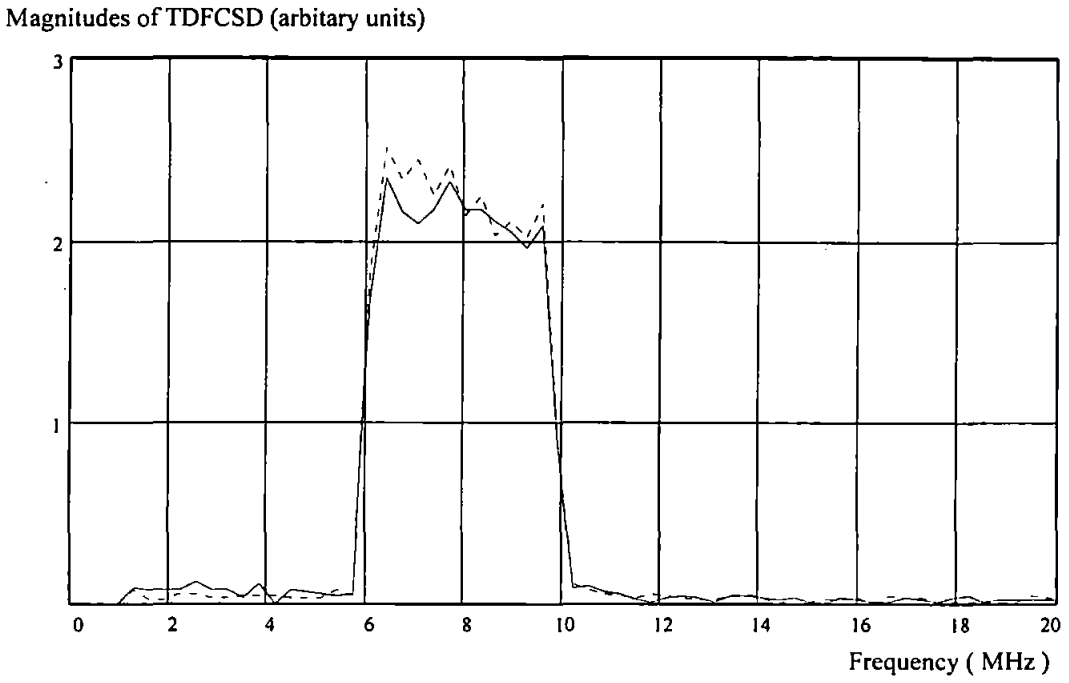

Figure 10-10. Magnitude of TDFCSDs

The SNR in the TDFCSDs were then estimated by comparing the mean square values of the magnitude terms of the TDFCSDs within the signal bandwidth of 6 to 10 MHz and the adjacent 4 MHz band from 10 to 14 MHz. The differences in the phase terms of the TDFCSDs were then calculated and a straight line fitted to the resulting phase difference terms in the range 6 to 10 MHz, as illustrated in figure 10-11. The time delay caused by the coaxial delay line was then estimated from the slope of this line.

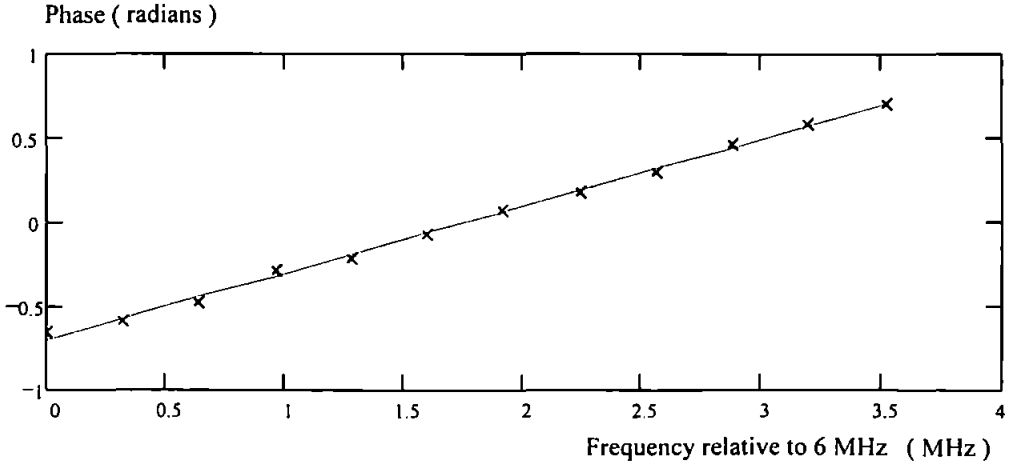

Figure 10-11. Difference between phase terms of the TDFCSDs, with straight line fitted.

10.5.3 Results: variation of SNR_o with SNR_i

The results from the 25 sets of measurements of the output SNR and estimated time delay for the 6 different input SNRs are given in table H-1 in appendix H. Predicted values of output SNRs are also tabulated, calculated using equation 10.11 to allow for quantisation noise. The mean measured values of output SNR, for each value of input SNR, are then compared with these predicted values in figure 10-12. The predicted values are plotted as a line, the mean measured values as points. The close agreement shown by figure 10-12 gives considerable confidence in all the analysis presented here. The difference between measured and predicted output SNR is generally less than 1 dB. In the estimation of output SNR in the Mathcad simulation, described in detail in appendix D, the output SNR was seen to vary with noise seed used and to have a standard deviation of approximately 1 dB. The agreement is therefore well within the expected random deviation.

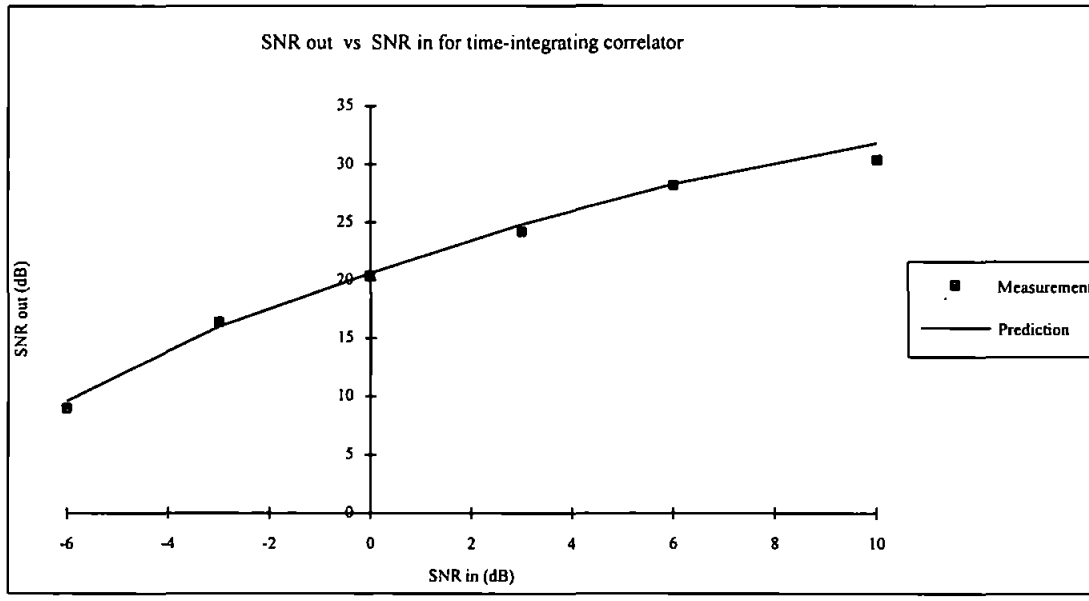

Figure 10-12. Measured and predicted output SNRs in the TDFCSD for a range of input SNRs

10.6 Accuracy of time delay measurement

Each of the 25 sets of measurements described above was used to estimate the length of the delay line. Table H-1 includes these measured delays. As was shown in chapter 5, the accuracy of estimate of this delay, or time difference of arrival (TDA), depends on the SNR in the TDFCSD. Equation 5.11 gives the variance of the phase errors for one TDFCSD

$$\sigma_{\phi}^2 = \frac{1}{2\left(\frac{S}{N}\right)_o} \tag{10.14}$$

where $\left(\frac{S}{N}\right)_o$ is the SNR in the TDFCSD. The phase terms used to estimate the time delay in this experiment were obtained from the phase differences between 2 TDFCSDs and hence their variance is doubled

$$\sigma_{\phi}^2 = \frac{1}{\left(\frac{S}{N}\right)_o} \tag{10.15}$$

Using equation 5.34,

$$\sigma_m^2 = \frac{12\,\gamma}{B_s^3\,T_s}\,\sigma_{\phi}^2 \tag{10.16}$$

and noting that the phase slope $m = 2\,\pi\,t_d$, where t_d is the TDA, we obtain the variance of the time delay

$$\sigma_{td}^2 = \frac{3\,\gamma}{\pi^2\,B_s^3\,T_s\left(\frac{S}{N}\right)_o} \tag{10.16}$$

For the parameters used in this experimental work ($\gamma = 32$, $B_s = 4$ MHz, $T_s = 100$ μs), this gives the standard deviation in the time delay estimation as

$$\sigma_{td} = \sqrt{\frac{1.52 \times 10^{-15}}{\left(\frac{S}{N}\right)_o}} \tag{10.17}$$

Substituting the measured values of $\left(\frac{S}{N}\right)_o$ (see table H-1) into equation 10.17 gives the predicted standard deviation of the time delay estimation for each value of SNR at the correlator input. Figure 10.13 shows the measured values of time delay plotted against the values of correlator input SNR used when they were obtained. The two curved lines show the mean estimate of time delay (61.1 ns) plus and minus one predicted standard deviation of

the estimation. Statistically, we would expect 32 % of the measured values to fall outside the plus or minus one standard deviation limits. 11 out of the 25 measurements (44 %) do actually fall outside these limits, but 25 measurements is not a large enough number upon which to base any strong conclusions. Without obtaining a very much larger number of estimates, we cannot state categorically that the predicted accuracy of the TDA estimation, derived in chapter 5, is confirmed experimentally, but the results displayed in figure 10-13 do give some confidence in the analysis.

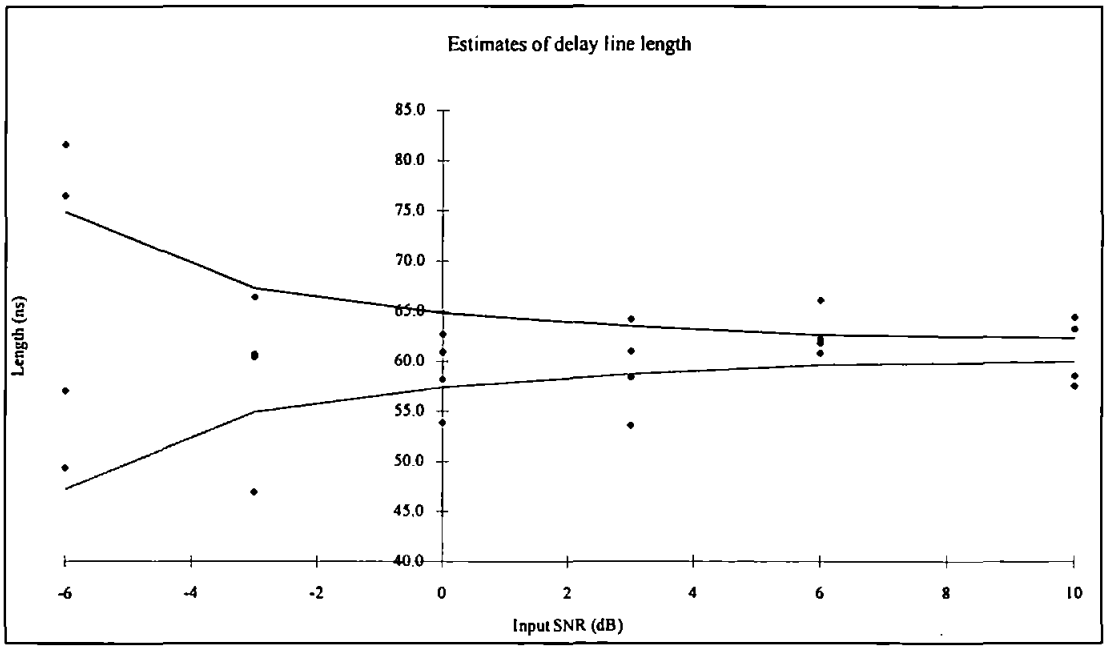

Figure 10-13. Estimates of delay line length plotted against the correlator input SNR used when the estimates were obtained. The two curved lines show the predicted plus or minus one standard deviation in the estimates.

10.7 Conclusions

The experimental correlator described here was not mechanically robust but, with care and continual adjustment, did yield results which clearly showed that a time-integrating acousto-optic correlator can be used to generate both the amplitude and phase terms of the TDFCSD. Both measurements of the SNR in the TDFCSD and the estimates of time delay between ccfs showed very close agreement with the predictions, once quantisation noise at the framegrabber had been taken into account.

Quantisation noise at the framegrabber was the dominant source of noise in the correlator and its effect was shown to be very much as predicted. It can have a significant effect on the SNR in the ccf and the TDFCSD and, if we want a high performance system, 8-bit quantisation is clearly not good enough. Examination of figure 10-6 shows that we need to ensure that the correlation peak spans at least 40 quantisation levels. 10-bit quantisation is the absolute minimum requirement for this, and 12-bit quantisation would be desirable. 12-bit quantisation would also be compatible with the 70 dB SNR at saturation offered by the CCD array.

The process of getting results was slow and laborious because the waveform generators took some time to recompute the input signals before each ccf could be recorded and the signal processing was not automated. The processing of the data from the CCD array was carried out using Mathcad since this made the processing very easy to modify. In a production system, in which no further changes to the processing is required, the processing could be done by a real time DSP system.

11. Conclusions and recommendations for further work

11.1 Conclusions

The increasing incidence of LPI radars and communication systems using spread spectrum techniques presents a serious problem for existing surveillance receivers and ESM systems. CW signals, or pulsed signals with a high duty cycle, enable the use of low transmitter powers and can be very difficult to detect, particularly when power management techniques are employed. Crystal video receivers or radiometers cannot be expected to offer the required sensitivity, which is of the order of -110 dBm. The rapidly varying low antenna elevations of ESM systems on mobile platforms will create fluctuations in received noise power that will mask the weakest signals (In a receiver of bandwidth 500 MHz, a -110 dBm signal is equivalent to a noise temperature of 1.5 K). A cross correlation receiver, applying threshold detection to the ccf or TDFCSD derived from the outputs of two adjacent receivers, can provide the required sensitivity and the TDFCSD offers the additional benefits of spectral information and high resolution direction finding.

The signals arriving at two adjacent receivers from a single point source will be spatially coherent, while the signals due to a uniformly distributed incoherent noise source will not. Hence, in a cross correlation receiver, the two sets of receiver system noise will be uncorrelated and the output of the correlator will contain a uniformly distributed noise signal made up of noise-noise, signal-noise and noise-signal cross correlations. If the input signal to noise ratio is not too low, the narrow time shifted acf of a signal from a point source can be detected against the noise background by a threshold detector. Reliable detection (e.g. $P_{fa} = 10^{-5}$, $P_d = 0.99$) requires a correlator output SNR of approximately 17.5 dB. The required system sensitivity of around -110 dBm can be achieved in a system with a bandwidth of 1 GHz using an integration time of 10 ms. The equations for output SNR in the ccf are independent of the form of the spread spectrum signal and Mathcad simulation produces results in very close agreement with these predictions. Even in the absence of antenna noise fluctuations, a ccf receiver has a sensitivity advantage over the

radiometer of at least 1.5 dB, for CW signals. For pulsed signals a ccf receiver can obtain an advantage over a crystal video receiver by coherently integrating over a number of pulses before applying threshold detection.

The TDFCSD, formed by windowing a small central portion of the ccf and taking the Fourier transform (by FFT), is the central and most important feature described in this work. Its use allows determination of the signal spectrum and can give better sensitivity than the ccf. By windowing, or applying a low pass time domain filter to the ccf, most of the noise is removed. This gives rise to enormous improvements in the SNR in the TDFCSD in comparison to the CSD derived directly from the ccf before windowing. The improvement is equal to the zoom factor, i.e. a zoom factor of 1000 gives an improvement of 30 dB in the output SNR. The wide bandwidths (hundreds of MHz or more) of spread spectrum signals causes their acfs to be very narrow (of the order of 10 ns or less). Receiver separations of the order of a few metres may be used so that the TDA is of the order of a few nanoseconds at most. Hence, the narrow acf peak is not displaced far from the centre of the ccf and very large zoom factors, typically 1000 or more, can be used. The relative bandwidths of the signal and the receiver determine whether use of the TDFCSD is more or less sensitive than use of the ccf. In wider bandwidth systems, where $B_s < 0.3\ B_n$, the TDFCSD offers greater sensitivity. The statistics of the magnitude terms in the TDFCSD follow Rayleigh/Ricean statistics and the output SNR required for reliable detection performance is 15 dB. The sensitivity offered by the TDFCSD is independent of receiver bandwidth. For example, a system using an integration time of 10 ms and a bandwidth of several GHz would have a sensitivity of approximately -112 dBm to a signal with a bandwidth of 100 MHz.

Useful AOA estimation can be achieved with a receiver antenna separation of only one metre. Errors of the order of 5 to 10 degrees can be expected at the absolute limits of detection, but rapid improvements to resolutions of a small fraction of a degree can be expected with a modest increase in signal strength. For a signal bandwidth of 100 MHz and a power of -70 dBm at the surveillance receiver inputs, a 1 m baseline and an integration time of 10 ms can give a theoretical bearing accuracy of one thousandth of a degree!

The signal processing operations required to produce the TDFCSD in real time for wide receiver bandwidths cannot be achieved using digital electronics, but are possible using acousto-optic correlation. Two types of acousto-optic correlator have been considered in detail. An analysis of Raman-Nath diffraction, from first principles, demonstrates the presence of information in the zeroth diffraction order of an acousto-optic cell. This leads to a general theory of space-integrating acousto-optic correlators which explains the operation of a zeroth order correlator not explained by the analysis usually offered in previous work on space integrating correlators. Experimental work confirms the predictions made by this theory. Unfortunately, the space-integrating correlator suffers from a number of disadvantages making it unsuitable for use in a cross correlation surveillance receiver.

The time-integrating acousto-optic correlator is ideally suited to the task of forming a windowed ccf in real time. It forms a true continuous correlation function and can handle broadband (500 MHz or more) signals. Experimental results clearly show that such a correlator does produce the true correlation function, that the TDFCSD can readily be derived from its output, and that the output SNR and TDA estimation accuracy are as predicted by analysis. The experimental correlator described in this thesis is a baseband correlator. Two such correlators are required for the analysis of the I and Q channels from an RF signal, and the bandwidth is limited by the TeO_2 acousto-optic cell used. Digital signal processing is carried out in Mathcad and is not real time. The correlator architecture that should be employed, in an operational system, is the electronic reference correlator, performing a complex correlation on IF signals and using a GaP acousto-optic cell. The output should be processed by a real time DSP system. A brassboard version of such a correlator, with a bandwidth of 500 MHz, is being built in the USA, though not, at present, with the intention of generating the TDFCSD.

11.2 Recommendations for further work

11.2.1 Multiple signal sources

Section 5.7 and appendix C demonstrated the ability of the TDFCSD to identify and direction find independently on two separate FMCW signals in the presence of a single large pulse. If a large enough receiver separation is used, it may be possible to separate some signals in the ccf before taking the FFT. Indeed, the ccf could be split up into a number of windows each one corresponding to a different AOA range. The TDFCSD for each window would then provide fine resolution on AOA and the ability to separate signals with similar AOAs but different spectra. Clearly, any system operating in a real EW scenario can expect to be faced with a number of LPI signals as well as a large number of pulses from other radars. Any signal entering the system must degrade the system's ability to detect other signals. The work carried out has done no more than demonstrate that it is possible to detect and direction find independently for multiple signals. An analysis of the performance of the system in the presence of multiple signals would be of considerable value. Such an analysis would also include a consideration of how large the separation, in AOA and frequency, of the signal sources must be for them to be identified separately. The first, and perhaps most difficult, problem would be to devise a meaningful and useful way of classifying multiple source performance; signals will vary in spectrum, AOA, power, pulse length, repetition interval. Any such evaluation of performance must be carried out in the context of realistic scenarios, and the best approach may be via computer simulation using real data.

11.2.2 Complete prototype system

The experimental time-integrating correlator described here demonstrated the principle of using an acousto-optic correlator to generate the TDFCSD. However, it was a laboratory baseband correlator with a very limited bandwidth. As explained in chapter 10, the correlator used in a real system should be an electronic reference correlator. The correlator being built by an American team, Anderson et al. [39,40,41], a brassboard electronic reference correlator with a bandwidth of 500 MHz, is almost exactly what is

required. A complete system could readily be built around this correlator and field tested. Duplicating the work of Anderson et al. is clearly of little academic value. Anderson et al already have a full system that could be adapted to generate the TDFCSD and perform the processing described in chapters 2 and 3 of this thesis. It is probable that they now know about these techniques and it seems highly likely that they will use them and field test the full system in the next few years. The decision to be made is whether to wait for whatever results the American team release, or to commission the construction of a system in the UK. It would involve significant expenditure, time and effort to build a complete prototype system, including the RF receivers and a real time DSP sub-system. This may be justifiable, however, since it would give more direct access to the results and allow control over the field testing.

11.2.3 Digital implementation

This thesis has concentrated on acousto-optic correlation techniques and not considered digital methods. Acousto-optics offers the only current possibility of performing the initial cross correlation, for bandwidths of the order of GHz, in real time. Digital systems are getting steadily faster, however, and for smaller bandwidths digital correlation might be acceptable now. One common digital technique is to use FFT processing. Two data sets are assembled and the FFT of one data set is multiplied by the complex conjugate of the FFT of the other data set. The inverse FFT of this product is then taken to produce the ccf. This approach would require enormous data sets with very little prospect of real time processing. It does not produce the true continuous ccf and is also wasteful of effort in that it produces the whole ccf rather than just the required central portion. The only prospect of real time digital correlation lies in the construction of a continuous hardware correlator involving shift registers and digital multipliers and adders. Such a system would require a very large number of components. For example, a system with an input bandwidth of 500 MHz, a ccf window width of 50 ns and an integration time of 1 ms would require a system clocking at 1 GHz comprising a 50 stage shift register and 50 multipliers to form a ccf every nanosecond and 50 circuits capable of clocking at 1 GHz and summing inputs over a period of 1 ms. The feasibility of building such a system depends on the number of levels required to quantise the input. A system using single bit quantisation is obviously much simpler to build than one using 8-bit quantisation (the

multipliers could simply be XOR gates for example). However, quantisation of the input can be expected to degrade the performance of the correlator. Further work is required to analyse and simulate the effects of using different numbers of quantisation bits. Digital correlator architectures could then be investigated in order to establish the optimum compromises between output SNR, bandwidth (speed) and complexity.

11.2.4 Other applications

The problem tackled in this thesis has been the military one of the detection and directing finding of LPI radars and communication systems. However, the techniques developed may have other applications. They can be applied to any situation where high resolution direction finding on broadband signal sources is useful. Applications might be found, for example, in navigation, surveying, medicine and radio astronomy.

Appendix A. Mathcad simulations of dual receiver cross correlating ESM system - single FMCW signal.

Set sample parameters

ie. set length of each sample, sampling frequency, and indexes to use in prosessing the signals.

Integration time: $Ts := 500$ μs No. of samples per data set: $N := 2^{17}$ $N = 131072$ $fs := \frac{N}{Ts}$

Sampling frequency: $fs = 262.144$ MHz $i := 0..N-1$ $I_i := i$ $f := \frac{I}{Ts}$ $t := \frac{I}{fs}$ $n := 0..\frac{N}{2}$

Note: all times are in μs and all frequencies are in MHz.

Set receiver system parameters

Receiver noise bandwidth: $B_n := 100$ MHz

$\eta := 2$ nominal noise power spectral density (this file deals in ratios and not absolute values.)

Noise power, referred to receiver input: $N_i := \eta \cdot B_n \cdot 10^6$ $N_i = 2 \cdot 10^8$ W $\sigma_n := \sqrt{N_i}$

Create band pass filter to simulate bandwidth of receivers using a iir low pass filter equivalent to a 10 pole Butterworth filter. $LPF := iirlow\left(butter(10), \frac{B_n}{fs}\right)$

Create 2 sets of AWGN of specified power and bandwidth

$na := gaussn(N) \cdot \sigma_n \cdot \sqrt{\frac{fs}{2 \cdot B_n}}$ $nb := gaussn(N) \cdot \sigma_n \cdot \sqrt{\frac{fs}{2 \cdot B_n}}$

$n1 := response(na, LPF, N)$ $n2 := response(nb, LPF, N)$

Set up time shift between signals due to separation of receivers and direction of arrival of signals

$\tau a := 0.02$ μs (20 ns)

For a receiver separation of $d := 10$ m, this corresponds to a direction of arrival of

$\theta a := asin\left(\frac{c \cdot \tau a}{d}\right) \cdot \frac{1}{deg}$ $\theta a = 36.9$ degrees

Create chirp pulses to simulate signals from 1 transmitter arriving at the 2 receivers

A 500 μs chirp sweeping over 20 MHz, which could be part of an FMCW signal, is generated. For this simulation it is assumed that this is exactly one cycle of the FMCW signal. First set the parameters.

Chirp centre frequency: $fca := 60$ MHz

Chirp bandwidth: $Bsa := 20$ MHz

Chirp time-bandwidth product: $Bsa \cdot Ts = 1 \cdot 10^4$

Then create 2 chirp signals, one without and one with a time delay, band pass filtered as by the receivers

$$cha(x) := \sin\left[2 \cdot \pi \cdot \left[\left(fca - \frac{Bsa}{2}\right) \cdot x + \frac{Bsa}{2 \cdot Ts} \cdot x^2\right]\right] \qquad cha1 := \overrightarrow{cha(t)}$$

$$cha2 := \overrightarrow{\left[cha(t - \tau a) \cdot rect\left[\frac{2 \cdot t - Ts - \tau a}{2 \cdot (Ts - \tau a)}\right] + cha(t + Ts - \tau a) \cdot rect\left(\frac{2 \cdot t - \tau a}{2 \cdot \tau a}\right)\right]}$$

$cha1 := response(cha1, LPF, N)$ $\qquad$ $cha2 := response(cha2, LPF, N)$

Add noise to signals to create receiver input signals with specified SNR

Signal to noise ratio at receiver input: $SNRina := -15$ **dB**

XXXXXXXXX

Then calculate the signal amplitude required to give this signal to noise ratio and add the signal vectors to the noise vectors to generate the inputs to the correlator.

Signal Amplitude: $Aa := \sqrt{2 \cdot \left(10^{\frac{SNRina}{10}} \cdot N_i\right)}$

Add signals to noise $\qquad s1 := Aa \cdot cha1 + n1 \qquad s2 := Aa \cdot cha2 + n2$

Display 1 μs of the receiver inputs. It is clear that the signals are well "buried in the noise". $\qquad k := 0 .. \frac{N}{500} - 1$

Signal in channel 1 (Units: volts. Scale dependent on system gain) $s := \max(s1) \cdot 1.1$

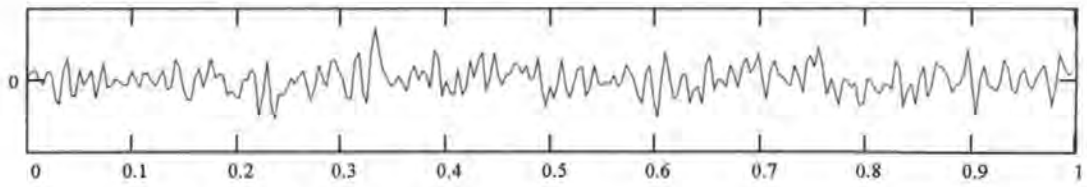

Signal in channel 2

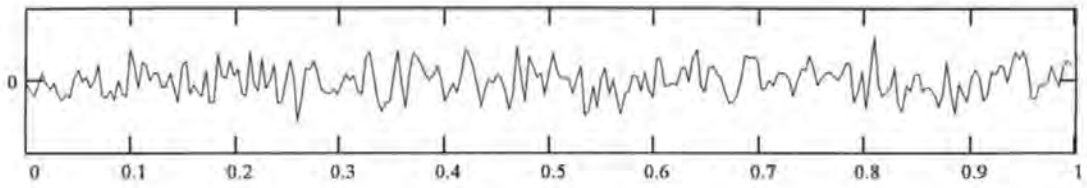

Time in μs

Calculating PSD and ACF of one signal and CSD and CCF of both signals by FFT method

$$PSD := \overrightarrow{mag(FFT(s1))^2} \qquad acf := \frac{1}{fs} \cdot Re(recenter(IFFT(PSD)))$$

$$CSD := \overrightarrow{(FFT(s1) \cdot \overline{FFT(s2)})} \qquad ccf := \frac{1}{fs} \cdot Re(recenter(IFFT(CSD)))$$

Estimating the signal to noise ratio in the output correlation function

Estimate from simulation: $SNRccfe := 10 \cdot \log\left(\frac{N \cdot \max(ccf)^2}{\sum \overrightarrow{ccf^2}}\right)$ SNRccfe = 19.006 dB

****

Theoretically predicted $SNRccfa := 10 \cdot \log\left[\frac{2 \cdot B_n \cdot Ts \cdot \left(10^{\frac{SNRina}{10}}\right)^2}{1 + 2 \cdot \left(10^{\frac{SNRina}{10}}\right)}\right]$ SNRccfa = 19.73 dB

****

autocorrelation function $p := \max(acf) \cdot 1.5$

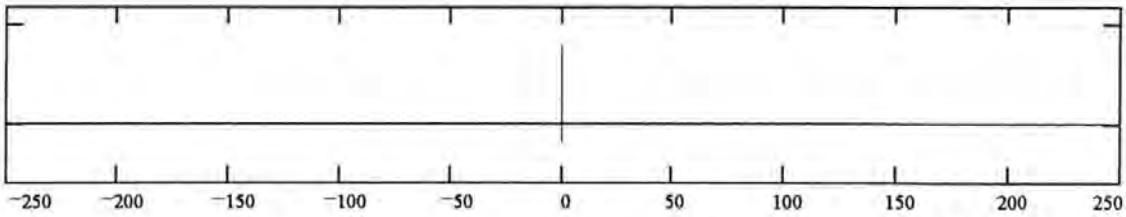

cross correlation function (magnified by 10 relative to acf) $p := 0.1 \cdot p$

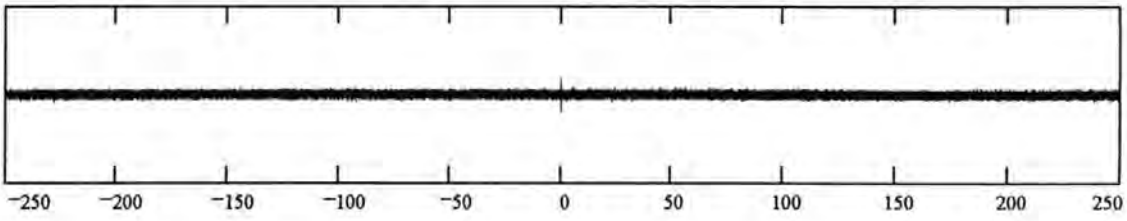

Power Spectral Density $p := \max(PSD) \cdot 1.5$

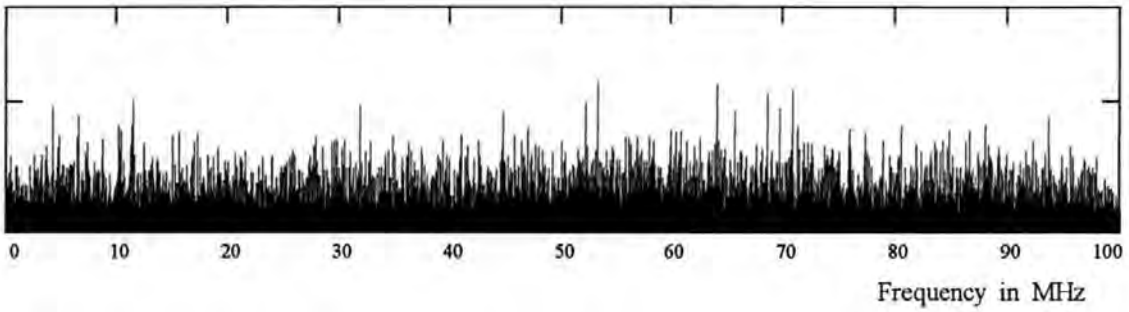

Cross Spectral Density

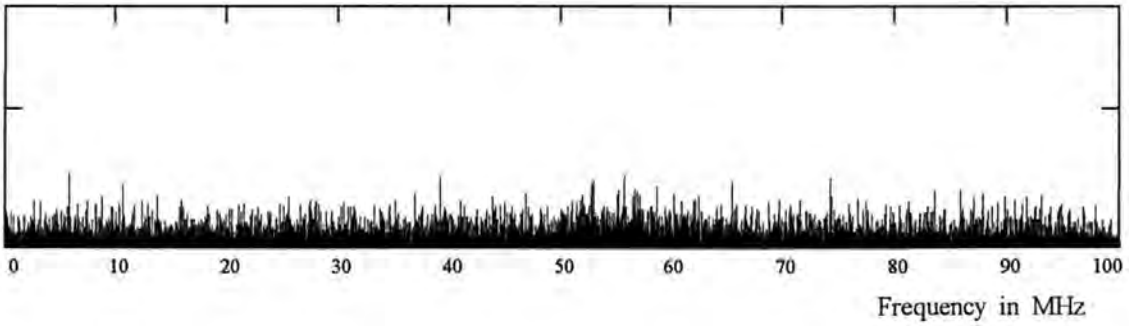

Selecting central portion of ACF and CCF. ie time domain filtering to reduce noise in PSD and CSD, for data set obtained by integration

$\frac{Bsa \cdot Ts}{4} = 2500$ XXXXXX $\gamma := 2048$ XXXXXX $width := ceil\left(\frac{N}{\gamma}\right)$ $start := floor\left(\frac{N}{2} - \frac{width}{2}\right)$ $j := 0..width - 1$

$wacf_j := acf_{j+start}$ $wccf_j := ccf_{j+start}$ $\tau_j := \frac{j+1}{fs} - \frac{Ts}{2 \cdot \gamma}$ $length(wacf) = 64$ $k := 0..ceil\left(\frac{width}{2}\right)$

Windowed acf $p := max(wacf) \cdot 1.2$

Time shift in μs

Windowed ccf $p := 0.2 \cdot p$

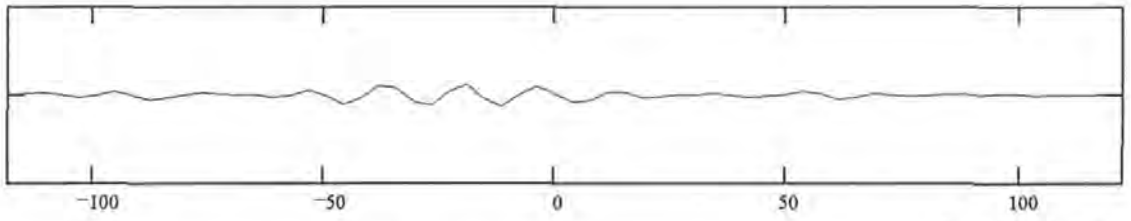

Time shift in ns

$TDFPSD := CFFT(recenter(wacf))$ $Rp := mag(TDFPSD)$

$TDFCSD := CFFT(recenter(wccf))$ $Rc := mag(TDFCSD)$

$f_k := \frac{k \cdot \gamma}{Ts}$ $Th := max(Rc) \cdot 0.5$ $B_k := if(Rc_k > Th, 1, 0)$ $dB := max(Rc) \cdot B$ $Bn := B_n$

TDFPSD $p := max(Rp) \cdot 1.2$

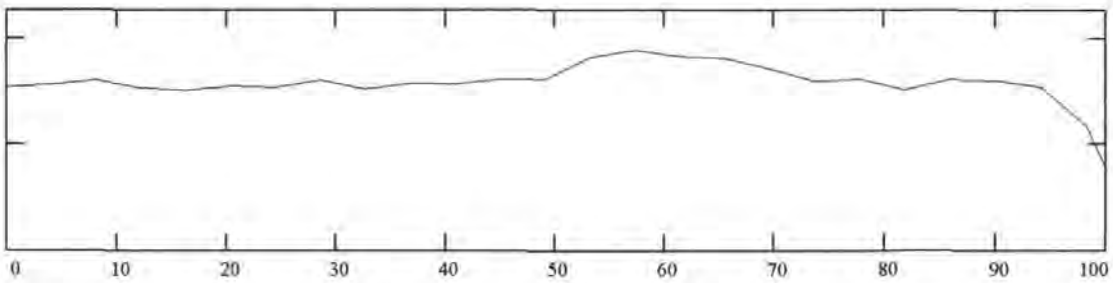

Frequency in MHz

TDFCSD $p := \max(Rc) \cdot 1.2$

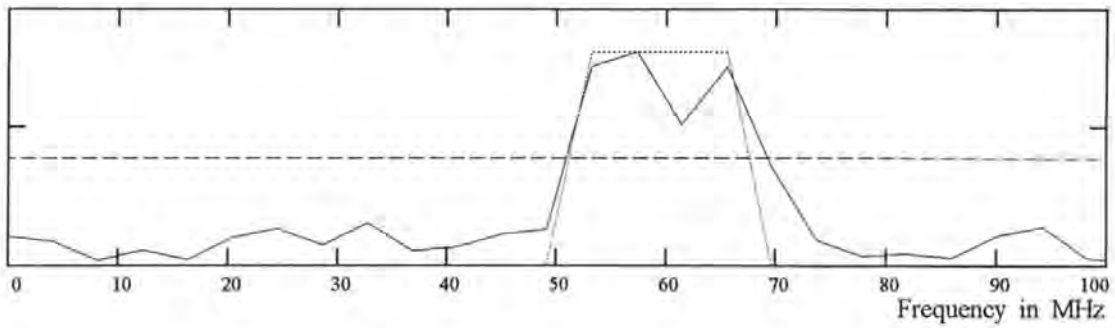

Signal to noise ratio in the TDFCSD

Estimating the signal to noise ratio in the TDFCSD

Separating the sections of the TDFCSD containing the signal and just noise

$$Nx_k := if\left[\left(fca - \frac{Bsa}{2} \geq f_k\right) + \left(f_k \geq fca + \frac{Bsa}{2}\right), Rc_k, 0\right]$$

$$Sx_k := if\left[\left(fca - \frac{Bsa}{2} \leq f_k\right) \cdot \left(f_k \leq fca + \frac{Bsa}{2}\right), Rc_k, 0\right]$$

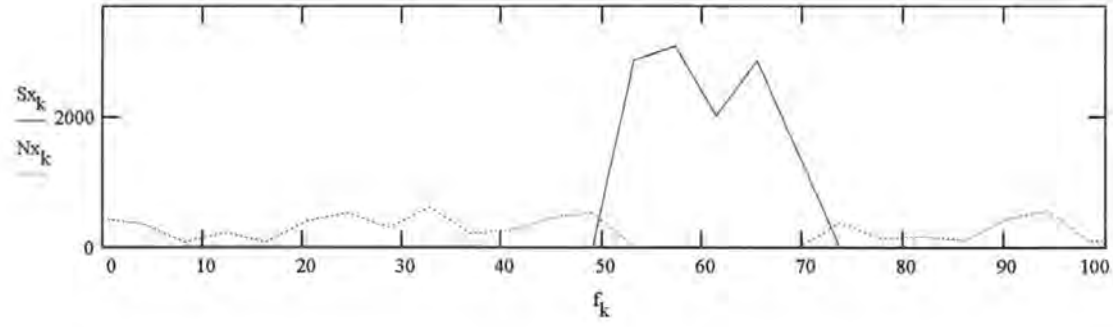

From simulation $SNRcsde := 10 \cdot \log\left(\frac{\sum \overrightarrow{Sx^2}}{\sum \overrightarrow{Nx^2}} \cdot \frac{B_n - Bsa}{Bsa}\right)$ $SNRcsde = 17$ dB

From theory $SNRcsda := 10 \cdot \log\left[\frac{\gamma \cdot \left(\frac{B_n}{Bsa}\right)^2 \cdot \left(10^{\frac{SNRina}{10}}\right)^2}{1 + 2 \cdot 10^{\frac{SNRina}{10}}}\right]$ $SNRcsda = 16.8$ dB

Estimating Phase Slope of the TDFCSD

$P := \text{phasecor}(\text{phase}(\text{TDFCSD})) - \text{phasecor}(\text{phase}(\text{TDFPSD}))$

Selecting appropriate part of bandwidth from application of threshold to the TDFCSD

$K_k := k \qquad \text{width} := \sum B \qquad \text{centre} := \frac{\sum \overrightarrow{(B \cdot K)}}{\sum B}$

$\text{start} := \text{ceil}\left(\text{centre} - \frac{\text{width}}{2}\right) \qquad \text{end} := \text{floor}\left(\text{centre} + \frac{\text{width}}{2}\right) \qquad \text{start} = 13 \qquad \text{end} = 16$

Selecting appropriate part of TDFCSD and calculating its phase slope (using a-priori knowledge of the signal bandwidth).

$\text{starta} := \text{ceil}\left[\left(\text{fca} - \frac{\text{Bsa}}{2}\right) \cdot \frac{\text{Ts}}{\gamma}\right] \qquad \text{enda} := \text{floor}\left[\left(\text{fca} + \frac{\text{Bsa}}{2}\right) \cdot \frac{\text{Ts}}{\gamma}\right] \qquad \text{starta} = 13 \qquad \text{enda} = 17$

$\text{Fstarta} := \frac{\text{starta} \cdot \gamma}{\text{Ts}} \qquad \text{Fenda} := \frac{\text{enda} \cdot \gamma}{\text{Ts}} \qquad \text{Fstarta} = 53.248 \qquad \text{Fenda} = 69.632$

$\text{inda} := 0 .. \text{enda} - \text{starta} \qquad \text{fa}_{\text{inda}} := \frac{\text{inda} \cdot \gamma}{\text{Ts}} \qquad \text{Da}_{\text{inda}} := P_{\text{inda} + \text{starta}}$

$\text{ma} := \text{slope}(\text{fa}, \text{Da}) \qquad \text{ca} := \text{intercept}(\text{fa}, \text{Da}) \qquad \text{Pa}_k := \text{ca} - f_{\text{starta}} \cdot \text{ma} + f_k \cdot \text{ma} \qquad \text{pa}_{\text{inda}} := \text{ca} + \text{fa}_{\text{inda}} \cdot \text{ma}$

Displaying phase slope of Time Domain Filtered Cross Spectral Density, with calculated straight line fit.

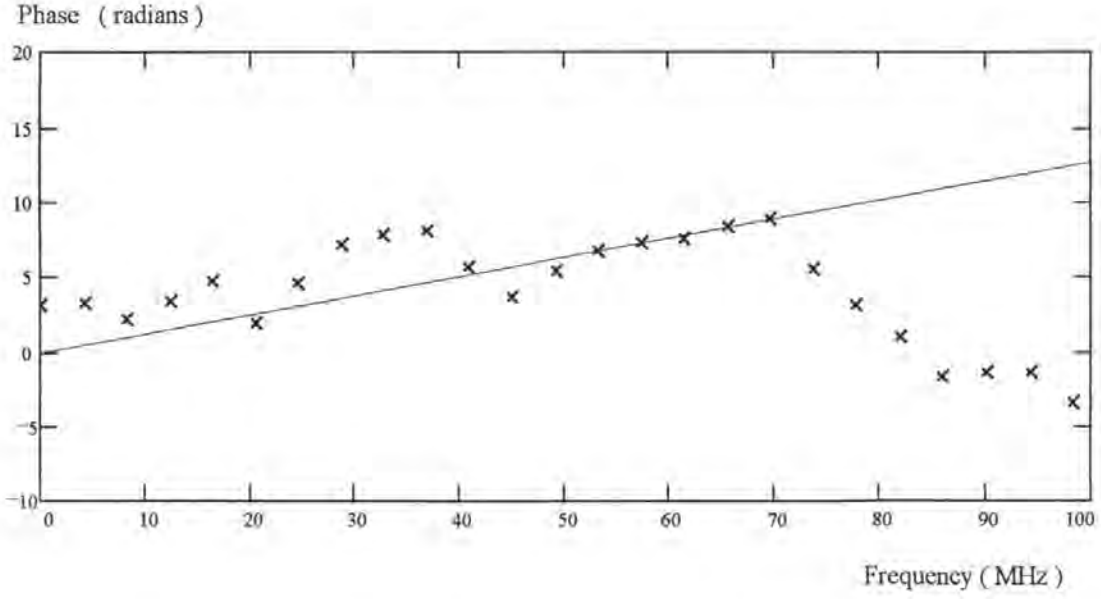

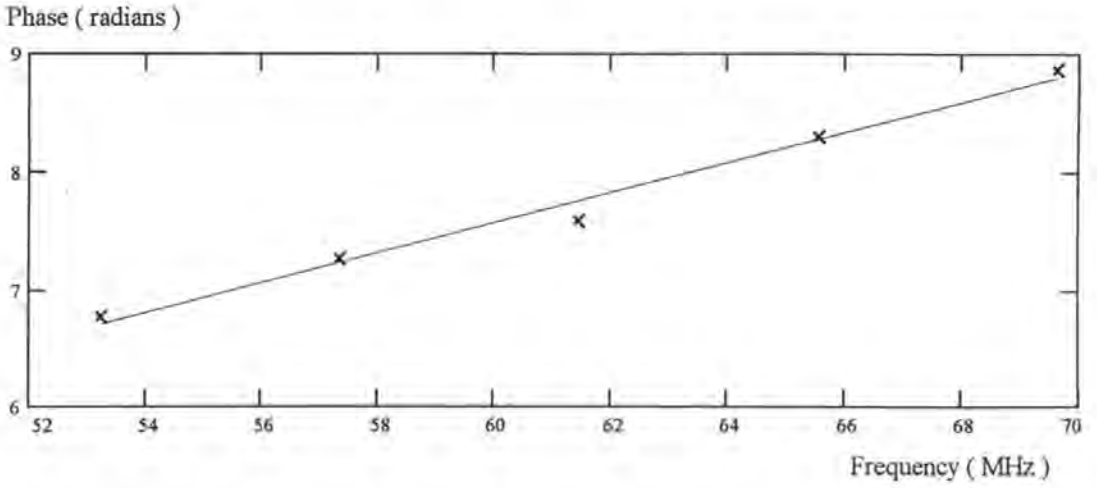

Calculating TDA from phase slope (and error in TDA):

$\tau ae := \frac{ma}{2 \cdot \pi}$ $\tau ae = 0.02035$ $\tau a = 0.02$ $\Delta \tau a := \tau ae - \tau a$ $\Delta \tau a \cdot 10^3 = 0.35$ ns

Calculating AOA and error in AOA estimation:

$\theta ae := \operatorname{asin}\left(\frac{c \cdot \tau ae}{d}\right) \cdot \frac{180}{\pi}$ $\theta ae = 37.62$ $\theta a = 36.87$ $\Delta \theta a := \theta ae - \theta a$ $\Delta \theta a = 0.75$ degrees

Predicted standard deviation of angle of arrival error

$$\sigma ae := \sqrt{\frac{3}{2 \cdot Bsa \cdot Ts}} \cdot \frac{c}{\pi \cdot d \cdot \cos(\theta a) \cdot B_n \cdot fact(SNRina)} \cdot \frac{180}{\pi}$$ $\sigma ae = 3.137$ degrees

Convert times from μs to ns, for summary

$\tau a := \tau a \cdot 10^3$ $\tau ae := \tau ae \cdot 10^3$ $\Delta \tau a := \Delta \tau a \cdot 10^3$

Summary

Sample length /μs	Ts = 500
Sampling frequency / MHz	fs = 262.144
Number of data points per signal	N = 131072
Noise bandwidth /MHz	$B_n = 100$
Oversampling factor	$\frac{fs}{2 \cdot B_n} = 1.3$
Signal centre frequency	fca = 60
Signal bandwidth /MHz	Bsa = 20
Input SNR /dB	SNRina = −15
Estimated SNR in the ccf /dB	SNRccfe = 19.006
Predicted SNR in the ccf /dB	SNRccfa = 19.7
Zoom factor	γ = 2048
Estimated SNR in TDFCSD /dB	SNRcsde = 17
Predicted SNR in TDFCSD /dB	SNRcsda = 16.8
Receiver separation /m	d = 10
Actual Time Difference of Arrival / ns	τa = 20
Estimated TDA / ns	τae = 20.347
Error in TDA estimation / ns	Δτa = 0.347
Actual angle of arrival /degrees	θa = 36.87
Estimated angle of arrval /degrees	θae = 37.62
Error in AOA estimation / degrees	Δθa = 0.75
Predicted s.d. of AOA estimation error	σae = 3.137

Appendix B. Mathcad simulation of dual receiver cross correlating ESM system - single biphase signal coded by a maximal length sequence

Set sample parameters

ie. set length of each sample, sampling frequency, and indexes to use in prosessing the signals.

Integration time: $Ts := 500$ μs No. of samples per data set: $N := 2^{17}$ $N = 131072$ $fs := \frac{N}{Ts}$

Sampling frequency: $fs = 262.144$ MHz $i := 0 .. N - 1$ $I_i := i$ $f := \frac{I}{Ts}$ $t := \frac{I}{fs}$ $n := 0 .. \frac{N}{2}$

Note: all times are in μs and all frequencies are in MHz.

Set receiver system parameters

Receiver noise bandwidth: $Bn := 100$ MHz

$\eta := 2$ nominal noise power spectral density (this file deals in ratios and not absolute values.)

Noise power, referred to receiver input: $N_i := \eta \cdot Bn \cdot 10^6$ $N_i = 2 \cdot 10^8$ W $\sigma_n := \sqrt{N_i}$

Create band pass filter to simulate bandwidth of receivers using a iir low pass filter equivalent to a 10 pole Butterworth filter. $LPF := iirlow\left(butter(10), \frac{Bn}{fs}\right)$

Create 2 sets of AWGN of specified power and bandwidth

$na := gaussn(N) \cdot \sigma_n \cdot \sqrt{\frac{fs}{2 \cdot Bn}}$ $nb := gaussn(N) \cdot \sigma_n \cdot \sqrt{\frac{fs}{2 \cdot Bn}}$

$n1 := response(na, LPF, N)$ $n2 := response(nb, LPF, N)$

Set up time shift between signals due to separation of receivers and direction of arrival of signals

Approximate time delay $\tau a := 0.02$ μs (20 ns)

For a receiver separation of $d := 10$ m, this corresponds to a diretion of arrival of

$\theta a := asin\left(\frac{c \cdot \tau a}{d}\right) \cdot \frac{1}{deg}$ $\theta a = 36.9$ degrees

Create a pair of maximal length sequence biphase coded signals to simulate signal from a transmitter arriving at the 2 receivers

Time delay $del := floor(\tau a \cdot fs)$ $del = 5$ Actual time delay $\tau a := \frac{del}{fs}$ $\tau a = 0.019$

Actual AOA $\theta a := asin\left(\frac{c \cdot \tau a}{d}\right) \cdot \frac{1}{deg}$ $\theta a = 34.9$ degrees

Code chip rate $rc := 10$ No. of samples per chip $k := \frac{fs}{rc}$ $k = 26.214$ $Bsa := 1 \cdot rc$

Carrier frequency $fca := 50$ No. of chips in sample $Ts \cdot rc = 5 \cdot 10^3$

Chip index $j := 0 .. Ts \cdot rc - 1$

No. of stages in shift register $n := 12$ Sequence length $2^n - 1 = 4095$

Initialise shift registers $\chi_j := if(j < n, 1, 0)$

Generate code sequence $\chi_j := if\left(j \geq n, mod\left(\chi_{j-1} + \chi_{j-4} + \chi_{j-6} + \chi_{j-12}, 2\right), \chi_j\right)$

Unipolar to bipolar conversion $\chi := \overrightarrow{(2 \cdot \chi - 1)}$ $length(\chi) = 5000$

$\chi^T = (1\ \ 1\ \ 1\ \ 1\ \ 1\ \ 1\ \ 1\ \ 1\ \ 1\ \ 1\ \ 1\ \ 1\ \ -1\ \ 1\ \ -1\ \ 1\ \ 1\ \ -1\ \ 1\ \ -1\ \ -1\ \ -1\ \ 1\ \ -1\ \ 1\ \ -1\ \ 1\ \ -1\ \ 1$

Generate modulating bipolar signal $chip1_i := \chi_{floor\left(\frac{i}{k}\right)}$

Generate the two signals as received (excluding noise)

$cha1 := \overrightarrow{(chip1 \cdot sin(2 \cdot \pi \cdot fca \cdot t))}$ $cha2_i := if(i < del, 0, cha1_{i-del})$

$cha1 := response(cha1, LPF, N)$ $cha2 := response(cha2, LPF, N)$

Display portion of two signals $m := 0 .. \frac{N}{250} - 1$ $sig1_m := cha1_m + 1.5$ $sig2_m := cha2_m - 1.5$

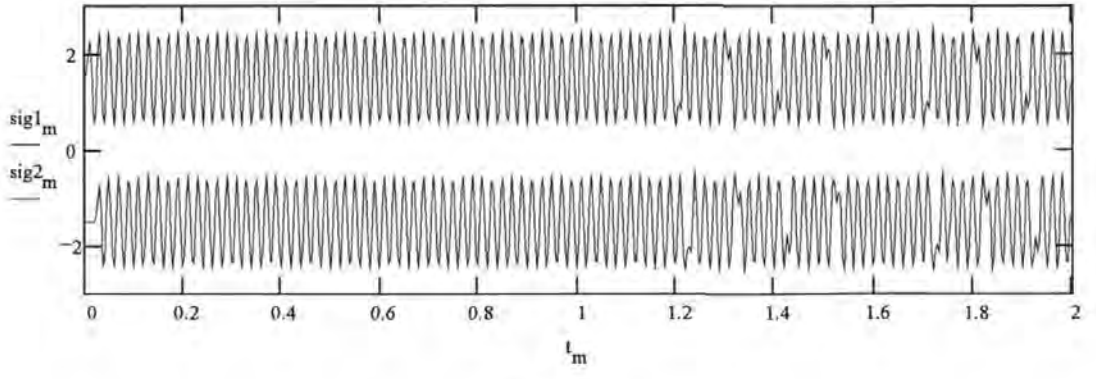

Add noise to signals to create receiver input signals with specified SNR

Signal to noise ratio at receiver input: SNRina := -12 **dB**

XXXXXXXXX

Then calculate the signal amplitude required to give this signal to noise ratio and add the signal vectors to the noise vectors to generate the inputs to the correlator.

Signal Amplitude: $Aa := \sqrt{2 \cdot \left(10^{\frac{SNRina}{10}} \cdot N_i\right)}$

Add signals to noise s1 := Aa·cha1 + n1 s2 := Aa·cha2 + n2

Display 1 μs of the receiver inputs. It is clear that the signals are well "buried in the noise". $k := 0 .. \frac{N}{500} - 1$

Signal in channel 1 (Units: volts. Scale dependent on system gain) s := max(s1)·1.1

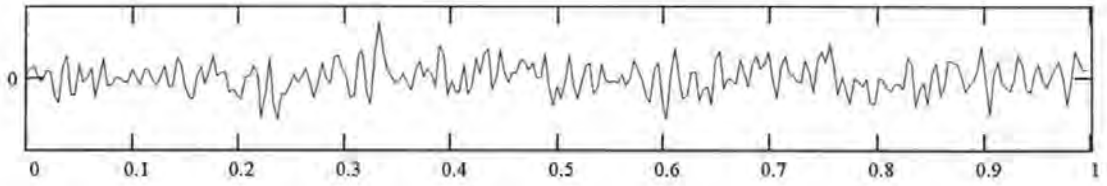

Signal in channel 2

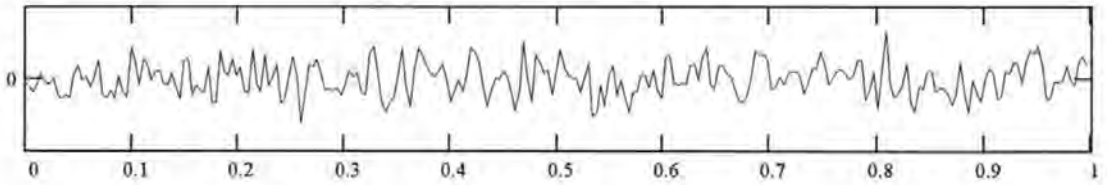

Time (μs)

Calculating PSD and ACF of one signal and CSD and CCF of both signals by FFT method

$PSD := \overrightarrow{mag(FFT(s1))^2}$ $acf := \frac{1}{fs} \cdot Re(recenter(IFFT(PSD)))$

$CSD := \overrightarrow{(FFT(s1) \cdot \overrightarrow{FFT(s2)})}$ $ccf := \frac{1}{fs} \cdot Re(recenter(IFFT(CSD)))$

Estimating the signal to noise ratio in the output correlation function

Estimate from simulation: $SNRccfe := 10 \cdot \log\left(\frac{N \cdot \max(ccf)^2}{\overrightarrow{\sum ccf^2}}\right)$ SNRccfe = 25.212 dB

****

Theoretically predicted $SNRccfa := 10 \cdot \log\left[\frac{2 \cdot Bn \cdot Ts \cdot \left(10^{\frac{SNRina}{10}}\right)^2}{1 + 2 \cdot \left(10^{\frac{SNRina}{10}}\right)}\right]$ SNRccfa = 25.48 dB

****

autocorrelation function $p := \max(acf) \cdot 1.2$

Time shift in μs

cross correlation function (magnified by 10 relative to acf) $p := 0.1 \cdot p$

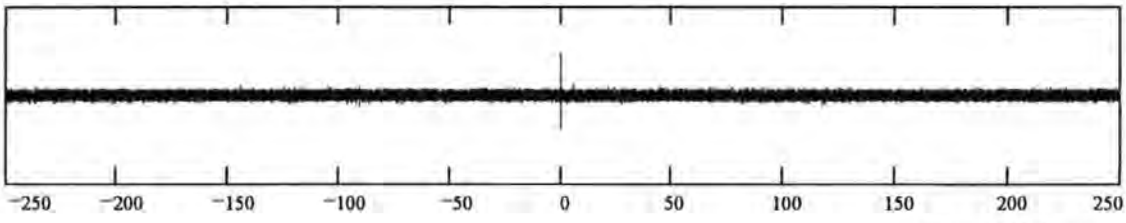

Time shift in μs

Power Spectral Density $p := \max(PSD) \cdot 1.5$ $n := 0 .. \frac{N}{2}$

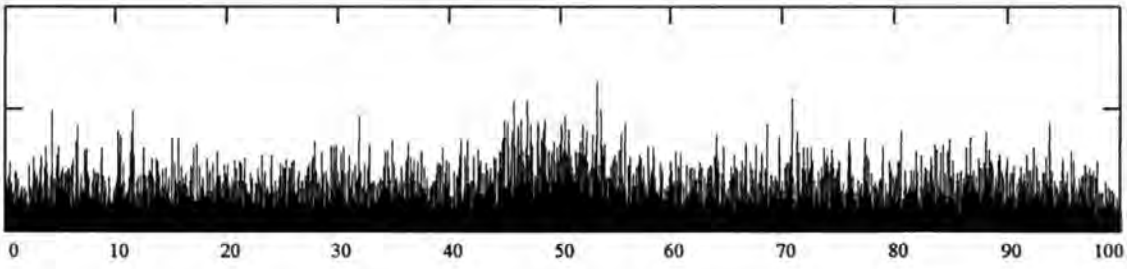

Frequency in MHz

Cross Spectral Density

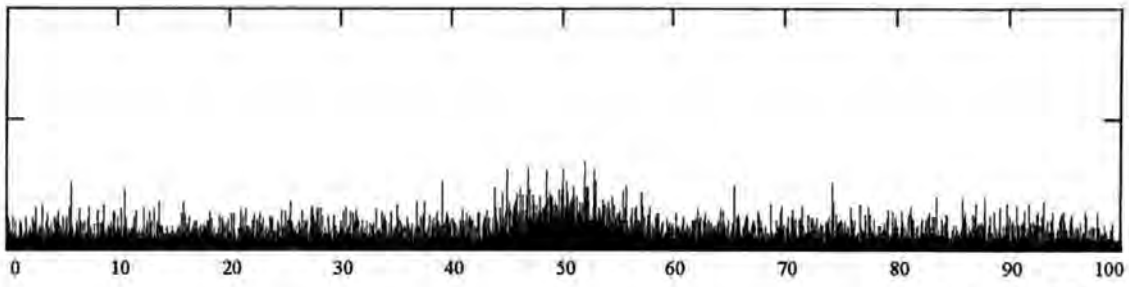

Selecting central portion of ACF and CCF. ie time domain filtering to reduce noise in PSD and CSD, for data set obtained by integration

$\frac{Bsa \cdot Ts}{4} = 1250$ XXXXXX $\gamma := 1024$ XXXXXX $width := ceil\left(\frac{N}{\gamma}\right)$ $start := floor\left(\frac{N}{2} - \frac{width}{2}\right)$ $j := 0 .. width - 1$

$wacf_j := acf_{j+start}$ $wccf_j := ccf_{j+start}$ $\tau_j := \frac{j+1}{fs} - \frac{Ts}{2 \cdot \gamma}$ $length(wacf) = 128$ $k := 0 .. ceil\left(\frac{width}{2}\right)$

Windowed acf $p := max(wacf) \cdot 1.2$

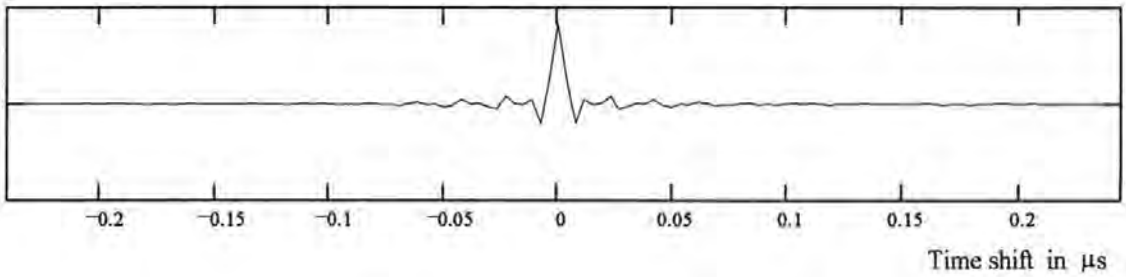

Windowed ccf $p := 0.2 \cdot p$

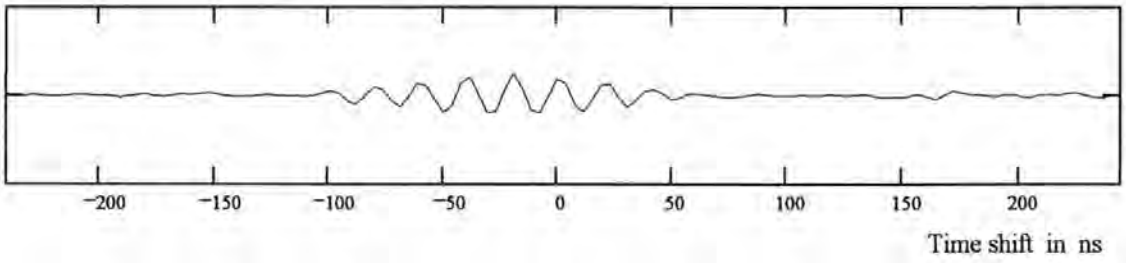

$TDFPSD := CFFT(recenter(wacf))$ $Rp := mag(TDFPSD)$

$TDFCSD := CFFT(recenter(wccf))$ $Rc := mag(TDFCSD)$

$f_k := \frac{k \cdot \gamma}{Ts}$ $Th := max(Rc) \cdot 0.5$ $B_k := if(Rc_k > Th, 1, 0)$ $dB := max(Rc) \cdot B$

TDFPSD $p := \max(Rp) \cdot 1.2$

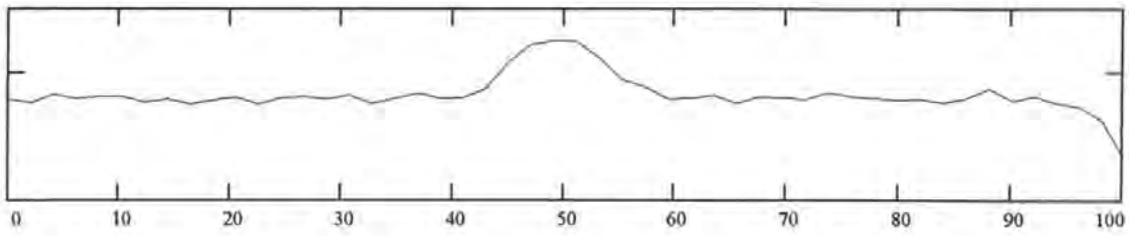

Frequency in MHz

TDFCSD $p := \max(Rc) \cdot 1.2$

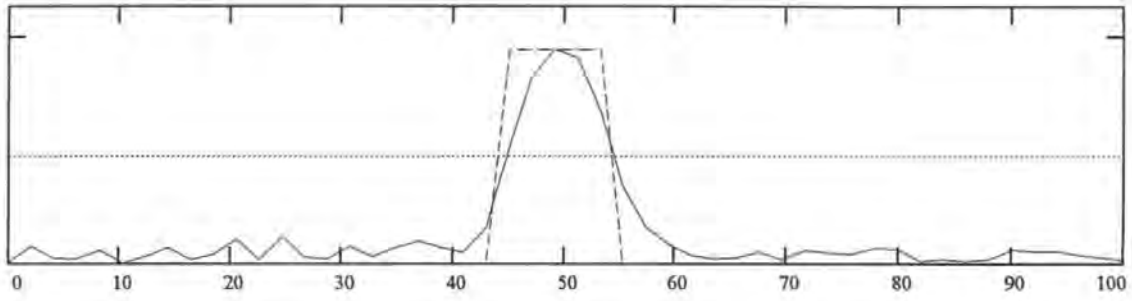

Frequency in MHz

Signal to noise ratio in the TDFCSD

Separating the sections of the TDFCSD containing the signal and just noise

$$Nx_k := if\left[\left(fca - \frac{Bsa}{2} \geq f_k\right) + \left(f_k \geq fca + \frac{Bsa}{2}\right), Rc_k, 0\right] \qquad Sx_k := if\left[\left(fca - \frac{Bsa}{2} \leq f_k\right) \cdot \left(f_k \leq fca + \frac{Bsa}{2}\right), Rc_k, 0\right]$$

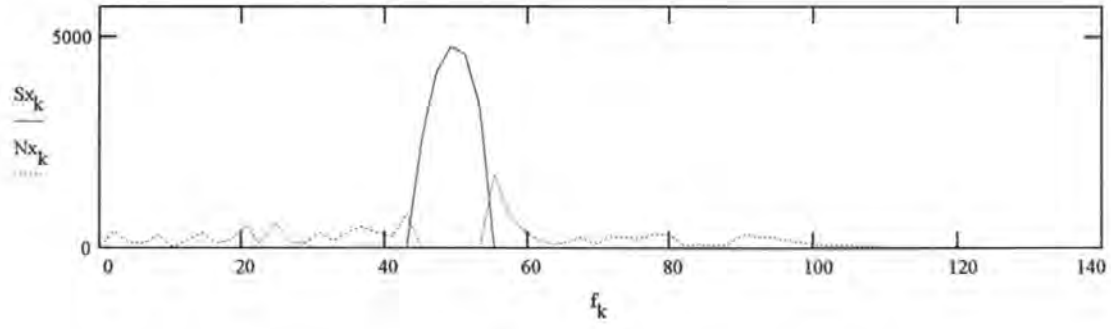

From simulation $SNRcsde := 10 \cdot \log\left(\frac{\sum \overrightarrow{Sx^2}}{\sum \overrightarrow{Nx^2}} \cdot \frac{Bn - Bsa}{Bsa}\right)$ $SNRcsde = 19.9$ dB

From theory $SNRcsda := 10 \cdot \log\left[\frac{\gamma \cdot \left(\frac{Bn}{Bsa}\right)^2 \cdot \left(10^{\frac{SNRina}{10}}\right)^2}{1 + 2 \cdot 10^{\frac{SNRina}{10}}}\right]$ $SNRcsda = 25.6$ dB

Estimating Phase Slope of the TDFCSD

$P := \text{phasecor}(\text{phase}(\text{TDFCSD})) - \text{phasecor}(\text{phase}(\text{TDFPSD}))$

Selecting appropriate part of bandwidth from application of threshold to the TDFCSD

$K_k := k \qquad \text{width} := \sum B \qquad \text{centre} := \frac{\sum \overrightarrow{(B \cdot K)}}{\sum B}$

$\text{start} := \text{ceil}\left(\text{centre} - \frac{\text{width}}{2}\right) \qquad \text{end} := \text{floor}\left(\text{centre} + \frac{\text{width}}{2}\right) \qquad \text{start} = 22 \qquad \text{end} = 26$

Selecting appropriate part of TDFCSD and calculating its phase slope (using a-priori knowledge of the signal bandwidth).

$\text{starta} := \text{ceil}\left[\left(\text{fca} - \frac{\text{Bsa}}{2}\right) \cdot \frac{\text{Ts}}{\gamma}\right] \qquad \text{enda} := \text{floor}\left[\left(\text{fca} + \frac{\text{Bsa}}{2}\right) \cdot \frac{\text{Ts}}{\gamma}\right] \qquad \text{starta} = 22 \qquad \text{enda} = 26$

$\text{Fstarta} := \frac{\text{starta} \cdot \gamma}{\text{Ts}} \qquad \text{Fenda} := \frac{\text{enda} \cdot \gamma}{\text{Ts}} \qquad \text{Fstarta} = 45.056 \qquad \text{Fenda} = 53.248$

$\text{inda} := 0 .. \text{enda} - \text{starta} \qquad fa_{\text{inda}} := \frac{\text{inda} \cdot \gamma}{\text{Ts}} \qquad Da_{\text{inda}} := P_{\text{inda} + \text{starta}}$

$ma := \text{slope}(fa, Da) \qquad ca := \text{intercept}(fa, Da) \qquad Pa_k := ca - f_{\text{starta}} \cdot ma + f_k \cdot ma \qquad pa_{\text{inda}} := ca + fa_{\text{inda}} \cdot ma$

Displaying phase slope of Time Domain Filtered Cross Spectral Density, with calculated straight line fit

Phase in radians

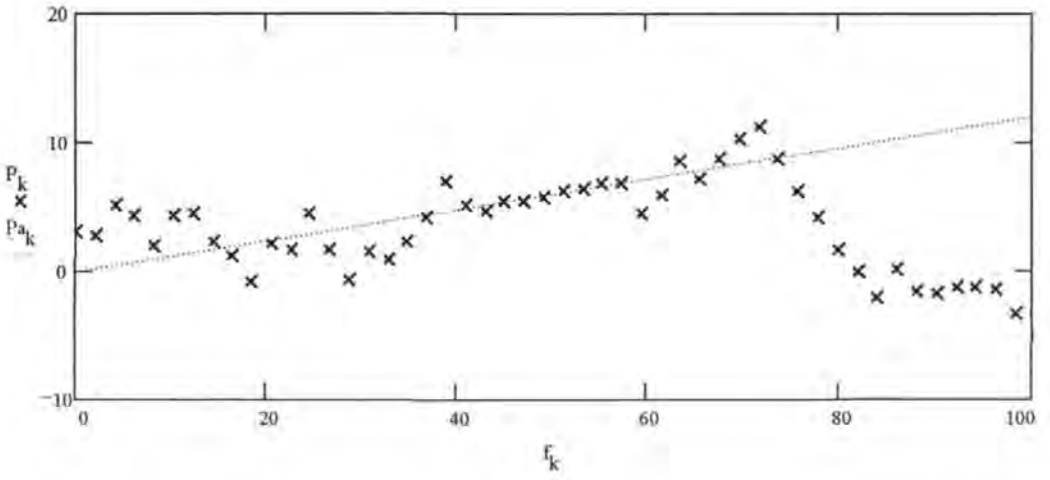

Frequency in MHz

Phase in radians

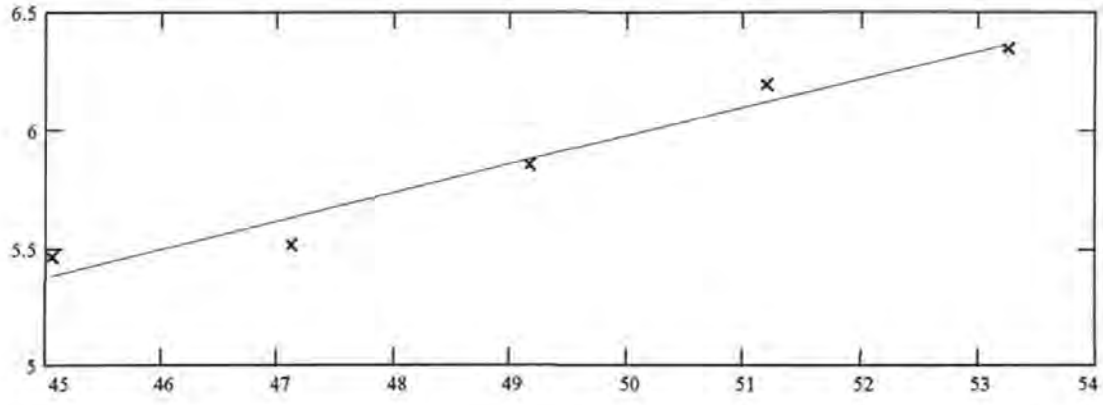

Frequency in MHz

Calculating TDA from phase slope (and error in TDA):

$\tau ae := \frac{ma}{2 \cdot \pi}$ $\tau ae = 0.01913$ $\tau a = 0.01907$ $\Delta \tau a := \tau ae - \tau a$ $\Delta \tau a \cdot 10^3 = 0.05$ ns

Calculating AOA and error in AOA estimation:

$\theta ae := \operatorname{asin}\left(\frac{c \cdot \tau ae}{d}\right) \cdot \frac{180}{\pi}$ $\theta ae = 35.019$ $\theta a = 34.904$ $\Delta \theta a := \theta ae - \theta a$ $\Delta \theta a = 0.114$ degrees

Predicted standard deviation of angle of arrival error

$\sigma ae := \sqrt{\frac{3}{2 \cdot Bsa \cdot Ts}} \cdot \frac{c}{\pi \cdot d \cdot \cos(\theta a) \cdot Bn \cdot fact(SNRina)} \cdot \frac{180}{\pi}$ $\sigma ae = 1.597$ degrees

Convert times from μs to ns, for summary

$\tau a := \tau a \cdot 10^3$ $\tau ae := \tau ae \cdot 10^3$ $\Delta \tau a := \Delta \tau a \cdot 10^3$

Summary

Sample length /μs	Ts = 500
Sampling frequency / MHz	fs = 262.144
Number of data points per signal	N = 131072
Noise bandwidth /MHz	Bn = 100
Oversampling factor	$\frac{fs}{2 \cdot Bn} = 1.3$
Signal centre frequency	fca = 50
Signal bandwidth /MHz	Bsa = 10
Input SNR /dB	SNRina = −12
Estimated SNR in the ccf /dB	SNRccfe = 25.212
Predicted SNR in the ccf /dB	SNRccfa = 25.5
Zoom factor	γ = 1024
Estimated SNR in TDFCSD /dB	SNRcsde = 19.9
Predicted SNR in TDFCSD /dB	SNRcsda = 25.6
Receiver separation /m	d = 10
Actual Time Difference of Arrival / ns	τa = 19.073
Estimated TDA / ns	τae = 19.128
Error in TDA estimation / ns	Δτa = 0.055
Actual angle of arrival /degrees	θa = 34.904
Estimated angle of arrval /degrees	θae = 35.019
Error in AOA estimation / degrees	Δθa = 0.114
Predicted s.d. of AOA estimation error	σae = −1.597

Appendix C. Mathcad simulation of dual receiver cross correlating ESM system - 2 FMCW signals with an interfering pulse.

Set sample parameters

ie. set length of each sample, sampling frequency, and indexes to use in prosessing the signals.

Integration time: $T_s := 50$ μs No. of samples per data set: $N := 2^{13}$ $N = 8192$ $f_s := \frac{N}{T_s}$

Sampling frequency: $f_s = 163.84$ MHz $i := 0..N-1$ $I_i := i$ $f := \frac{I}{T_s}$ $t := \frac{I}{f_s}$ $n := 0..\frac{N}{2}$

Note: all times are in μs and all frequencies are in MHz.

Set receiver system parameters

Receiver noise bandwidth: $B_n := 80$ MHz

$\eta := 2$ nominal noise power spectral density (this file deals in ratios and not absolute values.)

Noise power, referred to receiver input: $N_i := \eta \cdot B_n \cdot 10^6$ $N_i = 1.6 \cdot 10^8$ W $\sigma_n := \sqrt{N_i}$

Create band pass filter to simulate bandwidth of receivers using a iir low pass filter equivalent to a 10 pole Butterworth filter.

$LPF := \text{iirlow}\left(\text{butter}(4), \frac{B_n}{f_s}\right)$

Create 2 sets of AWGN of specified power and bandwidth

$na := \text{gaussn}(N) \cdot \sigma_n \cdot \sqrt{\frac{f_s}{2 \cdot B_n}}$

$nb := \text{gaussn}(N) \cdot \sigma_n \cdot \sqrt{\frac{f_s}{2 \cdot B_n}}$

$n1 := \text{response}(na, LPF, N)$

$n2 := \text{response}(nb, LPF, N)$

Set up time shift between signals due to separation of receivers and direction of arrival of signals

$\tau a := 0.02$ μs (20 ns) $\tau b := -0.01$ μs (-10 ns)

For a receiver separation of $d := 10$ m, this corresponds to a diretion of arrival of

$\theta a := \text{asin}\left(\frac{c \cdot \tau a}{d}\right) \cdot \frac{1}{\text{deg}}$ $\theta a = 36.9$ degrees $\theta b := \text{asin}\left(\frac{c \cdot \tau b}{d}\right) \cdot \frac{1}{\text{deg}}$ $\theta b = -17.5$ degrees

Create a set of chirp pulses to simulate signals from 2 transmitters arriving at the 2 receivers

A 500 μs chirp sweeping over 10 MHz, which could be part of an FMCW signal, is generated. For this simulation it is assumed that this is exactly one cycle of the FMCW signal. First set the parameters.

Chirp centre frequencies: $fca := 25\ MHz$ $fcb := 65\ MHz$

Chirp bandwidth: $Bsa := 20\ MHz$ $Bsb := 10\ MHz$

Chirp time-bandwidth product: $Bsa \cdot T_s = 1000$ $Bsb \cdot T_s = 500$

Then create 2 chirp signals, one without and one with a time delay, band pass filtered as by the receivers

$$cha(x) := \sin\left[2\cdot\pi\cdot\left[\left(fca - \frac{Bsa}{2}\right)\cdot x + \frac{Bsa}{2\cdot T_s}\cdot x^2\right]\right] \qquad cha1 := \overrightarrow{cha(t)}$$

$$cha2 := \overrightarrow{\left[cha(t-\tau a)\cdot rect\left[\frac{2\cdot t - T_s - \tau a}{2\cdot\left(T_s - \tau a\right)}\right] + cha\left(t + T_s - \tau a\right)\cdot rect\left(\frac{2\cdot t - \tau a}{2\cdot \tau a}\right)\right]}$$

$$chb(x) := \sin\left[2\cdot\pi\cdot\left[\left(fcb - \frac{Bsb}{2}\right)\cdot x + \frac{Bsb}{2\cdot T_s}\cdot x^2\right]\right] \qquad chb1 := \overrightarrow{chb(t)}$$

$$chb2 := \overrightarrow{\left[chb(t-\tau b)\cdot rect\left[\frac{2\cdot t - T_s - \tau b}{2\cdot\left(T_s - \tau b\right)}\right] + chb\left(t + T_s - \tau b\right)\cdot rect\left(\frac{2\cdot t - \tau b}{2\cdot \tau b}\right)\right]}$$

$cha1 := response(cha1, LPF, N)$ $cha2 := response(cha2, LPF, N)$

$chb1 := response(chb1, LPF, N)$ $chb2 := response(chb2, LPF, N)$

Generate interfering pulse, at frequency 30 MHz and 1 μs long

$$fIa := 30 \quad wa := 1 \quad \tau Ia := 0.01 \quad Inta(x) := \sin(2\cdot\pi\cdot fIa\cdot x)\cdot rect\left(\frac{x - 0.25\cdot T_s}{wa}\right)$$

$inta1 := \overrightarrow{Inta(t)}$ $inta2 := \overrightarrow{Inta(t - \tau Ia)}$

$inta1 := response(inta1, LPF, N)$ $inta2 := response(inta2, LPF, N)$

Add noise to signals to create receiver input signals with specified SNR

Signal to noise ratios at receiver input:

SNRina := -7 **dB** SNRinb := -10 **dB** SNRIa := 30 **dB**

XXXXXXXXX **XXXXXXXXX** **XXXXXXXXX**

Then calculate the signal amplitude required to give this signal to noise ratio and add the signal vectors to the noise vectors to generate the inputs to the correlator.

Signal Amplitudes: $Aa := \sqrt{2 \cdot \left(10^{\frac{SNRina}{10}} \cdot N_i\right)}$ $Ab := \sqrt{2 \cdot \left(10^{\frac{SNRinb}{10}} \cdot N_i\right)}$ $Ba := \sqrt{2 \cdot \left(10^{\frac{SNRIa}{10}} \cdot N_i\right)}$

Add signals and interfering pulse to noise

s1 := Aa·cha1 + Ab·chb1 + Ba·inta1 + n1

s2 := Aa·cha2 + Ab·chb2 + Ba·inta2 + n2

Display 1 μs of the receiver inputs. It is clear that the signals are well "buried in the noise", and that the interfering pulse dominates.

$k := 0 .. \frac{N}{1} - 1$

Signal in channel 1 (Units: volts. Scale dependent on system gain)

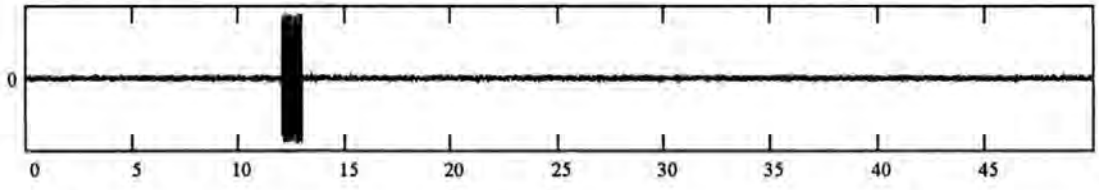

Signal in channel 2

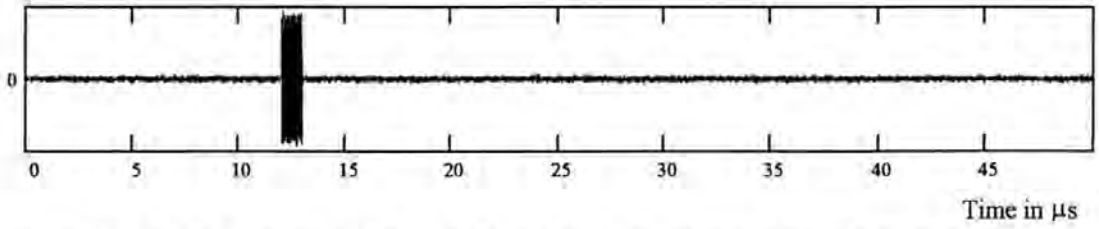

Calculating PSD and ACF of one signal and CSD and CCF of both signals by FFT method

$PSD := \overrightarrow{mag(FFT(s1))^2}$ $acf := \frac{1}{f_s} \cdot Re(recenter(IFFT(PSD)))$

$CSD := \overrightarrow{(FFT(s1) \cdot \overline{FFT(s2)})}$ $ccf := \frac{1}{f_s} \cdot Re(recenter(IFFT(CSD)))$ $j := 0 .. \frac{N}{2}$

Displaying CSD, dominated by interfering pulse

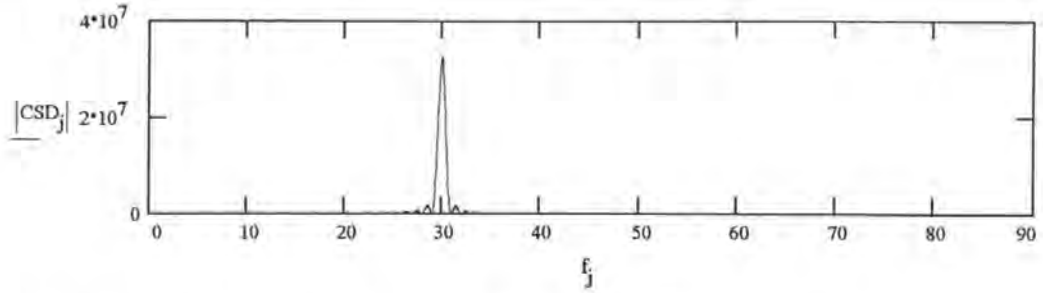

Pass signal through square law detector and video filter to locate pulse temporally

Generating video filter and then passing squared signal through that filter. Displaying filter output with threshold to be applied.

$VF := \text{iirlow}\left(\text{butter}(2), \frac{1}{f_s}\right)$ $v := \text{response}\left(\overrightarrow{s1^2}, VF, N\right)$ $th := \left(4 \cdot \sigma_n\right)^2$

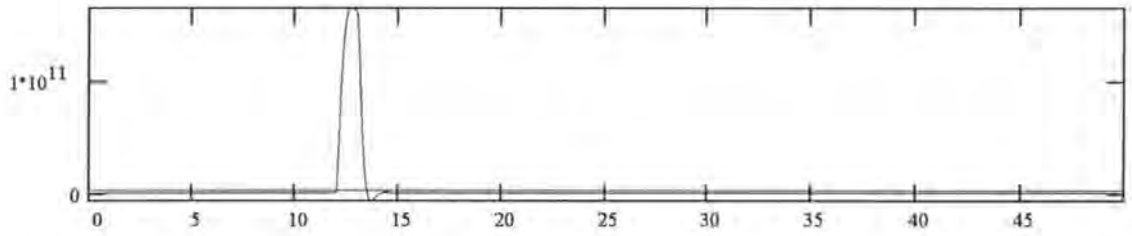

Applying threshold detector: $vs_i := \text{if}(v_i > th, 1, 0)$

Estimating width of pulse: $w := \frac{\sum vs}{f_s \cdot 1.2}$ $w = 1.236$

Estimating position of centre of pulse delay $= 0.3$ $cg := \frac{\sum\left(\overrightarrow{I \cdot vs}\right)}{f_s \cdot \sum vs} - \text{delay}$ $cg = 12.469$

Determining time range over which to apply notch filter $st := cg - \frac{w}{2}$ $end := cg + \frac{w}{2}$ $vs_i := \text{if}\left[\left(st < t_i\right) \cdot \left(t_i < end\right), 1, 0\right]$

and displaying

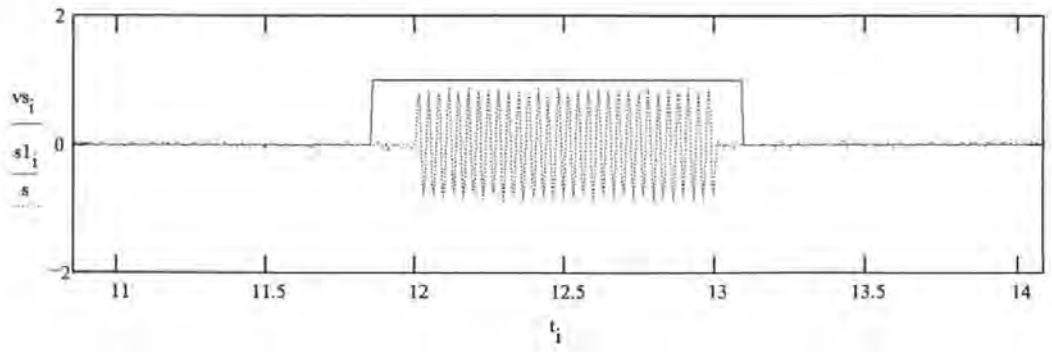

Separating out sections of input signals to which notch filter should be applied

$pulse1_i := if(vs_i = 1, s1_i, 0)$ $pulse2_i := if(vs_i = 1, s2_i, 0)$ $s1 := s1 - pulse1$ $s2 := s2 - pulse2$

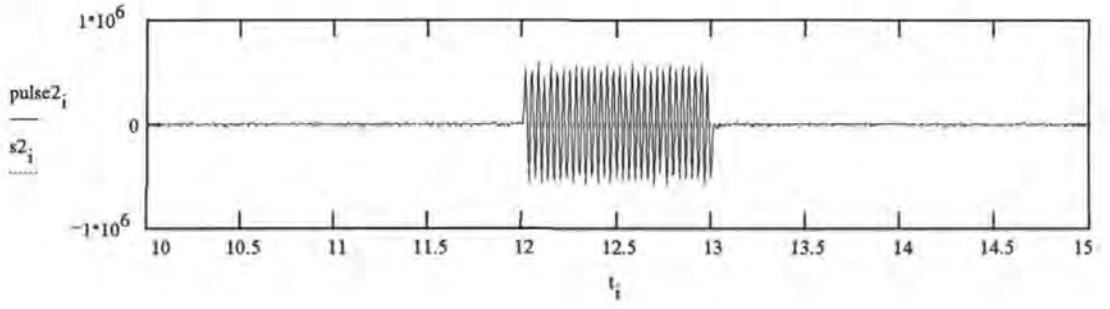

Calculating spectrum of interfering pulse and deriving parameters for notch filter

$j := 0..\frac{N}{2}$ $J_j := j$ $P := FFT(pulse1)$ $P := mag(P)$ $TH := 1000$ $PT_j := if(P_j > TH, 1, 0)$

Centre frequency: $F := \frac{\sum(\overrightarrow{(PT \cdot J)})}{T_s \cdot \sum PT}$ $F = 29.97$ Bandwidth: $W := \frac{\sum PT}{T_s}$ $W = 2.48$

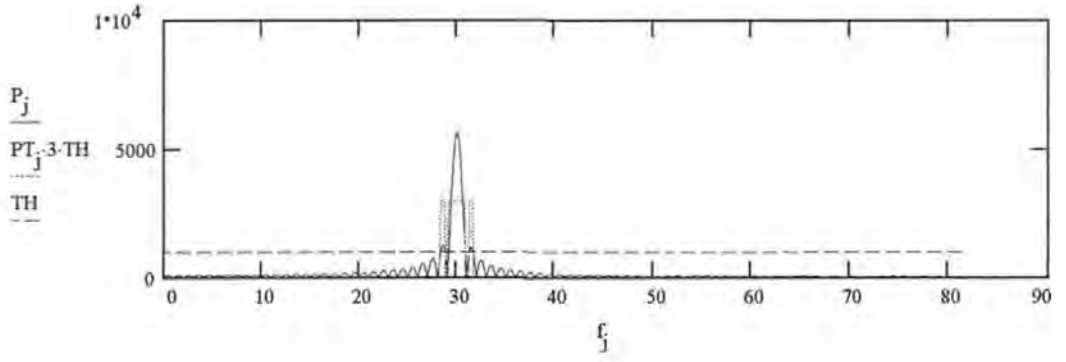

Generating notch filter, and displaying its frequency response

$NotchF := iirstop\left(butter(2), \frac{F - W}{f_s}, \frac{F + W}{f_s}\right)$ $x := 0, 0.001..0.5$

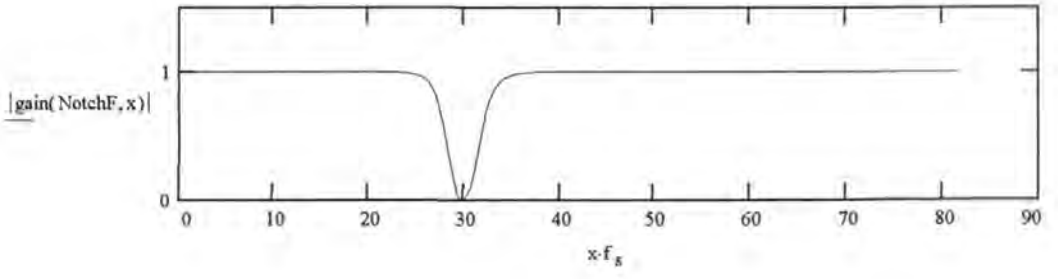

Filtering section of signals containing pulse and adding back to signals

$win_i := if\left[\left(cg - 0.5 \cdot w < t_i\right) \cdot \left(t_i < cg + 0.5 \cdot w\right), 1, 0\right]$

$s1 := \overrightarrow{s1 + (response(pulse1, NotchF, N) \cdot win)}$ $\quad$ $s2 := \overrightarrow{s2 + (response(pulse2, NotchF, N) \cdot win)}$

Clipping to remove "rabbit's ears".

$clip := 3 \cdot \sigma_n$

$s1_i := if\left(s1_i > clip, clip, if\left(s1_i < -clip, -clip, s1_i\right)\right)$ $\quad$ $s2_i := if\left(s2_i > clip, clip, if\left(s2_i < -clip, -clip, s2_i\right)\right)$

Signal in channel 1 (Units: volts. Scale dependent on system gain) $\quad s := \max(s1) \cdot 1.5$

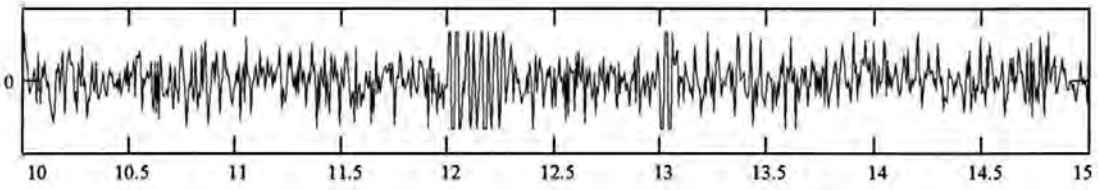

Signal in channel 2 (Units: volts. Scale dependent on system gain)

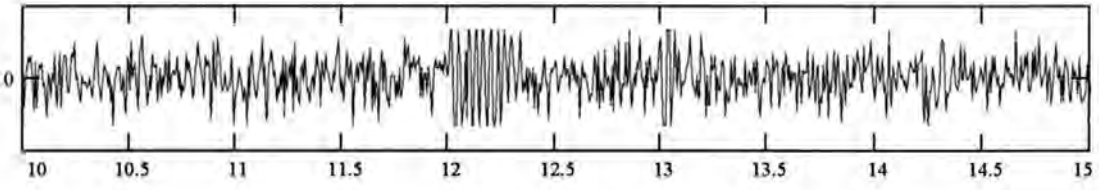

Calculating PSD and ACF of one signal and CSD and CCF of both signals by FFT method

$PSD := \overrightarrow{mag(FFT(s1))^2}$ $\quad$ $acf := \frac{1}{f_s} \cdot Re(recenter(IFFT(PSD)))$

$CSD := \overrightarrow{\left(FFT(s1) \cdot \overline{FFT(s2)}\right)}$ $\quad$ $ccf := \frac{1}{f_s} \cdot Re(recenter(IFFT(CSD)))$

Estimating the signal to noise ratio in the output correlation function

Estimate from simulation: $SNR_{ccfe} := 10 \cdot \log\left(\frac{N \cdot \max(ccf)^2}{\overrightarrow{\sum ccf^2}}\right)$ $SNR_{ccfe} = 23.879$ dB

****

Theoretically predicted

$$SNRccfa := 10 \cdot \log\left[\frac{2 \cdot B_n \cdot T_s \cdot \left(10^{\frac{SNRina}{10}}\right)^2}{1 + 2 \cdot \left(10^{\frac{SNRina}{10}}\right)}\right]$$

$SNRccfa = 23.57$ dB

****

$$SNRccfb := 10 \cdot \log\left[\frac{2 \cdot B_n \cdot T_s \cdot \left(10^{\frac{SNRinb}{10}}\right)^2}{1 + 2 \cdot \left(10^{\frac{SNRinb}{10}}\right)}\right]$$

$SNRccfb = 18.24$ dB

****

Displays $p := \max(acf) \cdot 1.5$

$j := 0..\frac{N}{2}$

autocorrelation function

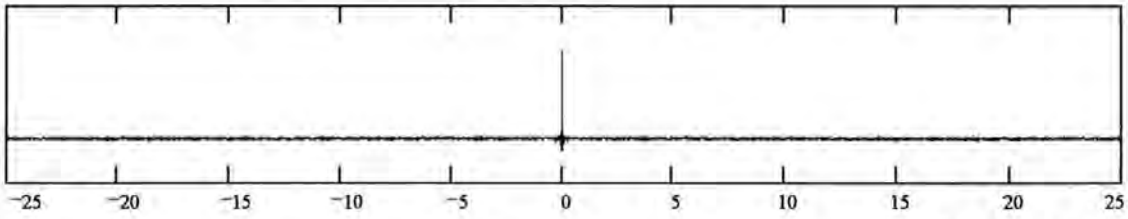

$p := \frac{p}{5}$

cross correlation function (magnified by 5 relative to acf)

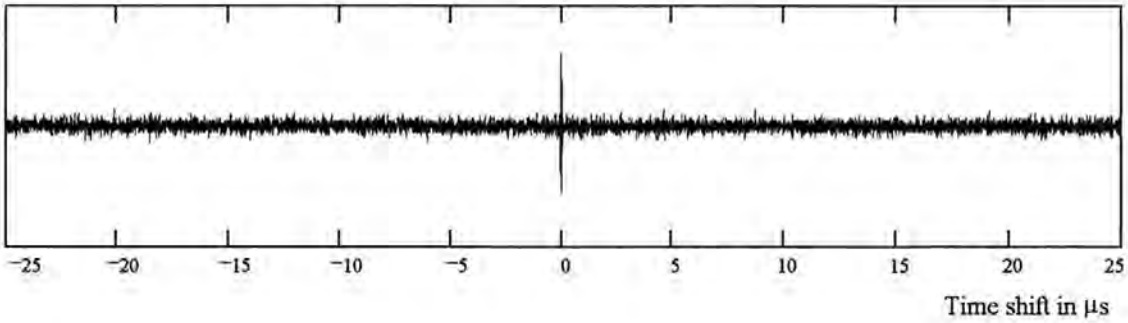

Power Spectral Density

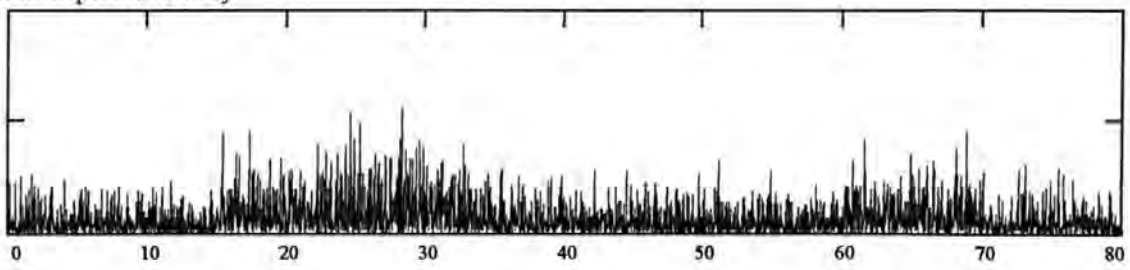

Cross Spectral Density

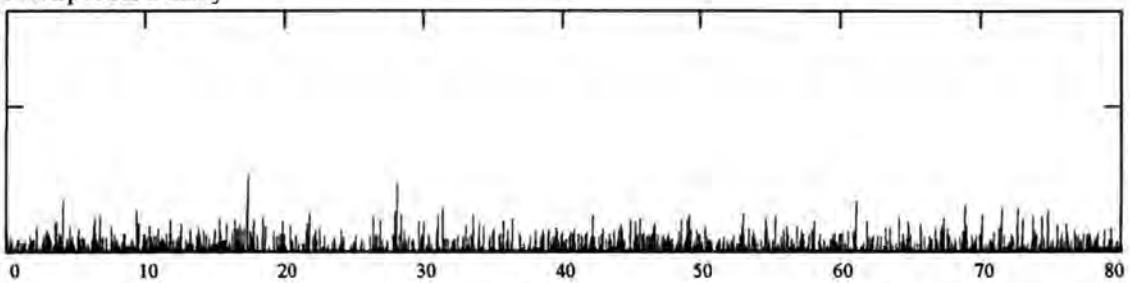

Selecting central portion of ACF and CCF. ie time domain filtering to reduce noise in PSD and CSD, for data set obtained by integration

XXXXXX

$\gamma := 128$ $j := 0..\frac{N}{\gamma} - 1$ $\tau_j := \frac{j+1}{f_s} - \frac{T_s}{2 \cdot \gamma}$ $wacf_j := acf_{j+\frac{N}{2} \cdot \left(1 - \frac{1}{\gamma}\right)}$ $wccf_j := ccf_{j+\frac{N}{2} \cdot \left(1 - \frac{1}{\gamma}\right)}$

XXXXXX

Windowed acf

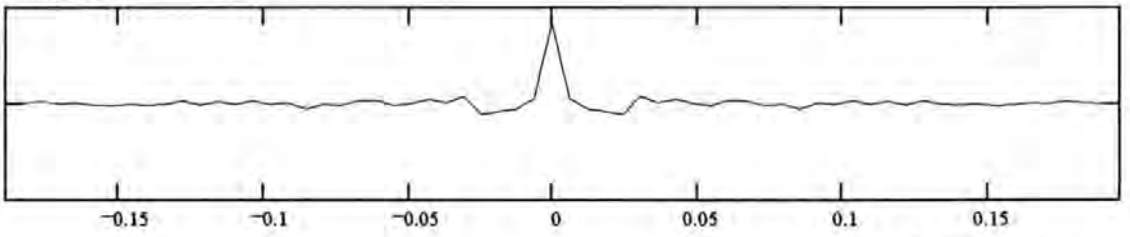

Windowed ccf

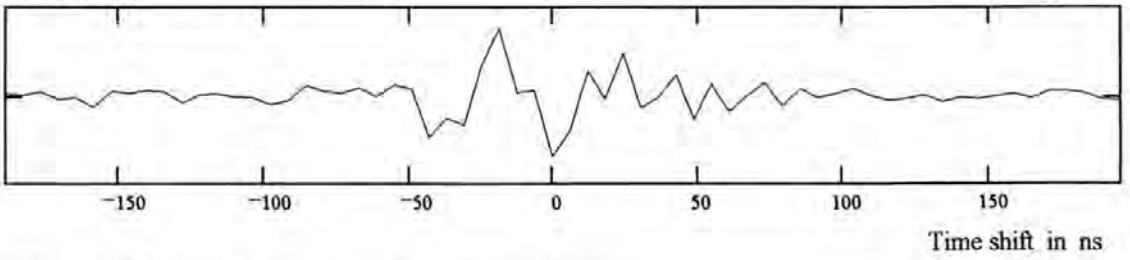

$TDFPSD := FFT(recenter(wacf))$ $R_p := mag(TDFPSD)$

$TDFCSD := FFT(recenter(wccf))$ $R_c := mag(TDFCSD)$ $length(R_c) = 33$

$k := 0 .. \frac{N}{2 \cdot \gamma}$ $f_k := \frac{k \cdot \gamma}{T_s}$ $Th := mean(R_c) \cdot \frac{f_s}{2 \cdot B_n} \cdot 1$ $B_k := if(R_{c_k} > Th, 2 \cdot Th, 0)$

TDFPSD

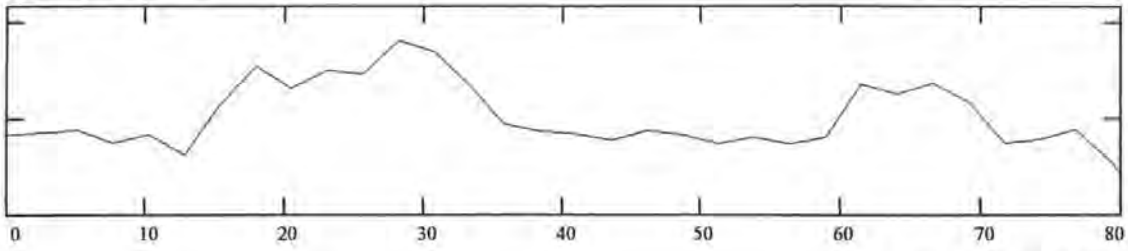

Frequency in MHz

TDFCSD

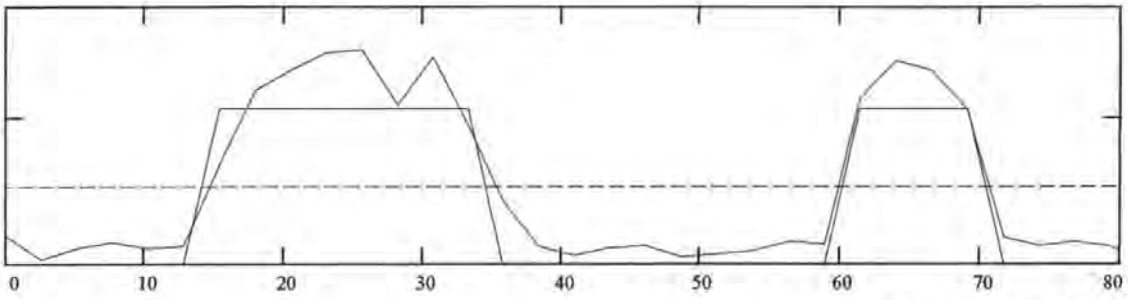

Frequency in MHz

Signal to noise ratio in the TDFCSD

$$SNRcsda := 10 \cdot \log\left[\frac{\gamma \cdot \left(\frac{B_n}{Bsa}\right)^2 \cdot \left(10^{\frac{SNRina}{10}}\right)^2}{1 + 2 \cdot 10^{\frac{SNRina}{10}}}\right] \qquad SNRcsda = 17.7 \quad dB$$

$$SNRcsdb := 10 \cdot \log\left[\frac{\gamma \cdot \left(\frac{B_n}{Bsb}\right)^2 \cdot \left(10^{\frac{SNRinb}{10}}\right)^2}{1 + 2 \cdot 10^{\frac{SNRinb}{10}}}\right] \qquad SNRcsdb = 18.3 \quad dB$$

Estimating Phase Slopes in the TDFCSD

$P := phasecor(phase(TDFCSD)) - phasecor(phase(TDFPSD))$

Selecting appropriate parts of TDFCSD and calculating its phase slope
(using a-priori knowledge of the signal bandwidth).

$$starta := ceil\left[\left(fca - \frac{Bsa}{2}\right)\cdot\frac{T_s}{\gamma}\right] \qquad enda := floor\left[\left(fca + \frac{Bsa}{2}\right)\cdot\frac{T_s}{\gamma}\right] \qquad starta = 6 \qquad enda = 13$$

$$startb := ceil\left[\left(fcb - \frac{Bsb}{2}\right)\cdot\frac{T_s}{\gamma}\right] \qquad endb := floor\left[\left(fcb + \frac{Bsb}{2}\right)\cdot\frac{T_s}{\gamma}\right] \qquad startb = 24 \qquad endb = 27$$

$$Fstarta := \frac{starta\cdot\gamma}{T_s} \qquad Fenda := \frac{enda\cdot\gamma}{T_s} \qquad Fstarta = 15.36 \qquad Fenda = 33.28$$

$$Fstartb := \frac{startb\cdot\gamma}{T_s} \qquad Fendb := \frac{endb\cdot\gamma}{T_s} \qquad Fstartb = 61.44 \qquad Fendb = 69.12$$

$$inda := 0..enda - starta \qquad fa_{inda} := \frac{inda\cdot\gamma}{T_s} \qquad Da_{inda} := P_{inda + starta}$$

$$indb := 0..endb - startb \qquad fb_{indb} := \frac{indb\cdot\gamma}{T_s} \qquad Db_{indb} := P_{indb + startb}$$

$$ma := slope(fa, Da) \quad ca := intercept(fa, Da) \quad Pa_k := ca - f_{starta}\cdot ma + f_k\cdot ma \quad pa_{inda} := ca + fa_{inda}\cdot ma$$

$$mb := slope(fb, Db) \quad cb := intercept(fb, Db) \quad Pb_k := cb - f_{startb}\cdot mb + f_k\cdot mb \quad pb_{indb} := cb + fb_{indb}\cdot mb$$

Displaying phase slopes of Time Domain Filtered Cross Spectral Density, with calculated straight line fit.

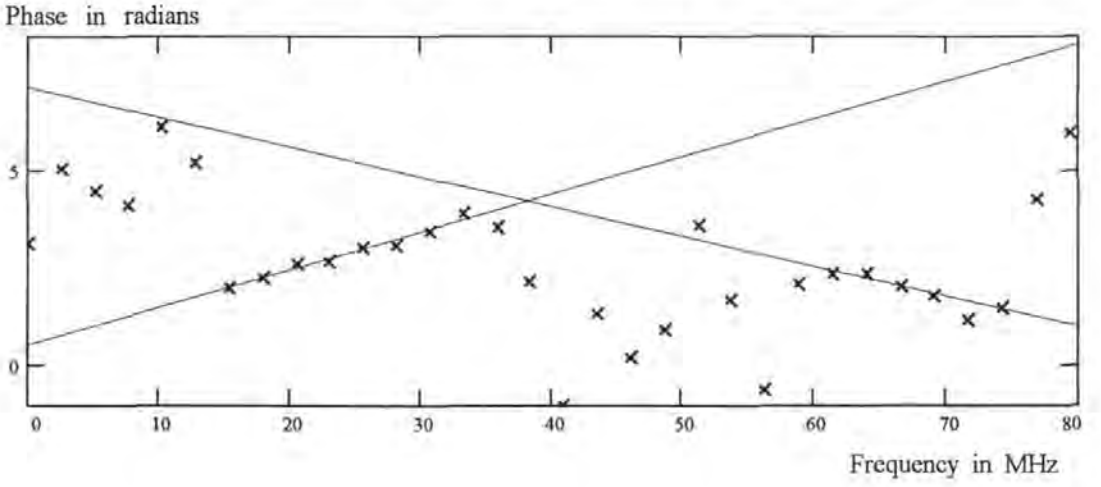

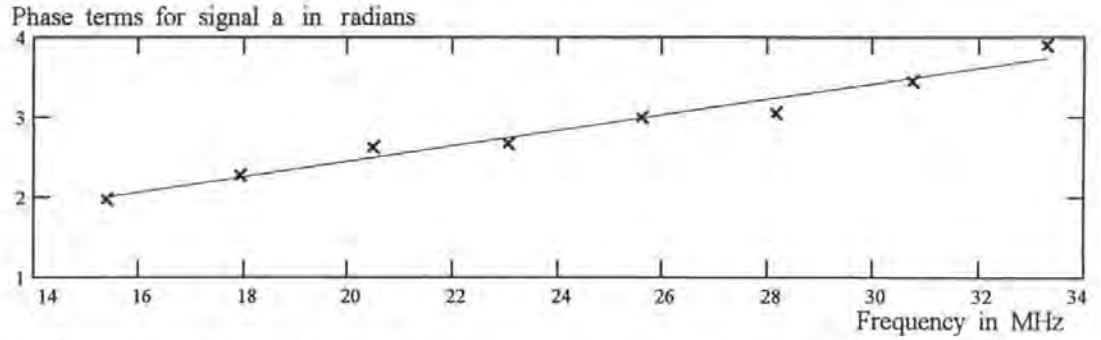

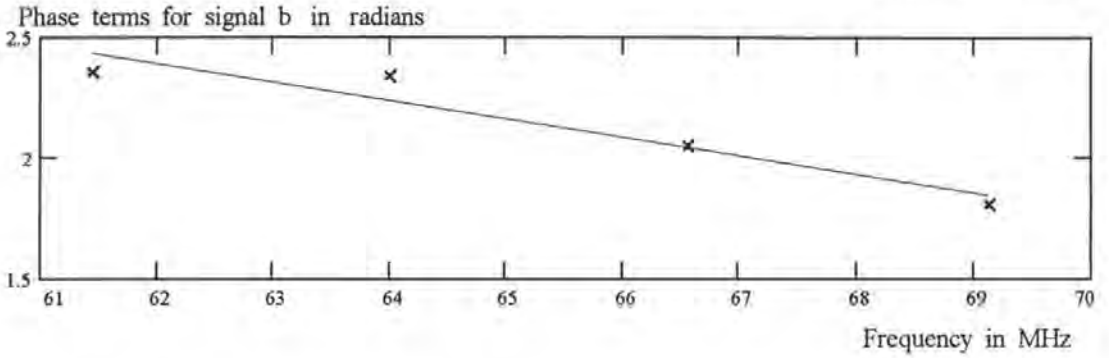

Calculating TDAs from phase slopes (and error in TDAs):

$\tau ae := \frac{ma}{2\cdot\pi}$ $\tau ae = 0.01542$ $\tau a = 0.02$ $\Delta\tau a := \tau ae - \tau a$ $\Delta\tau a \cdot 10^3 = -4.58$ ns

$\tau be := \frac{mb}{2\cdot\pi}$ $\tau be = -0.01218$ $\tau b = -0.01$ $\Delta\tau b := \tau be - \tau b$ $\Delta\tau b \cdot 10^3 = -2.18$ ns

Calculating AOAs and errors in AOA estimation: $c = 300$

$\theta ae := \text{asin}\left(\frac{c\cdot\tau ae}{d}\right)\cdot\frac{180}{\pi}$ $\theta ae = 27.562$ $\theta a = 36.87$ $\Delta\theta a := \theta ae - \theta a$ $\Delta\theta a = -9.308$

$\theta be := \text{asin}\left(\frac{c\cdot\tau be}{d}\right)\cdot\frac{180}{\pi}$ $\theta be = -21.431$ $\theta b = -17.458$ $\Delta\theta b := \theta be - \theta b$ $\Delta\theta b = -3.973$

Predicted standard deviation of angle of arrival error

$\sigma ae := \sqrt{\frac{3}{2\cdot Bsa\cdot T_s}}\cdot\frac{c}{\pi\cdot d\cdot\cos(\theta a)\cdot B_n\cdot fact(SNRina)}\cdot\frac{180}{\pi}$ $\sigma ae = 1.965$ degrees

$\sigma be := \sqrt{\frac{3}{2\cdot Bsb\cdot T_s}}\cdot\frac{c}{\pi\cdot d\cdot\cos(\theta b)\cdot B_n\cdot fact(SNRinb)}\cdot\frac{180}{\pi}$ $\sigma be = 21.058$ degrees

Convert times from μs to ns, for summary

$\tau a := \tau a\cdot 10^3$ $\tau ae := \tau ae\cdot 10^3$ $\Delta\tau a := \Delta\tau a\cdot 10^3$ $\tau b := \tau b\cdot 10^3$ $\tau be := \tau be\cdot 10^3$ $\Delta\tau b := \Delta\tau b\cdot 10^3$

Summary

Sample length /μs	$T_s = 50$	
Sampling frequency / MHz	$f_s = 163.84$	
Number of data points per signal	$N = 8192$	
Noise bandwidth /MHz	$B_n = 80$	
Oversampling factor	$\frac{f_s}{2 \cdot B_n} = 1$	
Signal bandwidth /MHz	Bsa = 20	Bsb = 10
Input SNR /dB	SNRina = −7	SNRinb = −10
Predicted SNR in the ccf /dB	SNRccfa = 23.6	SNRccfb = 18.2
Zoom factor	γ = 128	
Predicted SNR in TDFCSD /dB	SNRcsda = 17.7	SNRcsdb = 18.3
Receiver separation /m	d = 10	
Actual Time Difference of Arrival / ns	τa = 20	τb = −10
Estimated TDA / ns	τae = 15.423	τbe = −12.179
Error in TDA estimation / ns	Δτa = −4.577	Δτb = −2.179
Actual angle of arrival /degrees	θa = 36.87	θb = −17.458
Estimated angle of arrval /degrees	θae = 27.562	θbe = −21.431
Error in AOA estimation / degrees	Δθa = −9.308	Δθb = −3.973
Predicted s.d. of AOA estimation error	σae = 1.965	σbe = 21.058

Appendix D. Estimation of SNR in Mathcad simulation

Simulation of dual receiver cross correlating ESM system using frequency domain correlation, for one FMCW signal. Cut down version repeated many times to obtain output SNRs for different noise seeds

Set sample parameters

ie. set length of each sample, sampling frequency, and indexes to use in prosessing the signals.

Integration time: $T_s := 500\ \mu s$ No. of samples per data set: $N := 131072$ $f_s := \frac{N}{T_s}$

Sampling frequency: $f_s = 262.144$ MHz $i := 0..N-1$ $I_i := i$ $f := \frac{I}{T_s}$ $t := \frac{I}{f_s}$ $n := 0..\frac{N}{2}$

Set receiver system parameters

Receiver centre frequency: $f_c := 50$ MHz Receiver noise bandwidth: $B_n := 100$MHz

$\eta := 2$ nominal noise power spectral density (this file deals in ratios and not absolute values.)

Noise power, referred to receiver input: $N_i := \eta \cdot B_n \cdot 10^6$ $N_i = 2 \cdot 10^8$ W $\sigma_n := \sqrt{N_i}$

Create band pass filter to simulate bandwidth of receivers

$$Fil_n := if\left[\left(f_n > f_c - \frac{B_n}{2}\right)\cdot\left(f_n < f_c + \frac{B_n}{2}\right), 1, 0\right]$$

Create 2 sets of AWGN of specified power and bandwidth

$$n1 := IFFT\left(\overrightarrow{(FFT(gaussn(N))\cdot Fil)}\right)\cdot\sigma_n\cdot\sqrt{\frac{f_s}{2\cdot B_n}} \qquad n2 := IFFT\left(\overrightarrow{(FFT(gaussn(N))\cdot Fil)}\right)\cdot\sigma_n\cdot\sqrt{\frac{f_s}{2\cdot B_n}}$$

Set up time shift between signals due to separation of receivers and direction of arrival of signals

Choose nominal values, which can easily be changed and calculate the time difference of arrival of the signal at the two receivers. It is this time difference of arrival that the system will attempt to determine from the signals, at negative signal to noise ratios, arriving at the receivers.

Receiver separation $d := 10$ m Direction of arrival $\theta := 10 \cdot deg$

Time delay $\tau_d := \frac{d \cdot \sin(\theta)}{c} \cdot 10^6$ μs $\tau_d = 0.006$

Create a set of chirp pulses to simulate signal from a transmitter arriving at the 2 receivers

A 500 μs chirp sweeping over 10 MHz, which could be part of an FMCW signal, is generated. First we set the parameters.

Chirp centre frequency: $fo := 50$ MHz Chirp bandwidth: $B_p := 10$ MHz

Chirp length: $T_p := T_s$ Chirp time-bandwidth product: $B_p \cdot T_p = 5000$

Then we create 2 chirp signals, one without and one with a time delay, filtered as by the receivers

$$ch(x) := \sin\left[2\cdot\pi\cdot\left[\left(fo - \frac{B_p}{2}\right)\cdot x + \frac{B_p}{2\cdot T_p}\cdot x^2\right]\right] \qquad ch1 := \mathrm{Re}\left(\mathrm{IFFT}\left(\overrightarrow{(\mathrm{FFT}(ch(t))\cdot Fil)}\right)\right)$$

$$ch2 := \mathrm{Re}\left(\mathrm{IFFT}\left(\overrightarrow{\left[\mathrm{FFT}\left[ch\left(t-\tau_d\right)\cdot \mathrm{rect}\left[\frac{2\cdot t - T_s - \tau_d}{2\cdot\left(T_s-\tau_d\right)}\right] + ch\left(t+T_s-\tau_d\right)\cdot \mathrm{rect}\left(\frac{2\cdot t-\tau_d}{2\cdot\tau_d}\right)\right]\cdot Fil\right]}\right)\right)$$

Add noise to signals to create receiver input signals with specified SNR

First specify the signal to noise ratio: **Signal to noise ratio at receiver *input:*** $SNRin := -16$ **dB**

****

Then calculate the signal amplitude required to give this signal to noise ratio and add the signal vectors to the noise vectors to generate the inputs to the correlator.

Signal Amplitude: $A := \sqrt{2\cdot\left(10^{\frac{SNRin}{10}}\cdot N_i\right)}$ Add signals to noise $s1 := A\cdot ch1 + n1$

$s2 := A\cdot ch2 + n2$

Calculating CSD and CCF by FFT method

$$CSD := \overrightarrow{\left(\mathrm{FFT}(s1)\cdot\overline{\mathrm{FFT}(s2)}\right)} \qquad ccf := \frac{1}{f_s}\cdot \mathrm{Re}(\mathrm{recenter}(\mathrm{IFFT}(CSD)))$$

Estimating the signal to noise ratio in the output correlation function

Estimate from simulation: $SNR_{ccf} := 10\cdot\log\left(\frac{N\cdot\max(ccf)^2}{\overrightarrow{\sum ccf^2}}\right)$ $SNR_{ccf} = 17.192$ dB

****

Theoretically predicted signal to noise ratio: $SNR_{ccf} := 10\cdot\log\left[\frac{2\cdot B_n\cdot T_p^{\,2}\cdot\left(10^{\frac{SNRin}{10}}\right)^2}{T_s + 2\cdot T_p\cdot\left(10^{\frac{SNRin}{10}}\right)}\right]$ $SNR_{ccf} = 17.79$ dB

****

Selecting central portion of ACF and CCF. ie time domain filtering to reduce noise in PSD and CSD, for data set obtained by integration

XXXXXX

$\gamma := 1024 \quad j := 0..\frac{N}{\gamma} - 1 \quad \tau_j := \frac{j+1}{f_s} - \frac{T_s}{2\cdot\gamma} \quad wccf_j := ccf_{j+\frac{N}{2}\cdot\left(1-\frac{1}{\gamma}\right)} \quad p := \max(wccf)\cdot 1.2$

XXXXXX

Windowed ccf

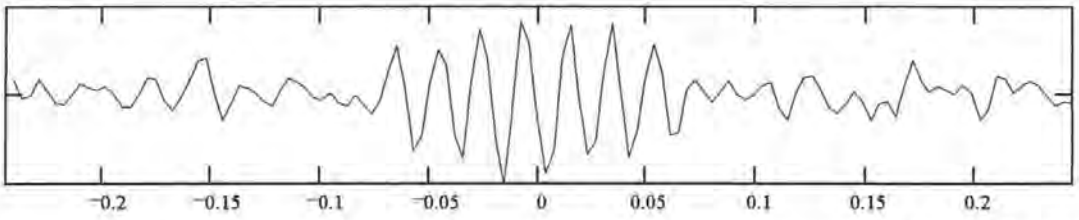

Time shift (μs)

$TDFCSD := (FFT(recenter(wccf))) \quad R_c := mag(TDFCSD) \quad length(R_c) = 65 \quad p := \max(R_c)\cdot 1.2$

$k := 0..\frac{N}{2\cdot\gamma} \quad f_k := \frac{k\cdot\gamma}{T_s} \quad Th := mean(R_c)\cdot 3 \quad B_k := if(R_{c_k} > Th, 1, 0)$

TDFCSD

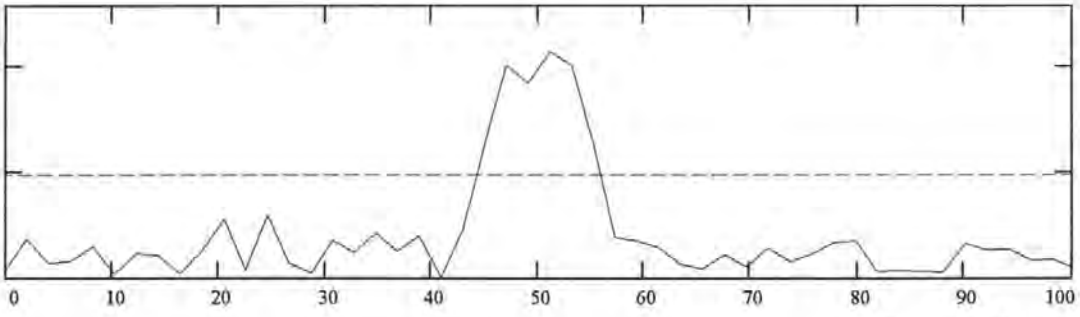

Frequency (MHz)

Estimating the signal to noise ratio in the TDFCSD

Separating the sections of the TDFCSD containing the signal and just noise

$$Sx_k := if\left[\left(fo - 0.45\cdot B_p < f_k\right)\cdot\left(f_k < fo + 0.45\cdot B_p\right), R_{c_k}, 0\right]$$

$$N1x_k := if\left[\left(fo - 0.51\cdot B_p < f_k\right)\cdot\left(f_k < fo + 0.51\cdot B_p\right), 0, R_{c_k}\right] \qquad Nx_k := if\left(f_k \le B_n, N1x_k, 0\right)$$

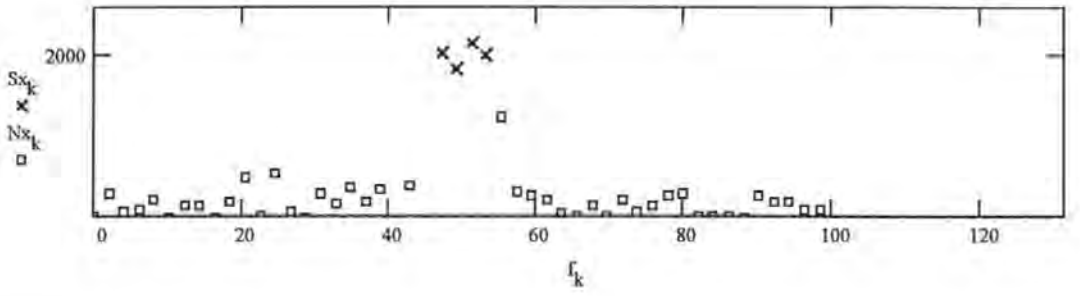

$$bins_k := if\left(Sx_k > 0, 1, 0\right) \qquad countS := \sum bins \qquad countS = 4$$

$$binn_k := if\left(Nx_k > 0, 1, 0\right) \qquad countN := \sum binn \qquad countN = 44$$

Estimate from simulation:

$$SNR_{CSD} := 10\cdot\log\left[\frac{\left(\overrightarrow{\sum(Sx^2)}\right)}{\left(\overrightarrow{\sum(Nx^2)}\right)}\cdot\frac{countN}{countS}\right] \qquad SNR_{CSD} = 15.728$$

****

Theoretically predicted value:

$$SNR_{CSD} := 10\cdot\log\left[\frac{\gamma\cdot\left(\frac{B_n}{B_p}\right)^2\cdot\left(10^{\frac{SNRin}{10}}\right)^2}{1 + 2\cdot 10^{\frac{SNRin}{10}}}\right] \qquad SNR_{CSD} = 17.89$$

The results obtained from 20 repeats of the simulation, using a different "randomize" seed each time are shown in table D-1

Randomize seed	SNR_{ccf} (dB)	SNR_{TDFCSD} (dB)	SNR_{TDFCSD} (dB)
1	17.40	19.36	19.60
2	18.94	18.14	19.22
3	17.29	18.12	19.16
4	18.30	17.21	17.80
5	16.61	17.10	17.53
6	18.36	18.19	19.15
7	18.47	17.42	18.64
8	17.03	19.30	19.84
9	17.74	17.90	18.56
10	17.97	17.14	17.71
11	17.28	15.36	16.26
12	17.15	18.02	18.92
13	18.18	18.13	19.04
14	17.88	16.91	17.83
15	17.48	16.25	17.19
16	17.74	19.06	19.81
17	17.76	17.12	18.71
18	18.41	16.74	16.82
19	16.49	16.72	17.23
20	16.37	16.91	17.79
Mean	**17.64**	**17.56**	**18.34**
Standard Deviation	**0.68**	**0.99**	**1.01**

Table D-1. Results of 20 repeats of the simulation.

Estimating the SNR in the TDFCSD presents some difficulty, compared to the ccf, because of the small number of signal points. The number of points considered as signal as opposed to noise depends on the bandwidth specified when making the selection. Columns 3 and 4 of table E-1 come from two slightly different specifications of bandwidth (column 3 corresponding to the wider specified bandwidth) If we combine the results of columns 3 and 4 we obtain:

$$\text{Mean } SNR_{TDFCSD} = 17.95 \text{ dB}$$

$$\text{Standard deviation in } SNR_{TDFCSD} = 1.07 \text{ dB}$$

Appendix E. Measurement of errors in phase terms in simulated TDFCSD

Simulation of dual receiver cross correlating ESM system using frequency domain correlation: slimmed down to estimate errors in phase slope (12 Oct 94)

Set sample parameters

ie. set length of each sample, sampling frequency, and indexes to use in prosessing the signals.

Integration time: $T_s := 500\ \mu s$ No. of samples per data set: $N := 131072$ $f_s := \frac{N}{T_s}$

Sampling frequency: $f_s = 262.144$ MHz $i := 0..N-1$ $I_i := i$ $f := \frac{I}{T_s}$ $t := \frac{I}{f_s}$ $n := 0..\frac{N}{2}$

Set receiver system parameters

Receiver centre frequency: $f_c := 50$ MHz Receiver noise bandwidth: $B_n := 100$ MHz

$\eta := 2$ nominal noise power spectral density (this file deals in ratios and not absolute values.)

Noise power, referred to receiver input: $N_i := \eta \cdot B_n \cdot 10^6$ $N_i = 2 \cdot 10^8$ W $\sigma_n := \sqrt{N_i}$

Create band pass filter to simulate bandwidth of receivers $Fil_n := if\left[\left(f_n > f_c - \frac{B_n}{2}\right)\cdot\left(f_n < f_c + \frac{B_n}{2}\right), 1, 0\right]$

Create 2 sets of AWGN of specified power and bandwidth

In fact this creates 2 samples of noise: 2 vectors of N data points each

$n1 := IFFT\left(\overrightarrow{(FFT(gaussn(N))\cdot Fil)}\right)\cdot\sigma_n\cdot\sqrt{\frac{f_s}{2\cdot B_n}}$ $n2 := IFFT\left(\overrightarrow{(FFT(gaussn(N))\cdot Fil)}\right)\cdot\sigma_n\cdot\sqrt{\frac{f_s}{2\cdot B_n}}$

Set up time shift between signals due to separation of receivers and direction of arrival of signals

Choose nominal values, which can easily be changed and calculate the time difference of arrival of the signal at the two receivers. It is this time difference of arrival that the system will attempt to determine from the signals, at negative signal to noise ratios, arriving at the receivers.

Receiver separation $d := 50$ m Direction of arrival $\theta := 30\cdot deg$

Time delay $\tau_d := \frac{d\cdot\sin(\theta)}{c}\cdot 10^6$ μs $\tau_d = 0.083$

Create a pair of chirp pulses to simulate signal from a transmitter arriving at the 2 receivers

A 500 μs chirp sweeping over 50 MHz, which could be part of an FMCW signal, is generated .
First set the parameters.

Chirp centre frequencies: $fo := 50$ MHz Chirp bandwidth: $B_p := 50$ MHz

Chirp length: $T_p := T_s$ μs

Chirp time-bandwidth product: $B_p \cdot T_p = 2.5 \cdot 10^4$ "Proccessing gain": $10 \cdot \log(2 \cdot B_p \cdot T_p) = 47$ dB

Then we create 2 chirp signals, with varying centre frequencies, one without and one with a time delay, band pass filtered as by the receivers

$$ch1 := Re\left(IFFT\left(\overrightarrow{(FFT(ch(t)) \cdot Fil)}\right)\right)$$

$$ch2 := Re\left(IFFT\left(\overrightarrow{\left[FFT\left[ch\left(t-\tau_d\right)\cdot rect\left[\frac{2\cdot t - T_s - \tau_d}{2\cdot\left(T_s-\tau_d\right)}\right] + ch\left(t+T_s-\tau_d\right)\cdot rect\left(\frac{2\cdot t-\tau_d}{2\cdot\tau_d}\right)\right]\cdot Fil\right]}\right)\right)$$

Add noise to signals to create receiver input signals with specified SNR

First specify the signal to noise ratio

Signal to noise ratio at receiver input: $SNRin := -11$ **dB**

****

Then calculate the signal amplitude required to give this signal to noise ratio and add the signal matices to the noise matrices to generate the inputs to the correlator.

Signal Amplitude: $A := \sqrt{2\cdot\left(10^{\frac{SNRin}{10}}\cdot N_i\right)}$ $10\cdot\log\left(\frac{A^2}{2\cdot N_i}\right) = -11$

Add signals to noise $s1 := A\cdot ch1 + n1$ $s2 := A\cdot ch2 + n2$

$$CSD := \overrightarrow{\left(FFT(s1)\cdot\overrightarrow{FFT(s2)}\right)} \qquad ccf := \frac{1}{f_s}\cdot Re(recenter(IFFT(CSD)))$$

Selecting central portion of ccf.

$\gamma := 256$ $j := 0..\frac{N}{\gamma} - 1$ $\tau_j := \frac{j+1}{f_s} - \frac{T_s}{2\cdot\gamma}$ $wccf_j := ccf_{j+\frac{N}{2}\cdot\left(1-\frac{1}{\gamma}\right)}$ $p := \max(wccf)\cdot 2$

****

Windowed ccf

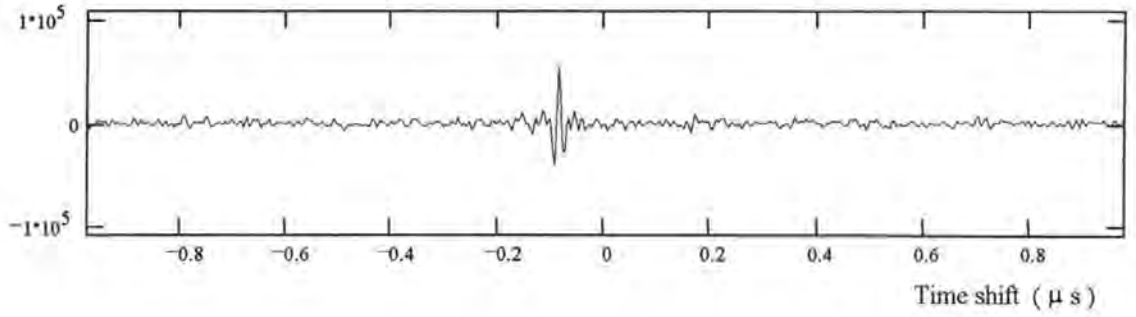

$TDFCSD := (FFT(recenter(wccf)))$ $R_c := mag(TDFCSD)$ $length(R_c) = 257$

$k := 0 .. \frac{N}{2 \cdot \gamma}$ $f_k := \frac{k \cdot \gamma}{T_s}$ $Th := mean(R_c) \cdot 1$ $B := movavg(R_c, 6)$ $B_k := if(B_k > Th, 1, 0)$

TDFCSD

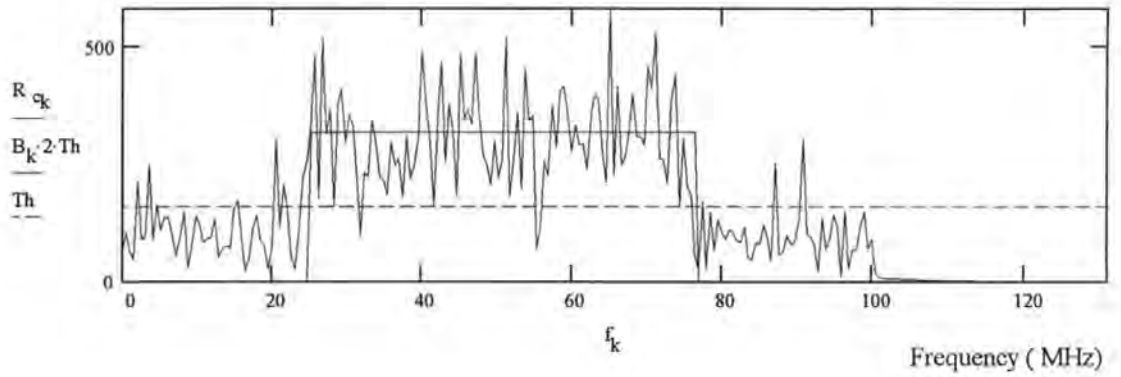

Selecting appropriate part of TDFCSD and calculating its phase slope.

$P := phasecor(phase(TDFCSD))$

$C := B$ $C_k := if[k=0, 0, if[(B_k=1) + (C_{k-1}=1), 1, 0]]$ $a := length(C) - \sum C$

$G := C - B$ $b := length(G) - \sum G - 1$

$a := ceil\left[\left(fo - \frac{B_p}{2}\right) \cdot \frac{T_s}{\gamma}\right]$ $b := floor\left[\left(fo + \frac{B_p}{2}\right) \cdot \frac{T_s}{\gamma}\right]$ $B_p = 50$

$\alpha := 0 .. b - a - 1$

$Fa := \frac{a \cdot \gamma}{T_s}$ $Fa = 25.088$ $Fb := \frac{b \cdot \gamma}{T_s}$ $Fb = 74.752$ $fa_\alpha := \frac{\alpha \cdot \gamma}{T_s}$

$D_\alpha := P_{\alpha + a}$ $m := slope(fa, D)$ $cc := intercept(fa, D)$ $Y_\alpha := cc + fa_\alpha \cdot m$

Displaying phase slope of TDFCSD, with calculated straight line fit.

Phase (radians)

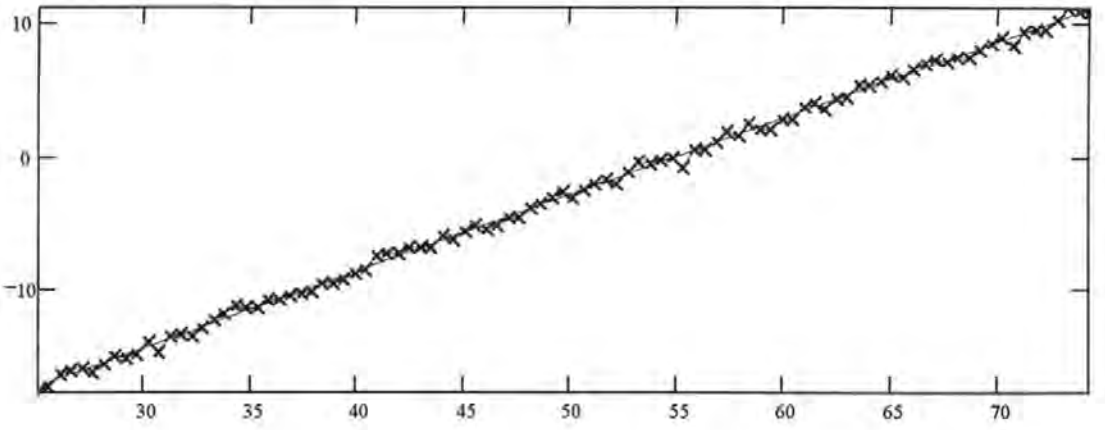

$Err_\alpha := D_\alpha - Y_\alpha$

$\sigma := stdev(Err)$

$$10 \cdot \log\left[\frac{\gamma \cdot \left(\frac{B_n}{B_p}\right)^2 \cdot fact(SNRin)^2}{1 + 2 \cdot fact(SNRin)}\right] = 7.463$$

$$\sigma_{th} := \sqrt{\frac{1 + 2 \cdot fact(SNRin)}{2 \cdot \gamma \cdot \left(\frac{B_n}{B_p}\right)^2 \cdot fact(SNRin)^2}}$$

$SNRin = -11$ $\gamma = 256$ $\sigma_{th} = 0.299$ $\sigma = 0.321$ $\frac{\sigma}{\sigma_{th}} = 1.07$

****

Results

SNRin (dB)	zoom factor γ	standard deviation theoretical	standard deviation measured	SNRin (dB)	zoom factor γ	standard deviation theoretical	standard deviation measured
30	1024	0.0005	0.019	-5	1024	0.045	0.051
	512	0.0007	0.01		512	0.063	0.069
	256	0.001	0.008		256	0.089	0.099
	128	0.0014	0.004		128	0.126	0.141
	64	0.002	0.003	-6	1024	0.054	0.06
	32	0.0028	0.004		512	0.076	0.081
	16	0.004	0.005		256	0.108	0.117
	8	0.0056	0.008	-7	1024	0.065	0.07
	1	0.0158	0.022		512	0.093	0.097
20	1024	0.0016	0.019		256	0.131	0.14
	512	0.0022	0.011	-8	1024	0.08	0.084
	256	0.0031	0.01		512	0.113	0.116
	128	0.0044	0.007		256	0.16	0.168
	64	0.0063	0.009	-9	1024	0.098	0.101
0	1024	0.019	0.029		512	0.139	0.14
	512	0.027	0.035		256	0.196	0.204
	256	0.038	0.048	-10	1024	0.121	0.123
	128	0.054	0.068		512	0.171	0.172
	64	0.077	0.096		256	0.242	0.249
	32	0.108	0.135	-11	1024	0.15	0.15
-1	1024	0.022	0.031		512	0.212	0.211
	512	0.032	0.039		256	0.299	0.307
	256	0.045	0.055	-12	1024	0.186	0.183
	128	0.063	0.078		512	0.263	0.262
	64	0.09	0.111		256	0.372	0.383
-2	1024	0.026	0.035	-13	1024	0.231	0.224
	512	0.037	0.045		512	0.327	0.326
	256	0.053	0.063		256	0.463	0.487
	128	0.074	0.089	-14	1024	0.288	0.272
	64	0.105	0.128		512	0.408	0.401
-3	1024	0.031	0.037		256	0.577	0.608
	512	0.044	0.051	-15	1024	0.36	0.331
-4	1024	0.037	0.044		512	0.509	0.486
	512	0.053	0.059		256	0.721	0.729
	256	0.074	0.084	-16	1024	0.451	0.399
	128	0.105	0.121		512	0.637	0.584
				-17	1024	0.565	0.479
					512	0.799	0.712

Table E-1.Standard deviation of errors in phase of TDFCSD as predicted by theory and as measured in Mathcad simulation.

Appendix F: Probability density functions

Probability density functions for signal plus narrwowband noise.

Consider a signal plus narrowband noise as depicted in figure 5-1, where A is constant and c and s are random gaussain variables of zero mean and common standard deviation σ.

The position of the tip of the resultant vector is described by the rectangular coordinates (x,y) = (A+c, s) or by the polar coordinates (r,θ). θ is the phase error caused by the noise components c and s. We wish to find the pdf of this phase error, $p_{\Theta}(\theta)$. We will also find the pdf $p_r(r)$ (the Ricean pdf).

The joint probablity

$$p_{xy}(x,y)=p_x(x)\cdot p_y(y)=\frac{1}{\sqrt{2\cdot\pi\cdot\sigma^2}}\cdot\exp\left[-\frac{(x-A)^2}{2\cdot\sigma^2}\right]\cdot\frac{1}{\sqrt{2\cdot\pi\cdot\sigma^2}}\cdot\exp\left(-\frac{y^2}{2\cdot\sigma^2}\right)$$

$$p_{xy}(x,y)=\frac{1}{2\cdot\pi\cdot\sigma^2}\cdot\exp\left[-\frac{1}{2\cdot\sigma^2}\cdot((x-A)^2+y^2)\right]$$

By definition $p_{r\theta}(r,\theta)\cdot dr\cdot d\theta=p_{xy}(x,y)\cdot dx\cdot dy$

but $dx\cdot dy=r\cdot dr\cdot d\theta$

Hence $p_{r\theta}(r,\theta)=r\cdot p_{xy}(x,y)$

$$p_{r\theta}(r,\theta)=\frac{r}{2\cdot\pi\cdot\sigma^2}\cdot\exp\left[-\frac{1}{2\cdot\sigma^2}\cdot(x^2-2\cdot A\cdot x+A^2+y^2)\right]$$

$$p_{r\theta}(r,\theta)=\frac{r}{2\cdot\pi\cdot\sigma^2}\cdot\exp\left(-\frac{A^2}{2\cdot\sigma^2}\right)\cdot\exp\left[-\frac{1}{2\cdot\sigma^2}\cdot(r^2-2\cdot A\cdot r\cdot\cos(\theta))\right]$$

To obtain the Ricean pdf, $p_r(r)$:

$$p_r(r)=\int_0^{2\cdot\pi} p_{r\theta}(r,\theta)\,d\theta$$

$$p_r(r)=\frac{r}{2\cdot\pi\cdot\sigma^2}\cdot\exp\left(-\frac{A^2}{2\cdot\sigma^2}\right)\cdot\exp\left(-\frac{r^2}{2\cdot\sigma^2}\right)\cdot\int_0^{2\cdot\pi}\exp\left(-\frac{A\cdot r}{\sigma^2}\cdot\cos(\theta)\right)d\theta$$

$$p_r(r)=\frac{r}{\sigma^2}\cdot I_0\left(\frac{A\cdot r}{\sigma^2}\right)\cdot\exp\left(-\frac{A^2+r^2}{2\cdot\sigma^2}\right)\qquad\text{(the Ricean pdf)}$$

To obtain $p_\theta(\theta)$:

$$p_\theta(\theta)=\int_0^{\infty}p_{r\theta}(r,\theta)\,dr$$

$$p_\theta(\theta)=\frac{1}{2\cdot\pi\cdot\sigma^2}\cdot\exp\left(-\frac{A^2}{2\cdot\sigma^2}\right)\cdot\int_0^{\infty}r\cdot\exp\left[-\frac{1}{2\cdot\sigma^2}\cdot(r^2-2\cdot A\cdot r\cdot\cos(\theta))\right]dr$$

$$p_\theta(\theta)=\frac{1}{2\cdot\pi\cdot\sigma^2}\cdot\exp\left(-\frac{A^2}{2\cdot\sigma^2}\right)\cdot\int_0^{\infty}r\cdot\exp\left[-\frac{1}{2\cdot\sigma^2}\cdot\left[(r-A\cdot\cos(\theta))^2-A^2\cdot\cos(\theta)^2\right]\right]dr$$

$$p_\theta(\theta)=\frac{1}{2\cdot\pi\cdot\sigma^2}\cdot\exp\left[-\frac{A^2}{2\cdot\sigma^2}\cdot\left(1-\cos(\theta)^2\right)\right]\cdot\int_0^{\infty}r\cdot\exp\left[-\frac{1}{2\cdot\sigma^2}\cdot(r-A\cdot\cos(\theta))^2\right]dr$$

By substituting $x=r-A\cdot\cos(\theta)$ we obtain

$$p_\theta(\theta)=\frac{1}{2\cdot\pi\cdot\sigma^2}\cdot\exp\left(-\frac{A^2\cdot\sin(\theta)^2}{2\cdot\sigma^2}\right)\cdot\int_{-A\cdot\cos(\theta)}^{\infty}(x+A\cdot\cos(\theta))\cdot\exp\left(-\frac{x^2}{2\cdot\sigma^2}\right)dr$$

$$p_\theta(\theta)=\frac{1}{2\cdot\pi\cdot\sigma^2}\cdot\exp\left(-\frac{A^2\cdot\sin(\theta)^2}{2\cdot\sigma^2}\right)\cdot\left[\int_{-A\cdot\cos(\theta)}^{\infty}x\cdot\exp\left(-\frac{x^2}{2\cdot\sigma^2}\right)dr+A\cdot\cos(\theta)\cdot\int_{-A\cdot\cos(\theta)}^{\infty}\exp\left(-\frac{x^2}{2\cdot\sigma^2}\right)dr\right.$$

Now, since

$$\frac{d}{dx}e^{-\frac{x^2}{2\cdot\sigma^2}}=-\frac{x}{\sigma^2}\cdot e^{-\frac{x^2}{2\cdot\sigma^2}}$$

$$\int_{-A\cdot\cos(\theta)}^{\infty} x\cdot\exp\left(-\frac{x^2}{2\cdot\sigma^2}\right)dr=\sigma^2\cdot\exp\left(-\frac{A^2\cdot\cos(\theta)^2}{2\cdot\sigma^2}\right)$$

and since

$$\int_{-a}^{\infty}\frac{1}{\sqrt{2\cdot\pi\cdot\sigma^2}}\cdot\exp\left(-\frac{x^2}{2\cdot\sigma^2}\right)dx=\text{cnorm}\left(\frac{a}{\sigma}\right)$$

$$A\cdot\cos(\theta)\cdot\int_{-A\cdot\cos(\theta)}^{\infty}\exp\left(-\frac{x^2}{2\cdot\sigma^2}\right)dr=\sqrt{2\cdot\pi\cdot\sigma^2}\cdot A\cdot\cos(\theta)\cdot\text{cnorm}\left(\frac{A\cdot\cos(\theta)}{\sigma}\right)$$

Hence

$$p_\theta(\theta)=\frac{\exp\left(-\frac{A^2\cdot\sin(\theta)^2}{2\cdot\sigma^2}\right)}{2\cdot\pi\cdot\sigma^2}\cdot\left(\sigma^2\cdot\exp\left(-\frac{A^2\cdot\cos(\theta)^2}{2\cdot\sigma^2}\right)+\sqrt{2\cdot\pi\cdot\sigma^2}\cdot A\cdot\cos(\theta)\cdot\text{cnorm}\left(\frac{A\cdot\cos(\theta)}{\sigma}\right)\right)$$

or

****

$$p_\theta(\theta)=\frac{1}{2\cdot\pi}\cdot\exp\left(-\frac{A^2}{2\cdot\sigma^2}\right)+\frac{A\cdot\cos(\theta)}{\sqrt{2\cdot\pi\cdot\sigma^2}}\cdot\text{cnorm}\left(\frac{A\cdot\cos(\theta)}{\sigma}\right)\cdot\exp\left(-\frac{A^2\cdot\sin(\theta)^2}{2\cdot\sigma^2}\right)$$

****

In the limit as $\frac{A}{\sigma}$ becomes very large, and θ becomes small

$\exp\left(-\frac{A^2}{2\cdot\sigma^2}\right)$ tends to zero $\cos(\theta)$ tends to 1

$\sin(\theta)$ tends to θ and $\text{cnorm}\left(\frac{A\cdot\cos(\theta)}{\sigma}\right)$ tends to 1

and the pdf of θ can be approximated as

$$p_\theta(\theta) = \frac{A}{\sqrt{2\cdot\pi\cdot\sigma^2}}\cdot\exp\left(-\frac{A^2\cdot\theta^2}{2\cdot\sigma^2}\right) \qquad \text{i.e. as a Gaussian pdf of standard deviation} \quad \frac{\sigma}{A}$$

To evaluate how good an approximation of the standard deviation this gives, we must compare it to the true value of the standard deviation of $p_\theta(\theta)$, which is given by:

$$\sigma_\theta = \left(\int_{-\pi}^{\pi} \theta^2\cdot p_\theta(\theta)\, d\theta\right)^{\frac{1}{2}}$$

Figure F-1 shows the form of $p_\theta(\theta)$ for signal to noise ratios of 0 dB and 3 dB (the peak becomes progressively larger, and more gaussian, as the SNR increases)

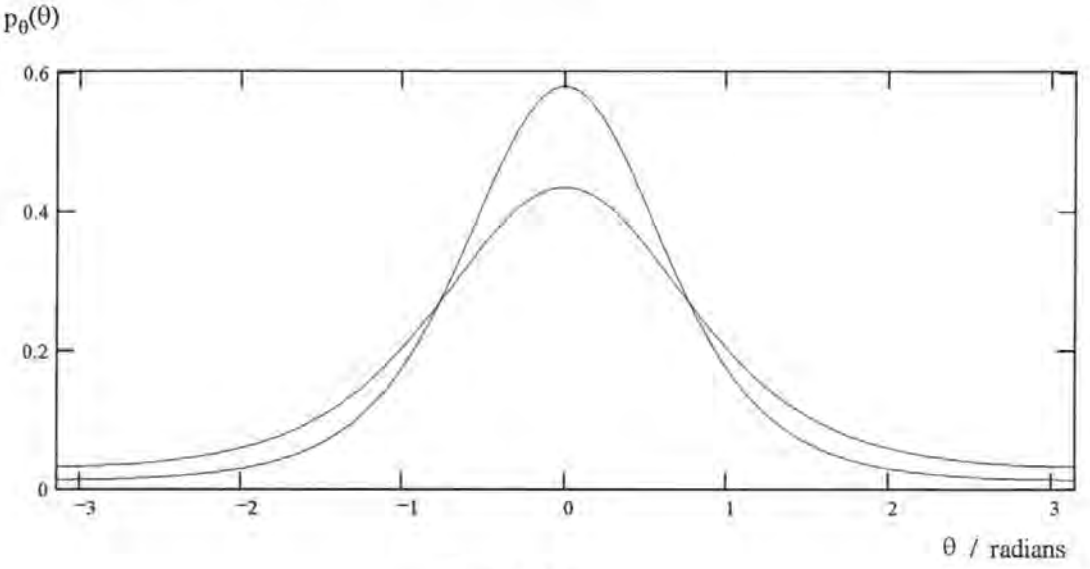

Figure F-1.

The percentage error in approximating the standard deviation of $p_\theta(\theta)$ as $\frac{A}{\sigma}$ is calculaed by:

$$A(SNR) := 10^{\frac{SNR}{20}} \qquad SNR := 0, 0.5 .. 20$$

$$E(SNR) := \left| \left[\frac{1}{A(SNR)\cdot\sqrt{\int_{-\pi}^{\pi} \theta^2\cdot P(\theta, A(SNR))\, d\theta}} - 1 \right] \cdot 100 \right|$$

Figure F-2 shows the percentage error, incurred by approximating the standard deviation of $p_\theta(\theta)$, plotted as a function of signal to noise ratio.

Percentage error of approximation

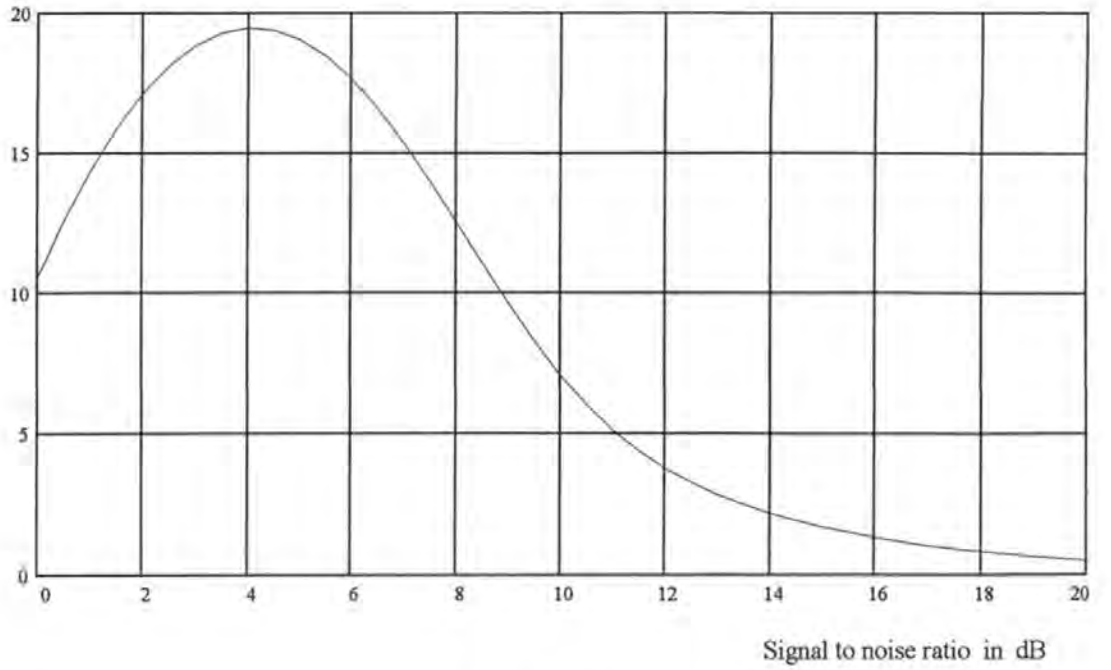

Figure F-2.

$E(14) = 2.182$

For signal to noise ratio greater than or equal to 14 dB the percentage error is less than 2.2%

Probabilities of false alarm and missed detection for Gaussian statistics

$r := 0, 0.1 .. 10$ $\quad SNR := 10, 10.5 .. 20$ $\quad fact(x) := 10^{\frac{x}{10}}$

$P_{fa}(x) := 1 - cnorm(x)$ $\quad P_{md}(SNR, x) := 1 - cnorm\left(\sqrt{fact(SNR)} - x\right)$ $\quad TOL := 10^{-9}$

Calculating required threshold levels for different probabilities of false alarm

$x := 3.09$	$L1 := root\left(P_{fa}(x) - 10^{-3}, x\right)$	$P_{fa}(L1) = 0.001$	$L1 = 3.09$
$x := 3.719$	$L2 := root\left(P_{fa}(x) - 10^{-4}, x\right)$	$P_{fa}(L2) = 1 \cdot 10^{-4}$	$L2 = 3.719$
$x := 4.265$	$L3 := root\left(P_{fa}(x) - 10^{-5}, x\right)$	$P_{fa}(L3) = 1 \cdot 10^{-5}$	$L3 = 4.265$
$x := 4.748$	$L4 := root\left(P_{fa}(x) - 10^{-6}, x\right)$	$P_{fa}(L4) = 1 \cdot 10^{-6}$	$L4 = 4.753$
$x := 5.199$	$L5 := root\left(P_{fa}(x) - 10^{-7}, x\right)$	$P_{fa}(L5) = 1 \cdot 10^{-7}$	$L5 = 5.199$
$x := 5.612$	$L6 := root\left(P_{fa}(x) - 10^{-8}, x\right)$	$P_{fa}(L6) = 1 \cdot 10^{-8}$	$L6 = 5.612$

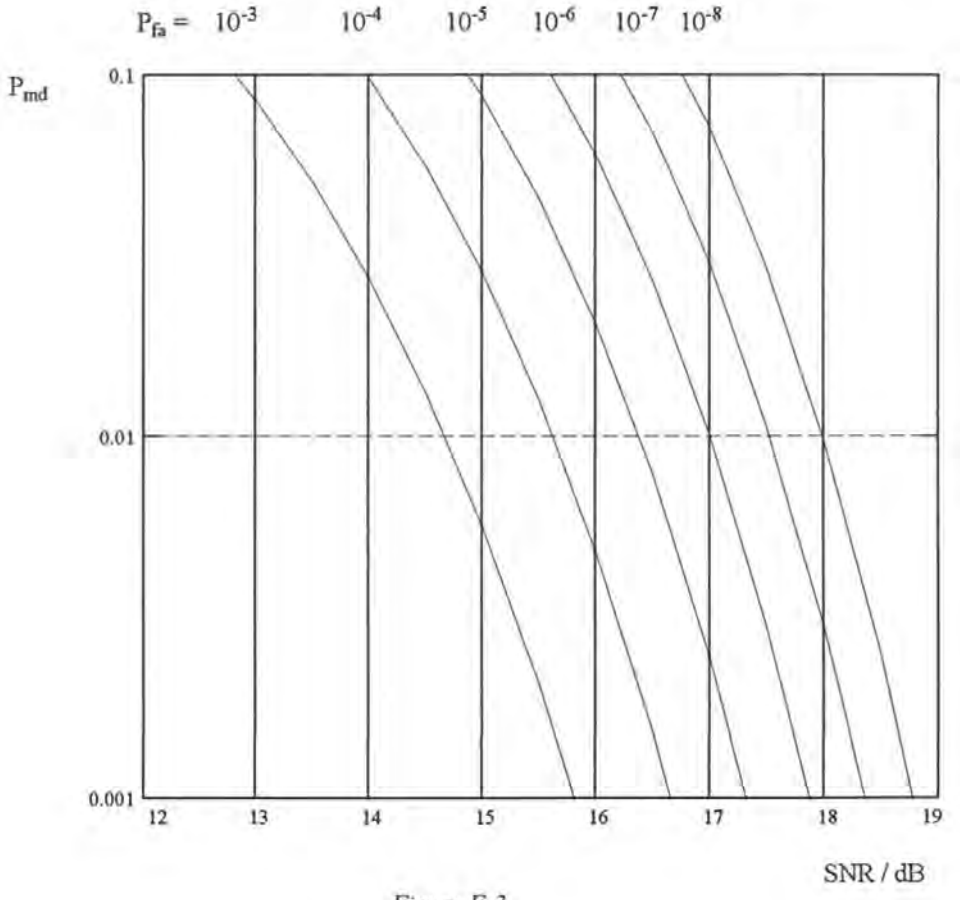

Figure F-3.

To find the required signal to noise ratio, SNRo, for a $P_{fa} = 10^{-7}$ and $P_{md} = 0.01$:

$x := 17.531$ $\quad SNRo := root\left(P_{md}(x, L5) - 0.01, x\right)$ $\quad SNRo = 17.531$

Probabilities of false alarm and missed detection for Rayleigh / Ricean statistics

$r := 0, 0.1 .. 10 \qquad SNR := 10, 10.5 .. 18 \qquad fact(x) := 10^{\frac{x}{10}}$

$$RN(SNR, r) := r \cdot I0\left(\sqrt{2 \cdot fact(SNR)} \cdot r\right) \cdot \exp\left[-\left(fact(SNR) + \frac{r^2}{2}\right)\right] \qquad R(r) := r \cdot \exp\left(-\frac{r^2}{2}\right)$$

$$P_{fa}(L) := \exp\left(-\frac{L^2}{2}\right) \qquad P_{md}(SNR, L) := \int_0^L RN(SNR, r)\, dr \qquad 1 - 0.99 = 0.01$$

Calculating required threshold levels for different probabilities of false alarm

$x := 3.717$	$L1 := root\left(P_{fa}(x) - 10^{-3}, x\right)$	$P_{fa}(L1) = 0.001$	$L1 = 3.717$
$x := 4.292$	$L2 := root\left(P_{fa}(x) - 10^{-4}, x\right)$	$P_{fa}(L2) = 1 \cdot 10^{-4}$	$L2 = 4.292$
$x := 4.799$	$L3 := root\left(P_{fa}(x) - 10^{-5}, x\right)$	$P_{fa}(L3) = 1 \cdot 10^{-5}$	$L3 = 4.799$
$x := 5.257$	$L4 := root\left(P_{fa}(x) - 10^{-6}, x\right)$	$P_{fa}(L4) = 1 \cdot 10^{-6}$	$L4 = 5.257$
$x := 5.678$	$L5 := root\left(P_{fa}(x) - 10^{-7}, x\right)$	$P_{fa}(L5) = 1 \cdot 10^{-7}$	$L5 = 5.678$
$x := 6.07$	$L6 := root\left(P_{fa}(x) - 10^{-8}, x\right)$	$P_{fa}(L6) = 1 \cdot 10^{-8}$	$L6 = 6.07$

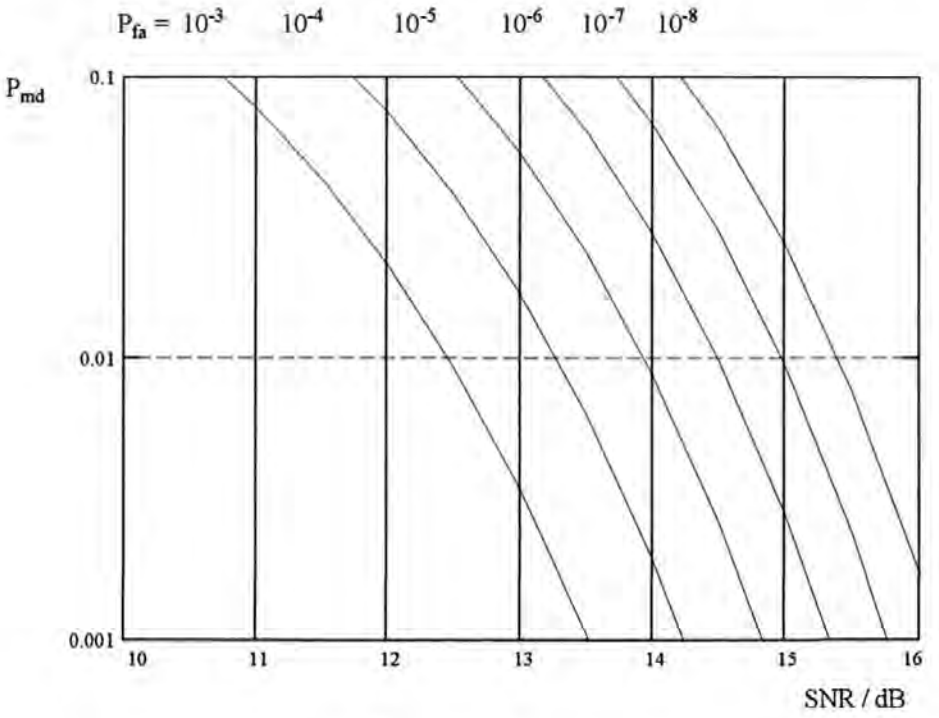

Figure F-4.

To find the required signal to noise ratio, SNRo, for a probability of missed detection of 0.01:

$x := 14.975 \qquad SNRo := root\left(P_{md}(x, L5) - 0.01, x\right) \qquad SNRo = 14.975$

Appendix G. Mathcad file used to process data from time-integrating correlator

TICORRc.mcd

Chirp from 6 to 10 MHz with noise SNR = +6 dB (exp no: 7-12-05)

No. of data points per frame: $N := 2048$ index: $i := 0..N-1$

No. of frames: $M := 2$ index: $j := 0..M-1$ $k := 0..N \cdot M-1$

Length of frame (μs): $T_s := 11$ Sampling frequency (MHz): $f_s := \frac{N}{T_s}$

Frequency scale (MHz): $f_i := \frac{i}{T_s}$ Time scale (μs): $t_i := \frac{i}{f_s}$

Known start frequency and bandwidth of chirp: $f_1 := 6$ $B_s := 4$

Read in data and form averaged data sets of 2048 points for 2 "frame grabs"

$y0_k := READ(ccf\_00a)$ $Y0_{i,j} := y0_{(i+j \cdot N)}$ $ccf0_i := \frac{1}{M} \cdot \left(\sum_j Y0_{i,j} \right)$

$y1_k := READ(ccf\_01a)$ $Y1_{i,j} := y1_{(i+j \cdot N)}$ $ccf1_i := \frac{1}{M} \cdot \left(\sum_j Y1_{i,j} \right)$ $ccfa := ccf1$

$y2_k := READ(ccf\_02a)$ $Y2_{i,j} := y2_{(i+j \cdot N)}$ $ccf2_i := \frac{1}{M} \cdot \left(\sum_j Y2_{i,j} \right)$ $ccfb := ccf2$

Display raw data

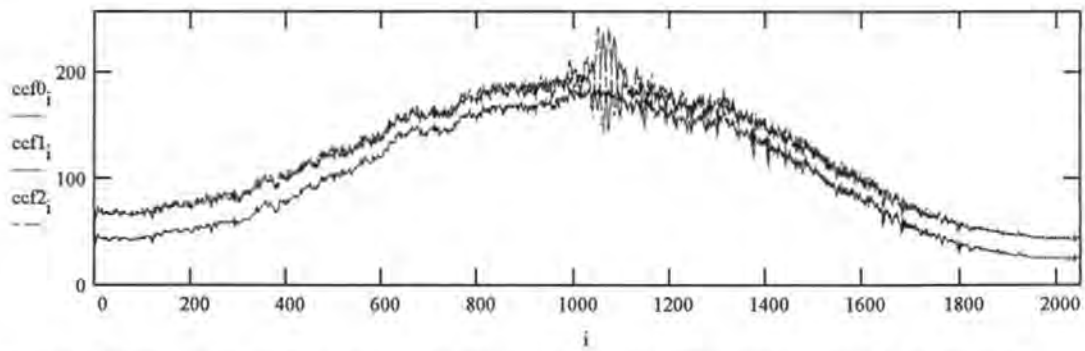

Subract background from ccfs with signal, subtract mean and perform moving average of adjacent cells.

$ccf1 := \overrightarrow{\left(ccf1 - ccf0 \cdot \frac{\sum ccf1}{\sum ccf0} \right)}$ $ccf1 := ccf1 - mean(ccf1)$ $ccf1 := movavg(ccf1, 2)$

$ccf2 := \overrightarrow{\left(ccf2 - ccf0 \cdot \frac{\sum ccf2}{\sum ccf0} \right)}$ $ccf2 := ccf2 - mean(ccf2)$ $ccf2 := movavg(ccf2, 2)$

Set vertical scale for display of ccfs: $p := \text{ceil}(\max(ccf2)\cdot 1.2)$

Display ccfs before windowing:

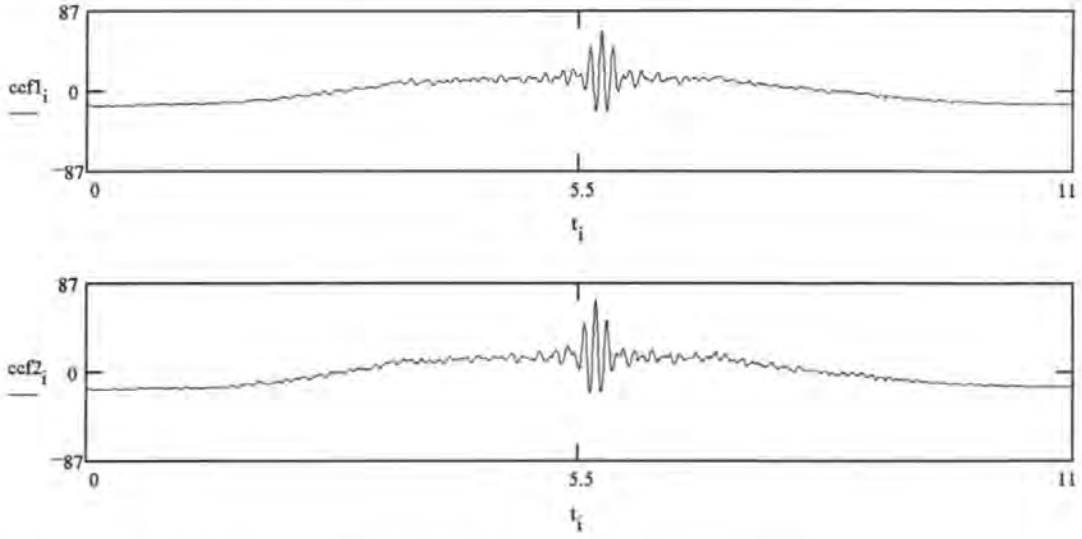

Set "zoom factor": $\gamma := 32$ Set centre of window (μs) : centre := 5.7

Calculate width of window (μs): $\text{width} := \left(\frac{100}{\gamma}\right)$ width = 3.125 $K := \text{ceil}(\text{width}\cdot f_s)$ K = 582

Index for windowed ccf , starting index of window in old range , and time scale in window

$k := 0..K-1$ $\text{start} := \text{ceil}\left[(\text{centre} - 0.5\cdot\text{width})\cdot f_s\right]$ start = 771 $\tau_k := \frac{k}{f_s}$

Pick out winowed ccfs, and remove any d.c. component

$cc1_k := ccf1_{k+\text{start}}$ $cc1 := cc1 - \text{mean}(cc1)$ length(cc1) = 582

$cc2_k := ccf2_{k+\text{start}}$ $cc2 := cc2 - \text{mean}(cc2)$

Determine no. of quantisation levels covered by central correlation peak (treat with caution)

$S_o := \frac{\max(ccf1) + \max(ccf2) - \min(ccf1) - \min(ccf2)}{4}$ $S_o = 45$ $p := \text{ceil}(\max(cc1)\cdot 1.5)$

Display ccfs after windowing ($\gamma = 32$)

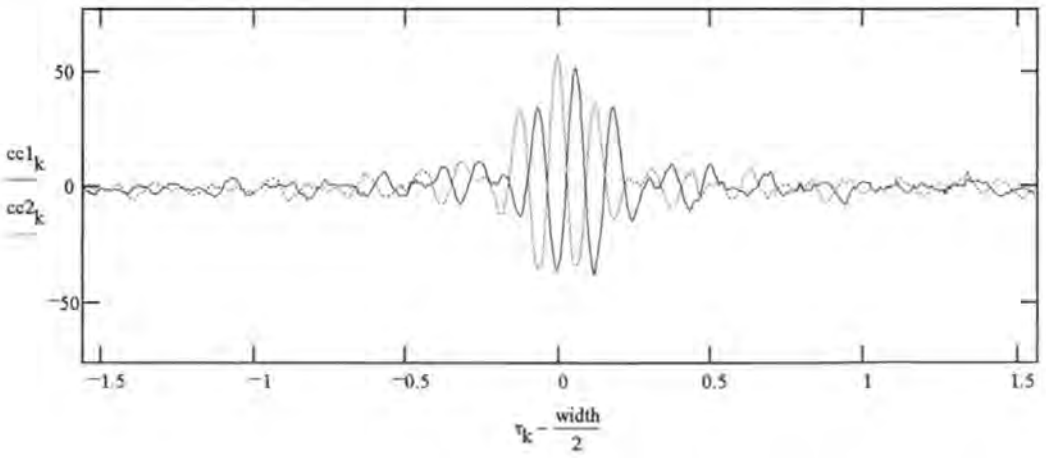

Calculate TDFCSDs and band pass filter between 1 and 16 MHz

$CSD1 := CFFT(recenter(cc1))$ $CSD2 := CFFT(recenter(cc2))$ $f_k := \frac{\gamma \cdot k}{100}$

$CSD1_k := if(f_k < 1, 10^{-4}, CSD1_k)$ $CSD2_k := if(f_k < 1, 10^{-4}, CSD2_k)$

$CSD1_k := if(f_k > 20, 10^{-4}, CSD1_k)$ $CSD2_k := if(f_k > 20, 10^{-4}, CSD2_k)$

Extract mgnitudes and phases of TDFCSDs, and phase difference vector

$M1 := mag(CSD1)$ $M2 := mag(CSD2)$

$P1 := phasecor(phase(CSD1))$ $P2 := phasecor(phase(CSD2))$ $P := P2 - P1$

Display magnitudes of TDFCSD $p := max(M2) \cdot 1.2$

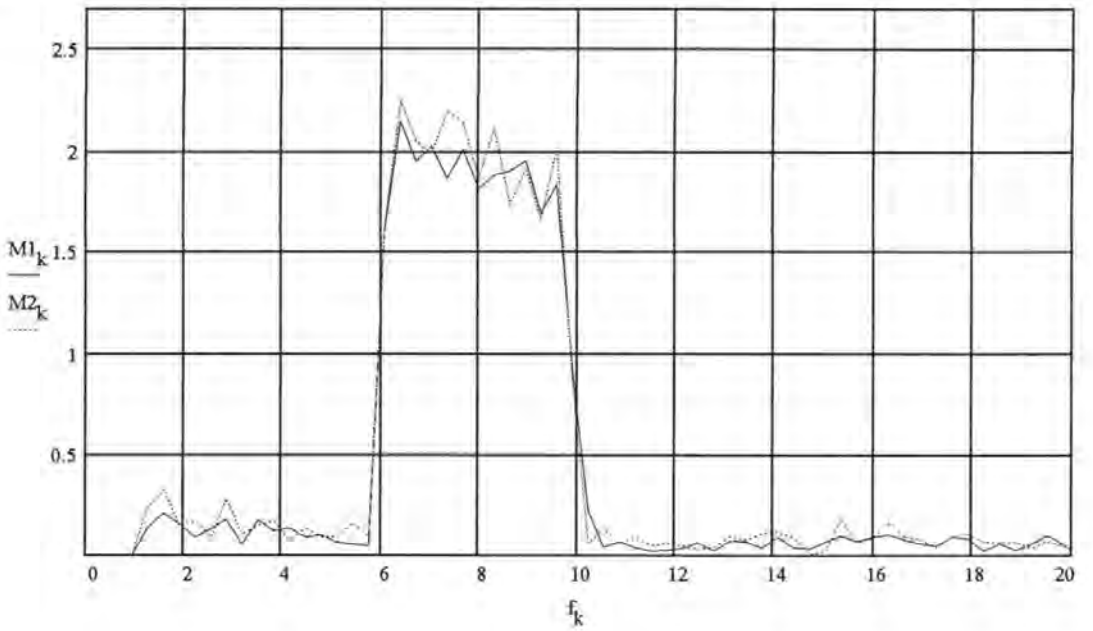

Extract signal terms in range 6 to 10 MHz and noise terms in range 10 to 14 MHz, and calculate mean SNR out

$Sig1_k := if[(f_k > 6) \cdot (f_k < 10), (M1_k)^2, 0]$ $Noise1_k := if[(f_k > 10) \cdot (f_k < 14), (M1_k)^2, 0]$

$Sig2_k := if[(f_k > 6) \cdot (f_k < 10), (M2_k)^2, 0]$ $Noise2_k := if[(f_k > 10) \cdot (f_k < 14), (M2_k)^2, 0]$

$SNR1 := \left(\frac{\sum Sig1}{\sum Noise1}\right)$ $SNR2 := \left(\frac{\sum Sig2}{\sum Noise2}\right)$ $SNR := \frac{\sum Sig1 + \sum Sig2}{\sum Noise1 + \sum Noise2}$

$10 \cdot \log(SNR1) = 27.727$ $10 \cdot \log(SNR2) = 28.287$ $10 \cdot \log(SNR) = 28$ dB

****

Determine start and finish indices for signal and set up index for signal band only

$a := \text{ceil}\left(\frac{100}{\gamma} \cdot f_1\right)$ $b := \text{floor}\left[\frac{100}{\gamma} \cdot (f_1 + B_s)\right]$ $\alpha := 0..b - a - 1$ $f\alpha_\alpha := \frac{\gamma \cdot \alpha}{100}$

Extract phase terms for just signal parts of TDFCSD and obtain differnce phase vector (minus mean)

$D1_\alpha := P1_{\alpha+a}$ $D2_\alpha := P2_{\alpha+a}$ $D := D2 - D1$ $D := \overrightarrow{(D - \text{mean}(D))}$

Calulate slope and intercept of best fit straight line, and equation of that line

$m := \text{slope}(f\alpha, D)$ $c := \text{intercept}(f\alpha, D)$ $Y_\alpha := c + f\alpha_\alpha \cdot m$

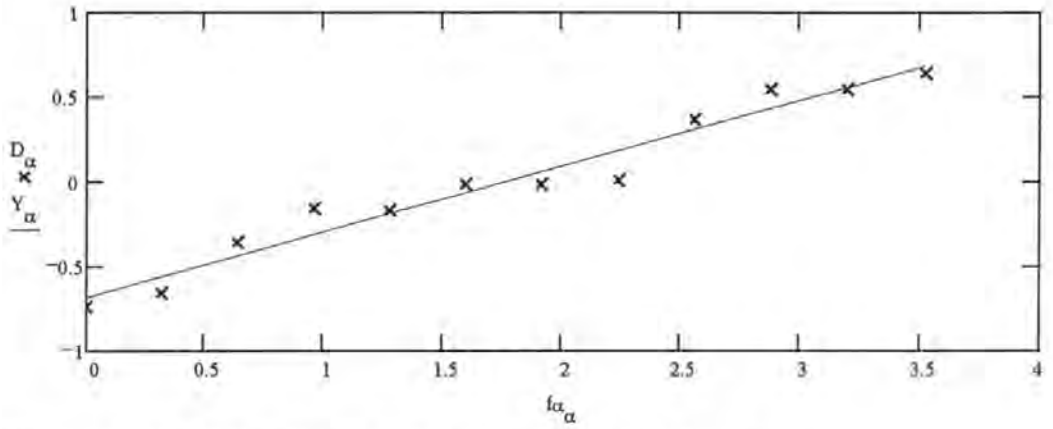

Calculate differences from best fit straight line and hence variance of phase errors

$E := D - Y$ $\text{var}(E) = 0.0083$ $\text{length}(E) = 12$ $\frac{2}{\text{SNR}} = 0.003$

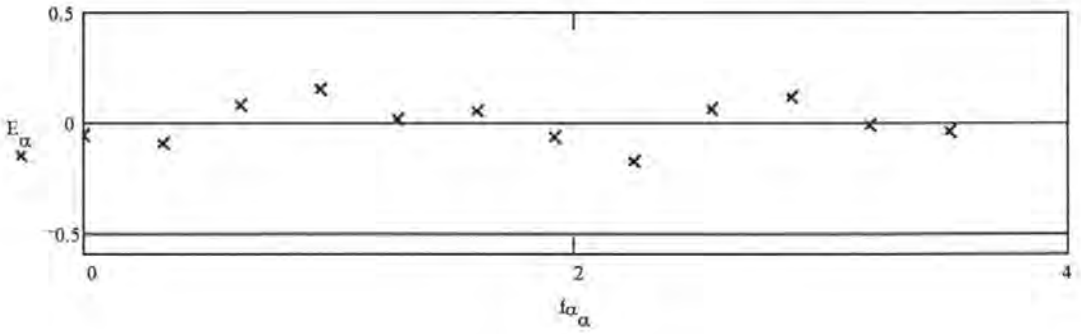

Calculate estimated length of delay line (ns) $t_d := \frac{m}{2 \cdot \pi}$ $t_d \cdot 10^3 = 61.8$ ns

****

Further filter CSDs:

$$CSD1_k := if\left(f_k > 10, 10^{-4}, CSD1_k\right) \qquad CSD2_k := if\left(f_k > 10, 10^{-4}, CSD2_k\right)$$

Create double sided CSDs from single sided CSDs:

$$CSD1_k := if\left(k > floor\left(\frac{K}{2}\right) - 1, \overline{CSD1_{K-k}}, CSD1_k\right) \qquad CSD2_k := if\left(k > floor\left(\frac{K}{2}\right) - 1, \overline{CSD2_{K-k}}, CSD2_k\right)$$

Regenerate ccfs from filtered CSDs:

$$ccf1 := recenter(ICFFT(CSD1)) \qquad ccf2 := recenter(ICFFT(CSD2))$$

Display: $p := ceil(Re(max(ccf1)) \cdot 1.5)$

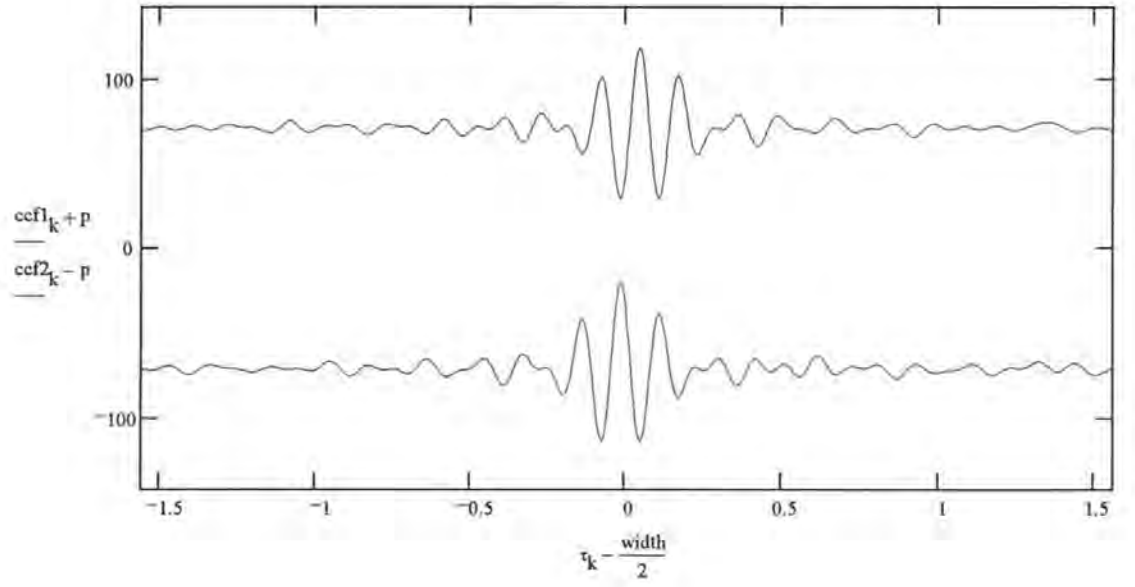

Appendix H. Results for time integrating acousto-optic correlator

The data collected comprised the results of 4 sets of measurements at six values of $SNR_{in.}$: +10, +6, +3, 0, -3 and -6 dB . One sample of the graphical results for each input SNR is displayed here, followed by a table of the final numerical results for all sets of measurements

Scales for graphical results:

Raw data from framegrabber

x-axis: pixels (2048)

y-axis: quantisation levels (256)

ccfs after subtraction of background

x-axis: time (μs)

y-axis: quantisation levels (256)

ccfs after windowing ($\gamma = 32$)

x-axis: time (μs)

y-axis: quantisation levels (256)

Magnitude of TDFCSD

x-axis: frequency (MHz)

y-axis: power density (W Hz^{-1} - arbitrary scale)

Phase difference between TDFCSDs

x-axis: frequency relative to 6 MHz (MHz)

y-axis: phase (radians)

Differences of phase difference from fitted straight line

x-axis: frequency relative to 6 MHz (MHz)

y-axis: phase (radians)

Graphical results for SNRin = +10 dB (exp. 7-06-04)

Raw data from framegrabber:

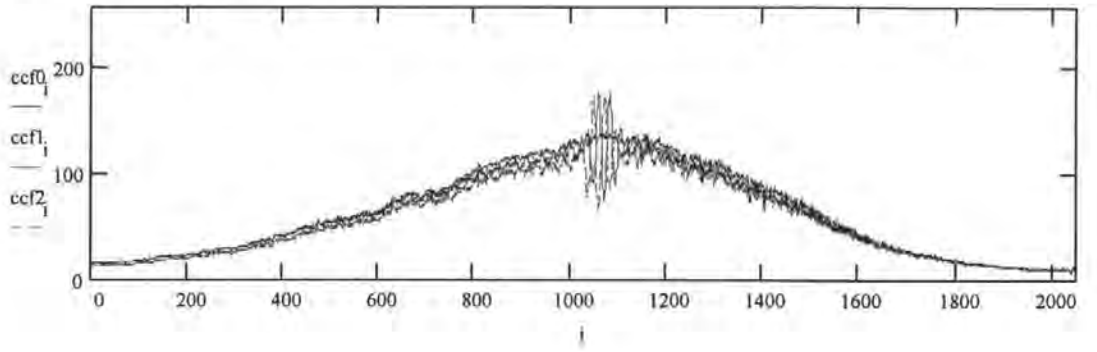

ccfs after subtraction of background:

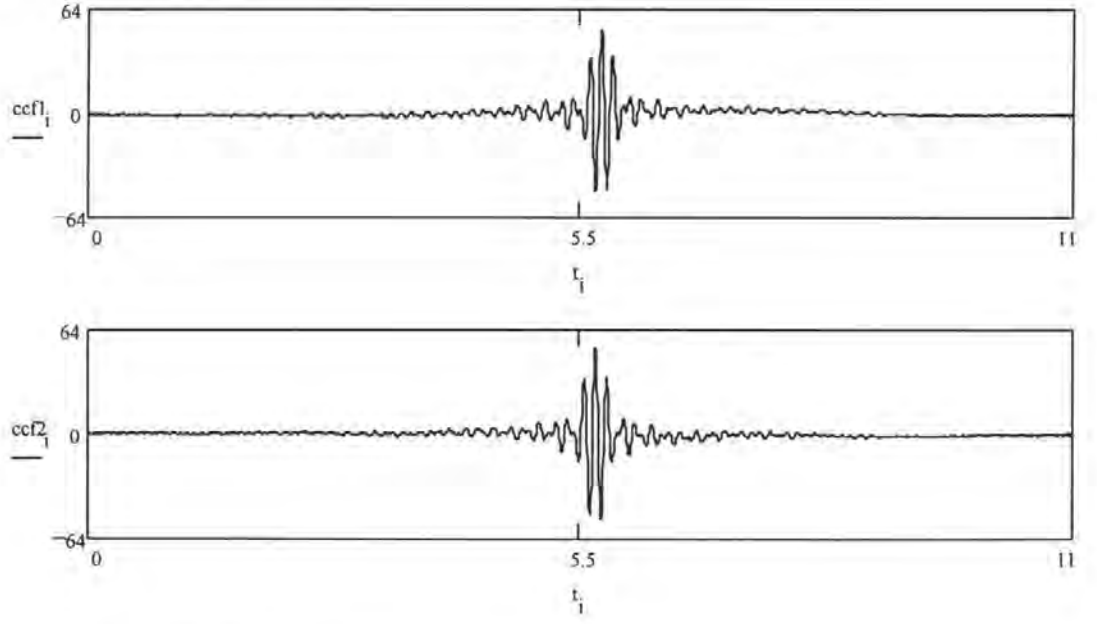

ccfs after windowing ($\gamma = 32$):

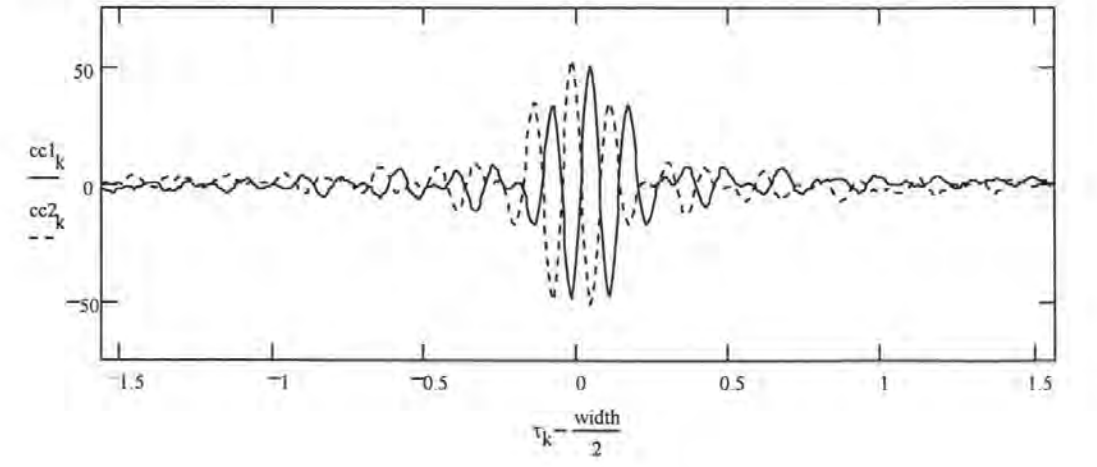

Magnitude of TDFCSDs:

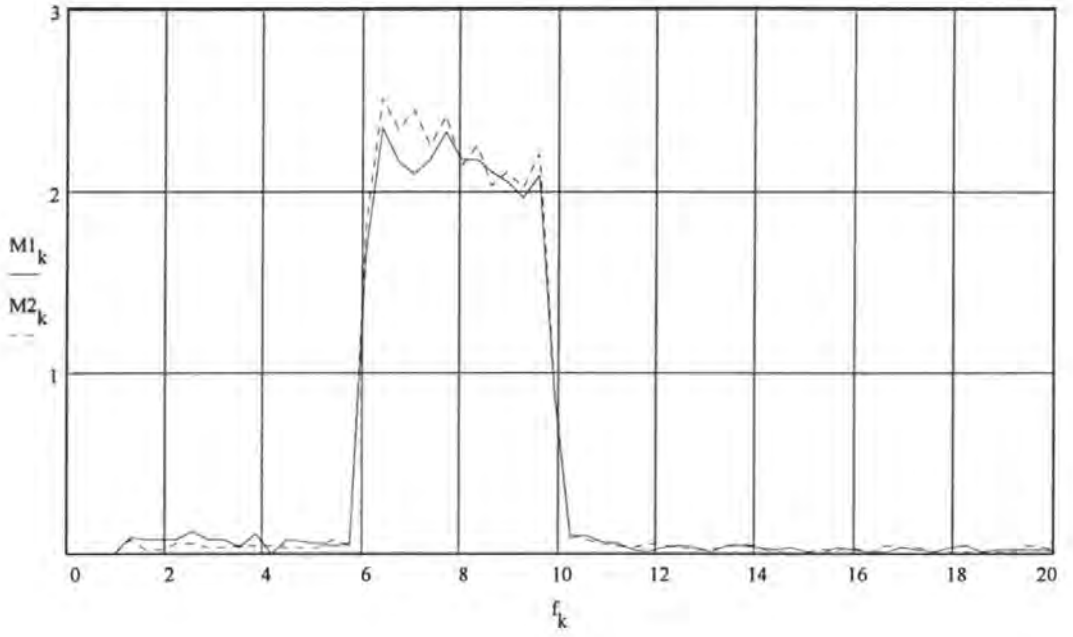

Phase difference between TDFCSDs:

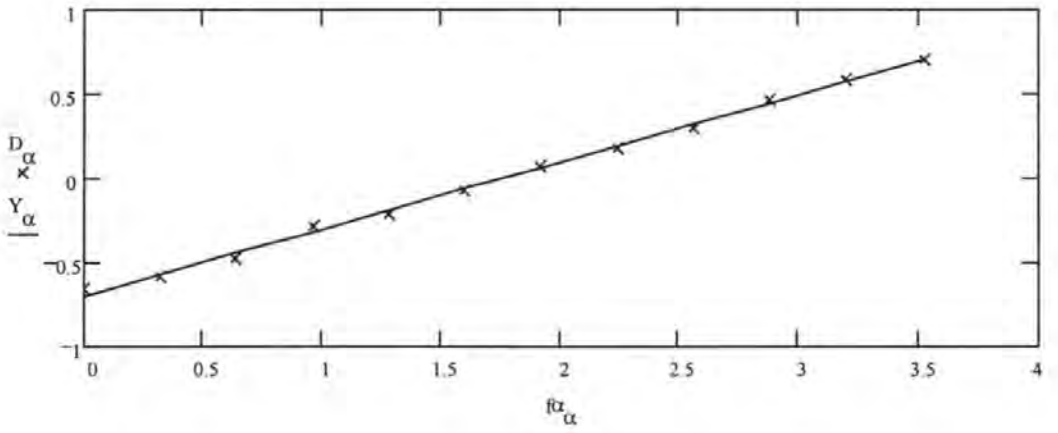

Differences of phase difference from fitted straight line

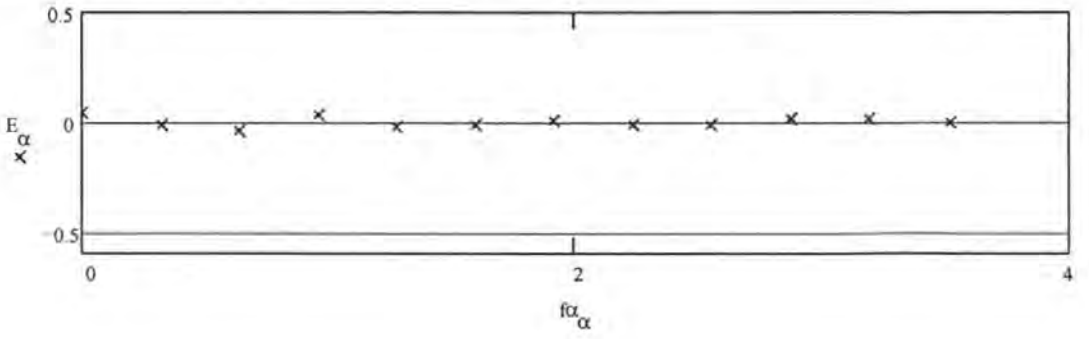

Graphical results for SNRin = +6 dB (exp. 7-12-05)

Raw data from framegrabber:

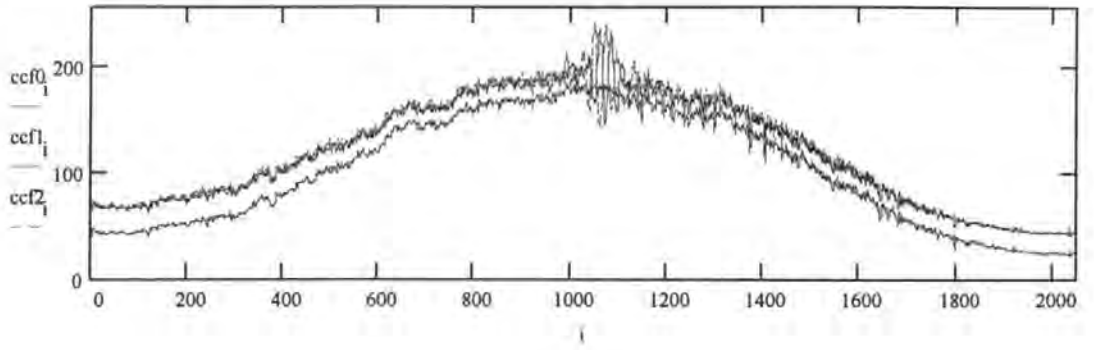

ccfs after subtraction of background:

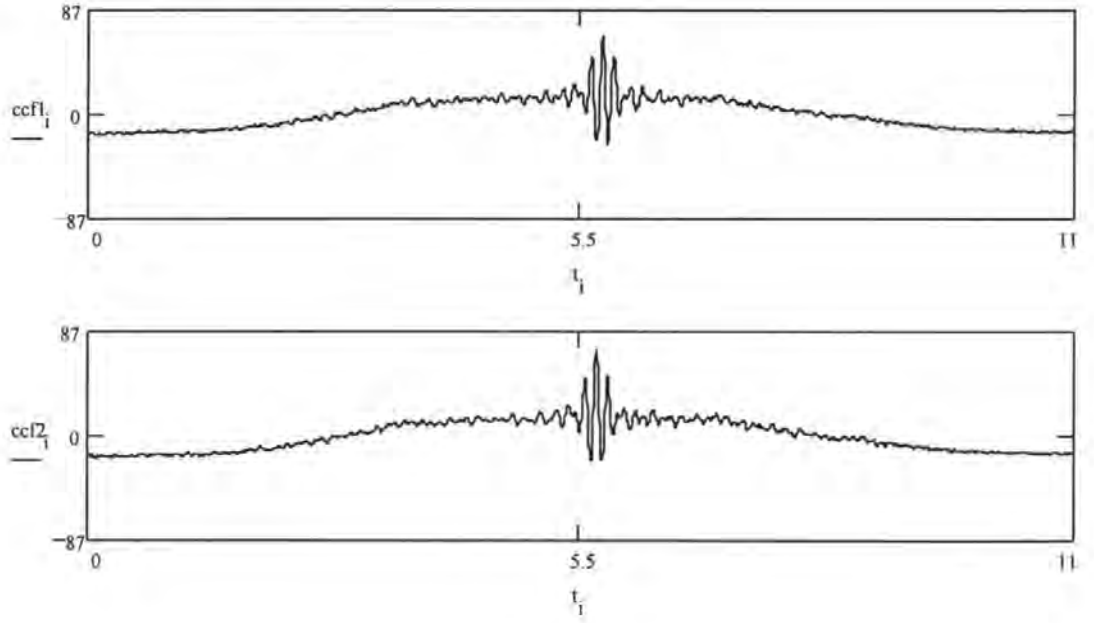

ccfs after windowing ($\gamma = 32$):

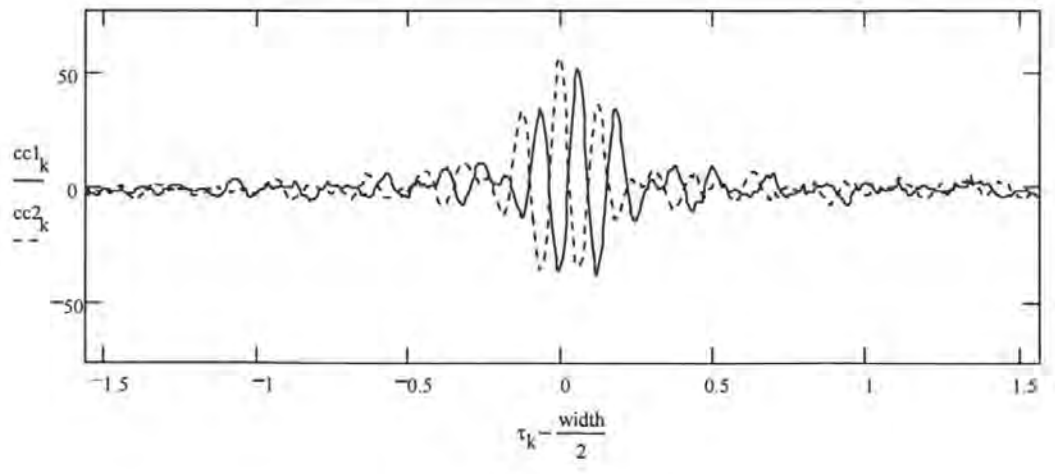

Magnitude of TDFCSDs:

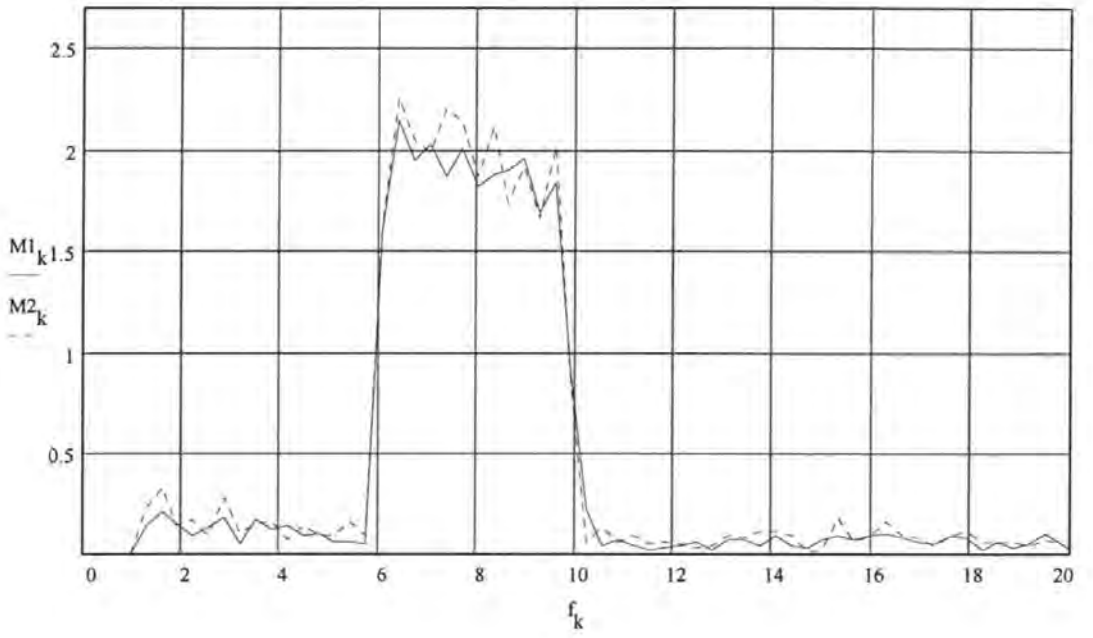

Phase difference between TDFCSDs:

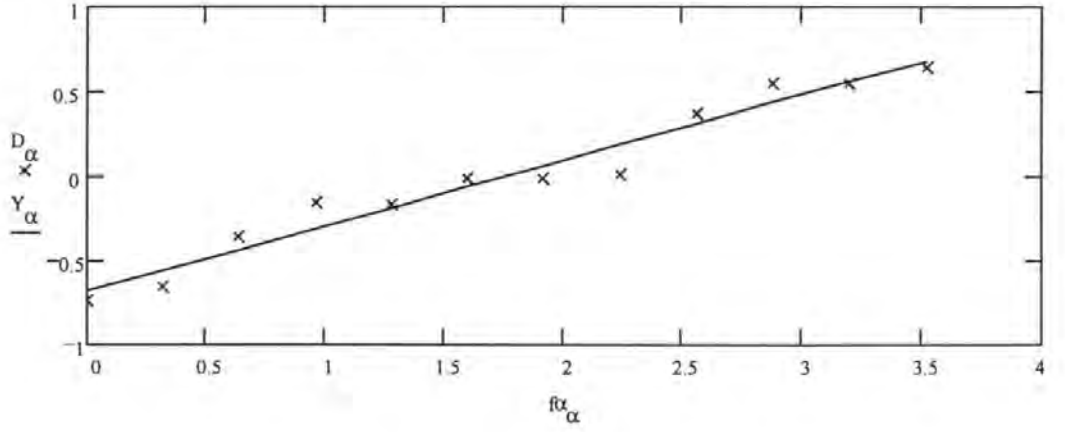

Differences of phase difference from fitted straight line:

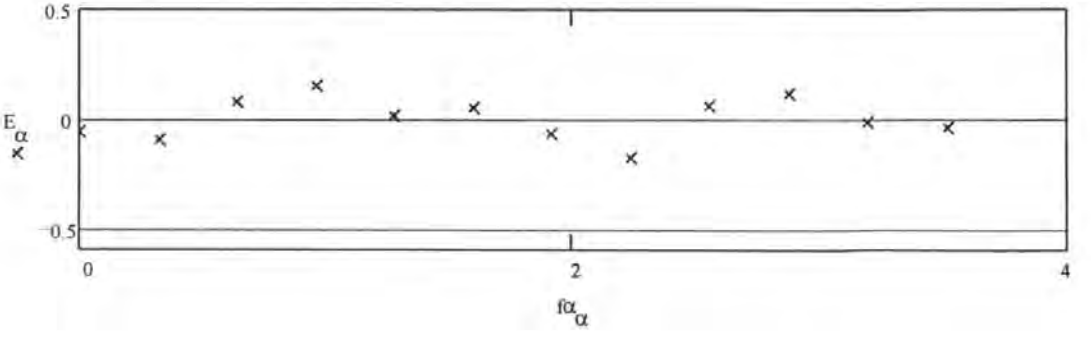

Graphical results for SNRin = +3 dB (exp. 7-12-01)

Raw data from framegrabber:

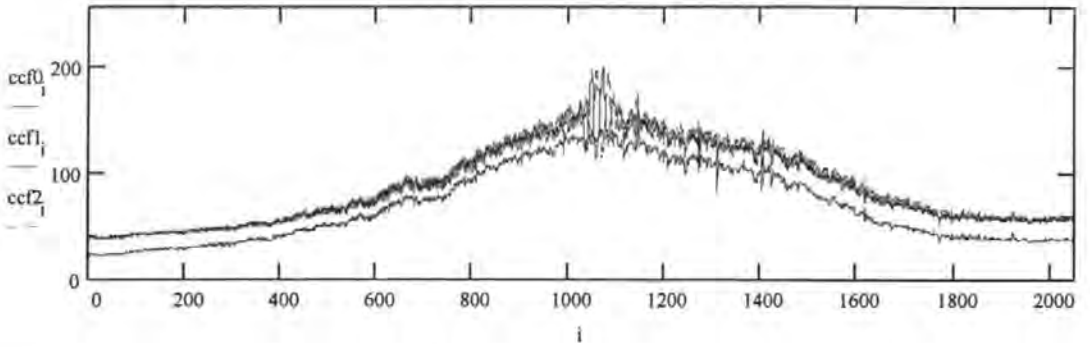

ccfs after subtraction of background:

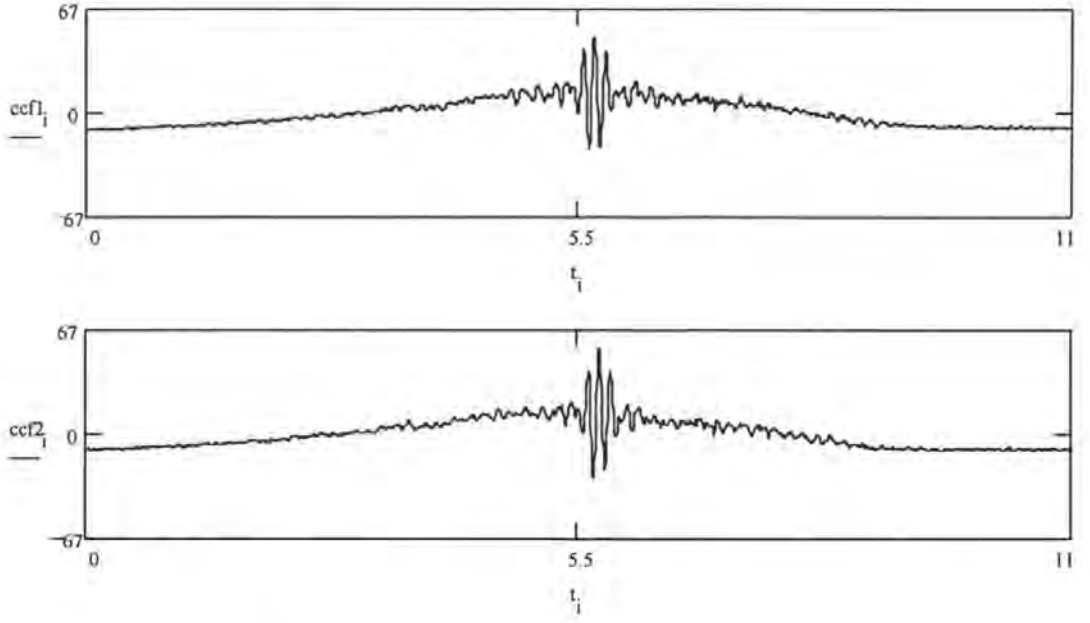

ccfs after windowing ($\gamma = 32$):

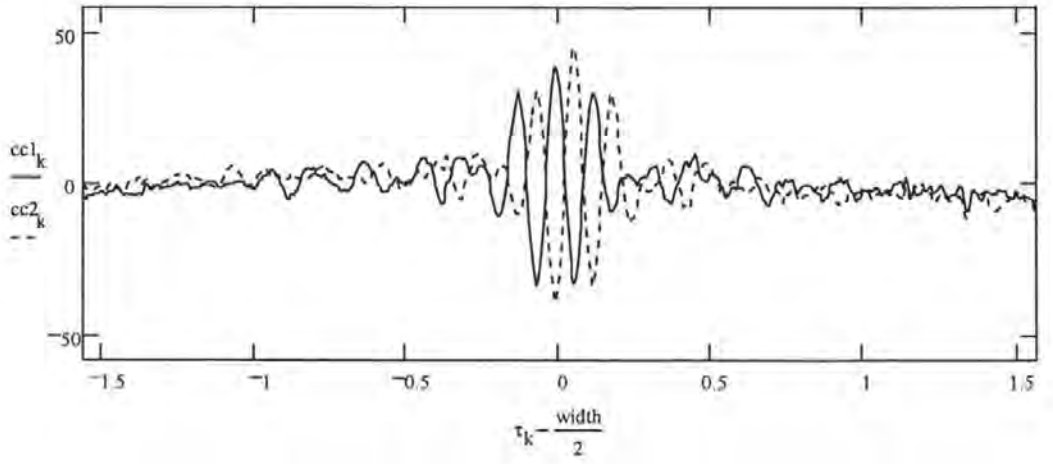

Magnitude of TDFCSDs:

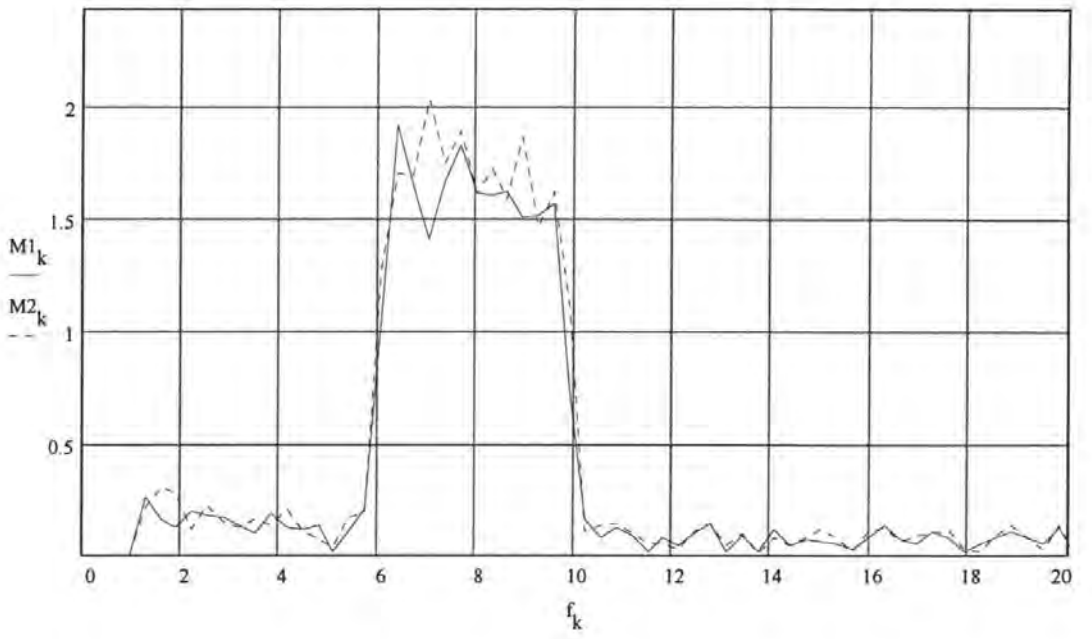

Phase difference between TDFCSDs:

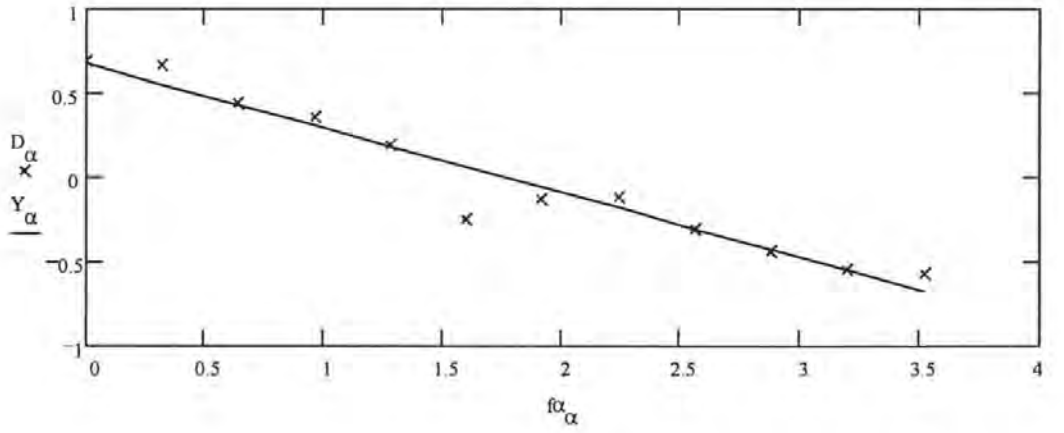

Differences of phase difference from fitted straight line

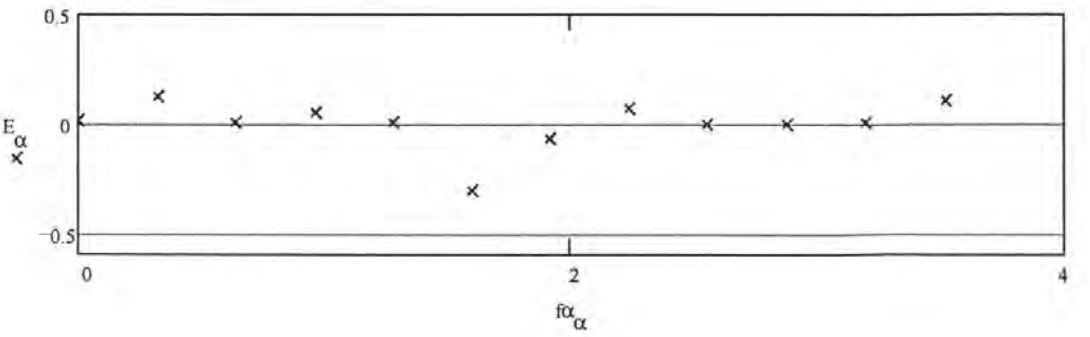

Graphical results for SNRin = 0 dB (exp. 7-06-04)

Raw data from framegrabber:

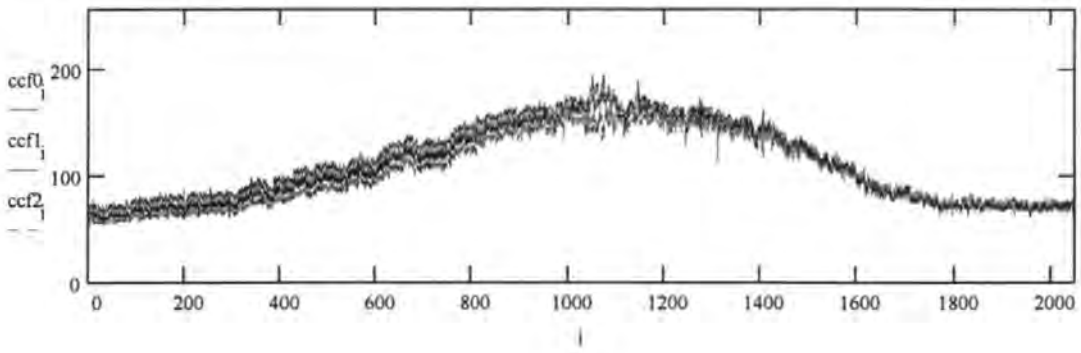

ccfs after subtraction of background:

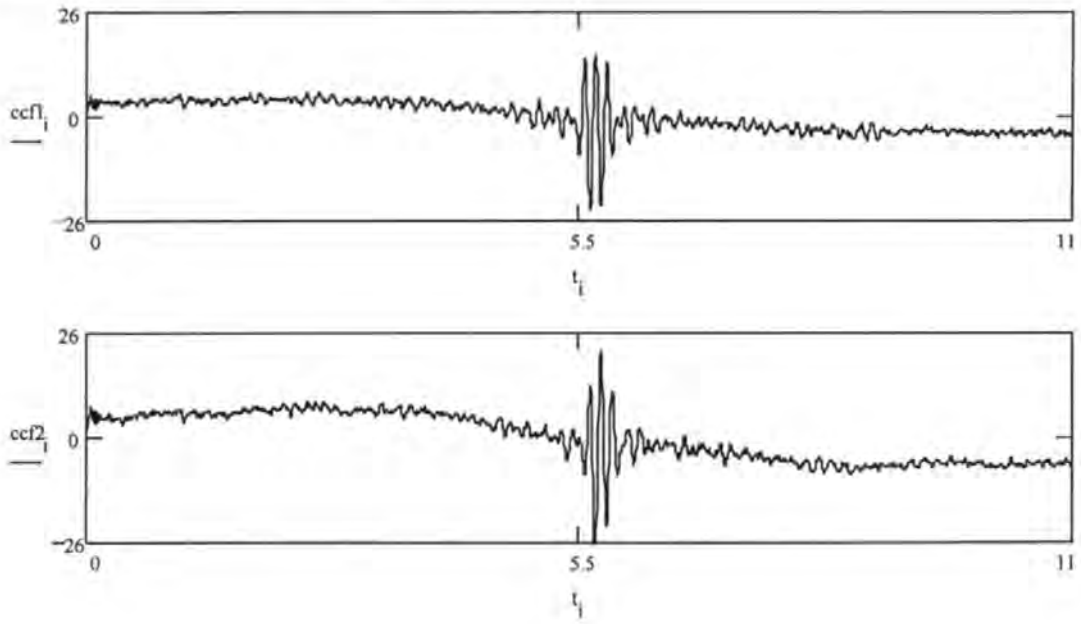

ccfs after windowing ($\gamma = 32$):

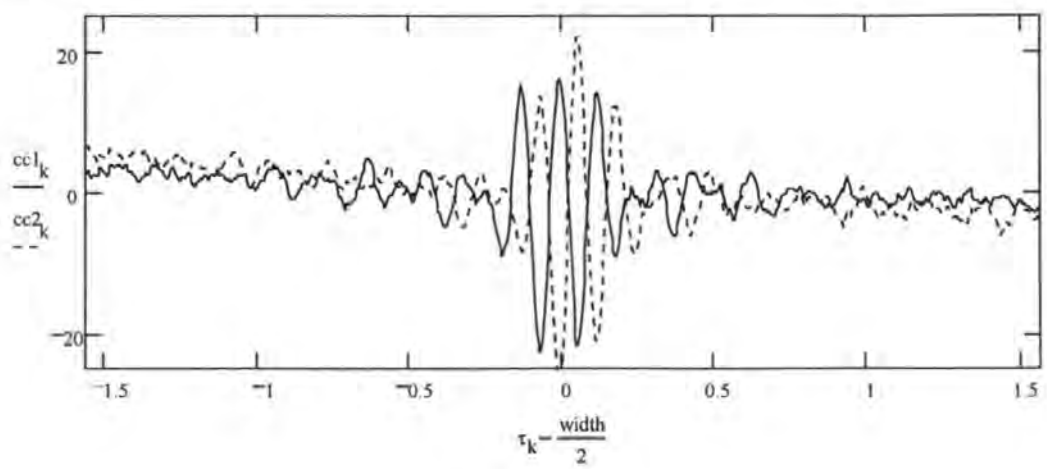

Magnitude of TDFCSDs:

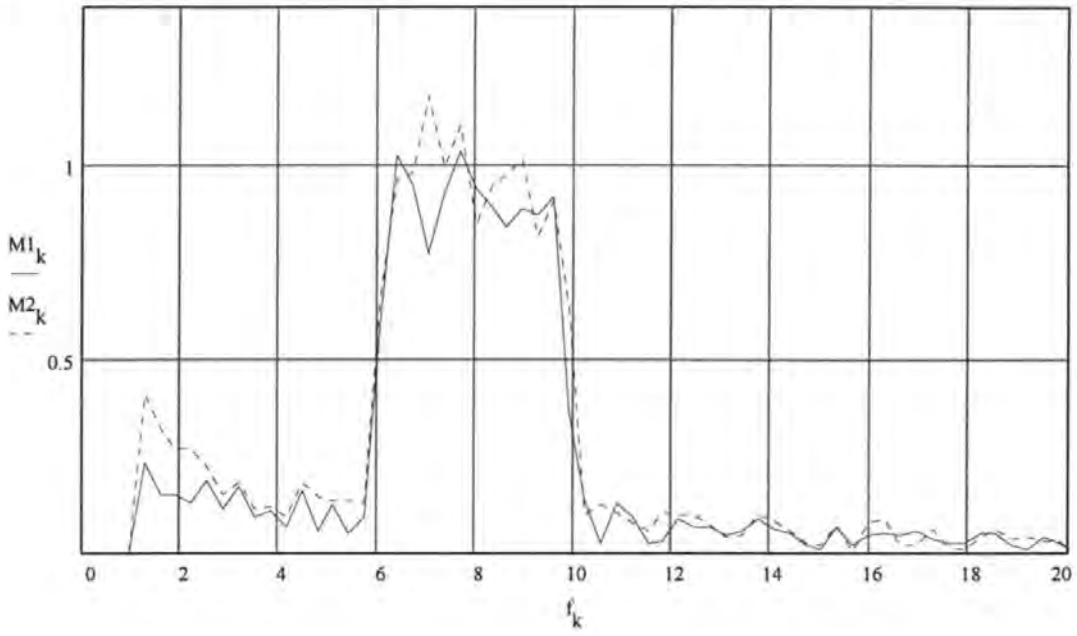

Phase difference between TDFCSDs:

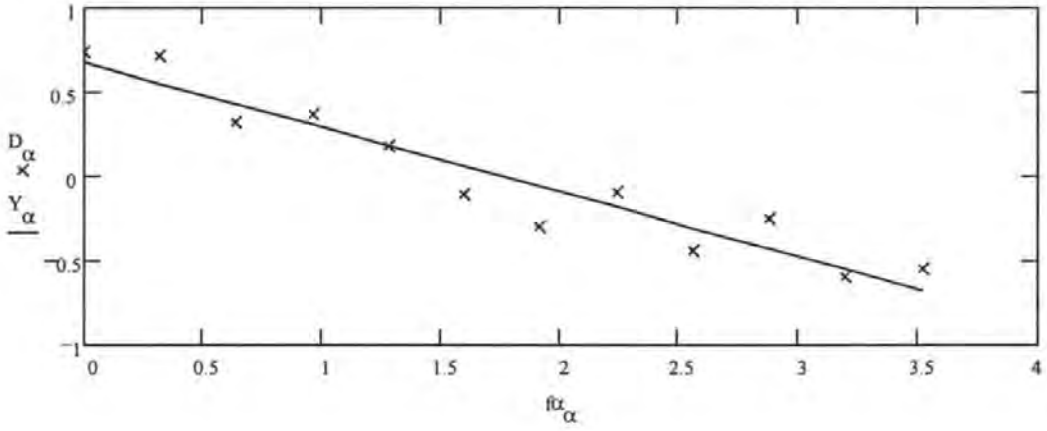

Differences of phase difference from fitted straight line:

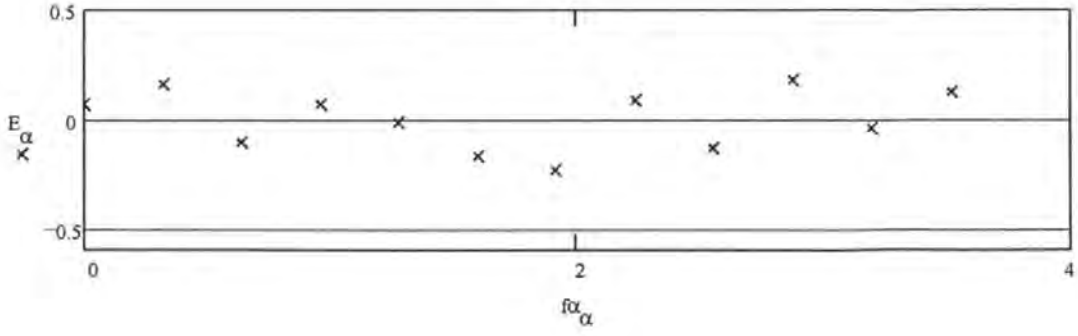

Graphical results for SNRin = -3 dB (exp. 7-15-01)

Raw data from framegrabber:

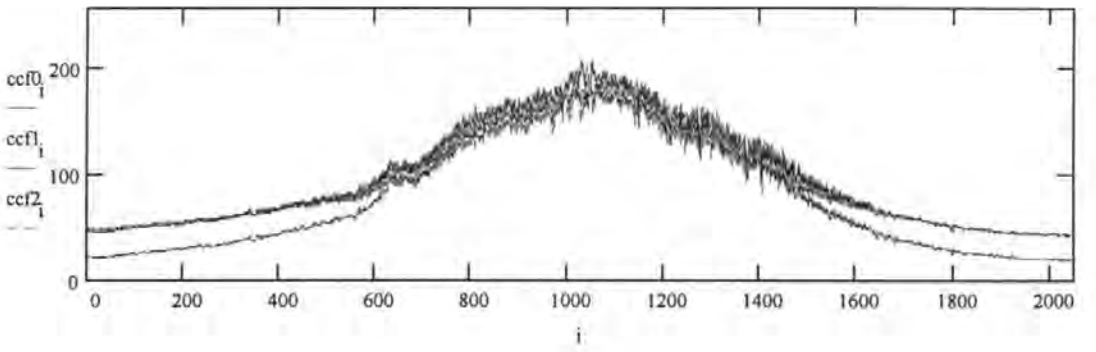

ccfs after subtraction of background:

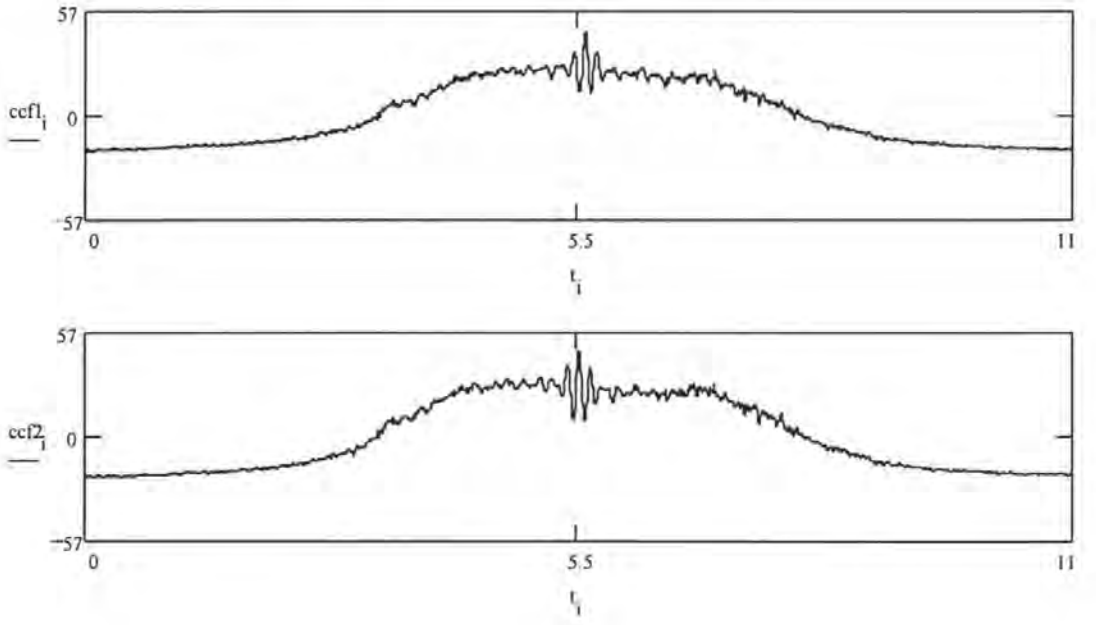

ccfs after windowing ($\gamma = 32$):

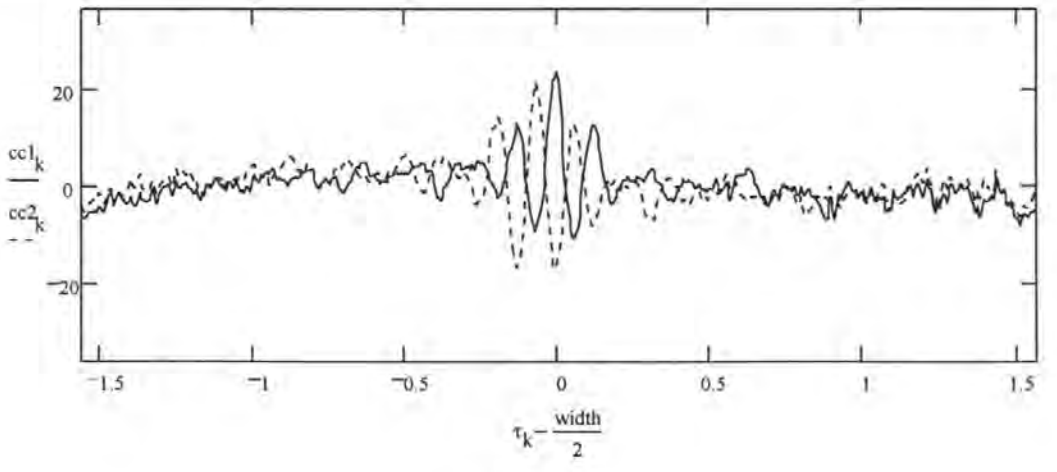

Magnitude of TDFCSDs:

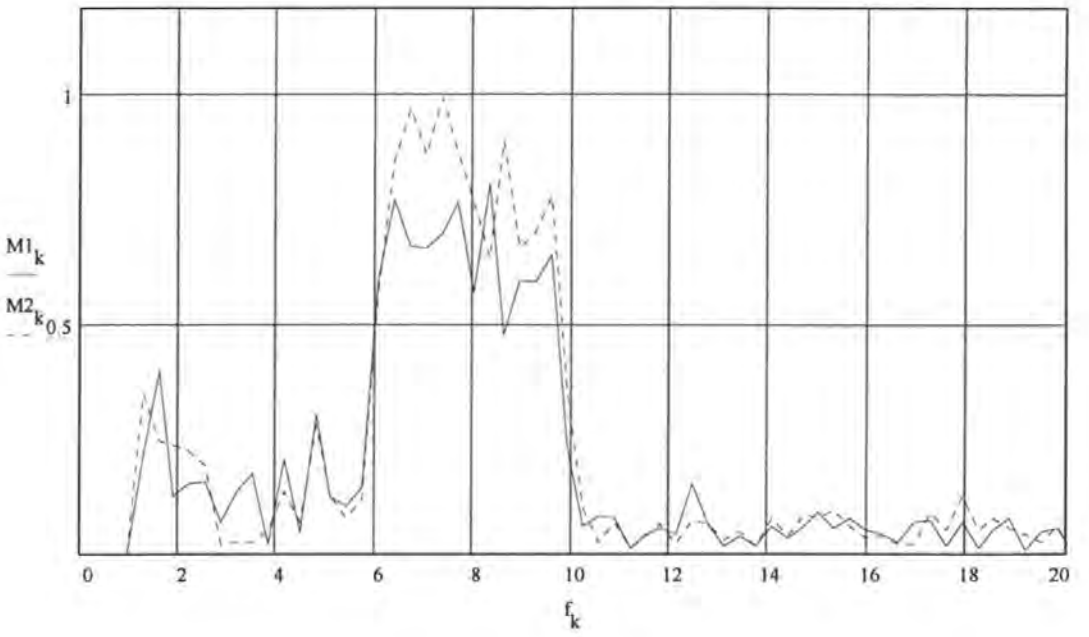

Phase difference between TDFCSDs:

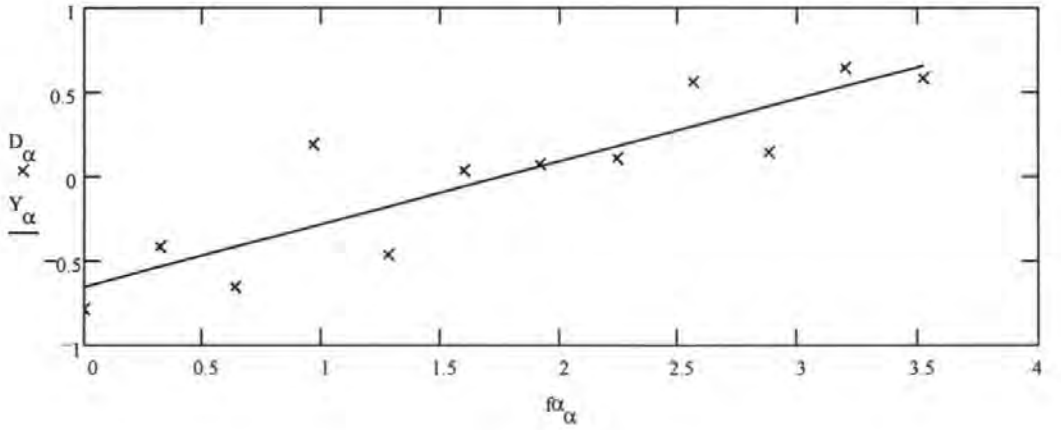

Differences of phase difference from fitted straight line:

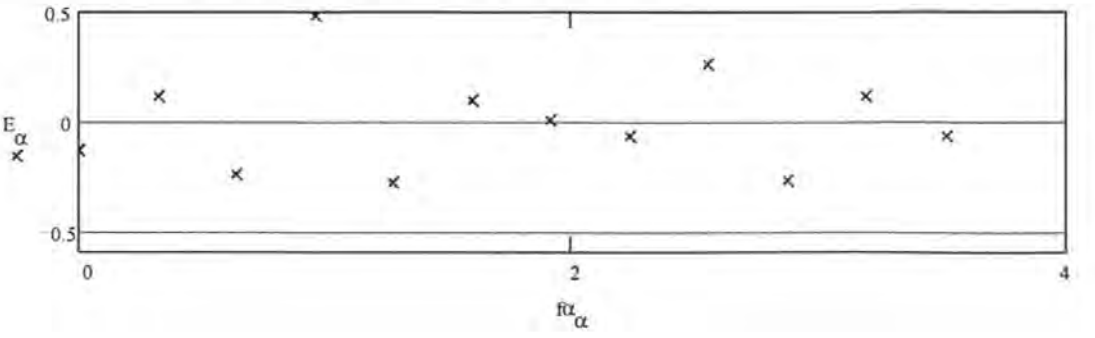

Graphical results for SNRin = -6 dB (exp. 7-06-04)

Raw data from framegrabber:

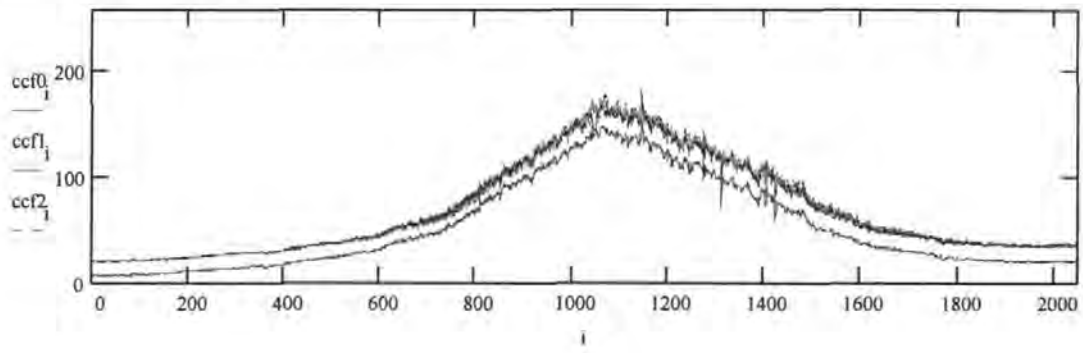

ccfs after subtraction of background:

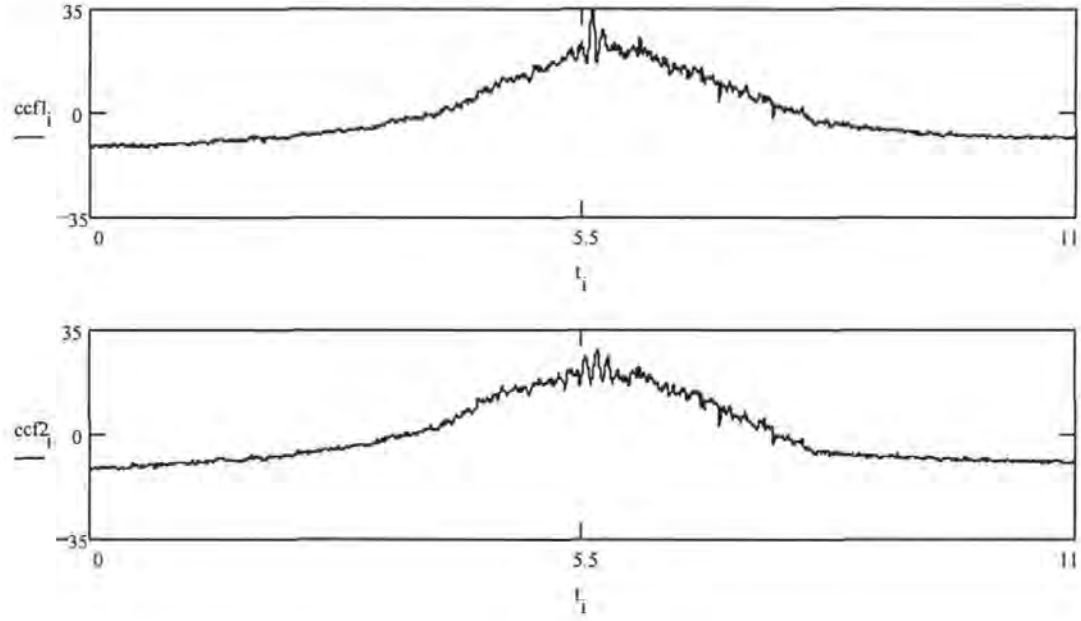

ccfs after windowing ($\gamma = 32$):

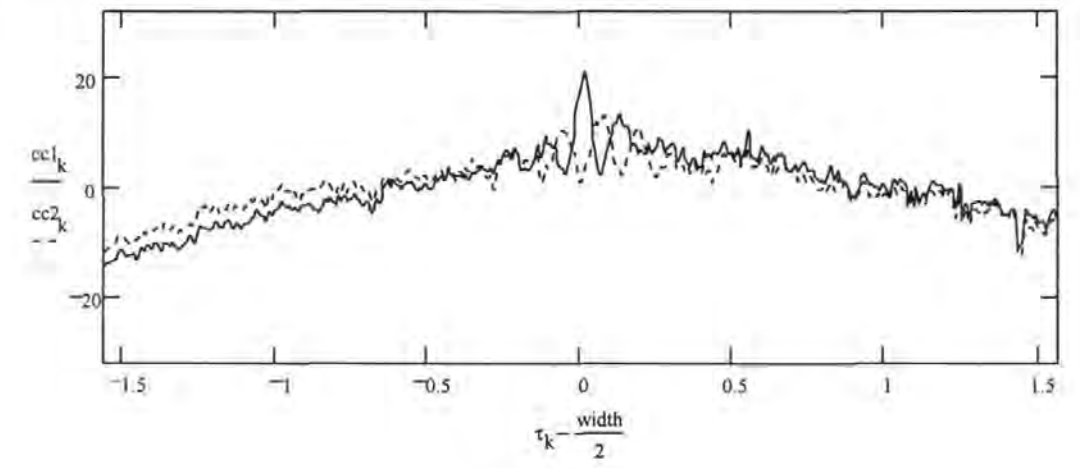

Magnitude of TDFCSDs:

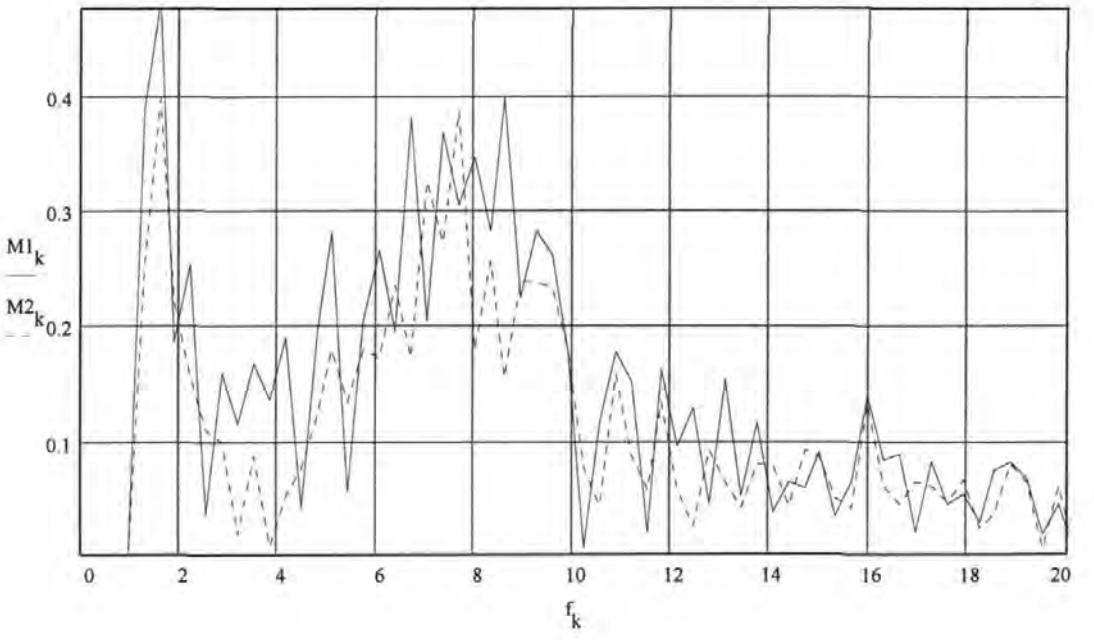

Phase difference between TDFCSDs:

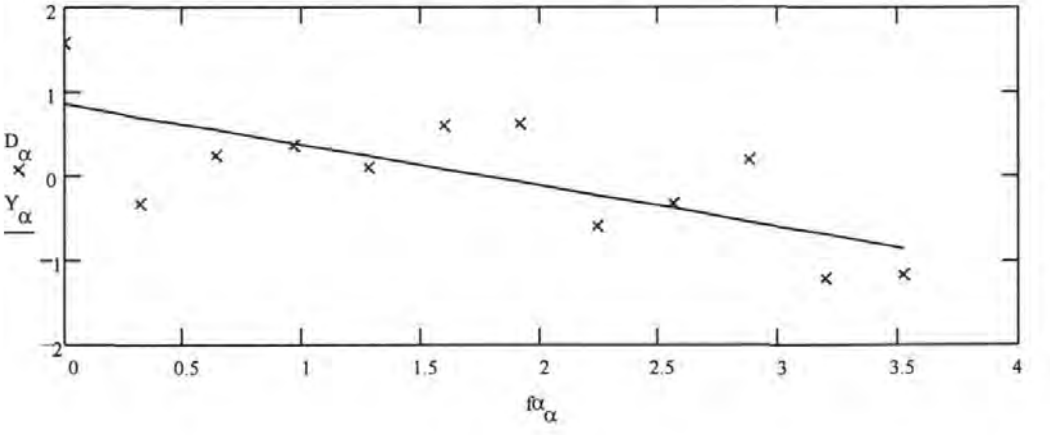

Differences of phase difference from fitted straight line:

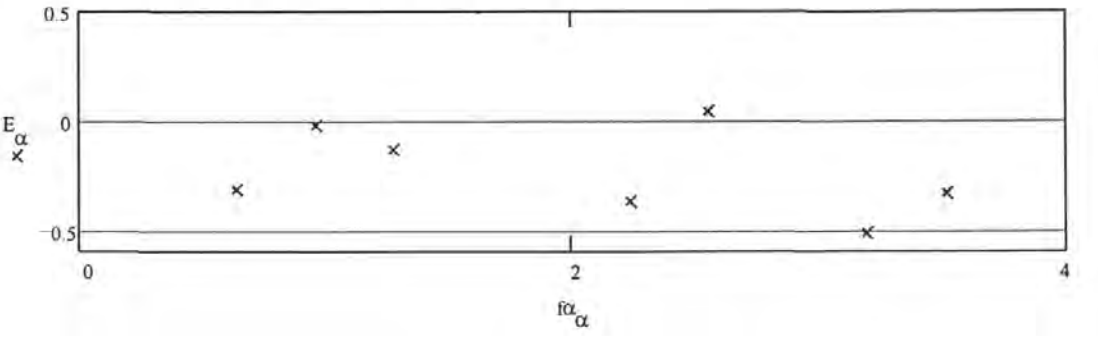

No.	SNR_{in} (dB)	SNR_o (dB) (measured)	height of acf peak	SNR_o (dB) (predicted)	phase variance	measured delay
7-06-01	+10	28.8	41	31.3	0.0013	57.5
7-06-02	+10	29.9	48	31.8	0.0012	58.5
7-06-03	+10	31.0	49	31.9	0.0005	64.4
7-06-04	+10	32.0	51	32.0	0.0005	63.2
7-12-05	+6	28.0	45	28.3	0.0083	61.8
7-12-06	+6	28.1	45	28.3	0.0100	60.8
7-12-07	+6	28.7	44	28.2	0.0038	62.2
7-12-08	+6	27.8	45	28.3	0.0018	66.1
7-12-01	+3	24.9	39	24.8	0.0109	61.0
7-12-02	+3	25.1	41	24.9	0.0126	58.4
7-12-03	+3	24.1	40	24.9	0.0170	64.2
7-12-04	+3	22.7	39	24.8	0.0102	53.6
7-14-01	0	20.8	20	20.4	0.0169	61.0
7-14-02	0	21.4	30	20.8	0.0593	62.7
7-14-03	0	18.7	25	20.6	0.0614	53.9
7-14-04	0	19.6	25	20.6	0.0348	60.9
7-15-01	0	21.5	32	20.8	0.0421	58.2
7-15-02	-3	16.2	15	15.9	0.1207	66.4
7-15-03	-3	16.5	11	15.6	0.0441	60.7
7-15-04	-3	16.0	23	16.1	0.1174	60.4
7-15-05	-3	16.8	21	16.1	0.0868	46.9
7-15-06	-6	8.8	4	9.6	0.2880	76.5
7-15-07	-6	8.3	4	9.6	0.7727	57.1
7-15-08	-6	8.6	4	9.6	0.9752	49.4
7-15-09	-6	10.3	4	9.6	0.6943	81.6
Averages						
	+10	30.4		31.8		61.1
	+6	28.2		28.3		
	+3	24.2		24.8		
	0	20.4		20.6		
	-3	16.4		16		
	-6	9		9.6		

Table H-1. Results of measurements of SNR in the output TDFCSD for various values of inputSNR for the experimental correlator shown in figure 11-2.

Appendix I: Details of equipment used

The following details are not exhaustive. Where the list of specification is relatively short all relevant details available are given. For items of test equipment, with specifications running to many pages, reference is made to the appropriate user's manual.

Acousto-optic cell

The Acousto-optic cell used in all experiments was a model OPT-1 Isomet cell with the following specifications

Interaction medium	TeO_2 - shear (110)
Operating wavelength	633 nm
Time bandwidth product	1500
Centre frequency	45 MHz
3 dB bandwidth	30 MHz
Active aperture	4 mm H × 31 mm L
Time aperture	50 μs
Acoustic velocity	617 ms^{-1}
Diffraction efficiency	> 50 % at 0.5 W RF power
Optical surface flatness	λ/10 or better
Maximum RF power	1 W CW

RF amplifier/modulator

Model no. 231A-1-45
Carrier frequency 45 ± 0.004 MHz

Power output:	Max	1.0 W min
	Min	0.1 mW max
	Quiescent	0.25 W nominal
On/off ratio	40 dB minimum	
Input voltage	28 ± 0.5 V d.c.	
Input current	400 mA nominal	

Polynomial waveform synthesiser

Anologic Data Precision model D2045 arbitrary waveform generator

High level output:	5.0 V p-p into 50 Ω
Maximum clock rate:	800 MHz
Waveform resolution:	8 bits
Waveform memory:	512 K points

For full specification see User's Manual

Diode laser supplied by Uniphase

The Uniphase "Model 3501 Diode Laser System" has integrated automatic temperature control. A driver unit provides power to the system and modulation is acheived through a separate input directly to the laser. The laser system specifications include the following

Beam circularity	> 98 %
Noise (rms, 30 Hz-20 MHz)	< 0.5 %
Input voltage range	3 to 0 volts
Modulation rise time (10 % -90 %)	20 ns
Modualtion fall time (90 % -10 %)	20 ns
Modulation settling time (±1 % of final power)	80 ns
Modulation bandwidth (3 dB points)	20 MHz
Modulation depth	100:1
Wavelength (±1.5 %)	670 nm
Linewidth (FWHM, 1mW)	<0.1 nm
Beam diameter (TEM_{oo}, $1/e^2$ points, ±3 %)	0.37 mm
Beam divergence (TEM_{oo}, ±1 %)	2.5 mrad
Maximum ouput power	1 mW
Polarization state	linear, stable

Measurements show that the input modulation voltage range is in fact 0 V (maximum power) to approx 2.4 V (minimum power). Hence a d.c bias of 1.2 V was added to all a.c. input signals. The noise equates to an input rms noise voltage of 0.5 % of 3 V, which is 0.015 V.

Diode laser supplied by Melles Griot

Part No. 56-DFL-SDL-7501-G1-xx7

Spectra Diode Labs, 15 mW output, 635 nm diode laser with thermoelectric cooling, beam circularisation and collimation, and built in bias-tee network allowing modulation at up to 300 MHz

additonal data as supplied by Melles Griot:

Temperature (°C)	25
Wavelength (nm)	631
Nominal power (mW)	15
Peak power (mW)	15
Optical efficiency (%)	65
Collimator's output power (mW)	9.8
Laser current (I_{op}, mA)	72.0
Monitor current (I_{mon}, mA)	0.237
Threshold current (I_{th}, mA)	53.0
Differential efficiency (mW/mA)	0.80
Beam size, major axis (mm, $1/e^2$)	8.00
Beam size, minor axis (mm, $1/e^2$)	7.16

Laser Driver

Part no. 06-DLD-203, providing d.c. drive and thermoelectric cooling to Melles Griot diode laser assembly

Full specifications are given in the Operator's manual.

CCD array

Loral Fairchild CAM1830 linescan camera using CCD181 high speed linear imaging sensor

2048 elements selected out of 2592 photosite array
10 μm × 10 μm photosites on 10 μm pitch

Typical output random noise (rms) 340 μV
Saturation output level 1 V
(Hence SNR for output level at saturation: 69.4 dB)

For further details see 1991 Loral Fairchild CCD imaging databook pp 99-109 and pp 209-214

The CAM1830 linescan camera was used with a PC containing 3 cards:

OVB7 Power supply board

Dipix P360F-4MB-C Framegrabber and DSP board

P360-DIS-SBO Piggyback Display Board/1MB memory

Full details of the above are given in the accompanying Dipix manuals.

Digital Oscilloscope

Analogic Data Precision Model 6100 Universal Waveform Analyser

Appendix J. Published work

1. Houghton, A.W. and Reeve, C.D.: 'A zeroth order non-heterodyning space integrating acousto-optic correlator', Inst. Phys. Conf. Ser. No 139: Part III, pp 325-328, presented at Opt. Comput. Int. Conf., Edinburgh, 22-25 Aug 1994.

2. Reeve, C.D. and Houghton, A.W.: 'Performance of an acousto-optic joint transform correlator', Inst. Phys. Conf. Ser. No 139: Part III, pp 321-324, presented at Opt. Comput. Int. Conf., Edinburgh, 22-25 Aug 1994.

3. Houghton, A.W. and Reeve, C.D.: 'Direction finding on spread spectrum signals using a cross correlation receiver', Microwaves 94 Conf. Proc. pp 304-308. (Int. Conf. sponsored by IEE/IEEE/MTT, Wembley, October 1994)

4. Reeve, C.D. and Houghton, A.W.: 'Performance modelling of an acousto-optic joint transform correlator', Microwaves 94 Conf. Proc. pp 430-433. (Int. Conf. sponsored by IEE/IEEE/MTT, Wembley, October 1994)

5. Houghton, A.W. and Reeve, C.D.: 'Detection and direction finding on spread spectrum signals using the time domain filtered cross spectral density, IEE Colloquium on High Resolution Spectral Estimation and Direction Finding, April 1995.

6. Houghton, A.W. and Reeve, C.D.: "Spread spectrum signal detection using a cross correlation receiver", Sixth International conference on 'Radio Receivers and Associated Systems', University of Bath, 26-28 September 1995.

7. Houghton, A.W. and Reeve, C.D.: "Detection of spread spectrum signals using the time domain filtered cross spectral density", IEE Proceedings: Radar, Sonar and Navigation.